THE UNIVERSITY *of* EDINBURGH

Drug screening to identify inhibitors of the structure-specific endonuclease ERCC1-XPF

Ewan Murray McNeil

Thesis presented for the degree of PhD
The University of Edinburgh
2012

Declaration

I hereby declare that this thesis has been composed by me and it has not been accepted in any previous applications for a degree at this time, or at any other university. The work described has been performed by me, except where expressly indicated otherwise. All sources of information have been specifically acknowledged. The experiments were designed in collaboration with my supervisor Professor David W. Melton.

Ewan Murray McNeil

Acknowledgements

I would like to express my gratitude to my supervisor Professor David W. Melton for his continued support and guidance over the past four years. In addition, I would also like to thank all members of the Melton lab past and present for their support and contribution to this project. I would also like to thank my second supervisor Dr E. Elizabeth Patton for her guidance and support. Without either, this project would not have come to fruition.

I would also like to thank our collaborators within the University of Edinburgh, particularly Professor Malcolm Walkinshaw, Dr Martin Wear, Dr Steven Shave, Dr Doug Houston and Dr Jacqueline Dornan. Without their knowledge and expertise, this project would not have been possible. I would also like to thank our collaborators at MRC Technology, particularly Dr Barbara Saxty and Dr Preeti Bakrania. Without their knowledge and expertise, this project also would not have been possible.

I would like to thank Cancer Research UK who financed my research and stipend. In addition I am grateful for the additional training that they provided. I also acknowledge MRC Technology who have financed the ERCC1-XPF inhibitor project.

Finally I would like to thank my family for their support. Without them, this thesis would not exist.

Table of Contents

Figures

Tables

Abstract

Malignant melanoma results in 132,000 cases worldwide each year with an incidence rate that is increasing faster than for any other skin cancer. In the UK, cutaneous melanoma is the sixth most commonly diagnosed cancer and the second most common in young people aged 15-34 (excluding non-melanoma skin cancer). Furthermore, while less common than NMSC, malignant melanoma accounts for 4% of skin cancer cases and 74% of skin cancer-related deaths. Although early surgical removal of primary tumours is an effective treatment, patients that develop metastatic melanoma have a very poor prognosis (5 year survival rate is only 5%).

Elevated expression of a number of DNA repair genes has been reported in primary melanomas that subsequently metastasised when compared to non-recurrent primary tumours. In addition, patients who do not respond to chemotherapy have elevated expression of DNA repair genes. One chemotherapeutic that is effective against a range of other cancers, but not melanoma is cisplatin. Elevated levels of the DNA repair protein ERCC1, which is needed to remove cisplatin-induced DNA damage, has been found to be an indicator of poor prognosis in ovarian and lung cancer.

To test our hypothesis that elevated ERCC1 levels account for an increased resistance to cisplatin in melanoma, a xenograft experiment was performed. Our results show that ERCC1 proficient melanoma xenografts initially responded to cisplatin treatment however resistance soon followed. Tumours deficient in ERCC1 however could be cured after only two treatments of cisplatin, indicating a novel method to overcome chemoresistance in metastatic melanoma.

The aim of the project was to identify novel compounds to improve therapy of melanoma. To achieve this, in collaboration with Dr Patton we performed a cell culture screen to identify compounds which display specificity against melanoma cell lines. In addition, we sought to identify compounds which would overcome

cisplatin resistance. We identified a series of nitrofuran compounds which are potent against melanoma and neuroblastoma cell lines and enhanced the toxicity of cisplatin through an ERCC1 independent pathway. In addition, we showed that melanin pigmentation is protective against nitrofuran toxicity.

We have proposed the structure specific endonuclease, ERCC1-XPF, as a drug target to overcome chemoresistance. We collaborated with Professor Walkinshaw to perform an *in silico* screen for protein-protein interaction inhibitors to disrupt the obligate dimerization between ERCC1 and XPF. In addition we directly inhibited the endonuclease activity by developing XPF endonuclease domain inhibitors and utilised a range of biochemical, molecular biology and cell culture assays to validate ERCC1-XPF inhibitors.

Furthermore, we developed an *in vitro* endonuclease assay for ERCC1-XPF, FEN1 and DNase1 and utilised these to demonstrate compound specificity of our validated ERCC1-XPF inhibitors. In collaboration with MRC Technology we utilised the ERCC1-XPF endonuclease assay to perform a high throughput screen. We characterised hit compounds to demonstrate physical binding and *in vitro* specificity for ERCC1-XPF.

In conclusion, we have discovered new compounds which may prove beneficial for the treatment of malignant melanoma.

Abbreviations

A	Amps
Å	Angstrom
Da	Dalton
°C	Degrees Celsius
g	Gram
l	Litre
m	Metre
’	Minutes
M	Molar
Mr	Molecular weight
Mol	Moles
RFU	Relative fluorescence units
RU	Response units
”	Seconds
Tm	Transition melting temperature
v/v	Volume against volume
w/v	Weight against volume
p	Pico (10^{-12})
n	Nano (10^{-9})
µ	Micro (10^{-6})
m	Milli (10^{-3})

TPA	12-O-tetradecanoylphorbol-13-acetate
EDC	1-Ethyl-3-(3-diaminopropyl) carbodiimide hydrochloride
BME	2-Mercaptoethanol
FAM	6-Carboxyfluorescein
ATP	Adenosine triphosphate
APS	Ammonium persulphate
APE1	Apurinic/apyrimidinic endonuclease
ATA	Aurintricarboxylic acid
BER	Base excision repair
bp	Base pair

BCA	Bicinchoninic acid
BHQ	Black hole quencher
BSA	Bovine serum albumin
BRCA	Breast cancer susceptibility protein
BPB	Bromophenol blue
Kcat	Catalytic constant of an enzyme
CTCF	CCCTC-binding factor
CDDP	Cisplatin (cis-diamminedichloroplatinum(II))
CS	Cockayne syndrome
CODASS	Combined Docking and Similarity Search
CTR1	Copper transporter 1
CPDs	Cyclobutane-pyrimidine dimers
CTLA-4	Cytotoxic T-lymphocyte-associated antigen 4
Δ	Delta (Change)
DNase1	Deoxyribonuclease 1
DNA	Deoxyribonucleic acid
DMSO	Dimethyl sulphoxide
KD	Dissasociation constant
DTT	DL-Dithiothreitol
ds-	Double strand
DSBR	Double strand break repair
DSBs	Double-strand DNA breaks
DMEM	Dulbecco's modified Eagle medium
EDULISS	Edinburgh University Ligand Selection System
EDTA	Ethylenediaminetetraacetic acid
EMA	European Medicines Agency
ERCC1	Excision repair cross-complementation group 1
FDA	Federal Drug Agency
FEN1	Flap endonuclease 1
FAD	Flavin adenine dinucleotide
FMN	Flavin mononucleotide
FACS	Fluorescence-activated cell sorting
FCS	Foetal calf serum
GG-NER	Global genomic NER
IC50	Half maximal inhibitory concentration

HhH_2	Helix-hairpin-helix motif
IMAC	Immobilized metal ion affinity chromatography
ICL	Interstrand crosslink
LOPAC	Library of pharmacologically active compounds
LIDAEUS	Ligand Discovery at Edinburgh University
LE	Ligand efficiency
Rmax	Maximum achievable response
Vmax	Maximum reaction rate
MRC	Medical Research Council
mRNA	Messenger RNA
MMEJ	Microhomology-mediated end-joining
MMR	Mismatch repair
MAPK	Mitogen-activated protein kinase
MEF	Mouse embryonic fibroblast
MRP	Multidrug resistance protein
TEMED	N′-Tetramethylethylenediamine
NHS	*N*-Hydroxysuccinimide
NHEJ	Non-homologous end joining
NMSC	Non-melanoma skin cancer
NLS	Nuclear localisation signal
nt	Nucleotide
NER	Nucleotide excision repair
MGMT	O^6-alkylguanine DNA alkyltransferase gene
AGT	O^6-alkylguanine DNA alkyltransferase protein
OR	Odds ratio
OD	Optical density
PTU	Phenylthiourea
PTEN	Phosphatase and tensin homologue
PBS	Phosphate buffered saline
PI3K	Phosphoinositide 3-kinase
PHYRE	Protein Homology/analogY Recognition Engine
6-4PPs	Pyrimidine-(6,4)-pyrimidone photoproducts
PDB	RCSB Protein data bank
ROS	Reactive oxygen species
RT-PCR	Real-time polymerase chain reaction

ΔERCC1-XPF	Recombinant Δ_{95}ERCC1-Δ_{666}XPF protein
RNA	Ribonucleic acid
RT	Room temperature
SMC	Scottish Medicines Consortium
COMET	Single cell gel electrophoresis assay
SNP	Single nucleotide polymorphisms
ss-	Single strand
SSA	Single-strand annealing
siRNA	Small interfering RNA
SDS-Page	Sodium dodecyl sulfate polyacrylamide gel electrophoresis
SD	Standard deviation
SEM	Standard error of the mean
SRB	Sulphorhodamine B
SPR	Surface plasmon resonance
STP	Surface triplet propensities program
TAMRA	Tetramethylrhodamine
TPR	Tetratricopeptide repeats
TDA	Thermal denaturation assay
TC-NER	Transcription-coupled NER
TLS	Trans-lesion synthesis
TCA	Trichloroacetic acid
UFSRAT	Ultra Fast Shape Recognition with Atom Types
UV	Ultraviolet irradiation
XP	Xeroderma pigmentosum
XPA	Xeroderma pigmentosum complementation group A
XPF	Xeroderma pigmentosum complementation group F
ApeXPF	XPF protein from *Aeropyrum pernix*
Z′	Z-factor

1 Chapter 1: Introduction

1.1 Malignant melanoma

1.1.1 Melanoma incidence rates

In the UK, 91,100 new cases of non-melanoma skin cancers were diagnosed in 2009 compared to malignant melanoma where 11,877 new cases were diagnosed (1). Although malignant melanoma is less common, mortality is greater and resulted in 2,203 deaths whereas non-melanoma skin cancer accounted for only 546 deaths (1). Excluding non-melanoma skin cancer, malignant melanoma is the sixth most common cancer in the UK population and is the second most common cancer in the 15-34 year old age group (1).

Worryingly, incident rates of malignant melanoma have increased by 70% between a period of 1997-9 and 2006-8, faster than any other cancer (1). Interestingly the incidence rate for malignant melanoma is higher in women though mortality rates in women are lower than in men, likely due to a greater proportion of thinner malignancies (1). In the UK, 5-year survival rates for malignant melanoma are 90% for women and 81% for men though once the tumour reaches >3.5mm in thickness, this reduces to 55% and 47% respectively (1). For metastatic disease, this is further reduced to around 5%.

1.1.2 Melanoma risk factors

The main risk factor for malignant melanoma is exposure to UV radiation however risk can also be correlated with other factors. For example, patients with a single atypical naevus have a 60% increased risk of melanoma or 10-fold increased risk for those with 5 or more atypical naevi (2). Previous medical history of atopic dermatitis is associated with increased risk (3) and Parkinson's disease patients have a 7-fold increased risk (4). Although the reason for this is unknown, it may be linked to variations in pigmentation genes which are associated with both conditions (5, 6). In addition, being fair skinned, freckled, or having red hair is also associated with a 3-8 fold increased risk of developing melanoma (7). It is thought that about 10% of melanomas are as a result of inherited mutations, as such previous history of

melanoma, or family history of melanoma, are therefore associated with increased melanoma risk (8).

Sunburn has also been correlated with increased risk of developing melanoma with childhood sunburn being even more damaging than adulthood sunburn (9, 10). People who have had a single event of bad sunburn are twice as likely to develop malignant melanoma (11). In addition, studies show that regular sunbed use before the age of 30 results in a 75% increased risk of developing melanoma (12, 13). Studies show that use of sun creams does help to reduce damage caused by UV radiation and lowers risk of developing melanoma (14, 15).

1.1.3 Genetic changes in melanoma

A common mutation found in 40-70% of metastatic melanomas is a V600E mutation in B-Raf that results in a 10 times greater activity of the MAPK pathway than with wild type B-Raf (16–18). A second common mutation which activates the MAPK pathway occurs in N-Ras which is activated in 10-15% of metastatic melanomas (19). Activation of B-Raf or N-Ras initially promotes cell proliferation and naevus development. However, prolonged activation of the MAPK pathway results in cell cycle arrest and cellular senescence by activation of cyclin-dependent kinase inhibitors such as p21Cip1, p16Ink4a and p27Kip1 (19). It is therefore necessary for other factors to become mutated (such as p53 deregulation, p16Ink4a loss or by Akt3 activation) to overcome cell cycle arrest in naevi and facilitate progression to melanoma (19).

To overcome cellular senescence, activation of the PI3K pathway occurs in 70% of sporadic melanomas and is often found in conjunction with V600E B-Raf mutations (19, 20). Typically PI3K pathway activation occurs due to loss of PTEN or by activation of Akt3 and facilitates the deregulation of apoptosis and promotes chemoresistance (19). It has been shown that activated Akt3 phosphorylates V600E B-Raf resulting in reduced MAPK pathway activity thus restoring cell proliferation as observed in early naevus development (19).

The role of p16Ink4a in melanoma is also well established and is frequently mutated in 10-50% of melanoma cases (21, 22). Furthermore through alternative splicing of the CDKN2A gene, the two products p16Ink4a and p14ARF are transcribed from exons 1α, 2 and 3 or exons 1β and 2 respectively (21, 23). It is thought that p16Ink4a disrupts the transition from G1 to S phase of the cell cycle by forming a complex with CDK4/6 (21, 23). This inhibits CDK4/6 binding to Cyclin D proteins and results in decreased phosphorylation of Rb and prevents transcription of genes required for S phase transition (21, 23). When p16Ink4a is deleted in melanoma, phosphorylation occurs on Rb protein and allows transcription of S phase genes, thus resulting in increased cell proliferation (21, 23).

Unlike many other cancers, in melanoma p53 mutations occur in only 20-25% of cases (24). The p53 pathway is instead altered by loss of p14ARF (24). This acts by reducing inhibition of MDM2 and thus increased suppression of p53 by MDM2 promoting melanomagenesis and an escape from senescence (24).

1.1.4 DNA repair in melanoma

Genomic instability and mutation is an enabling characteristic for the development of cancer, as described by Hanahan and Weinberg (25). In cancer, mutation is often achieved by mutagenic agents, loss of DNA damage detection, or by loss of DNA repair ability (25). In patients with the DNA repair deficiency syndrome, xeroderma pigmentosum (XP), patients have a >1000-fold increased risk of developing UV-induced skin cancers (26). This shows that a decrease in DNA repair ability promotes tumour formation. In contrast, once a cancer has established it is then favourable to have higher levels of DNA repair as this protects against chemotherapy.

It is proposed that a reduced DNA repair capacity acts as a predisposing factor for melanoma. As such, several studies have identified gene polymorphisms which correlate with an increased risk of melanoma. These include Broberg *et al.* who identified variants of RMI1 with an odds ratio (OR) of 1.5 (27). This protein is known to associate with the BLM helicase involved in homologous recombination (27). Tomescu *et al.* identified three polymorphysims in the XPD gene which result

in OR of 2.0, 2.6 and 2.8 (28). Zhang *et al.* found a single nucleotide polymorphism (SNP) in the PARP1 gene with an OR of 1.89 (29). Furthermore, they found that association was highest in sun exposed sites, particularly on the head and neck (29).

Kauffmann *et al.* looked at the difference between DNA repair gene expression in primary melanoma tumours that metastasized within a 4 year time period versus those that did not metastasize (30). They showed that proteins involved in several DNA repair pathways are increased in metastatic tumours, including the Nucleotide Excision Repair (NER), Base Excision Repair (BER), Mismatch Repair (MMR), Trans-Lesion Synthesis (TLS) and Double Strand Break Repair (DSBR) pathways (30).

In a study by Jewell *et al.*, they found that there was an association between over-expression of certain DNA repair genes, and poor relapse-free survival (31). These included RAD51, RAD52, TOP2A and RAD54B. Furthermore, they showed that following chemotherapy (the majority of cases were treated with dacarbazine) DNA repair gene expression was also increased (31). This included genes involved in the removal of DNA bases through direct reversal (MGMT), NER (ERCC1, XPA), BER (XRCC1), MMR (MLH1, MSH2) and non-homologous end joining (NHEJ) (XRCC5, XRCC6) pathways (31). Importantly however, this study did not reach statistical significance due to a low sample size. Increased expression of TOPO2A and XRCC5 has since been confirmed by Song *et al.* (32).

1.2 Current therapeutics and clinical trials

1.2.1 Dacarbazine

Currently the DNA alkylating agent dacarbazine is the main front line therapy for metastatic melanoma and was first approved for treating metastatic melanoma in 1975. However, response rates to dacarbazine are low and observed responses are nearly always partial (33). In clinical studies, dacarbazine has a response rate of 7-20% resulting in a median survival of 6-9 months (33, 34). Furthermore, in a study by Chapman *et al.,* the Dartmouth regimen (dacarbazine, cisplatin, carmustine and tamoxifen) was shown to have an increased response rate of 18.5% versus 10.2% for

dacarbazine alone however median survival time was unchanged at 7 months for both regimes (35). In a study by Bedikian *et al.* combination of dacarbazine with the Bcl-2 antisense oligonucleotide, oblimersen, showed an improved overall response (36). They found that the overall response rate was 13.5% while 2.8% of patients showed complete response (36). In contrast, patients treated with dacarbazine alone showed an overall response rate of 7.5% and only 0.8% of patients had complete response (36). Furthermore progression free survival was deemed to be longer (2.8 months versus 1.6 months) and median overall survival was increased (9.0 months versus 7.8 months) with combinational therapy (36).

Dacarbazine is therefore far from the 'ideal' therapy and more effective therapies are urgently needed. Herein we review the response rates of other agents which have been pursued for the treatment of metastatic melanoma.

1.2.2 O^6-Benzylguanine

O^6-benzylguanine is a potent inhibitor of the O^6-alkylguanine DNA alkyltransferase (AGT) DNA repair protein (gene name MGMT) and is expressed at high levels in melanoma (37). O^6-benzylguanine was developed in the early 1990's and during this time preclinical data showed benefit for melanoma therapy in cell culture models (38). The purpose of O^6-benzylguanine was to enhance toxicity of existing alkylating agents used for melanoma therapy (38). During DNA damage, AGT functions to repair DNA alkylating lesions by binding, and accepting the alkyl group from the O^6 position on guanine residues onto a cysteine residue of the AGT active site (39).

In preclinical trials of O^6-benzylguanine with the DNA alkylating agent temozolimide, mouse melanoma xenografts showed delayed tumour growth upon O^6-benzylguanine treatment (39). Similar levels of delayed tumour growth were also observed with an additional DNA alkylating agent, carmustine (39).

A Phase 2 clinical trial of O^6-benzylguanine with carmustine has been reported measuring clinical response following previous chemotherapeutic treatment (37). In the chemotherapy naive cohort, 6% patients showed complete response while

22% showed stable disease (37). In the prior-chemotherapy cohort, only 17% of patients displayed stable disease (37). In addition, median overall survival of chemotherapy naive patients was recorded to be 211 days whereas this was only 120 days for those with prior chemotherapy (37). Toxicity issues were also observed in both cohorts with 55-63% of patients showing grade 2 or 3 toxicity including neutropenia, thrombocytopenia and anaemia symptoms (37).

Although AGT was depleted in all patients by O^6-benzylguanine, the response rate was poor and was not significantly greater than that expected for higher dose carmustine alone (37). The authors for this study suggest that because O^6-benzylguanine augments toxicity of carmustine in all cells, a lower dose of carmustine is therefore required and is equivelant to a higher dose of carmustine alone (37). They also propose that with AGT depleted, an alternative pathway may be utilized for DNA repair (37). Further exploration of O^6-benzylguanine and carmustine was not supported by the authors (37). That being said, the evaluation of O^6-benzylguanine and temozolomide on melanoma remains to be assessed.

1.2.3 Cisplatin

Cisplatin (cis-diamminedichloroplatinum(II)) is generally regarded as ineffective against malignant melanoma. In clinical trials however, cisplatin was shown to have objective response in 10.4% of patients with 6% patients showing partial remission (40). Furthermore, in combination with other chemotherapeutics, response rates are often better. In combinational therapy, treatment of melanoma with cisplatin and dacarbazine showed response rates of 24-55% (41). Another combination which has shown promise is combination of cisplatin with amifostine (WR-2721) which protects normal tissues from the toxic effects of alkylating agents and cisplatin (42, 43). This combination was reported to show an objective response of 45% (42, 43). In a more recent study, the response rate was reported to be 23.3% compared to 16.3% for those receiving cisplatin only (44). The duration of response was 7.3 months (44). Taken together, the response rates of cisplatin against melanoma are poor; however they are comparable to dacarbazine which remains the

standard therapy for melanoma. Development of combinational therapy with cisplatin for the treatment of melanoma remains a possibility.

1.2.4 Vemurafenib (PLX4032)

The serine-threonine protein kinase B-RAF is found to be mutated in 40-60% of patients with malignant melanoma resulting in constitutive activation of the mitogen activated protein kinase (MAPK) pathway (18). In contrast, B-RAF is only mutated in 7-8% of most other cancer types (18). Vemurafenib (PLX4032) is an inhibitor of mutated B-RAF with selective potency against B-RAF harbouring the V600E mutation (34). Vemurafenib made headlines after successfully passing Phase 1 and 2 trials in 2010 and then passed Phase 3 clinical trials in 2011 against malignant melanoma (18, 34). Vemurafenib was subsequently approved for clinical use by the Federal Drug Agency (FDA) in 2011 (34).

In the Phase 3 trials for vemurafenib against metastatic melanoma, 2107 patients with unresectable stage 3C or 4 disease were screened for B-RAF status (34). Of these, 675 tested positive for B-RAF V600E and were subsequently randomized for treatment with either vemurafenib or dacarbazine (34). At 6 months, the overall survival for patients receiving vemurafenib was 84% whereas overall survival for those receiving dacarbazine was 64% (34). Furthermore, progression free survival was 5.3 months for those receiving vemurafenib and only 1.6 months for those receiving dacarbazine (34). In this study, most patients receiving vemurafenib had a decrease in tumour size with a 48% confirmed objective response rate and median time to response of 1.45 months (34). Of the vemurafenib group, 10 patients were later discovered to harbour a V600K mutation, and 40% of these had shown a partial response (34). In comparison, most patients treated with dacarbazine showed no detectable decrease in tumour volume and only 5% had a confirmed response (34). In addition, the median time to response was 2.7 months (34).

Although vemurafenib shows significantly better response rates than dacarbazine, there are increased side effects associated with this treatment. In Phase 3 clinical trials, adverse side effects lead to dose modification or interruption of treatment in 38% of patients, predominantly due to cutaneous events, arthralgia, fatigue or photosensitive skin reactions (34). In 18% of patients, cutaneous

squamous-cell carcinoma, keratoacanthoma, or both developed (34). In patients receiving dacarbazine alone, dose modification or interruption of treatment only occurred in 16% of patients, predominantly due to fatigue, nausea, vomiting and neutropenia (34).

In a long term follow-up of the Phase 2 clinical trial at a median follow-up time of 12.9 months, the confirmed overall response rate was 53%, of which 6% of patients showed complete response (45). Furthermore, they showed that the median duration of response was 6.7 months and the median progression free survival was 6.8 months (45). In contrast to the Phase 3 study, they document 26% of patients treated by vemurafenib to develop cutaneous squamous-cell carcinoma or keratoacanthoma (45). Median overall survival was assessed to be 15.9 months (45).

1.2.5 Mechanisms of vemurafenib resistance

During vemurafenib treatment, it is known that resistance eventually develops despite inhibition of mutant B-RAF (46, 47). This is known to correlate with an increase of RAS-GTP, C-RAF and p-AKT (46). Furthermore, sequencing has revealed that an additional acquired mutation occurs in K-RAS (K117N) (46). Research shows that overexpression of K-RAS harboring the K117N mutation in melanoma cell lines resulted in a 5-7 fold increase in vemurafenib resistance (46). Mutations of K-RAS are known to activate pathway signaling and thus it is likely this results in acute activation of C-RAF resulting in stabilization of C-RAF homodimers and thus downstream MEK activation (46). In vemurafenib resistant melanoma cell lines, siRNA directed against C-RAF resulted in a 5-7 fold increase of vemurafenib sensitivity whereas no effect was observed in vemurafenib sensitive cell lines (46). Overexpression of C-RAF in vemurafenib sensitive cell lines resulted in an 18 fold increase in vemurafenib resistance (46).

An additional mechanism of vemurafenib resistance is thought to occur due to dimerization of aberrantly spliced B-RAF harboring the V600E mutation (47). In six out of 19 patients with acquired resistance to vemurafenib, splice isoforms of B-RAF V600E allowed dimerization in a RAS-independent manor (47). This resulted in a 61kDa isoform of B-RAF V600E lacking exons 4-8 encoding a protein lacking the N-terminal region which negatively regulates the C-terminal kinase domain and

RAS binding domain (47). This therefore results in direct downstream pathway activation (47).

1.2.6 Ipilimumab

Ipilimumab is a human IgG1 monoclonal antibody therapy that specifically blocks the cytotoxic T-lymphocyte-associated antigen 4 (CTLA-4) which acts as a negative regulator of T-cell activation and proliferation. Inhibition of CTLA-4 facilitates lymphocyte infiltration into the tumour leading to tumour cell death (48, 49). In 2011, ipilimumab was the first new drug since dacarbazine to be licensed for use against melanoma by the Federal Drug Agency (FDA) and European Medicines Agency (EMA) (48, 50). In April 2012, use of ipilimumab in Scotland was prevented by the Scottish Medicines Consortium (SMC) citing that the cost of treatment in relation to the health benefits and economic case was not sufficient to gain acceptance by the SMC.

In a Phase 3 clinical trial studying the effects of ipilimumab and a glycoprotein 100 peptide vaccine in a randomized double-blind study, it was shown that ipilimumab is active against melanoma (51). This vaccine was used as an active control and is derived from the melanosomal protein gp100 (51). In monotherapy, gp100 illicts an immune response but has limited antitumour activity (52). However it has been shown to improve efficacy of high-dose interleukin-2 therapy in metastatic melanoma (53). They observed median overall survival of patients receiving ipilimumab and the gp100 vaccine to be 10.0 months, ipilimumab alone to be 10.1 months and the gp100 vaccine only cohort to be 6.4 months (51). This resulted in overall survival of patients receiving ipilimumab to be 45.6% at 12 months reducing to 23.5% after 24 months (51). For those receiving only the gp100 vaccine, this corresponded to only 25.3% at 12 months and 13.7% at 24 months (51). These observations are consistent with the Phase 2 trial of ipilimumab monotherapy on melanoma (54). In addition, for those receiving ipilimumab only versus gp100 only, a 36% reduction in risk of progression was observed (51). Furthermore, in the Phase 3 study, ipilimumab was assessed to have a 10.9% overall response rate with

stable disease in a further 17.5% of patients (51). Of the responders, 60.0% continued to show objective response for at least 2 years of treatment (51).

Side effects of ipilimumab treatment have been reported in 60% of patients with 10-15% of patients showing grade 3 or 4 symptoms (51). In the main side effects are immune-related with events often affecting the skin or gastro-intestinal tract (51). Side effects include diarrhoea, vitiligo, colitis, anorexia, fatigue, leukocytosis and inflammation of the pituitary requiring hormone replacement therapy (51).

1.2.7 Sorafenib

Sorafenib is a multikinase inhibitor with known activity against RAF, VEGF, c-Kit and Ret kinases (55). In melanoma therapy, sorafenib has been shown to have a limited objective response rates of only 16% in patients and only show stable disease (56). More recently however, various clinical trials with sorafenib have focused on combinational therapeutic strategies with the aim of achieving greater response rates. These include combinations with dacarbazine (57, 58), carboplatin and paclitaxel (55, 59).

In Phase 1 and 2 clinical trials, combinational therapy of sorafenib and dacarbazine has been shown to have an objective response rate of 12% with the median time to response of 48 days, and a median response of 46.7 weeks (58). An additional 37% of patients showed stable disease with a median duration of 13.3 weeks (58). In an earlier clinical trial, the overall response rate was assessed to be 24% (57). Furthermore, this trial was of double-blind format and assessed progression free survival of combinational therapy to be 21.1 weeks versus 11.7 weeks in the dacarbazine only cohort (57). That being said, no difference in the overall survival was observed between these two groups (57).

Combinational therapy of sorafenib with carboplatin and paclitaxel has not been of clinical benefit (59). Although in Phase 1 clinical trials 62% of patients had stable disease or an objective response (55), this was not mirrored in a phase 3 clinical trial (59). In this Phase 3 clinical trial looking at sorafenib, carboplatin and

paclitaxel as a second line treatment for melanoma, the progression free survival of sorafenib with carboplatin and paclitaxel was assessed to be 17.4 weeks and had a response rate of 12% (59). In the carboplatin and paclitaxel only cohort, the progression free survival was 17.9 weeks and had a response rate of 11% indicating no additional benefit conferred by sorafenib (59).

1.3 DNA repair and the role of ERCC1-XPF

The ERCC1-XPF heterodimer is a 5′-3′ structure-specific endonuclease that is involved in a number of DNA repair pathways in mammalian cells. It is essential for nucleotide excision repair (NER) and has important roles in interstrand crosslink (ICL) repair and double-strand break repair (DSBR). As such it has a key role in the response of cancers to a range of DNA-damaging chemotherapeutics. In the ERCC1-XPF heterodimer, ERCC1 is catalytically inactive and instead regulates DNA and protein-protein interactions, while XPF provides the endonuclease activity and also contains an inactive helicase-like motif and is involved in DNA binding and additional protein-protein interactions.

1.3.1 Overview of DNA repair mechanisms

One of the main risk factors associated with melanoma is thought to arise from UVB radiation due to nucleic acids absorbing light within the 260-280nm wavelength (1, 60). DNA damage resulting from UVB radiation is categorised into two main subtypes, cyclobutane-pyrimidine dimers (CPDs) and 6-4 photoproducts (6-4PPs) (61). CPDs are the most abundant accounting for 75% of the lesions whereas 6-4 photoproducts account for 25% of lesions (61). Although CPDs are the more common, 6-4 photoproducts are more serious as they cause greater helical distortions. As shown in Figure 1.1, DNA damage resulting from UVB radiation is predominantly repaired by the nucleotide excision repair (NER) pathway.

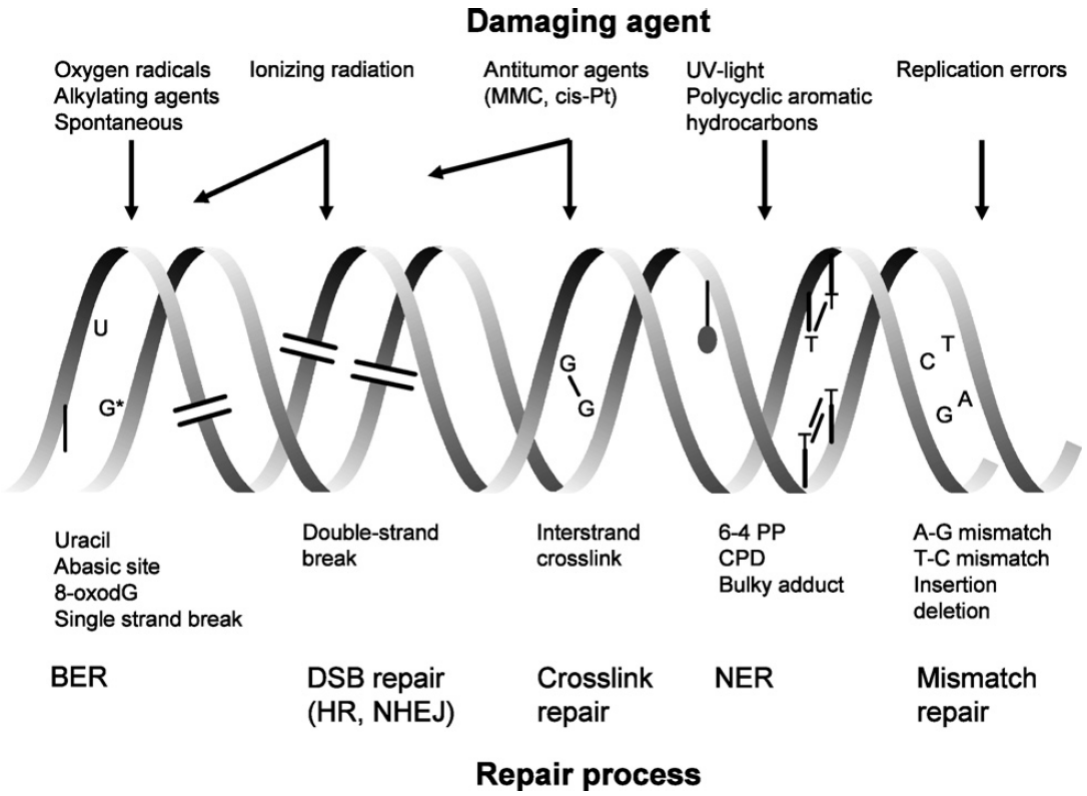

Figure 1.1: Summary of DNA damaging agents and the repair mechanisms used to repair DNA damage. Figure from (62).

1.3.2 ERCC1-XPF is essential for nucleotide excision repair

UV irradiation-induced cyclobutane pyrimidine dimers (CPDs) and pyrimidine-(6,4)-pyrimidone photoproducts (6-4PPs), chemically-induced helix-distorting and bulky DNA lesions are all repaired by NER (63). *In vivo* NER requires around 30 proteins, but the incision step can be reconstructed *in vitro* with just six core factors, XPC/RAD23B, XPA, RPA, TFIIH, XPG and ERCC1-XPF (64). To complete NER *in vitro*, PCNA, DNA polymerases δ, ε, and κ, DNA ligases I and III, RFC, RPA and XRCC1 are also involved. In global genomic NER (GG-NER) (65), DNA damage is recognised by the XPC/RAD23B complex which detects helical distortions rather than the lesion itself. This is shown in Figure 1.2. It is thought that XPC/ RAD23B binding induces further bending of the DNA which may act as the trigger for recruiting additional factors to the lesion. For recognition of DNA damage such as CPDs, which only mildly distort DNA, the XPE/UV-DDB complex is also

required. In transcription-coupled NER (TC-NER) (66), repair is triggered when RNA polymerase II stalls at a lesion, resulting in recruitment of several proteins including CSA and CSB. Following either of these damage recognition steps, a common repair mechanism proceeds with recruitment of the TFIIH complex, containing XPB and XPD, which possess ATP-dependent helicase activities to unwind DNA around the damage site to form an open complex. XPA and RPA proteins are then recruited to stabilise the NER intermediate. XPA recognises a helical kink at the damage site (67) and acts as a scaffold for binding to TFIIH, RPA and ERCC1-XPF, while RPA binds to ss-DNA. ERCC1-XPF and XPG endonucleases are then recruited to incise the damaged DNA strand 5′ and 3′, respectively, to the lesion. Recruitment of ERCC1-XPF is thought to be mediated by both ERCC1/XPA and XPF/RPA interactions (68, 69).

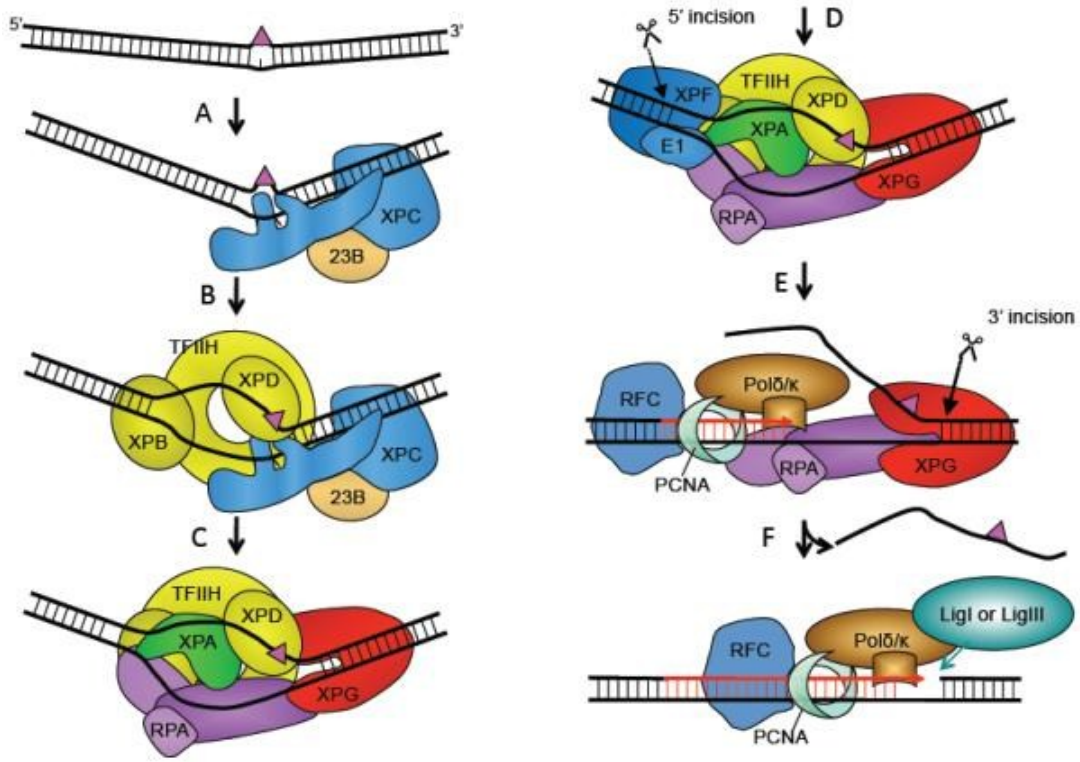

Figure 1.2: Figure showing the nucleotide excision repair pathway. (A) A bulky DNA lesion shown by the purple triangle is recognised by XPC-RAD23B. (B) This then facilitates recruitment of the TFIIH complex. (C) The lesion is verified by XPD allowing recruitment of XPA, RPA and XPG. (D) The ERCC1-XPF complex is then recruited and incises the

DNA 5′ to the DNA damage lesion. (E) XPG then incises the DNA 5′ to the DNA damage lesion and (F) repair is completed by Polδ/κ, PCNA and DNA ligase IIIα or ligase I. Figure from (70).

1.3.3 ERCC1-XPF is involved in double-strand break repair (DSBR)

Double-strand DNA breaks (DSBs), induced by ionising radiation, free radicals and chemotherapeutics, such as cisplatin, mitomycin-C and the topoisomerase inhibitor, etoposide, can be repaired by homologous recombination (HR), or non-homologous end joining (NHEJ). While the main HR pathway is error-free, NHEJ involves the ligation of free DNA ends in a Ku70/Ku86-dependent process resulting in error-prone repair, due to addition or loss of bases, or to ligation of the wrong ends. The importance of ERCC1-XPF in DSBR was initially shown in budding yeast, where mutations in RAD10, or RAD1, the yeast orthologues of ERCC1 and XPF, suppressed HR (71). Mammalian cells with mutant ERCC1-XPF are sensitive to DSBs (72) and both the HR and NHEJ pathways for DSBR are attenuated (73–75). The key activity of ERCC1-XPF in both types of DSBR is its ability to remove non-homologous 3′ single-stranded flaps at broken ends before they are rejoined (72). This is achieved in the error-prone RAD52-dependent single-strand annealing (SSA) subpathway of HR (76, 77) and in the mechanistically distinct RAD52 and Ku70/Ku86-independent microhomology-mediated end-joining (MMEJ) subpathway of NHEJ (72, 78, 79).

1.3.4 ERCC1-XPF is involved in interstrand crosslink repair

ICL repair operates to remove crosslinks induced by chemotherapeutics such as cisplatin, psoralens and mitomycin-C (80). Such lesions are particularly toxic since they prevent helix unwinding and so act as a potent block to transcription and replication. A review of the sensitivity of mammalian NER mutants to ICL agents found that, while all NER mutants were more sensitive than wild-type cells, mutants in ERCC1 or XPF were in general hypersensitive (80). In eukaryotes the mechanism of ICL removal depends on the phase of the cell cycle during which the lesion is

encountered (81). If incision adjacent to an ICL occurs in G0 or G1 then repair may be completed during this stage. Alternatively, if the ICL persists into S phase it will be converted into a DSB when it causes replication to stall. Incisions are thought to be made to either side of the crosslink on one DNA strand to unhook the lesion and allow stalled replication complexes to proceed. The DNA is repaired by HR using the newly synthesised strand as template and may use a NER-dependent mechanism to remove the remaining lesion (82). Although the precise mechanism is not known, most models for ICL repair employ an ERCC1-XPF- dependent step (80, 81). Importantly, ERCC1-XPF is able to incise to either side of an ICL (83) and, although not the only nuclease involved, ERCC1-XPF has been shown to be required for both S-phase-dependent and -independent ICL repair (84, 85).

1.3.5 Non-repair related roles for ERCC1 and XPF

ERCC1-XPF is involved in telomere maintenance and the interactions made with the telomere protein, TRF2, are described in a later section. A role for ERCC1, but not XPF, in mitotic progression has been suggested by the observation that knock-down of ERCC1, but not XPF, in human hepatocellular carcinoma cells caused cell cycle delay and multinucleation (86). This result is not readily reconcilable with the premature polypoidy observed in the livers of both ERCC1 knockout (87) and XPF knockout mice (88) and could result from unrepaired endogenously generated interstrand crosslinks uncoupling the normal relationship between replication and cell division, rather than a non-repair related role for ERCC1. A similar role in mitosis, but this time for XPF, has been proposed from studies where knocking down XPF in cultured cells led to abnormal nuclear morphology and mitosis (89). XPF was found to interact and colocalise with the kinesin protein, Eg5 (89). Again the effect of XPF knock-down on mitosis could be indirect, resulting from unrepaired endogenous DNA damage rather than a direct role in mitosis. An alternative explanation perhaps made more likely by the observation that Eg5 boosted ERCC1-XPF activity in the standard *in vitro* assay. Recently a role for ERCC1-XPF has been proposed during transcription initiation (90, 91). Le May *et al.* propose a model whereby ERCC1-XPF and the NER machinery are required to

demethylate DNA in some promoter regions creating DNA strand breaks that facilitates the transcription factor CTCF (CCCTC-binding factor) binding and DNA loop formation (91).

1.3.6 Nucleotide excision repair deficiency disorders

Inherited defects in human NER genes result in rare syndromes such as xeroderma pigmentosum (XP), Cockayne syndrome (CS), or trichothiodystrophy. While XP is considered a repair syndrome, CS and trichothiodystrophy are regarded as transcription syndromes (63). Diagnostic features of XP are dry scaly skin, abnormal pigmentation patterning in sun-exposed areas and severe photosensitivity, resulting in >1000-fold increased risk of developing UV-induced skin cancers (26). In 20-30% of XP patients there is also progressive neurological degeneration, emphasising the importance of NER in repair of endogenous DNA damage (63). CS patients are also photosensitive, but do not exhibit pigmentation abnormalities, or an increased cancer risk (63, 26). CS patients also show developmental defects and neurological symptoms (63). In XP, GG-NER is always defective and TC-NER may also be affected, while in CS, TC-NER is lost, but GG-NER is retained (63, 26).

Characterisation of the *ERCC1* (92) and *XPF* genes (93, 94) made possible the identification of mutations in patients. Mutations in the *ERCC1* or *XPF* genes can result in the even rarer XF-E syndrome (95). Patients show characteristics of XP and CS, but also exhibit additional neurologic, hepatobiliary, musculoskeletal and haematopoietic symptoms (95). In addition to a complete loss of TC- and GG-NER, cells derived from XF-E patients also show hypersensitivity to ICL agents due to the additional role of ERCC1-XPF in ICL repair (95). This distinguishes the XF-E syndrome from either XP, CS, or combined XP/CS (95).

1.3.7 Patients with ERCC1-XPF mutations

Only two patients with *ERCC1* mutations have been observed: one (XP202DC) harbouring a Lys226X nonsense mutation with a IVS6-26G-A splice mutation, a second (165TOR) with a Gln158Stop mutation inherited from the mother and a

Phe231Leu mutation from the father (96, 97). *XPF* mutations have been characterised in 14 patients, 9 harbour an Arg799Trp mutation (96). This is proposed to be situated in an interaction domain between the XPF nuclease and ERCC1 central domains (98). An Arg153Pro mutation in the helicase-like domain may disrupt protein-protein interactions resulting in XF-E syndrome (95). Other mutations observed are Pro379Ser and Arg589Trp, both in the helicase-like domain (96). While it is yet to be shown for any of the XPF mutations that they actually disrupt specific protein-protein interactions, there is evidence that the Arg153Pro XF-E mutation results in the protein failing to reach the nucleus, probably due to misfolding (99). The locations of *ERCC1* and *XPF* mutations resulting in amino-acid substitutions are shown in Figure 1.3.

1.4 The ERCC1-XPF structure-specific endonuclease

The ERCC1-XPF complex is a structure-specific endonuclease which cleaves DNA at ds- to ss- junctions, nicking the ds- DNA on the 5′ strand 2 nucleotides from the junction (100). This structure-specificity was first demonstrated for RAD10-RAD1, the yeast orthologues of ERCC1 and XPF (101). ERCC1-XPF is active in *in vitro* endonuclease assays utilising a variety of substrates, including stem-loops and structures with 3′ overhangs (100). The minimum loop size required for cleavage is 6 nt, but the preference is for larger, 22-40 nt loops (100, 102).

1.4.1 Domain architecture of the ERCC1-XPF complex

The ERCC1 protein is thought to have arisen from a gene duplication of XPF in the eukaryotic lineage (103). In Archaebacteria only XPF is present, forming homodimers with each protein containing nuclease and HhH_2 domains. Archaeal XPF monomers interact primarily through HhH_2 domains, with an additional interaction through the β5 strand of the nuclease domains (98). In addition to nuclease and C-terminal HhH_2 domains, mammalian XPF also contains an N-terminal helicase-like domain, but lacks residues essential for helicase activity (104). An overview of the ERCC1 and XPF domains is shown in Figure 1.3. The ERCC1

protein differs from XPF in that it contains a catalytically inactive central domain and lacks the helicase-like domain. ERCC1 mediates DNA binding and many of the protein-protein interactions of the ERCC1-XPF complex. The HhH_2 domains of ERCC1 and XPF show a high degree of conservation (103, 105). In human XPF, the second HhH motif lacks the characteristic GhG hairpin, instead being replaced by a short three residue β-turn, nevertheless XPF still adopts a canonical HhH_2 folded structure (105).

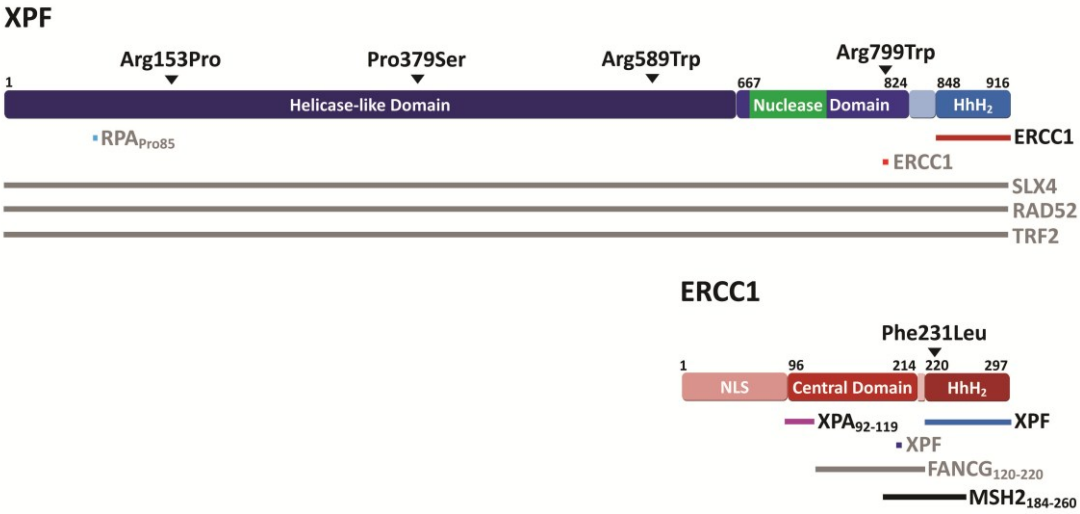

Figure 1.3: Domain architecture of ERCC1 and XPF proteins. The active site within the XPF nuclease domain is shown as a green box. Confirmed protein-protein interacting regions are mapped and identified with black text; undefined or unconfirmed protein-protein interactions are identified by grey text. Amino acid substitution mutations identified in XP or XF-E patients are also indicated. NLS, putative nuclear localisation signal. The same colour scheme shown here to identify the protein domains is used in all the Figures.

1.4.2 Dimerisation of ERCC1 and XPF occurs through their HhH_2 domains

The key protein-protein interaction of ERCC1 and XPF is the dimerization of their hydrophobic C-terminal regions to form a stable heterodimer through the double helix-hairpin-helix motifs in their HhH_2 domains (105, 106). It is thought that during protein folding XPF acts as a scaffold for ERCC1 and that ERCC1 may be

unable to fold correctly *in vitro* in the absence of XPF (105). Without dimerization it was conventionally thought that neither protein was stable and each was rapidly degraded due to aggregation following exposure of their hydrophobic interaction regions (105, 107). However, recent siRNA experiments have indicated that, while XPF protein levels were decreased when ERCC1 was knocked down, the converse was not true (108). There is no catalytic activity in the absence of dimerization. Indeed, although the catalytic domain is within XPF and ERCC1 is catalytically inactive, ERCC1 remains indispensable for activity of the complex (105).

1.4.3 What residues are essential for dimerization?

The ERCC1 and XPF HhH_2 domains have a 1534Å^2, predominantly hydrophobic, interacting surface (105). Each domain forms five core α-helical structures (XPF: H1, 849-853; H2, 860-868; H3, 873-877; H4, 881-887; H5, 891-903. ERCC1: H1, 233-240; H2, 247-257; H3, 260-265; H4, 268-272; H5, 280-288), with ERCC1 forming an additional α-helical structure in its N-terminus (ERCC1, 226-229) (107). In both ERCC1 and XPF the H1 and H2 helices constitute the first HhH motif, with H4 and H5 constituting the second motif (105). From cross-saturation techniques, XPF residues from Gln849 to Ala906 appear to interact with ERCC1 residues Arg234 to Leu294 (107).

Two residues essential for interaction are XPF Phe905 and ERCC1 Phe293, which anchor the two proteins together (see Figure 1.4). ERCC1 Phe293 positions into a 280Å^2 hydrophobic pocket on XPF (105). This interaction is protected by ERCC1 Leu294 which locks Phe293 in position (105). In mutational studies, deletion of ERCC1 Phe293 resulted in abolition of dimerization and enzyme activity (93, 109). A reciprocal arrangement exists for the XPF Phe905 residue, which positions into a 220Å^2 hydrophobic pocket on ERCC1, although no mutational studies have been performed on this XPF residue (105). In the human patient 165TOR, ERCC1 encoded by the allele with the Gln158Stop mutation cannot form active protein due to its inability to heterodimerize. The second allele from this patient, with the Phe231Leu mutation, does produce functional protein. Reduced binding affinity for XPF Phe905, due to the Phe231Leu mutation in the ERCC1 interaction pocket, could

explain the reduced levels of ERCC1-XPF complex and moderate sensitivity to UV and crosslinking agents observed in cells from this patient (97).

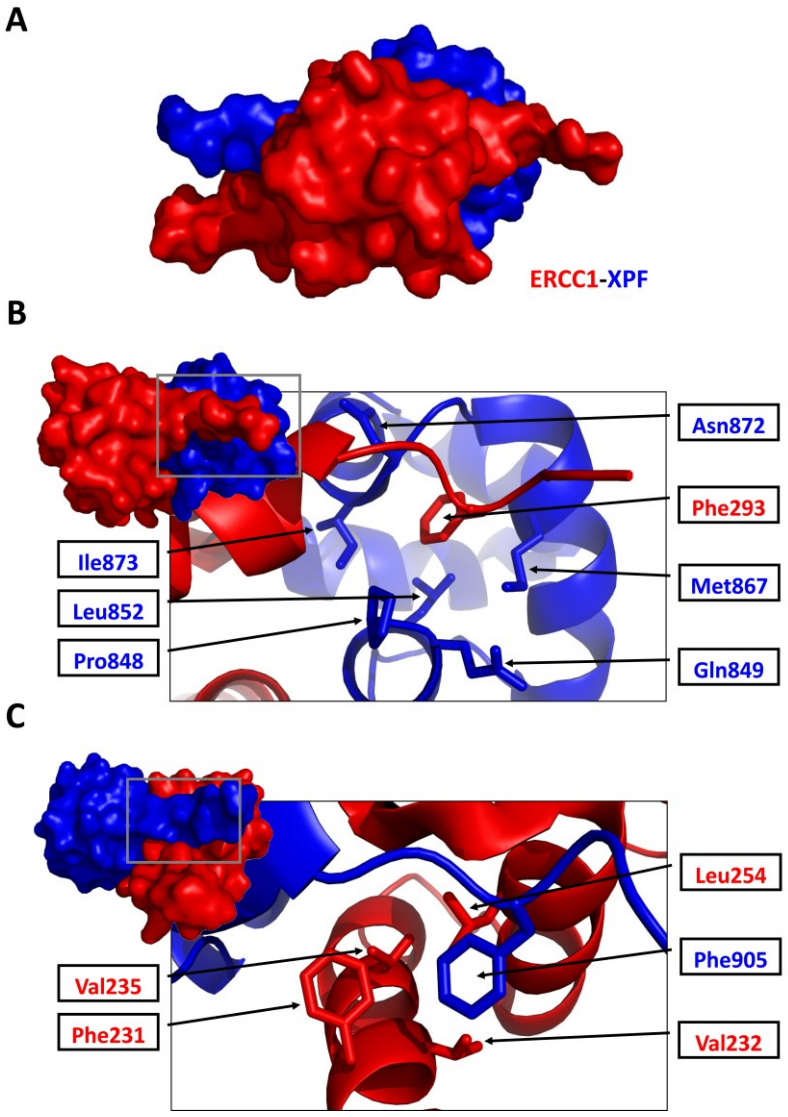

Figure 1.4: Interaction of ERCC1 and XPF through their HhH_2 domains. (A) Heterodimer of the HhH_2 domains of ERCC1 (red) and XPF (blue). (B) Expanded cartoon representation of the region boxed on XPF, identifying key interacting residues in the XPF pocket for ERCC1 Phe293. (C) Expanded cartoon representation of the region boxed on ERCC1, identifying key interacting residues in the ERCC1 pocket for XPF Phe905. Figure created using PyMOL v0.99 with the ERCC1-XPF HhH_2 domain crystal structure (PDB code 2A1J)(106).

1.4.4 How does DNA binding by the HhH_2 domains influence endonuclease activity?

It has been proposed that the ERCC1-XPF HhH_2 domains form two independent binding sites to complex with ss-DNA (105, 106). This interaction is thought to be necessary for the proper orientation of ERCC1-XPF at the ds- to ss-DNA junction (100). Tripsianes *et al.* monitored chemical shift perturbations upon DNA binding and found that both hairpin regions of ERCC1 contacted DNA, proposing that residues Val245 and Asn246 of the first HhH motif and Gly276, Leu277, Gly278 and Lys281 of the second hairpin interact with DNA (105). Under their experimental conditions, Tripsianes *et al.* could not detect DNA interaction by XPF (105). Similarly, Tsodikov *et al.* proposed DNA contacts to be made by ERCC1 residues Lys243 and Lys247 of the first and Gly276 and Gly278 of the second HhH domains (106). In contrast however, they proposed XPF makes DNA interactions via Gly857, Lys861 and Gly889 (106). They showed that the recombinant ERCC1-XPF HhH_2 domain complex binds with 6-fold preference to two ss-DNA strands over ds-DNA and measured the binding affinity (KD) to be 0.2 μM (106). Interestingly, Su *et al.* showed that recombinant ERCC1-XPF protein harbouring ERCC1 Lys247Ala and Lys281Ala mutations had a 2-fold reduced DNA binding affinity and was inactive *in vitro*, whereas XPF harbouring Lys861Ala and Arg864Ala mutations had a 1.6-fold reduction in DNA binding affinity and retained *in vitro* activity (110). Furthermore, *in vivo* only the ERCC1 double mutant resulted in a mild NER defect, suggesting that defects in DNA binding of the ERCC1-XPF complex can be partly overcome by the other NER proteins (110). Das *et al.* utilised an XPF HhH_2 homodimer and demonstrated that this can bind ds-DNA and form a stable complex with ss-DNA (111). They showed that upon binding of two, 10 nt ss-DNA fragments to the homodimer, chemical shift perturbations were observed for XPF residues between Lys861 and Val870 and proposed that Lys861, Arg864, Ser865, His868, His869 and Asn890 were directly involved in making DNA contacts (111). In addition, they showed that the bases are orientated away from the HhH_2 domain with the exception of one base that orientates into a 140$Å^2$ pocket in the XPF HhH_2 domain (111). This pocket is formed due to an altered conformation for Lys861 and

Asn890 upon DNA binding and proposed hydrogen bond formation with the side chain of Asn890 (111).

1.4.5 A model for the structure of ERCC1-XPF bound to DNA

Das *et al.* proposed a model for ERCC1-XPF whereby the ds- and ss- DNA binding of the ERCC1-XPF HhH_2 domains position the complex at the ds- to ss-DNA junction, incorporating the nucleotide binding pocket that they mapped onto the XPF HhH_2 domain in the XPF HhH_2 homodimer crystal structure (111). In their model, the ERCC1 central domain does not make contact with DNA as shown by Tsodikov *et al.* (106, 112). In addition the non-cleaved DNA strand winds around the back of the ERCC1-XPF HhH_2 domain before contacting the nucleotide binding domain and the model does not show how the central and HhH_2 domains of ERCC1 are connected.

Bowles *et al.* showed in an *in vitro* endonuclease assay that ERCC1-XPF may have a sequence-specific preference for nucleotides immediately surrounding the cleavage site (102). As a result, they have also proposed a model whereby XPF contains a nucleotide binding pocket, but instead, although there is no evidence in support, they suggest that this may reside in the nuclease domain, rather than in the XPF HhH_2 domain as shown above by Das *et al.* (111). Their very schematic model shows the helicase domain inside the loop of the stem-loop substrate DNA. The minimum loop size for ERCC1-XPF enzymatic activity is 6 nucleotides (100, 102). Based upon our homology model, the narrowest part of the XPF helicase-like domain would require a minimum loop size of approximately 12 nucleotides to be accommodated, so this model seems unlikely. In addition, in their model the ERCC1 central and XPF HhH_2 domains do not make the DNA contacts shown by Tsodikov *et al.* (106, 112).

Using the published crystal structures, and homology models for ERCC1 and XPF domains, we propose an alternative model for how the ERCC1-XPF complex associates with DNA (113). This model takes into account all of the known protein-protein, and protein-DNA interactions made by ERCC1 and XPF as published in the literature (113) (and reviewed in this introduction) (Figure 1.5). Unlike the other

models, our model also has the C-terminal end of each ERCC1 and XPF domain in close proximity to the N-terminal end of the next domain in the sequence. Similar to the other models, we show the ERCC1 HhH_2 domain making contact with ds-DNA, however after the DNA strands have separated, we additionally show the ERCC1 central domain also making contact with ss-DNA. With regards to XPF, instead of a nucleotide binding domain on the XPF central domain as suggested by Bowles *et al.* (102), we show the nucleotide binding domain to be present in the HhH_2 region of XPF as demonstrated by Das *et al.* (111). We further propose that this is localised adjacent to the XPF nuclease domain and so may act to present the DNA backbone towards the XPF nuclease domain for catalysis. Our predicted structure of the XPF helicase domain has a clamp-like structure and, although there is no evidence to indicate how it is positioned with respect to the rest of the protein, we have shown it clamped around the nuclease domain with its RPA binding site in a suitable position to contact RPA bound to the non-damaged DNA strand.

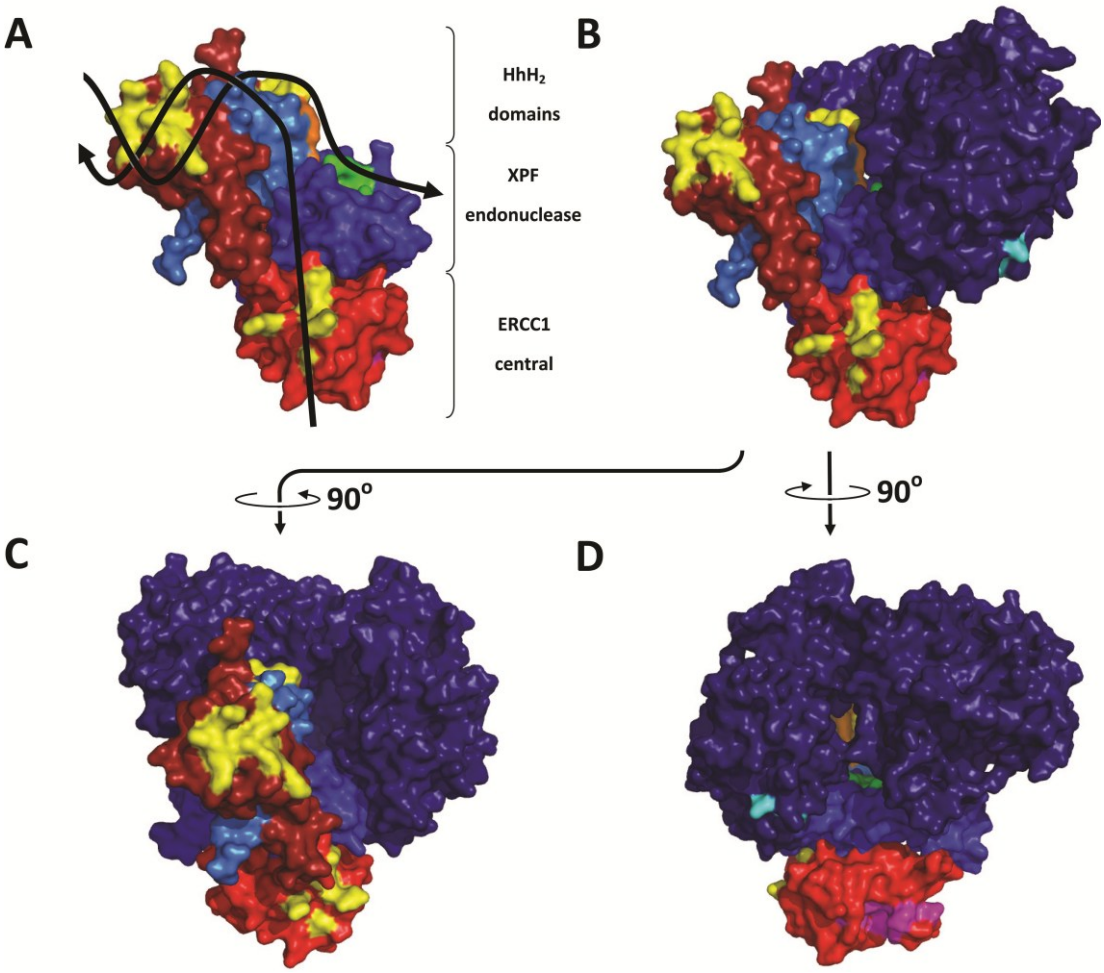

Figure 1.5: Proposed model for ERCC1-XPF interaction with the DNA substrate. (A) Showing the ERCC1 HhH_2 and central domains (red) and XPF HhH_2 and nuclease domains (blue). DNA binding regions are shown in yellow; the XPF nuclease active site is shown in green; the nucleotide binding pocket on the XPF HhH_2 domain is shown in orange; the XPA binding site on the ERCC1 central domain is coloured magenta. The ERCC1 nuclear localisation signal ($ERCC1_{1\text{-}98}$) and XPF domain linking regions (XPF_{666} and $XPF_{825\text{-}847}$) are not shown as crystal structures are not available and there is insufficient sequence conservation for homology modelling. (B) Same view as in A, but with the addition of the proposed position of the XPF helicase-like domain and omitting the DNA substrate. The RPA binding site on the XPF helicase-like domain is shown in cyan. (C) As in B, but with a 90° anti-clockwise rotation of the ERCC1-XPF complex. (D) As in B, but with a 90° clockwise rotation of the ERCC1-XPF complex. Figure created in PyMOL v0.99 using the ERCC1-XPF HhH_2 domain crystal structure (PDB code 2A1J)(106), the ERCC1 central domain crystal structure (PDB code 2A1I)(106) and PHYRE-generated homology models of the XPF endonuclease and helicase-like domains. The model was created by firstly

identifying the known interacting regions on each domain, and then positioning each domain such that their known biological role could be performed while facilitating known interactions. The length of protein domain linker regions were also taken into account.

1.4.6 Do ERCC1 and XPF interact through regions other than their HhH_2 domains?

It is unclear whether the XPF nuclease domain interacts with the central domain of ERCC1, similar to the nuclease domain interactions observed with Archaebacterial XPF (106). In several studies stable interactions between these domains did not form, although transient interactions cannot be excluded (109, 106). In support of this notion, the XPF patient carrying the Arg799Trp mutation exhibited 5-fold decreased NER activity due to ERCC1-XPF instability. Based on sequence alignments to Archaeal Hef (similar to human XPF), Nishino *et al.* mapped the Arg799Trp mutation to the middle of the β5 strand of the XPF nuclease domain, proposing an interaction with the ERCC1 central domain (98). Further evidence is required to prove the existence of this interaction in human ERCC1-XPF.

1.4.7 Are human XPF homodimers of functional significance?

XPF HhH_2 interaction domains form homodimers *in vitro* mimicking the homodimerisation of Archaeal XPF (114). In mixtures of ERCC1 and XPF HhH_2 domains at ambient temperatures the heterodimer is the predominant form, but at temperatures over 50˚C ERCC1 HhH_2 domains aggregate leaving XPF HhH_2 domains to homodimerise. It has been proposed that XPF homodimers may act as an inactive storage complex in cells to protect against the risks of non-specific DNA cleavage (107). However, if human XPF does form homodimers *in vivo* it must be at very low levels since, in ERCC1-deficient cells, or after ERCC1 siRNA knockdown, only low levels of XPF are found (103, 108).

1.4.8 The XPF nuclease domain

The nuclease site of the ERCC1-XPF complex has been mapped to XPF residues 681-751, it contains a V/IERKX_3D motif conserved between XPF protein family members and binds Mg^{2+} or Mn^{2+} as a metal co-factor (115). The presence of the metal is not necessary for DNA binding and does not alter the DNA binding affinity.

1.4.9 Key residues for catalytic activity

Active site mutations identified Asp687, Asp715, Lys727 and Asp731 as essential for catalytic activity, whereas mutation of residues Arg689 and Arg726 resulted in residual activity (115). Asp687, Glu690, Asp715 and Glu725 have all been directly implicated in metal binding (115). Enzlin and Schärer proposed that residues Asp687 and Asp715 coordinate metal ion binding and residue Asp731 may function to activate a water molecule to act as a nucleophile for phosphodiester bond hydrolysis (115). Mutation of residues Glu690 and Glu725 led to reduced nuclease activity in the presence of Mg^{2+} but not Mn^{2+}, suggesting an altered active site incompatible with the greater stringency requirements for Mg^{2+} compared to Mn^{2+} binding (115). This suggests that the biologically relevant metal cofactor is Mg^{2+} , but in *in vitro* ERCC1-XPF endonuclease assays Mn^{2+} is the preferred metal (102, 106). Although an Arg689Ala mutation resulted in residual nuclease activity *in vitro,* activity was retained *in vivo* but with a shifted incision pattern, suggesting that this residue may be involved in correct positioning of the substrate in the active site for incision (110). Positioning of key amino acids in the nuclease site of XPF is shown in Figure 1.6.

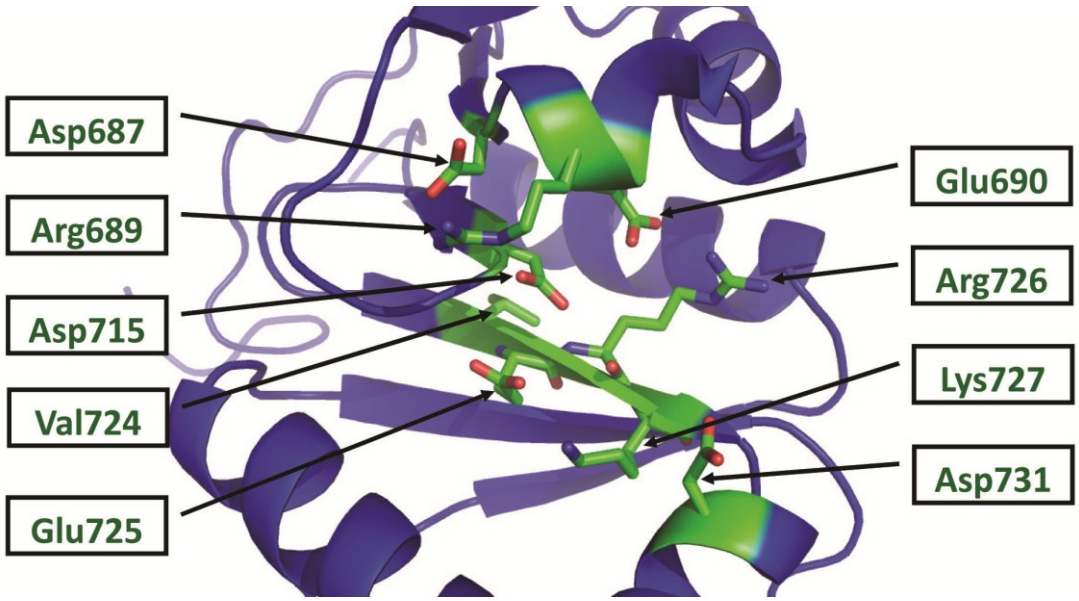

Figure 1.6: The nuclease domain of XPF. Cartoon representation of XPF identifying amino acids and their side chains. Residues Asp687, Glu690, Asp715 and Glu725 are implicated in metal binding (67). No metal ion has been shown. Figure created using PyMOL v0.99 with a homology model of XPF generated using the Protein Homology/analogY Recognition Engine v2.0 (PHYRE)(108).

1.4.10 The XPF helicase-like domain

The XPF helicase-like domain is related to superfamily-2 helicases, it comprises five sub-domains, but lacks critical residues essential for helicase activity (103, 104, 116). In the first of the Walker A motifs, usually required for ATP and DNA binding, the GKT consensus is not present (104, 117). The second Walker B motif lacks acidic residues present in the DEAD/DExH box motif, meaning that Mg^{2+} is unable to bind and catalytic activity is lost (104, 117). Instead, it is thought that the helicase-like domain binds at the junction between ds- and ss-DNA and contributes to substrate specificity (103, 116). The presence of leucine-rich motifs indicates a potential role for protein-protein interactions (118, 119). An Arg153Pro substitution within this domain resulted in XF-E syndrome, with hypersensitivity to UV irradiation and ICL agents (95). Although hypersensitivity may have resulted from disruption of protein-protein interactions required for both NER and ICL repair, it is most likely this was due to XPF misfolding resulting from substitution of the

basic Arginine residue for the hydrophobic Proline. This is in agreement with the reduction in nuclear ERCC1-XPF levels observed (95).

1.4.11 The ERCC1 central domain

The ERCC1 central domain is weakly homologous to the XPF nuclease domain, but has lost the active site residues required for metal binding and catalytic activity (106). Instead, the ERCC1 central domain has acquired the ability to bind DNA and form additional protein-protein interactions, particularly with XPA to recruit the ERCC1-XPF complex for NER. Deletion of the first 91 amino acids of ERCC1 does not affect endonuclease activity, while deletion of an additional 11 residues results in a loss of activity, although it is not known whether this is due to protein instability, or loss of a key interaction activity (93).

1.4.12 Central domain binding to DNA

The ERCC1 central domain surface has a V-shaped groove lined by basic (Arg106, Arg108, Arg144, Arg156) and aromatic (Phe140, Tyr145 and Tyr152) residues, thought to constitute both the DNA binding and XPA interaction domains (106, 112). Through chemical shift perturbations the DNA interacting region has been identified as residues Asn99, Ile102, Leu132, Lys213, Ala214 and Gln134 (120). This region binds preferentially to ss-DNA in an orientation-dependent manner, with an 8-fold greater preference for 5' than 3' overhangs (106). In low salt conditions, the ERCC1 central domain binds ds-DNA with comparable affinity to ss-DNA (106). However, at physiologically relevant salt concentrations, it has a binding affinity (KD) of 2.5-10μM for ss-DNA, while binding of ds-DNA is almost undetectable (106, 120).

1.4.13 Central domain interaction with XPA

The interaction between ERCC1 and XPA maps to ERCC1 residues 92-119 and XPA residues 59-114 (68, 121). In the XPA-binding domain on ERCC1, two motifs are present; a TGGGFI motif essential for binding, and an EEEEEEE motif

shown to be contributory, but not essential for interaction (121). Interestingly, the TGGGFI motif was not identified in any other mammalian proteins (112). Binding studies, with a truncated XPA_{59-93} peptide, confirmed the involvement of Gly72, Gly73 and Gly74 in the binding to ERCC1 (112). A second truncated XPA_{67-80} peptide bound stably to $ERCC1_{96-214}$ in a stoichiometric 1:1 ratio, with a binding affinity (KD) of 0.78μM (112).

An XPA peptide bound to the hydrophobic V-shaped groove on ERCC1 with the Gly72, Gly73 and Gly74 residues of XPA forming a U-turn in the 1039$Å^2$ ERCC1 binding site (112). A number of interactions between individual XPA and ERCC1 residues have been described at this binding site, although there are some differences in interpretation of the same crystal structure (112, 122, 123). There is main chain hydrogen bonding between XPA Gly72, Gly73 and Gly74 and adjacent ERCC1 residues and stacking of aromatic side chains, making the binding site an attractive candidate for small molecule ligands (see below). Furthermore, an XPA Phe75Ala mutation abrogates binding to ERCC1 (112). Tsodikov *et al.* and Tripsianes *et al.* have measured the binding affinity (KD) of XPA to ERCC1 to be 540nM and 1μM, respectively (112, 120).

1.4.14 Is simultaneous binding of ERCC1 to DNA and XPA possible?

Interaction of XPA and ERCC1 is required for NER activity *in vivo*, confirming its role in recruiting ERCC1-XPF to DNA damage, but *in vitro* nuclease activity of ERCC1-XPF does not require XPA (112). It is controversial whether ERCC1 is able to bind DNA and XPA simultaneously. Tsodikov *et al.* used fluorescence anisotropy and measured competitive binding of XPA and DNA to the ERCC1 central domain (112). In contrast, Tripsianes *et al.* monitored chemical shift perturbations upon XPA binding, showing that the strongest response from ERCC1 was in residues Leu139, Phe140 and Phe141 in the deep hydrophobic groove (120). In addition, other residues important for ERCC1/XPA interaction were Gln107, Asn110, Ser142, Arg144, Asn147 and Arg156 (120). Tripsianes *et al.* concluded that

XPA and DNA have distinct binding sites on ERCC1 and suggested that simultaneous binding is possible (120).

1.4.15 How does the ERCC1-XPF complex associate with XPA?

XPA binds at ds- to ss-DNA junctions and localises at the junction 5′ to the lesion to recruit ERCC1-XPF (124). However, in light of a model proposed by Das *et al*., positioning ERCC1-XPF at the DNA junction 5′ to the damage lesion (111), Shell and Chazin argued that, for steric reasons, XPA must instead localise to the 3′ DNA junction (125). For this latter model to be correct and for the ERCC1/XPA interaction to occur, both DNA junctions would need to be in close proximity. Instead, we propose that XPA binds at the 5′ DNA junction and recruits the ERCC1-XPF complex, forcing the DNA junction to advance and so make space for ERCC1-XPF to bind DNA. In support of this, partial unwinding of the DNA junction occurs *in vitro* facilitating XPF cleavage 2 nt upstream of the junction. This process could be driven by a domain rearrangement within ERCC1-XPF upon DNA binding, similar to that known to occur in Archaeal XPF (126).

1.4.16 Mutation of the XPA binding site of ERCC1 affects NER but does not affect repair of interstrand crosslinks

Endonuclease activity and DNA binding of the ERCC1-XPF heterodimer were not affected by ERCC1 mutations lacking the Asn110, Tyr145 and Tyr152 residues required for interaction with XPA (122). Proteins containing the XPA binding site mutations expressed in ERCC1-deficient cells failed to associate with XPA and were only able to partially restore UV resistance (122). However, expression of these mutant proteins in ERCC1-deficient cells fully restored resistance to mitomycin-C, cisplatin and ionising radiation (122), suggesting that the ERCC1/XPA interaction is required for NER, but not for ICL or DSB repair. Given that cisplatin causes mainly monoadducts and intrastrand crosslinks, which are both repaired by NER, in addition to the much less frequent, but more genotoxic, interstrand crosslinks that are repaired by a combination of endonucleolytic cleavage and HR, partial, rather than complete

restoration of cisplatin resistance by an ERCC1 protein that cannot interact with XPA would have been anticipated.

1.4.17 Interaction of XPF with RPA

During NER the ERCC1-XPF complex binds to the ss-DNA binding protein RPA, which protects the undamaged strand, in addition to XPA, but the RPA interaction is less well understood (69, 127–129). Using affinity columns, Bessho *et al.* demonstrated that XPA binds ERCC1, whereas interaction with RPA was mediated by XPF (69). Furthermore, in a pull-down assay ERCC1-XPF bound weakly to DNA and binding was unaffected by XPA addition (127). However, upon adding RPA, the ERCC1-XPF complex was recruited to DNA more efficiently (127). Mutant XPF constructs and a yeast two-hybrid approach showed that XPF binds to the p70 subunit of RPA via its N-terminus (128). In addition, XPF containing a Pro85Ser substitution was unable to interact with RPA, but still interacted with ERCC1 and retained nuclease activity *in vitro*, although the interpretation was complicated by the additional observation that the mutant XPF was mislocalised to the cytoplasm (128). XPF Arg86Ala and Thr89Ala substitutions may also inhibit interaction with RPA (128). Furthermore, addition of RPA increased specificity and activity of ERCC1-XPF cleavage of DNA in *in vitro* endonuclease assays, whereas addition of XPA had no effect (127). When wild-type and Pro85Ser mutant XPF were expressed in XPF-defective CHO UV41 cells, only the control protein fully restored NER ability and UV resistance, suggesting that the XPF/RPA interaction is required for NER (127).

1.5 Important non-NER related interactions of ERCC1-XPF

1.5.1 XPF/SLX4 interaction in ICL repair

Recent research has identified SLX4 (also known as FANCP) as a molecular scaffold for endonucleases SLX1, ERCC1-XPF and MUS81/EME1 to facilitate the processing of branched DNA substrates (130–135). The SLX4 scaffold may also bind additional factors, such as mismatch repair proteins MSH2/MSH3, telomere

binding proteins TRF2/RAP1 and polo-like kinase 1 (131). Depletion of SLX4 induced hypersensitivity to DNA crosslinking agents, but not to UV-induced DNA damage (130, 136). In a comparison of SLX4- and ERCC1-deficient mouse embryonic fibroblast (MEF) cell lines with two Fanconi anaemia cell lines (FANCA, FANCC), where there is hypersensitivity to ICLs, the SLX4 and ERCC1 mutants showed the greatest sensitivity and only the ERCC1-deficient cell line also showed hypersensitivity to UV (136).

Size exclusion chromatography indicated two cellular pools of ERCC1-XPF, one associated with the SLX4 complex and presumed responsible for the HR/ICL repair activities of ERCC1-XPF, and the other interacting with XPA and RPA and presumed responsible for NER (130). Direct interaction of the ERCC1-XPF complex with SLX4 has been demonstrated by yeast two-hybrid assays. The interaction is mediated within the N-terminal 669 residues of SLX4, probably through a conserved MLR domain, but the interaction domain on XPF is unmapped (130, 131). Expression of SLX4 lacking the SLX1 interacting motif (a C-terminal deletion mutant) in SLX4-deficient MEF cells was sufficient to complement hypersensitivity to mitomycin-C, while expression of SLX4 deficient in the interaction with XPF (N-terminal deletion) was unable to complement mitomycin-C hypersensitivity, indicating the importance of the SLX4/XPF interaction in ICL repair (136). Interestingly, an endonuclease assay, utilising a DNA stem loop to determine cleavage specificity of ERCC1-XPF and SLX4/SLX1, showed that SLX1 nicked ds-DNA on the opposite strand to ERCC1-XPF (132).

1.5.2 FANCG and the ERCC1 central domain

FANCG-deficient cells are sensitive to ICL agents due to an inability to make a dual incision at the site of a crosslink (81). In a yeast two-hybrid assay the ERCC1 central domain was reported to interact with FANCG, which forms part of the Fanconi anaemia core complex (137). The ERCC1/FANCG interaction is believed necessary to recruit ERCC1-XPF to the crosslink. Direct interaction of ERCC1 with FANCG could explain how XPF has previously been shown to colocalise with FANCA in cells, presumably through a ternary complex with FANCG (138). Site-

directed mutagenesis indicated that the FANCG/ERCC1 interaction occurred through tetratricopeptide repeats (TPR) in FANCG (137). Complementation of FANCG-deficient cells with mutant FANCG proteins indicated that TPR 1, 2, 5 and 6 were all important in correcting sensitivity to the crosslinking agent mitomycin-C (139).

1.5.3 MSH2 interaction with ERCC1

Using a yeast two-hybrid approach it has been proposed that the mismatch repair protein MSH2 interacts with RAD10, the yeast homologue of human ERCC1, along with several other NER proteins (140). In humans, MSH2 forms a heterodimer with MSH6 (heterodimer known as MutSα), or MSH3 (known as MutSβ) (141). To facilitate repair, MutSβ recognises an ICL, then in association with ERCC1-XPF, is required for the initial processing and unhooking of the lesion (141). It is thought that the ERCC1/MSH2 interaction, involving ERCC1 residues 184-260, is required for ICL repair and cisplatin resistance in an XPA-independent mechanism (142).

1.5.4 RAD52 interaction with XPF

ERCC1-XPF and RAD52 are important for single-strand annealing (SSA), a DNA double-strand break repair mechanism that involves annealing homologous single-stranded ends to bridge double-strand breaks (143). Direct physical interaction has been demonstrated between ERCC1-XPF and RAD52 *in vitro* (144). It is thought that the interaction promotes cleavage of 3′ overhangs allowing processing of non-homologous ends for repair (143). XPF interacts with the N-terminal DNA binding region of RAD52 in a DNA-independent manner (144). RAD52 forms a heptamer around DNA and when a 6:1 ratio of RAD52:XPF is reached the endonuclease activity of ERCC1-XPF increases 3-fold. Super-stoichiometric amounts of RAD52 inhibit XPF activity, presumably by binding to DNA and inhibiting ERCC1-XPF recruitment (144).

1.5.5 TRF2 interaction with ERCC1-XPF in telomere maintenance

ERCC1-XPF is involved in telomere maintenance and it is thought that this occurs by its interaction with the TRF2 complex independent of DNA binding (145). To protect telomeres from being recognised as double-strand breaks, 3′ overhangs at the ends of chromosomes, known as G-strands, loop back and insert into duplex DNA to form t-loops (145). TRF2 promotes t-loops and associates with ERCC1-XPF at telomeres (145). In TRF2-deficient cells, a partial loss of telomeres and associated 3′ overhangs was observed that was dependent on ERCC1-XPF expression (145, 146). Overhangs are retained in ERCC1-deficient cells following inhibition of TRF2, suggesting that ERCC1-XPF is the main nuclease responsible for 3′ overhang cleavage and is inhibited by TRF2 (145).

Only a minor fraction (~1%) of ERCC1-XPF complexes with TRF2, while other proteins essential for NER did not associate, suggesting an NER-independent mechanism for ERCC1-XPF in telomere maintenance (145). As no direct interaction of ERCC1-XPF to TRF2 has been demonstrated, the interaction may occur through a tertiary complex. TRF2 can interact with SLX4 independently of XPF and it is therefore possible that interaction with XPF is through the SLX4 scaffold (131, 132).

It has also been proposed that XPF may have a nuclease-independent role in negatively regulating TRF2-mediated control of telomeres (147). Mutant XPF proteins with nuclease site mutations deficient in endonuclease activity still localised with TRF2 and were able to complement TRF2-mediated telomere shortening in XPF-deficient cells, with activity similar to that of wild-type XPF (146, 147). However, nuclease activity of XPF is required for TRF2 binding to telomeric DNA, suggesting the mechanism of negative regulation of TRF2 by nuclease inactive XPF is due to ternary complex formation with TRF2, likely via SLX4 and inhibiting DNA binding (148).

1.6 Aim of thesis

The aim of this project was to identify novel compounds that could be beneficial for the treatment of malignant melanoma. Herein, we document our efforts to

perform both a phenotypic drug screen for novel compounds, and a targeted approach to identify inhibitors of the ERCC1-XPF complex. We utilise high throughput and *in silico* screening methods to identify compounds and utilise a range of biochemical, biophysical and cell culture techniques to validate compounds.

In Chapter 3, we characterise the effect of standard chemotherapeutic agents on melanocytes and melanoma. Furthermore we perform a phenotypic drug screen to identify novel compounds active against melanoma. Finally, in this chapter we identify a class of nitrofuran compounds and demonstrate activity against melanoma.

In Chapter 4, we identify ERCC1-XPF as a drug target to overcome chemoresistance to platinum based chemotherapy. We establish an *in vitro* endonuclease assay suitable for high throughput compound screening. Furthermore, we setup two specificity assays that can be utilised for screening compounds.

In Chapter 6, we identify target sites on the ERCC1-XPF protein and collaborate with Professor Malcolm Walkinshaw from the University of Edinburgh to perform an *in silico* drug screen. We identify, and characterise ERCC1-XPF inhibitor compounds through a range of biochemical, biophysical and cell culture techniques.

In Chapter 7, we perform further *in silico* screening and collaborate with Dr Barbara Saxty at MRC Technology to perform a high throughput screen and identify additional ERCC1-XPF inhibitors. In this chapter, we also characterise these inhibitors.

2 Chapter 2: Materials and Methods

2.1 Materials

2.1.1 General reagents

Reagents obtained from MRC Human Genetics Unit general stores:

1M Tris pH8.0

5M NaCl

20x TBE

0.5M EDTA pH8.0

Phosphate Buffered Saline: 140mM NaCl, 3mM KCl, 2mM KH_2PO_4, 10nM Na_2HPO_4 pH7.4.

Reagents obtained from Sigma-Aldrich:

1M $MgCl_2$ *(Sigma-Aldrich M1028-10x1ML)*

1M $MnCl_2$ *(Sigma-Aldrich M1787-100ML)*

1M KCl *(Sigma-Aldrich 60142-100ML-F)*

1M $CaCl_2$ *(Sigma-Aldrich 21115-100ML)*

DTT: 10mM DL-Dithiothreitol *(Sigma-Aldrich D0632). Stored at -20°C*

Dimethyl sulfoxide (DMSO)

2-Mercaptoethanol (BME)

N′-Tetramethylethylenediamine (TEMED) *(Sigma-Aldrich T9281-25ML)*

Ammonium persulphate (APS) *(Sigma-Aldrich 3678)*

Tween-20 *(Sigma-Aldrich P9416)*

Consumables obtained from Greiner:

Black 96-well plates *(Greiner 655086)*

Consumables obtained from Star labs:

Solution basins *(Star labs 25-0051N)*

Reagents from general lab supplies:

Urea

0.22µm syringe filters

Formamide

40% Acrylamide Bis-Acrylamide Solution (w/v Acrylamide 19:1 Bis-Acrylamide)

Glacial acetic acid

Pierce® BCA Protein Assay Kit *(Pierce® 23327)*

Isopropanol

Tris-base

Glycine

2.1.2 Mammalian cell culture

Consumables obtained from Beckman Coulter:

Coulter Isoton® II diluent *(Beckman Coulter NC9343512)*

Reagents obtained from Invitrogen:

Dulbecco's Modified Eagle Medium (DMEM) *(Invitrogen GIBCO® 41965)*

RPMI Medium 1640 *(Invitrogen GIBCO® 11875)*

100x Non-Essential Amino Acids *(Invitrogen GIBCO® 11140)*

100x Sodium Pyruvate *(Invitrogen GIBCO® 11360)*

Reagents obtained from MRC Human Genetics Unit general stores:

Foetal Calf Serum (FCS)

100x L-glutamine: 200mM L-glutamine

200x Penicillin-Streptomycin: 7g/l Penicillin ($10x10^8$U/l), 13g/l Streptomycin.

Trypsin/Versene: 50% (v/v) Trypsin, 50% (v/v) Versene

Trypsin solution: 2g/l Trypsin, 0.001% (v/v) Phenol Red, 0.06g/l Penicillin, 0.13g/l Streptomycin, PBS pH 7.8.

Versene solution: 0.4g/l Sodium EDTA, 0.001% (v/v) Phenol Red, PBS

Reagents obtained from Sigma-Aldrich:

12-O-tetradecanoylphorbol-13-acetate (TPA)

Freezing medium: Produced from supplemented cell culture medium with additional FCS (20% final) and 10% (v/v) DMSO. Freezing medium stored at -20°C prior to use.

Cell lines used:

Cell line	*Species*	*Origin*	*Source*
A375	Human	Melanoma	The European Collection of Cell Cultures *(ECACC)*
HBL	Human	Melanoma	Gentaur *(Brussels, Belgium)*
SH5Y5Y	Human	Neuroblastoma	Prof. D.J. Porteous *Molecular Medicine Centre, University of Edinburgh*
PEO4	Human	Ovarian Cancer	Dr G.C. Sellar, *Cancer Research Centre, University of Edinburgh*
MRC5v1	Human	Fibroblast	Prof. A.R. Lehmann. *MRC Cell Mutation Unit, University of Sussex*
3-1-1-T1a (Ercc1 proficient)	Mouse	Melanocyte	(149)

3-1-1-T1a cre neo #5 (Ercc1 deficient)	Mouse	Melanocyte	(149)
Melan A	Mouse	Melanocyte	Prof. D.C. Bennett. *Biomedical Sciences Research Centre, University of London*
13-4-1	Mouse	Melanocyte	Melton group
13-4-2	Mouse	Melanocyte	Melton group
13-4-S1B-S1B2W	Mouse	Melanocyte	Melton group
$PF20^T$	Mouse	Fibroblast	(150)

2.1.3 Protein gel

Tris-glycine running buffer: 192mM Glycine *(Fisher G/0800/60)*, 25mM Tris (*VWR 103156X)*, 0.1% (w/v) SDS, pH8.3.

Transfer buffer: 192mM Glycine *(Fisher G/0800/60)*, 25mM Tris (*VWR 103156X),* pH8.3.

4x Stacking Buffer: 492mM Tris-HCl, pH6.8.

4x Resolving Buffer: 1.56M Tris pH8.8.

5x protein loading buffer: 225mM Tris-HCl pH6.8, 5% SDS, 50% Glycerol, 0.05% (w/v) Bromophenol Blue (*Sigma-Aldrich* B5525).

Fermentas PageRuler™ Plus Prestained Protein Ladder *(Fermentas SM1811)*

Expedeon InstantBlue™ Coomassie Blue Satin *(Expedeon ISB01L)*

2.1.4 Western blotting

Merck Millipore Immobilon-P PVDF transfer membrane *(Merck IPVH00010)*

TBS-T: 5mM Tris-HCl, 75mM NaCl, 0.05% (v/v) Tween-20, pH7.4.

Blocking buffer: 10% (w/v) milk powder, TBS-T.

Amersham ECL Plus Western Blotting Detection System *(Amersham RPN2132)*

Amersham Hyperfilm™ ECL *(Amersham 28906837)*

Antibodies used:

Target Protein	*Primary antibody*	*Secondary antibody*
ERCC1	FL297 Rabbit polyclonal antibody 1:1000 *(Santa Cruz® sc-10785)*	HRP-conjugated Goat anti-rabbit 1:3000 *(Dako P0448)*
XPF	XPF Ab-5 (Clone 51) Mouse monoclonal antibody 1:1000 *(Thermo Scientific MS-1385)*	HRP-conjugated Rabbit anti-mouse 1:2000 *(Dako P0260)*
GAPDH	MAB375 Mouse monoclonal antibody 1:20000 *(Chemicon Millipore MAB375)*	HRP-conjugated Rabbit anti-mouse 1:2000 *(Dako P0260)*

2.1.5 Sulphorhodamine B assay

TCA Solution: Trichloroacetic acid *(Sigma-Aldrich T4885-500G)* prepared as 100% (w/v) stock solution and diluted to a 25% (w/v) TCA working solution.

SRB solution: 0.4% (w/v) Sulphorhodamine B *(Sigma-Aldrich S9012-5G),* 1% (v/v) acetic acid solution.

1% (v/v) Acetic acid solution: 1% (v/v) of glacial acetic acid *(BDH reagents 10001)*

10mM Tris pH10.5: 10mM Tris *(VWR 103156X)*, pH10.5.

2.1.6 Propidium iodide FACS Assay

Stock Solution: For 2 litres: 2000mg Trisodium Citrate, 121mg Tris Base, 1044mg Spermine Tetrahydrochloride, 2mL Nonidet NP40, pH7.6.

Solution A: 10mg Trypsin in 500mL Stock Solution, Stored at -20ºC.

Solution B: 250mg Trypsin Inhibitor and 50mg RNAse A in 500mL Stock Solution, Stored at -20ºC.

Solution C: 208mg Propidium Iodide and 500mg Spermine Tetrahydrochloride in 500mL Stock Solution, Stored at -20ºC.

2.1.7 Annexin V Apoptosis Assay

eBioscience® Annexin V Apoptosis Detection Kit FITC *(eBioscience® 88-8005)*

2.1.8 Standard ERCC1-XPF assay

ERCC1-XPF: Purified recombinant ΔERCC1-XPF produced by Dr Martin Wear. See later for details of expression and purification protocols. Purified recombinant ΔERCC1-XPF stored on ice at 4°C. Protein remained stable for 1-2 weeks before significant breakdown observed. Protein remained active for ~6 months.

Protein buffer: PBS pH7.4, 5% (v/v) Glycerol.

ERCC1-XPF Buffer: Assay buffer prepared prior to use. See later for details.

ERCC1 assay substrate

ERCC1-XPF substrate (Purchased from ATDBio)	6FAM-GCC AGC GCT CGG TTT TTT TTT TTT TTT TTT TTT TCC GAG CGC TGG C-BHQ-1

2.1.9 FEN1 assay

FEN1: Recombinant human FEN1 protein purchased from Abcam *(ab95382)* and stored at -20°C in aliquots. Once thawed, FEN1 stored on ice for up-to 2 weeks.

10x FEN1 buffer: 0.5M Tris pH8.0, 0.1M $MgCl_2$, 10mM DTT, 0.1% (v/v) Tween-20. Buffer aliquoted and stored at -20°C prior to use.

FEN1 assay substrates

FEN1 assay specific substrates* (Purchased from Sigma-Aldrich)	CAC GTT GAC TAC CGC TCA ATC CTG ACG AAC ACA TC-BHQ-1
	6FAM-GA TGT CAA GCA GTC CTA ACT TTG AGG CAG AGT CCG C
	GC GGA CTC TGC CTC AAG ACG GTA GTC AAC GTG
ERCC1-XPF substrate (Purchased from ATDBio)	6FAM-GCC AGC GCT CGG TTT TTT TTT TTT TTT TTT TTT TCC GAG CGC TGG C-BHQ-1

*FEN1 assay specific substrates annealed in 50mM Tris pH 8.0, 100mM KCl, 5mM $MgCl_2$ by first incubating the mixture at 95^{o}C for 5 min, followed by gradual cooling to room temperature. The annealed double-stranded DNA substrates were stored at -20^{o}C as 25µM stocks.

2.1.10 DNase1 assay

DNase1: Lyophilized Deoxyribonuclease 1 from bovine pancreas purchased from Sigma-Aldrich *(Sigma-Aldrich DN25)*. Powder resuspended at 10mg/ml and stored in aliquots at -20°C prior to use.

10x DNAse1 buffer: 0.5M Tris pH8.0, 0.1M $CaCl_2$, 0.1M KCl. Buffer aliquoted and stored at -20°C prior to use.

DNase1 assay substrate

DNase1 assay specific substrate (purchased from ATDBio)	6FAM-CCC-GGG-CCC-GGG-CCC-BHQ-1

2.1.11 DNA Sequencing Gel

DNA formamide/EDTA sample buffer: 10mM EDTA pH8.0, 98% (v/v) formamide.

BPB containing formamide/EDTA sample buffer: 10mM EDTA pH8.0, 98% (v/v) formamide, 0.05% (w/v) Bromophenol Blue (*Sigma-Aldrich* B5525).

DNA marker: prepared using 0.4μM (final concentration) of the following DNA oligos. DNA marker stored at -20°C. For use on sequencing gels, DNA marker was diluted 10x in the appropriate enzyme reaction buffer then sample buffer was added.

Name	*Source*	*Sequence*
6FAM	Sigma-Aldrich	6FAM
6FAM+6	Sigma-Aldrich	6FAM-GCC AGC
6FAM+7	Sigma-Aldrich	6FAM-GCC AGC G
6FAM+8	Sigma-Aldrich	6FAM-GCC AGC GC
6FAM+9	Sigma-Aldrich	6FAM-GCC AGC GCT
6FAM+10	Sigma-Aldrich	6FAM-GCC AGC GCT C
6FAM+15	(DNase1 substrate)	6FAM-CCC-GGG-CCC-GGG-CCC-BHQ-1
6FAM+24	(Gifted by Marion Walker)	6FAM-CCCTGGGCTCTGTAAAGAATAGTG
6FAM+36	(FEN1 substrate)	6FAM-GA TGT CAA GCA GTC CTA ACT TTG AGG CAG AGT CCG C
6FAM+46	(ERCC1-XPF substrate)	6FAM-GCC AGC GCT CGG TTT TTT TTT TTT TTT TTT TTT TCC GAG CGC TGG C-BHQ-1

2.1.12 Protein Crystallisation

Crystallisation Screens obtained from Molecular Dimensions Inc.

JCSG-plus™ Screen *(Molecular Dimensions MD1-37)*

Morpheus™ *(Molecular Dimensions MD1–46/MD1–47)*

PGA-LM HT-96 Crystallization Screen™ *(Molecular Dimensions MD1-51)*

Clear Strategy Screen™ I (HT-96) *(Molecular Dimensions MD1-31)*

Clear Strategy Screen™ II (HT-96) *(Molecular Dimensions MD1-32)*

Structure Screen 1 & 2 (HT-96) *(Molecular Dimensions MD1-30)*

ProPlex (HT-96) *(Molecular Dimensions MD1-42)*

Stura Footprint Screen™ + MacroSol™ (HT-96) *(Molecular Dimensions MD1-43)*

Consumables obtained from Molecular Dimensions Inc.

Greiner 24 well Combo Plate (SBS format) *(Molecular Dimensions MD3-16)*

The MRC Crystallization Plate *(Molecular Dimensions MD11-00)*

ClearVue Sheets *(Molecular Dimensions MD6-01S)*

2.1.13 Biacore Surface Plasmon Resonance Assay

Consumables obtained from Biacore

Ni^{2+}-nitrilotriacetic acid (NTA) sensor chips

1-ethyl-3-(3-diaminopropyl) carbodiimide hydrochloride (EDC)

N-hydroxysuccinimide (NHS)

Running buffer: PBS pH7.4, 5% (v/v) Glycerol,

2.1.14 Thermal Denaturation Assay

BioRad iQ Real-Time PCR Plates *(BioRad 223-9441)*

BioRad Microseal® 'B' Adhesive Seals *(BioRad MSB-1001)*

5000x SYPRO® Orange Protein Gel Stain *(Invitrogen S6650)*

Protein buffer: PBS pH7.4, 5% (v/v) Glycerol,

2.1.15 Size-exclusion chromatography

Superdex-200 size-exclusion column

Running buffer: 50mM Tris pH8.0, 50mM NaCl, 0.5mM $MgCl_2$, 1mM BME,

2.1.16 Compounds

Cisplatin *(Faulding Pharmaceuticals DBL®, 100mg/100ml)*

Oxaliplatin (*Sigma-Aldrich O9512)*

Dacarbazine (*Sigma-Aldrich D2390)*

Bio1E7 *(Maybridge BTB05727, ACD Code:MFCD00276733)*

UCN-01 (*Sigma-Aldrich U6508)*

Emodin (*Sigma-Aldrich E7881)*

Aurintricarboxylic acid (ATA) (*Sigma-Aldrich A1895)*

Compound Libraries

Sigma LOPAC^{1280}™ Library (*Sigma-Aldrich LO1280)*

BIOMOL® Kinase Inhibitor Library *(Enzo® Life Sciences BML-2832-0100)*

BIOMOL® Phosphatase Inhibitor Library *(Enzo® Life Sciences BML-2834-0100)*

All compounds selected for follow-up from Sigma LOPAC^{1280}™ Library were purchased direct from Sigma-Aldrich using the supplied product code.

ERCC1-XPF Inhibitor Compounds

ERCC1-XPF Inhibitor compounds typically purchased in 10mg aliquots and prepared to 100mM in DMSO. Compounds were aliquoted and stored at -20°C.

Suppliers include: ASINEX, ChemBridge Corporation, Enamine Limited, Sigma-Aldrich, Specs.

ERCC1-XPF Inhibitors:

Compound	*Supplier*	*Product Code*
UOE #1	Specs	AK-918/43077820
UOE #2	Specs	AG-690/40753973
UOE #18	Specs ASINEX	AG-690/13155004 BAS 01132391
UOE #26	Specs	AN-023/15595059
UOE #44	Specs	AP-845/41686949

2.1.17 Software

Adobe Photoshop CS4 *for image analysis and image manipulation.*

ChemAxon Marvin Beans (64bt) Suite *for compound structure viewing and drawing.*

DeLano Scientific PyMOL v0.99 *for protein structure viewing and manipulation.*

FlowJo 7.6.4 *for cell cycle and Annexin V assay analysis.*

ImageJ *for Western Blot quantification.*

Microsoft Office 2010

SigmaPlot 12.0 f*or graphical analysis of IC50 and thermal denaturation assays.*

SPSS Inc. 12.0 *for statistical analysis.*

2.2 Methods

2.2.1 Mammalian cell culture

Cell lines were maintained using standard aseptic technique in a Class II biological safety cabinet. Cell culture flasks were incubated at 37°C in 5% CO_2.

2.2.2 Maintenance of cell lines

Cells were maintained in DMEM or RPMI supplemented with 10% FCS, Non-Essential Amino Acids, Sodium Pyruvate, L-glutamine and Penicillin-Streptomycin. Ercc1 proficient and Ercc1 deficient mouse melanocytes were additionally supplemented with TPA.

Cells were passaged every 2-4 days by removing cell culture medium, washing the cells in PBS, then incubating with the serine-protease trypsin for 5 minutes until cells were detached. Cells were then re-suspended in fresh medium and centrifuged at 1,300rpm for 5 minutes. The cell pellet was re-suspended in fresh medium for future culture or plating. Cells were routinely passaged at 1/4 to $1/16^{th}$ confluences dependent upon the cell line and culture period.

2.2.3 Cryogenic storage of cell lines

For cryogenic preservation of cells, cells were trypsinised and pelleted as described above then re-suspended in freezing medium. Cells were transferred to -70°C then subsequently transferred to liquid nitrogen stocks. Conversely to thaw cells, vials were rapidly warmed at 37°C then diluted in medium to dilute DMSO. Cells were centrifuged at 1,300rpm for 5 minutes to pellet cells and remove remaining DMSO, then re-suspended in cell culture medium before plating into a cell culture flask. Medium was changed 24 hours later or cultures were split if confluent.

2.2.4 Counting cells

Cell suspension was diluted 1:100 in Coulter Isoton® II diluent then counted using a Coulter Counter Z series.

2.2.5 Compound preparation

Compounds purchased for *in vitro* validation were solubilized in DMSO using standard aseptic technique. Compounds were then stored at -20^{o}C in aliquots to

minimize freeze thaw cycles. Compounds were typically prepared at 100mM or at their highest DMSO compound solubility.

2.2.6 Compound screening on cell lines

To screen compounds on cell lines in either single or combined regimes, compounds were diluted in medium to 2x their maximum working concentration then added directly to the plate. For a concentration series, typically a 2-fold dilution series (100µl) would be performed in the assay plate with culture medium prior to the addition of cells (100µl). The DMSO concentration was maintained at less than 0.75% DMSO to negate DMSO induced toxicity. A single cell suspension was prepared by trypsinisation and counted as above. Cells were added directly to the plate at a predetermined concentration. Plates were transferred to the incubator at 37°C and 5% CO_2 for a predetermined period then the assays were stopped as per the SRB protocol below. For A375 cells, 500 cells per well were incubated for 5 days. For 3-1-1-T1a cells, 1000 cells per well were incubated for 6 days.

2.2.7 Analysis of IC50 data

Analysis of IC50 data was performed using SigmaPlot 12.0. Data were fitted to a one-site competition algorithm using the following formula;

$$y = \min + \frac{\max - \min}{1 + 10^{x - \log IC50}}$$

In all cases, the maximum was constrained to 100% activity and the minimum was constrained to 0% activity. If data were not compatible with this algorithm, a sigmoidal dose-response curve algorithm with variable hillslope was utilized. This equation is as follows;

$$y = \min + \frac{\max - \min}{1 + 10^{(\log IC50 - x)Hillslope}}$$

2.2.8 Sulphorhodamine B assay

96 well cell culture plates were fixed with 50µl 25% (w/v) TCA added directly to culture medium for 1 hour at 5°C, and then washed 10x with water using a Titertek® Handiwash 110 plate washer. Plates were dried at 60°C for 45 minutes or dried overnight at RT. Cells were stained with 50µl SRB for 30 minutes and then washed 4x with 1% acetic acid solution to remove unbound dye. Following drying, bound SRB dye was extracted in 150µl 10mM Tris pH10.5 and the plate was shaken for 1 hour at 600rpm using a Heidolph Titramax 1000. Plates were read using a plate reader at 540nm.

2.2.9 Protein quantification

Protein concentration was measured using the Pierce® BCA Protein Assay Kit. 25µl of protein samples were added to a 96 well plate (if within the 0.025-2mg/ml assay detection limit) alongside known concentrations of Bovine Serum Albumin (BSA) standards. 100µl of prepared BCA was added per well and the plate was incubated for 30 minutes at 37°C and read at 562nm using a spectrophotometer. Protein concentrations were determined based upon the BSA standards curve.

2.2.10 SDS-Page Gel

Protein gels were prepared and run using the BioRad Mini-PROTEAN3™ electrophoresis system using a Tris-glycine buffering system. Either 10% Acrylamide or 16% Acrylamide gels were prepared dependent upon whether protein breakdown was expected. The top of the resolving gel was leveled using isopropanol, which was removed prior to the stacking gel being poured. Both gels were prepared with 4% stacking gels and 15 well combs.

	10% Resolving Gel	16% Resolving Gel	4% Stacking Gel	
4x Buffer	2.5	2.5	1.25	ml
dH2O	4.8	3.5	3.2	ml
40% Acrylamide	2.5	4	0.5	ml
10% SDS	100	100	50	µl
10% APS	100	100	50	µl
TEMED	10	10	5	µl

Samples were mixed with 5x protein loading buffer and heated to 80°C for 5 minutes before loading. Gels were run at 70V then increased to 120V when the proteins aligned at the interface between the stacking and resolving gels.

2.2.11 Coomassie Staining

Proteins were visualized by coomassie blue staining using Expedeon InstantBlue™ coomassie stain. Firstly the gel was removed from its glass plates then briefly washed in H_2O. The gel was then placed into InstantBlue™ for 1 hour. Unbound dye was removed from the gel by washing in H_2O. Gels were imaged using a flatbed scanner at 600dpi for electronic record.

2.2.12 Western Blotting

Proteins were transferred from SDS-Page gel onto an Immobilon-P PVDF transfer membrane using methods described by Towbin *et al.* (151). Transfer was performed using the BioRad Mini-Trans-Blot system at either 40mA overnight at 4°C or at 400mA for 1 hour at 4°C using an icepack and magnetic stirrer. Following transfer, the membrane was removed from the cassette and washed for 5 minutes in TBS-T. Membranes were then placed in blocking buffer for 1 hour followed by a further three TBS-T washes. Membranes were then incubated with the primary antibody for the appropriate duration and conditions then washed a further 3 times in TBS-T. Membranes were then incubated with the secondary antibody for 1 hour at

the appropriate secondary antibody dilution then washed a further 3 times in TBS-T. Membranes were then incubated with ECL-plus chemoluminescent reagent for 1 minute then visualized using autoradiography film or using the GE ImageQuant LAS 4000 system.

2.2.13 Propidium iodide FACS Assay

The Propidium iodide Assay was performed in order to analyze DNA content in the cells. The method used was a modified version of that documented by Vindeløv *et al.* (152).

To perform the assay, cells were plated in 35mm petri dishes then varying concentrations of cisplatin were added 24 hours later. After a predetermined treatment time, cells were harvested with trypsin and centrifuged. Cells were then washed with PBS and the pellet was re-suspended in 100µl citrate buffer. Cells were stored at -20°C until all samples were collected. Samples were processed by addition of 450µl of solution A for 2 minutes, 375µl of solution B for 10 minutes then finally 250µl of solution C for 10 minutes. Samples were stored on ice prior to analysis.

Cells were analyzed in collaboration with Elizabeth Freyer (MRC Human Genetics Unit Technical Services) using a BD Biosciences FACSAria™ II FACS machine. Data were analyzed using FlowJo v7.6.4.

2.2.14 Annexin V Apoptosis Assay

The Annexin V assay functions by use of a fluorescently labeled Annexin V dye which binds to phosphatidylserine proteins. Under normal conditions, phosphatidylserine is predominantly located in the inner leaflet of the plasma membrane and so is unavailable for dye binding. Upon initiation of apoptosis, phosphatidylserine translocates to the outer leaflet of the plasma membrane marking the cell as a target for phagocytes. Here, Annexin V FITC binds labeling the cell as undergoing the early phases of apoptosis. In combination with propidium iodide staining which is excluded from cells during the early stages of apoptosis, early stage apoptosis can be differentiated from from late stage apoptosis and necrotic cells.

To perform the assay, cells were plated in 35mm petri dishes with phenol red-free medium then varying concentrations of cisplatin were added 24 hours later. After 48 hours treatment, cells were harvested by either cell scraper or detachment with trypsin and processed using the eBioscience® Annexin V Apoptosis Detection Kit. Briefly, cells were washed in PBS then 1x binding buffer before being re-suspended at 1-5x10^5 cells in 100µl 1x binding buffer. 5µl Annexin V FITC was added for 15 minutes then cells were washed with 1x binding buffer. Cells were then resuspended in 200µl binding buffer and stored on ice in the dark. Prior to analysis, cells were resuspended and 5µl propidium iodide staining solution was added.

Cells were analyzed in collaboration with Elizabeth Freyer (MRC Human Genetics Unit Technical Services) using a BD Biosciences FACSAria™ II FACS machine. Data were analyzed using FlowJo v7.6.4.

2.2.15 Recombinant ERCC1-XPF expression and purification

Protein expression was performed by Ann-Marie Ritchie and protein purification was performed by Dr Martin Wear. Briefly, codon optimized ERCC1 and XPF constructs were cloned into pET-28a expression vectors for expression in *E. coli*. Constructs were designed to contain cleavable N-terminal His-tags. Optimized expression conditions were determined by standard 3x3x3x2 matrix of expression conditions including heat/cold shock protocols resulting in 54 conditions tested per construct.

Optimized expression conditions for the $_{\Delta 95}$ERCC1 construct containing the ERCC1 central and HhH_2 domains were in the BL21 (DE3) Star strain in LB medium with 1% glucose, heat/cold shock, 1mM IPTG, 15˚C O/N. Protein expression yield was 3-5mg/l and ~50% of ERCC1 protein was in the soluble fraction. Purification from scale up cultures of 2-4l was performed by 3-step process by IMAC (1ml IMAC FF), Gel filtration (Superdex 200) and Cation IEX (1ml SP HP). The immobilized metal ion affinity chromatography (IMAC) column was used to coordinate and purify his-tagged protein. The Gel filtration column was then used to further purify the sample to remove traces of remaining proteins by size exclusion chromatography. The final Cation IEX column was then used to further purify the

protein by ion exchange chromatography separating ΔERCC1 from any other remaining proteins based upon their ionic charge. Purified protein was deemed to be >95% purity with a final yield of ~1mg/l from the original culture. Protein was stable and existed as a soluble mono-disperse protein with the expected Mr of 22.78kD plus a 3.56kD N terminal his-tag. Optimized conditions for the $_{\Delta 666}$XPF construct containing the XPF nuclease and HhH_2 domains were expression in BL21 (DE3) Star strain in LB medium with 1% glucose, heat/cold shock, 1mM IPTG, 15˚C O/N. Protein expression yield was 5-7mg/l however only ~5% of XPF was in the soluble fraction. Refolding protocols resulted in >95% soluble protein with a final yield of 1-2mg/l however the gel filtration indicated an apparent Mr of 150-180kDa rather than the expected Mr of 27.82kD with a 3.56kD N terminal his-tag. This was thought to resemble an octamer or XPF dimer in a TX-100 detergent micelle. XPF was unstable in the absence of detergent.

Coexpression of ERCC1 and XPF was performed using $_{\Delta 95}$ERCC1 cloned into the pET28a Kan^R and the $_{\Delta 666}$XPF expression cassette recloned into an Amp^R plasmid backbone. Purified protein was deemed to be >95% purity with a final yield of ~10mg/l from the original culture. Protein was stable and existed as a soluble mono-disperse protein with the expected Mr of 50.6kD plus the two N terminal his-tags totalling 7.12kD.

2.2.16 Standard ERCC1-XPF assay

The ERCC1-XPF assay was performed in black 96-well plates at a final volume of 100µl. Each reaction contained 50mM Tris pH8.0, 50mM NaCl, 5mM $MnCl_2$, 1mM BME, 100nM recombinant ΔERCC1-XPF protein and 200nM substrate. Assays were set up and run at RT.

To screen compounds against ΔERCC1-XPF, assays were set up by first preparing compounds in the assay plate using a 2-fold dilution series with a 40µl final volume. DMSO concentrations were maintained at a maximum of 1%. ΔERCC1-XPF buffer was prepared fresh and 50µl was added to each well then mixed briefly on a plate shaker (20”, 600rpm). The assay was incubated for 30’ at RT to allow compound to bind to the ΔERCC1-XPF protein then 10µl of substrate

was added. Plate was read using PerkinElmer Victor 3 multilabel plate reader and analysed at 3 hours post substrate addition. Data were analysed using Microsoft Excel 2010 and IC50 values were generated using SigmaPlot 12.0 software.

2.2.17 Pre-incubated ERCC1-XPF assay

The pre-incubated ERCC1-XPF assay was performed in black 96-well plates at final volume of 100µl. Prior to reaction, ΔERCC1-XPF was incubated at RT in 1x reaction buffer for 72 hours. Each reaction contained 50mM Tris pH8.0, 50mM NaCl, 0.5mM $MgCl_2$, 1mM BME, 50nM recombinant ΔERCC1-XPF protein and 200nM substrate. Assays were set up and run at RT.

To screen compounds against pre-incubated ΔERCC1-XPF, assays were set up as for the standard ERCC1-XPF assay (Section 2.2.14) except the plates were analysed at 1 hour post substrate addition.

2.2.18 FEN1 assay

The FEN1 assay was performed in black 96-well plates at a final volume of 100µl. Each reaction contained 10µl of 10x FEN1 buffer, 20nM recombinant FEN1 protein and 50nM substrate. Assays were set up and run at RT.

To screen compounds against FEN1, assays were set up by first preparing compounds in the assay plate using a 2-fold dilution series with a 40µl final volume. DMSO concentrations were maintained at a maximum of 1%. 1x FEN1 buffer was prepared from 10x stock and recombinant FEN1 added. Tubes were mixed by gentle inversion. 50µl FEN1 buffer was added to each well and mixed briefly on a plate shaker (20", 600rpm). Assay was incubated for 30' at RT then 10µl of ERCC1-XPF assay substrate was added. Plate was read using PerkinElmer Victor 3 multilabel plate reader and analysed at 1 hour post substrate addition. Data were analysed using Microsoft Excel 2010 and IC50 values were generated using SigmaPlot 12.0 software.

2.2.19 DNase1 assay

The DNase1 assay was performed in black 96-well plates at a final volume of 100µl. Each reaction contained 10µl of 10x DNase1 buffer, 0.5ng DNase1 protein and 200nM substrate. Assays were set up and run at RT.

To screen compounds against DNase1, assays were set up by first preparing compounds in the assay plate using a 2-fold dilution series with a 40µl final volume. DMSO concentrations were maintained at a maximum of 1%. 1x DNase1 buffer was prepared from 10x stock and DNase1 was added following a 1:40 dilution from stock. Tubes were mixed by gentle inversion. 50µl DNase1 containing buffer was added to each well and mixed briefly on a plate shaker (20", 600rpm). Assay was incubated for 30' at RT then 10µl substrate was added. Plate was read using a PerkinElmer Victor 3 multilabel plate reader and analysed at 30 minutes post substrate addition. Data were analysed using Microsoft Excel 2010 and IC50 values were generated using SigmaPlot 12.0 software.

2.2.20 DNA "Sequencing" Gel

DNA sequencing gel was prepared from 5g urea, 5ml 40% acrylamide solution, 0.5ml 20x TBE and 0.7ml H_2O. Gel was warmed to 80°C to dissolve urea then 0.22µm syringe filtered. 75µl APS and 7.5µl TEMED were added then a 1.0mm thick gel was cast with a 15 well comb using the Bio-Rad Mini-PROTEAN3 electrophoresis system. No stacking gel was added. Electrolyte chambers were filled with 1x gel running buffer.

Gel was pre-warmed at 15mA for 10 minutes prior to rinsing urea from wells and loading samples. Samples were prepared by mixing 10µl sample with 6µl sample buffer then heating to 80°C for 5 minutes before loading. Gels were loaded with 6µl sample buffer containing BPB in lane 1 and 6 µl DNA marker/sample buffer in lane 2. Samples in subsequent lanes were prepared in sample buffer without BPB as this comigrated with 4nt DNA obscuring potential DNA bands. DNA fragments were separated by running at 15mA until BPB was ¾ of the way down the gel. DNA

sequencing gels were visualised using the GE Healthcare ImageQuant LAS4000 v1.0 or FujiFilm FLA-5100 Fluorescent Image Analyser.

2.2.21 Protein Crystallisation

ΔERCC1-XPF protein crystallisation screens were set up using a 24 well vapour diffusion hanging drop format or 96 well vapour diffusion sitting drop format. 24 well screens were setup using 500µl reservoir solution and a 1µl protein: 1µl reservoir solution hanging drop. The 96 well screens were setup using a Douglas Instruments Oryx8 crystallisation robot with 50µl reservoir solution and a 0.5µl protein: 0.5µl reservoir solution sitting drop. Screens were setup at 4°C and 18°C. Protein was concentrated to 10mg/ml prior to use and used within 5 days of production.

2.2.22 BIAcore Surface Plasmon Resonance Assays

The BIAcore Surface Plasmon Resonance (SPR) assay is a highly sensitive assay used to monitor molecular interactions in real time. It functions by exploiting a phenomenon called Surface Plasmon Resonance and occurs in thin conducting films at an interface between different refractive indexes. Under total internal reflection conditions, reflecting light causes an electric field intensity termed an evanescent wave field, which leaks across into the medium of lower refractive index. As such, at a certain angle of reflection a drop in intensity of light is observed, this is termed the SPR angle. Changes to the surface of the sensor chip caused by binding of small molecules to target protein on the chip, results in changes to the refractive index and can be measured as a change in the SPR angle. The change in angle is then converted to response units (RU). This is shown in Figure 2.1.

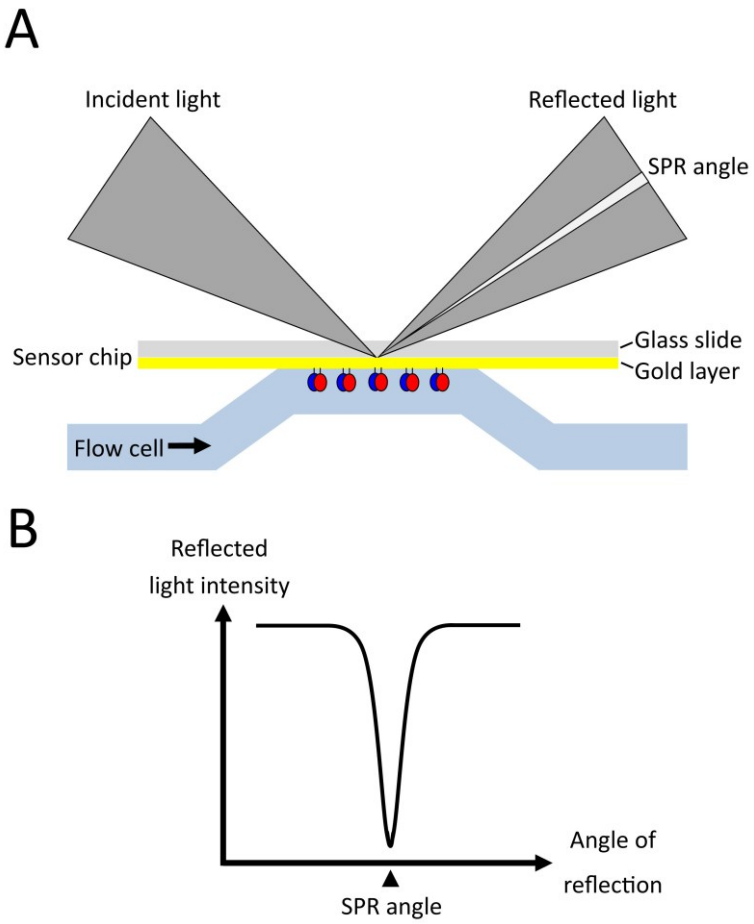

Figure 2.1: Diagram showing the principals of the Biacore SPR assay. (A) Showing ΔERCC1-XPF bound to the sensor chip. Upon total internal reflection, the Surface Plasmon Resonance phenomenon causes a minimum in the reflected light known as the SPR angle. (B) The SPR angle can be measured. An inhibitor bound to ΔERCC1-XPF would change the refractive properties and alter the SPR angle.

The SPR assays were performed in collaboration with Dr Martin Wear using a BIAcore T100 machine. Assays were performed by first immobilising and covalently stabilising His-tagged ΔXPF or ΔERCC1-XPF proteins to a Ni^{2+}-nitrilotriacetic acid (NTA) sensor chip using a protocol developed by Wear *et al.* (153). Briefly an NTA sensor chip was Ni^{2+} primed with 25µl of 500µM $NiSO_4$ at 5 µl/min then the dextran surface carboxylate groups were activated with 20µl of 0.2M 1-ethyl-3-(3-diaminopropyl) carbodiimide hydrochloride (EDC); 50mM N-hydroxysuccinimide (NHS) at 5µl/min. His-tagged ΔXPF or ΔERCC1-XPF proteins

were then captured and covalently stabilized on the surface by injection at 25µl/min. Non-covalently bound proteins were removed from the surface using assay running buffer supplemented with 250mM EDTA at 20µl/min.

Compounds were initially examined in the BIAcore SPR assay using a single concentration screen and maintained at 1% DMSO. Following analysis and 'hit' identification, a concentration screen was performed using an 8 point, 2-fold dilution series of compound. Results were analysed using the software supplied with the instrument (v2.02, GE Healthcare).

2.2.23 Thermal Denaturation Assay

Thermal Denaturation Assays of ΔERCC1-XPF were performed on a modified BioRad IQ5 ICycler RT-PCR machine. This RT-PCR machine has been setup for Thermal Denaturation and use with the environmentally sensitive SYPRO Orange dye. Thermal Denaturation functions by proteins unfolding with increased temperature resulting in an increase in exposed hydrophobic regions of proteins. This results in a large increase in fluorescence from the SYPRO Orange dye when measured at an excitation of 485nm and emission spectrum of 575nm.

TDA was performed in a 96 well plate format with a well volume of 50µl. Firstly additional protein buffer and then 5µM ΔERCC1-XPF were added to the plate. Protein buffer contained PBS with 5% glycerol and 1mM $MgCl_2$. Compounds were then diluted and added at a 500µM final concentration. SYPRO Orange was added to the plate at 5x standard concentration (diluted from 5,000x stock). The wells were then mixed by gently pipetting and the plate was centrifuged at 4,000rpm for 5 minutes. Reaction plates were placed in the BioRad IQ5 ICycler RT-PCR machine and cycled from 20°C to 80°C with 30 second 1°C increments. Interaction of compounds with ΔERCC1-XPF was observed by a change in the transition melting temperature (ΔTm). Data were analysed using Microsoft Excel 2010 and Tm values were generated using SigmaPlot 12.0 software.

2.2.24 Size-exclusion chromatography

Size exclusion chromatography was performed on ΔERCC1-XPF protein using a Superdex 200 size exclusion column. This column has a dynamic range of 10kDa to 600kDa and an exclusion limit of 1.3MDa.

The size exclusion column had previously been calibrated by Dr Martin Wear with control proteins and a standard curve was adopted for these experiments. Standard curve was based upon: *Protein ($V_{elution}$)[Mr]*: IgG (1.25ml)[150kDa]; BSA (1.5ml)[67kDa]; beta-Lactoglobulin (1.6ml)[18.4kDa]; Cytochrome-C (1.85ml)[12.3kDa]; Vitamin B12 (2.05ml)[1.4kDa]; Cytidine (2.2ml)[0.3kDa]; The total column volume (Vt) was 2.38ml and the column void volume (Vo) was 0.78ml.

Protein samples were prepared by incubation at room temperature for 24 hours with, or without 200μM compound UOE #18. ΔERCC1-XPF was additionally loaded without preincubation. Size exclusion chromatography was performed by directly injecting sample onto the column with a 50μl/min flowrate in running buffer. Eluent from the column was subsequently collected in 50μl fractions into a 96 well plate. All experiments were performed at 4°C in refrigerated cabinets. Elution profiles were monitored and elution volumes were calculated.

2.2.25 Protein structure visualisation

Protein homology modelling was performed using the Protein Homology/Analogy Recognition Engine v2.0 (PHYRE^2) (154).

Crystal structures from the Protein Data Bank and predicted PHYRE^2 protein models were visualised using PyMOL v0.99.

2.2.26 *In silico* Drug Screening and Molecular docking

In silico drug screening and molecular dockings were performed by Dr Steven Shave and Dr Douglas Houston from Professor Malcolm Walkinshaw's Group. The first series of *in silico* screening, corresponding to Chapter 5 herein was

performed by Dr Steven Shave. The second series of *in silico* screening, corresponding to Chapter 6, was performed by Dr Douglas Houston.

For the initial *in silico* ERCC1-XPF interaction screen, Dr Steven Shave used the ERCC1-XPF crystal structure (PDB code; 2A1J) to generate a series of site points mapping the target site on the XPF protein. He then used the Ligand Discovery at Edinburgh University (LIDAEUS) program (155) to screen the Edinburgh University Ligand Selection System (EDULISS) database (156). LIDAEUS is a rigid docking program used for high-throughput virtual screening and uses the EDULISS database of >5 million commercially available compounds as its compound library (155, 156). He then used the Ultra Fast Shape Recognition with Atom Types (UFSRAT) tool, which uses 48 descriptors defining molecular shape and electrostatic properties, to discover additional molecules capable of making similar interactions. This generated a list of ~460 compounds from the Chembridge, Maybridge and Specs dataset with similar structures to the defined sets of points. The compounds were then further screened using the program Autodock. The compounds were filtered to remove duplicate structures and by mlogP (if under 3.5 then there is an 80% chance of being soluble) to remove insoluble compounds. The final lists were then ranked by ligand efficiency as calculated by the following formula;

$$\mathbf{LE=(-RTln(KD))/N}$$

Whereby:

LE = Ligand efficiency (kcal/mol/N)

R = Gas Constant (J/K/mol)

T = Temperature (K)

KD = Dissasociation constant (M)

N = Number of non-hydrogen atoms

A similar *in silico* screen was performed for the XPF endonuclease domain. As no human XPF endonuclease domain crystal structure exists, a homology model was first created using the Protein Homology/Analogy Recognition Engine (PHYRE) and

optimised by energy minimisation with the GROMACS tool (154). *In silico* screening was performed on an Archaeal XPF homologue crystal structure (PDB code; 2BGW) and the homology model.

A second more elaborate *in silico* screen was subsequently performed by Dr Douglas Houston. Here a Combined Docking and Similarity Search (CODASS) programme was used. This process also utilised EDULISS and LIDAEUS and the top scoring 50,000 were screened again in a flexible docking programme (155, 156). The top scoring 100 were then run through a battery of similarity search algorithms creating a tailored database of 20,000 compounds. These were then rescreened through the flexible docking programme and the top scoring 5,000 rescreened in an iterative process. Finally, the top 5,000 were run through a second independent programme and were filtered in pose match and scoring algorithms to generate a list of 300 compounds.

3 Chapter 3: Cell based drug screen for compounds active against melanoma

3.1 Aim of chapter

The aim of this chapter was to understand the effect of standard therapeutics and identify novel therapeutics for the treatment of malignant melanoma. We aim to identify two classes of compounds using cell based screening methods, those which are selectively active against malignant melanoma, and secondly, compounds which overcome the chemoresistance of malignant melanoma to the chemotherapeutic agent cisplatin.

3.2 Introduction

3.2.1 Mechanism of cisplatin resistance

Cisplatin is a platinum based chemotherapeutic agent known to have efficacy against a wide range of solid malignancies including testicular cancer, ovarian cancer and lung cancer (157, 158). Importantly, although initial response is often documented, resistance commonly occurs in a fraction of tumours which initially respond (157). In malignant melanoma, cisplatin is predominantly ineffective from the outset.

Cisplatin adducts result in helical distortions to the DNA and in doing so activate multiple DNA damage repair mechanisms, notably nucleotide excision repair and mismatch repair (157). Concurrent with this, cisplatin damage is known to result in arrest at the S and G2 phases of the cell cycle allowing an opportunity for the genome to restore integrity and facilitate cell cycle progression (157). Should repair not be possible, the onset of apoptosis follows (157).

In response to cisplatin a wide range of signaling mechanisms are triggered notably activation of apoptosis through p53 and activation of stress response through the MAPK pathway (157). It is thought that activation of p53 occurs through a signaling cascade involving the ATM, ATR and CHEK1 proteins which then phosphorylate and stabilize p53 through serine 20 (157). This leads to nuclear and cytoplasmic effects that result in permeabilisation of the mitochondrial membrane or increased signaling of death receptors (157). It is also thought that activation of the

MAPK pathway occurs through CHEK1 activation at various pathway branch points (157).

One major mechanism of cisplatin resistance is through decreased accumulation of intracellular cisplatin levels and this can occur through a plethora of transporter proteins involved in both cisplatin influx and efflux (157). Two proteins involved in cisplatin accumulation which when aberrantly regulated in cancer result in decreased intracellular cisplatin levels are the copper transporter 1 (CTR1) protein and the multidrug resistant protein 2 (MRP2) (159, 160). Firstly, cisplatin uptake into the cells is known to occur through the CTR1 protein (159). As such, it has been shown that pretreatment of cells with copper, the main substrate for CTR1, results in a cisplatin protective effect (161, 162). In contrast, cells treated with copper chelators result in cisplatin accumulation and potentiation of cisplatin toxicity (161, 162). Secondly, it has been shown that ABC ATPase like multidrug resistance proteins, particularly MRP2, are responsible for the majority of cisplatin efflux (160, 163). As such, high expression of MRP2 mRNA has been shown to correlate with resistance to cisplatin while inhibition with siRNA reduced chemoresistance (163). Furthermore, patients harbouring polymorphisms of MRP2 in non-small cell lung carcinoma have been shown to have significantly increased response to platinum-based chemotherapy (160).

Cancer cells can also become resistant to cisplatin via increased efficiency of DNA repair or by increased coping strategies when DNA damage is present (157). One mechanism of increased DNA repair is through the NER pathway and as such, increased ERCC1-XPF endonuclease mRNA or protein levels have been implicated in response to cisplatin based regimes (157). It is also thought that the translesion synthesis is upregulated allowing transcription to proceed even in the presence of DNA damage lesions (157).

Cisplatin resistance is a major problem for treatment of solid malignancies with platinum-based chemotherapy and novel chemotherapeutics are necessary to overcome resistance. In this chapter, we aim to identify novel compounds to potentiate the toxic effects of cisplatin in melanoma cells. Here we utilize a non-targeted approach to identify novel inhibitors as a plethora of mechanisms exist that

may overcome cisplatin resistance including increased intracellular cisplatin accumulation, initiation of apoptosis, or by inhibiting DNA repair.

3.2.2 Nitrofurans

Nitrofuran compounds, including Nifurtimox, are the main frontline treatment for the parasitic infection Chagas disease (164). Chagas disease is the commonest parasitic infection of Southern America, resulting from infection by *Trypanosoma cruzi* (164). It is thought that nitrofuran compounds act as prodrugs undergoing enzyme based activation by nitroreductases (164). The nitroreductase family of proteins is sub-divided into two classes, Type 1 enzymes are oxygen insensitive and contain an FMN cofactor functioning by reducing the nitro-group using a two electron reduction reaction promoting DNA damage as shown in Figure 3.1 (164, 165). Type 2 nitroreductases are oxygen sensitive and contain FAD or FMN cofactors (164, 165). These enzymes act by reducing the nitro-group by a one electron reduction to generate an unstable nitro-radical which in the presence of oxygen undergoes futile cycling to generate superoxide (O_2^-) and regeneration of the parent nitro-compound, this is shown in Figure 3.1 (164, 165). In trypanosomes and bacteria, the Type 1 mechanism is utilized for nitrofuran activation whereas in humans, both Type 1 and Type 2 activation can be utilized (164).

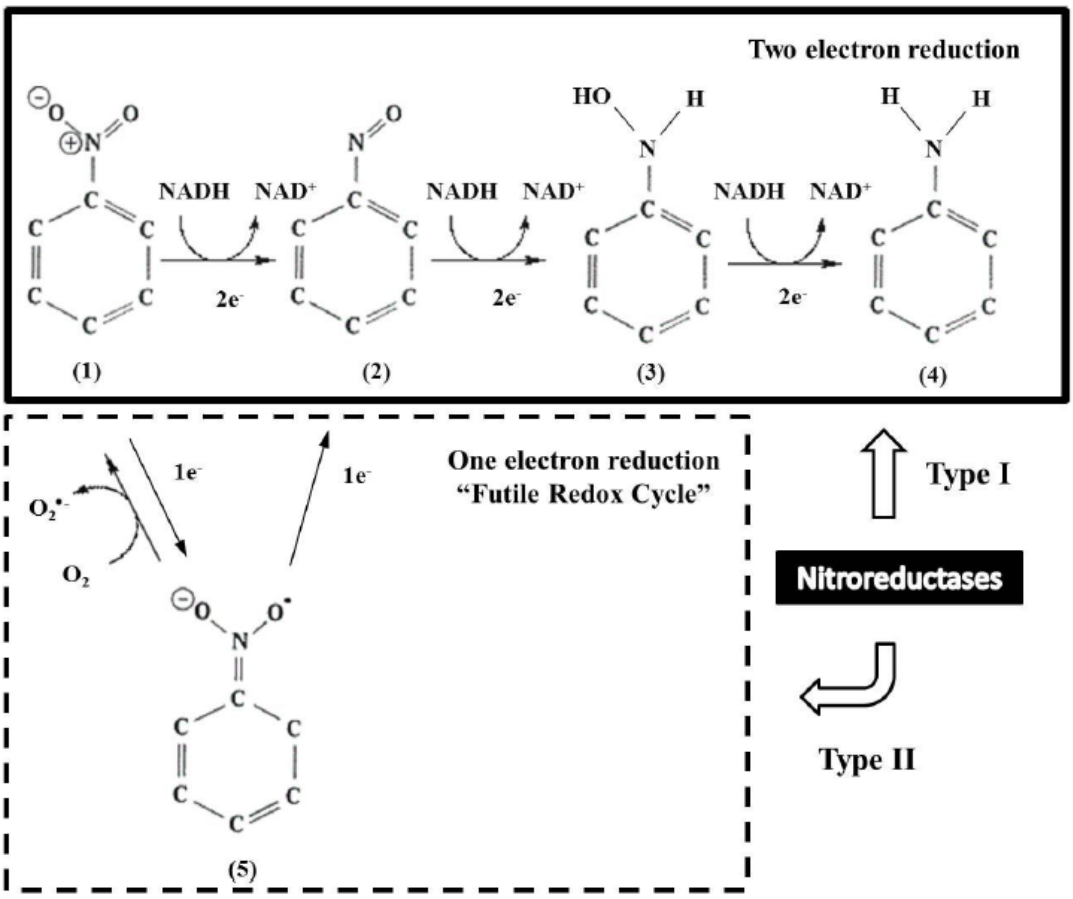

Figure 3.1: Showing the mechanism of nitrofuran activation by nitroreductases. Type 1 nitroreductases function by reducing the nitro-group by a two electron reduction reaction to form nitroso (2), hydroxylamino (3) and amino group intermediates (4). The Type 2 nitroreductases function by reducing the nitro-group by a one electron reduction to generate an unstable nitro-radical (5) which in the presence of oxygen generates superoxide and the parent nirofuran (1) through futile cycling. In the absence of oxygen, the unstable nitro-radical (5) can be reduced to the nitroso intermediate (2). Figure from reference (165).

In human cells, nitrofuran compounds result in a significant increase in superoxide formation and result in increased DNA damage (164, 166). Additionally, in alkaline comet assays following treatment with nitrofuran compounds, a dose dependent increase in the tail moment occurs indicating the formation of DNA single and/or double strand breaks (166). Furthermore, DNA damage is more potent on mitochondrial DNA rather than nuclear DNA (166).

In *E.coli* where nitrofuran activation occurs through Type 1 nitroreductases it is controversial whether nucleotide excision repair is the predominant mechanism for DNA damage repair (164, 167). In contrast to early research, Ona *et al.* show that *E.coli* harbouring NER defects were hypersensitive to treatment with nitrofuran compounds (167). Furthermore, they show that *E.coli* harbouring mutations in the translesion synthesis pathway, particularly Pol IV, were also hypersensitive to nitrofuran induced DNA damage (167). This suggests *E.coli* tolerates nitrofuran induced DNA damage by means of translesion synthesis and DNA repair by NER (167). It remains to be determined whether this is also the case in humans.

3.2.3 Nifurtimox in neuroblastoma

In 2006, a 5 year old patient with recurrent neuroblastoma who was unresponsive to salvage chemotherapy contracted Chagas disease (168). In addition to continued attempts with salvage chemotherapy, the patient was also administered Nifurtimox to treat Chagas disease (168). Upon this combination, the patient showed clinical response and the neuroblastoma went into remission (168). The clinical response of the neuroblastoma was attributed to the Nifurtimox treatment (168).

Since then, Nifurtimox has undergone and passed Phase 1 clinical trials for relapsed or refractory neuroblastoma (169). A further Phase 2 clinical trial for refractory or relapsed neuroblastoma or medulloblastoma is currently under way with an estimated primary completion date in 2014. In addition, a study by Koto *et al.* has furthered the notion of Nifurtimox in cancer therapy showing that in combinational therapy with tetrathiomolybdate (which is an inhibitor of the cellular antioxidant protein, SOD1) it can act synergistically to increase cellular ROS and apoptosis in medulloblastoma (170).

Currently Nifurtimox is of considerable focus in neuroblastoma and medullablastoma due to impressive response rates such as reported in 2006 (168). We postulate that, as the precursor cells to neuroblastoma and melanocytes both arise from the neural crest lineage in early development, it may be possible nifurtimox will also be active on refractory or relapsed melanoma. In this chapter, we explore this theory further.

3.2.4 Role of melanin in response to UV and ROS

The role of melanin in cells is thought be for the protection of cells from UV radiation (171). Two main forms of melanin exist, eumelanin and pheomelanin. Eumelanin is the most common and is a brown-black polymer. This differs structurally from pheomelanin which is less common and is red-brown in colour. Protection from UV by melanin has been proposed to occur through two distinct mechanisms, firstly by directly absorbing UV acting as a UV filter, and secondly by scavenging ROS formed upon UV radiation (171). As the mechanism of Nifurtimox induced DNA damage is due to formation of ROS during nitrofuran activation, it is proposed that melanin may also absorb nitrofuran induced ROS. Furthermore melanin, particularly pheomelanin, has been reported to act as a potent UVB photosensitizer by production of ROS upon UV light (171, 172). In this chapter, we explore whether nitrofuran compounds are also affected by melanin.

3.3 Results

3.3.1 Cell culture assay validation

To investigate the effect cisplatin and other DNA damaging agents have upon melanoma cell lines a colourimetic Sulphorhodamine B (SRB) assay was validated for use (173). The cell lines chosen for the majority of experiments were the human malignant melanoma cell line A375, and Ercc1 proficient and Ercc1 deficient mouse cell lines. The Ercc1 proficient mouse melanocyte cell line (herein referred to as 3-1-1-T1a) was previously generated by transformation of isolated primary melanocytes from an $Ercc1^{Flox/Flox}$ mouse as described by Selfridge *et al.*(174). Following xenograft, cells were re-isolated with the histological and pathological appearance of mouse melanoma as described by Song *et al.*(149). An isogenic Ercc1 deficient derivative cell line was produced following Cre-mediated recombination (Ercc1 3-1-1-T1a cre/neo #5) (149).

The SRB assay was chosen due to the repeatability and robustness of this technique for compound screening. To maximise the therapeutic effect of compound

inhibition on our cell lines, it was considered that a 5-6 day culture period would be optimal. As such, to determine the optimal plating density, cells were plated at varying concentrations and monitored over a 4-6 day period. At each of the time points, cells were fixed by TCA as detailed in the SRB staining protocol. Fixed plates were stored until all plates were collected then they were stained and analysed together. As shown in Figure 3.2A, the optimal plating density for the 3-1-1-T1a cell line was deemed to be 1000 cells per well over an incubation period of 6 days. In Figure 3.2B, the optimal plating density for the A375 cell line was deemed to be 500 cells per well with an incubation period of 5 days.

To validate the assay for compound screening, the effect of DMSO on our cell lines was determined. As shown in Figure 3.2C, DMSO was plated at increasing concentrations on A375 cells and cell growth was monitored after 5 days. Here no effect was observed up to 0.75% DMSO. In all experiments, DMSO concentration was limited to 1% with a DMSO control and reduced to below 0.75% whenever possible.

As results of assays would be expressed and interpreted relative to control growth values, it was important to determine whether SRB bound to cells proportionately to an increasing cell density. This would be expected as SRB binds the basic regions of cell surface proteins (173, 175). In Figure 3.2D, cells were plated at a known density then fixed shortly following cell adhesion. We confirm that binding of SRB to cells was linear with respect to cell density.

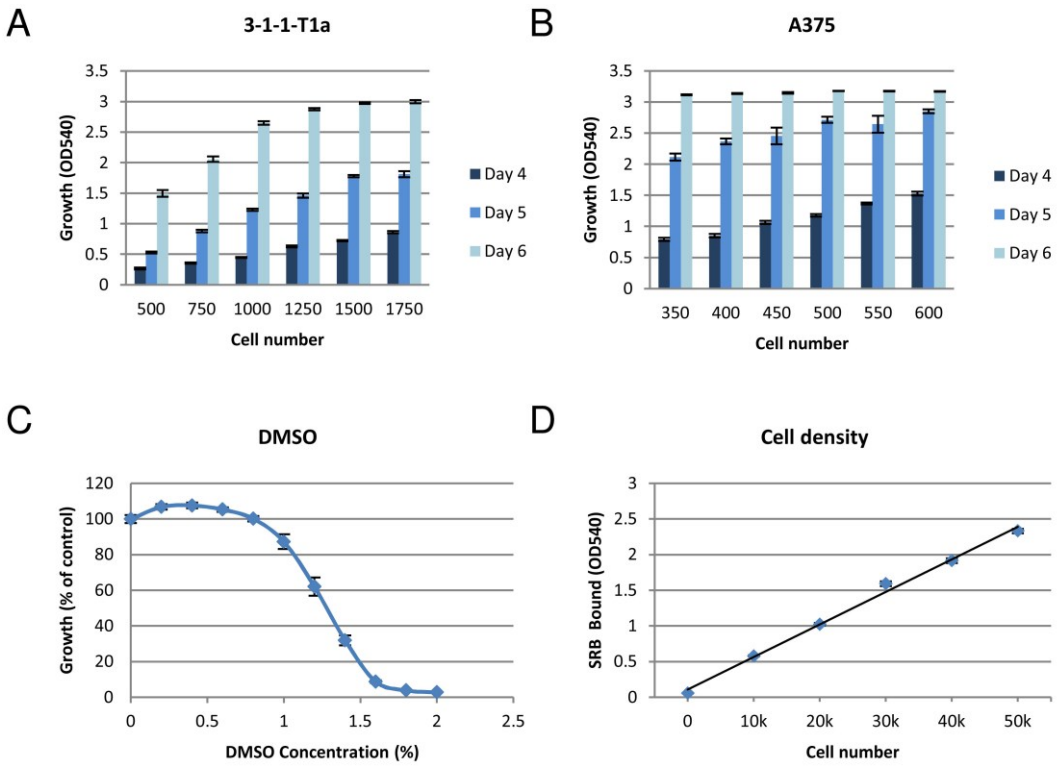

Figure 3.2: Validation experiments of the SRB assay. (A) Showing the effect of increasing 3-1-1-T1a and (B) A375 plates cell number upon cell growth at 4, 5 and 6 days post plating. Growth was expressed as OD540 following SRB staining +/- SEM. (C) Showing the effect of DMSO upon growth of A375 cells after 5 days (seeded at 500 cells per well into DMSO containing medium). Growth values expressed as percentage of non-treated control +/- SEM following SRB staining. (D) Showing A375 cells plated at a known density then fixed and stained with SRB following adhesion. Total SRB bound following staining of cells was measured at OD540.

3.3.2 Effect of standard chemotherapeutic agents

We sought to observe the effect of common chemotherapeutics upon our cell lines and determine whether ERCC1 was required to repair the resulting DNA damage. For this, we chose to use the isogenic Ercc1 proficient and Ercc1 deficient mouse melanoma cells. As shown in Figure 3.3A, we also performed a toxicity curve of cisplatin upon the human A375 cell line showing an IC50 concentration of 0.5µM. As predicted, repair of DNA following cisplatin damage was dependent upon Ercc1. In Figure 3.3B, the Ercc1 deficient cell line was around 20-fold more sensitive to

cisplatin damage with the Ercc1 deficient cisplatin IC50 of 3.4±0.7nM, compared to 56.5±3.4nM for the Ercc1 proficient cells. With oxaliplatin which has a similar mechanism of DNA damage but is less toxic, Figure 3.3C shows that the Ercc1 deficient cell line was also 28-fold more sensitive to oxaliplatin treatment, with the Ercc1 deficient cisplatin IC50 of 26nM compared to 740nM for the Ercc1 proficient cells. This indicates that ERCC1 is required for the repair of DNA damage caused by both cisplatin and oxaliplatin. An analogous experiment was performed with the alkylating agent dacarbazine. In Figure 3.3D, the IC50 of the Ercc1 proficient cell line was 2.6μM compared to 2.4μM of the Ercc1 deficient cell line indicating no increased sensitivity was observed and confirming that DNA damage resulting from dacarbazine treatment does not require ERCC1 for repair. This is as predicted as dacarbazine is known to cause DNA damage requiring BER for repair, a pathway in which ERCC1 has no known role, thus no enhanced toxicity would be expected in ERCC1 deficient cells.

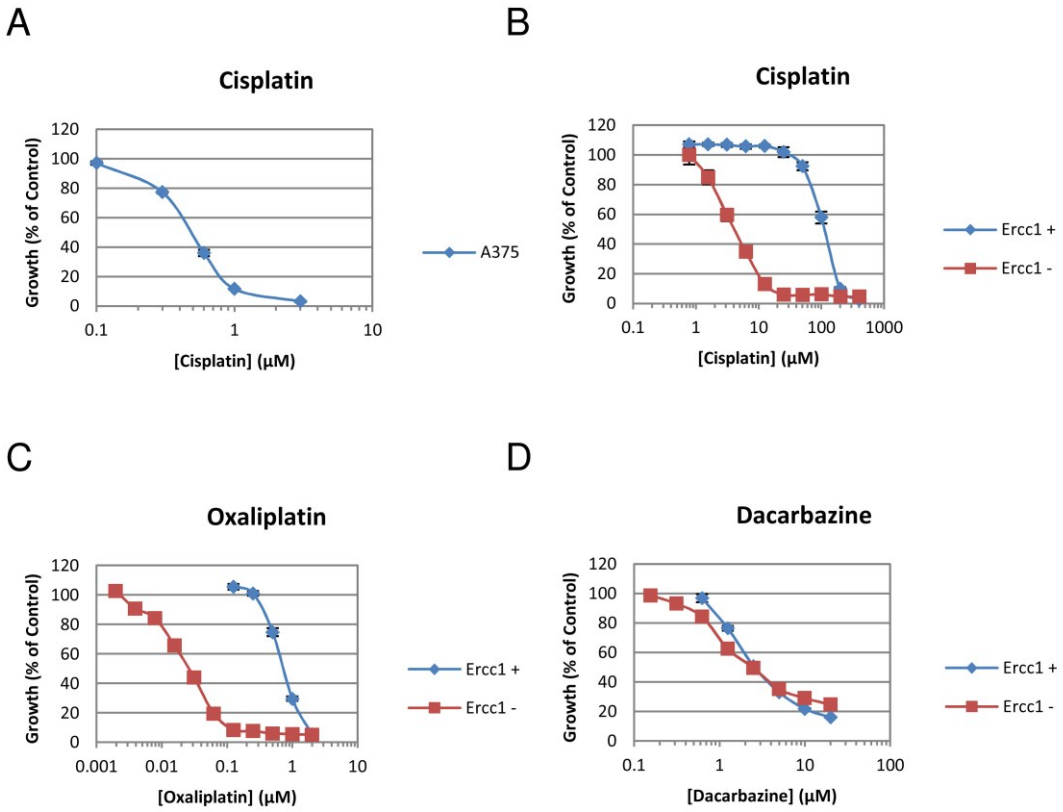

Figure 3.3: Showing the effect of chemotherapeutics upon cell lines. (A) Toxicity curve of cisplatin on the A375 cell line following 5 day drug treatment. (B) Toxicity curve of Cisplatin, (C) Oxaliplatin and (D) Dacarbazine on the Ercc1 proficient (3-1-1-T1a) and isogenic Ercc1 deficient (3-1-1T1a Cre Neo #5) cell lines. Growth values expressed as percentages of the non-treated control +/- SEM.

3.3.3 FACS analysis in response to cisplatin treatment

We sought to determine if the typical G2/S-phase arrest in response to cisplatin occurred in melanoma. This 'standard' response is thought to occur due to increased interstrand crosslinks caused by cisplatin which holds DNA strands together thus preventing DNA replication and subsequent anaphase segregation of sister chromosomes. To assess cell cycle changes in response to cisplatin, a FACS assay using propidium iodide staining was employed. In Figure 3.4, three concentrations of cisplatin were chosen, 0.3µM cisplatin as this has little effect on

A375 cell growth rate, 1μM cisplatin as growth in response to this concentration is almost static and 3μM cisplatin which is toxic. As expected at 3μM cisplatin, significant growth arrest was observed with cells being arrested in S-phase and leading to a significant sub-G1 population, likely as a result of apoptotic cell death. At both 0.3μM and 1μM cisplatin following 24-hours of treatment, substantial increases in S and G2-phase populations were observed. At 48-hours and 72-hours of cisplatin treatment, the proportion of cells observed in S and G2-phase were reduced. This result was surprising. It is thought that this could represent a cisplatin induced change to the DNA repair or stress response pathways enabling the cells to better cope with cisplatin induced damage. It is hypothesised that this 'recovery' may be as a result of an increased expression of ERCC1-XPF in response to cisplatin, which is known to occur at the same time (176).

We then sought to determine whether presence of ERCC1 would affect cell cycle progression following cisplatin treatment. As demonstrated in Figure 3.3B, the Ercc1 deficient melanocyte cell line is 20-fold more sensitive to cisplatin than the isogenic, Ercc1 proficient melanocyte cell line. As such, 100nM and 300nM cisplatin concentrations were chosen for the Ercc1 proficient cell line and lower concentrations of 10nM and 30nM were chosen for the Ercc1 deficient cell line. In Figure 3.5A, we show using the propidium iodide cell cycle analysis that in both Ercc1 proficient and Ercc1 deficient cells a G2 arrest and increased sub-G1 populations are observed following cisplatin treatment. This observation was most pronounced for the 300nM and 30nM cisplatin concentrations. We then sought to determine whether this cisplatin induced sub-G1 population was as a result of apoptotic cell death in both cell lines. In Figure 3.5B, we show using Annexin V FACS analysis that after 48 hours cisplatin treatment of 300nM for the Ercc1 proficient cells, and 30nM for the Ercc1 deficient cells, that cisplatin results in an Annexin V positive, propidium iodide positive Q2 population of 19% and 24% respectively indicating late apoptotic cells. This is concurrent with a much smaller increase in their Annexin V positive, propidium iodide negative (Q3) population indicating early apoptosis. Furthermore, in both cell lines, the Q1 and Q2 populations of the Annexin V staining is correlatable to the magnitude of the sub-G1 population

in the propidium iodide cell cycle assay. The increased sub-G1 population observed in the propidium iodide analysis can therefore be attributed to apoptotic cell death.

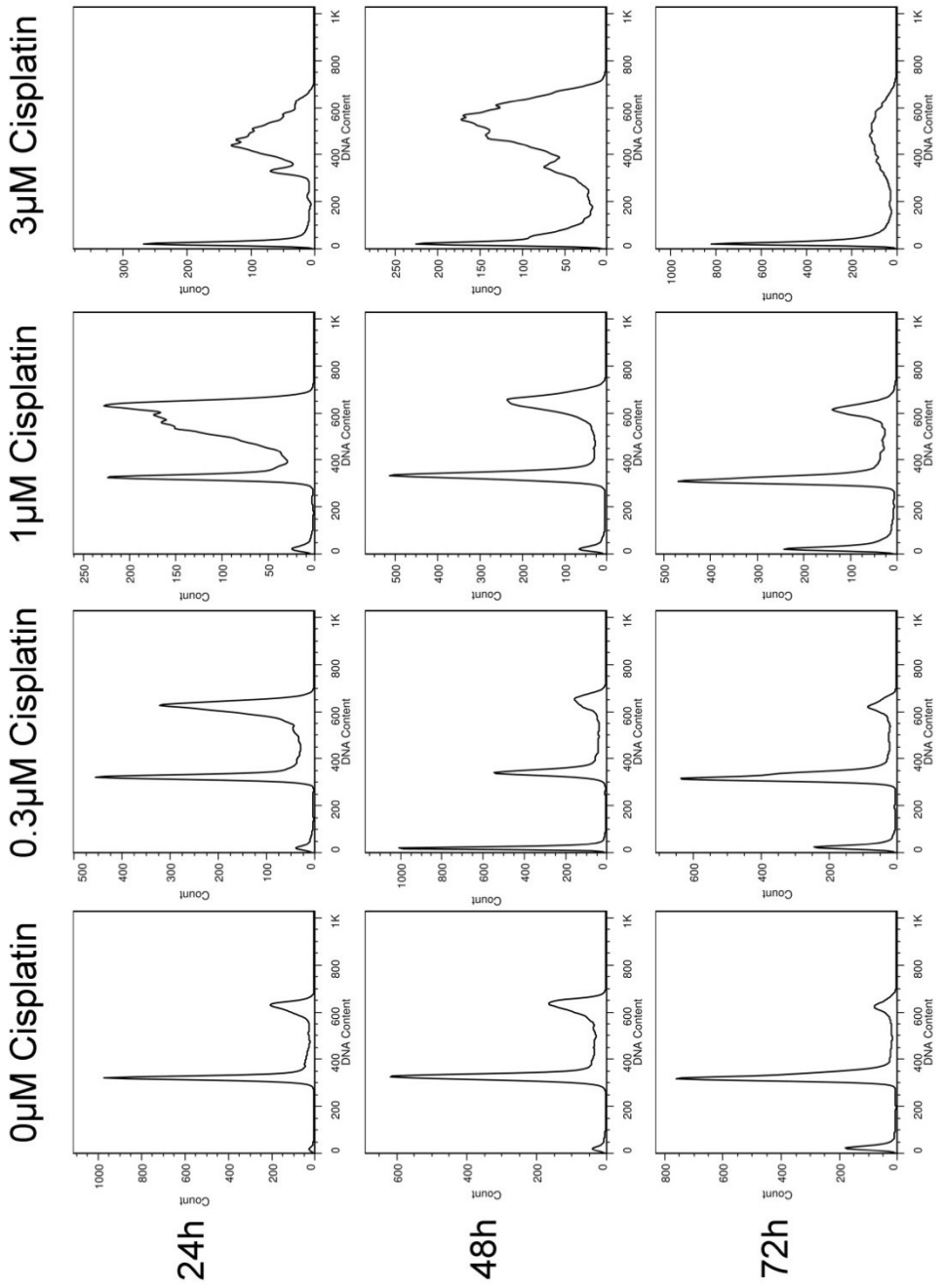

Figure 3.4: Propidium iodide FACS analysis following cisplatin treatment on A375 cells. Total DNA content was measured following 24, 48 and 72 hours treatment with increasing cisplatin concentrations. This experiment was performed in duplicate and results are representative of both repeats.

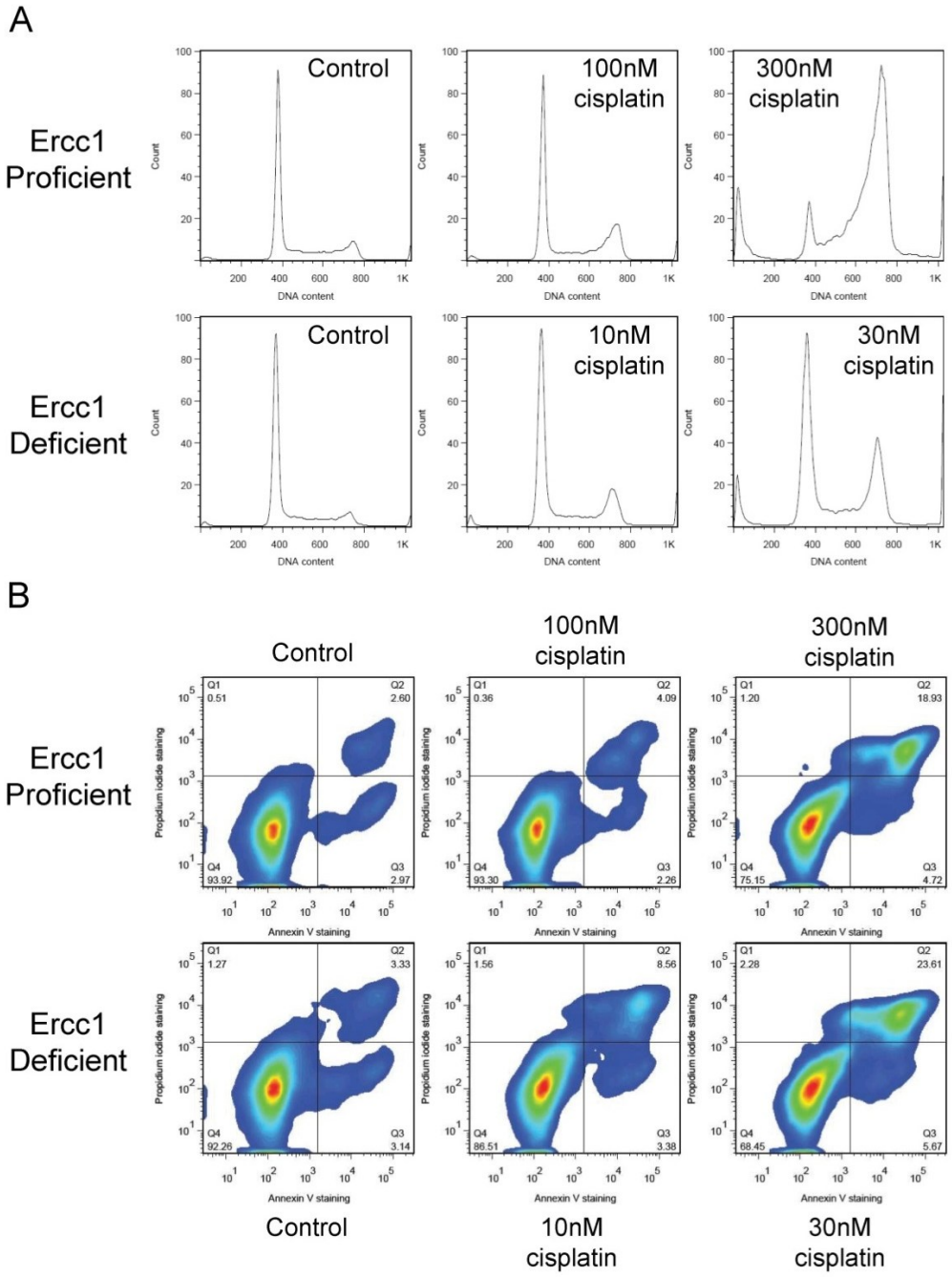

Figure 3.5: FACS analysis of cisplatin treatment upon Ercc1 proficient (3-1-1-T1a) and Ercc1 deficient melanocytes (3-1-1-T1a cre/neo #5). (A) Showing propidium iodide staining for total DNA content following 48h cisplatin treatment. In this assay, all cells were collected and analysed. Gating was set to include the sub-G1 population. (B) Quantification of apoptosis by Annexin V staining following 48h cisplatin treatment. Shown are the

respective quadrants and the percentage of cells in each quadrant is shown. The Q1 quadrant represents necrotic cells, the Q2 quadrant represents late apoptotic cells, the Q3 quadrant represents early apoptotic cells and the Q4 quadrant represents live cells. Both experiments were performed in duplicate and results are representative.

3.3.4 Phenotypic drug screen for novel compounds

Utilization of zebrafish for phenotypic compound screening has many advantages. Firstly, this technique allows for the direct visualization of discrete tissues and organs in real time in a whole embryo by light microscope (177). Furthermore, screening is rapid with organ progenitors being visible from 36 hours post fertilization (hpf) and hatching occurring at 46-72 hpf (177). Independent feeding occurs at 5 days post fertilization (177). For assessing the effect of compounds on specific cell types *in vivo*, transgenic techniques where cells express GFP under the control of specific promoters can be utilized to label cells (177). In the case of the melanocytes, these can be directly visualized in wild-type embryos due to expression of melanin. A schematic figure showing a zebrafish pigmentation screen and tail regeneration screen is shown in Figure 3.6.

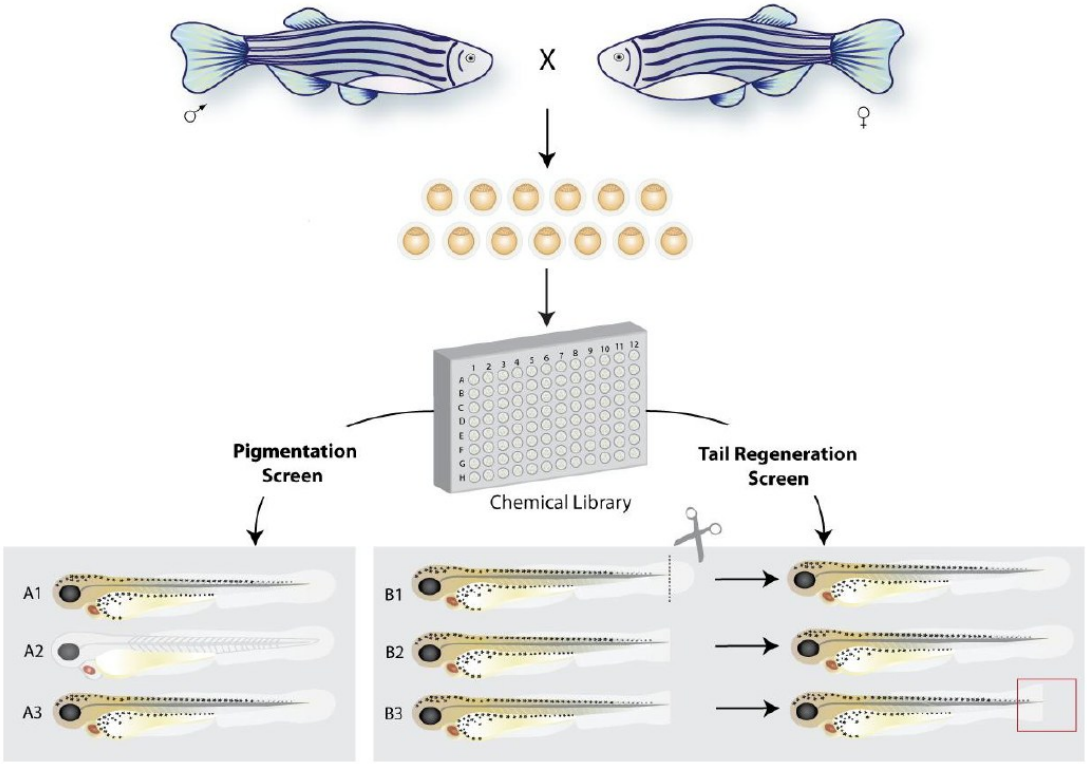

Figure 3.6: Phenotypic drug screen on zebrafish. Showing a schematic of a zebrafish screen. Zebrafish embryos are plated into 96-well plates. Compounds are added and the phenotypes are monitored. Screens commonly performed are pigmentation screens where a disappearance of pigmentation is sought or a regeneration screen following tail clipping. Figure from (177).

A drug screen was established to discover two novel classes of compounds for the treatment of malignant melanoma. The first class of compounds we sought to discover were those which were specifically active on melanoma. To assess if compounds were specifically active on melanoma, and to assess general *in vivo* toxicity, data from our cell culture screen was compared to that from an *in vivo* zebrafish screen performed by a post-doctorate researcher of Dr Elizabeth Patton, Dr Nicholas Temperley. Comparing both *in vivo* and *in vitro* data would allow us to determine if the observed effect on the zebrafish melanocytes was due to direct interaction with the melanocytes rather than a melanocyte developmental defect. A schematic of the screening approach is shown in Figure 3.7A.

The second class of compounds were those which sensitise melanoma cells to cisplatin. The rational for this class was that Ercc1 deficient melanocytes were 20-fold more sensitivity to cisplatin when compared to Ercc1 proficient melanocytes. Furthermore, deletion of ERCC1 in a melanoma xenograft experiment leads to sensitivity to cisplatin. Using our established cell culture model with the Ercc1 proficient and deficient cell lines shown in Figure 3.3B, we decided to screen potential compounds on our Ercc1 proficient cell line in the presence and absence of 10nM cisplatin. At this chosen concentration, should a compound replicate the enhanced sensitivity caused by a genetic deletion we would range from almost control growth to almost complete toxicity. In addition we opted to screen compound libraries at 10μM and 1μM. These concentrations were chosen to maximum our chances of finding compounds with activity taking into account differing potencies of the screened compounds.

For the screen, we initially opted to use the Sigma LOPAC^{1280}™ Library. This library consists of 1280 compounds which are pharmaceutically active and have a known mechanism. Furthermore, this screen has the advantage that compounds can be readily purchased for compound validation. We subsequently also used the BIOMOL® Kinase Inhibitor and BIOMOL® Phosphatase Inhibitor libraries. These libraries contain 80 and 33 compounds respectively and have well defined activity as kinase or phosphatase inhibitors in key cell signalling pathways including the MAPK, PI3K, PTEN and NF-κB pathways.

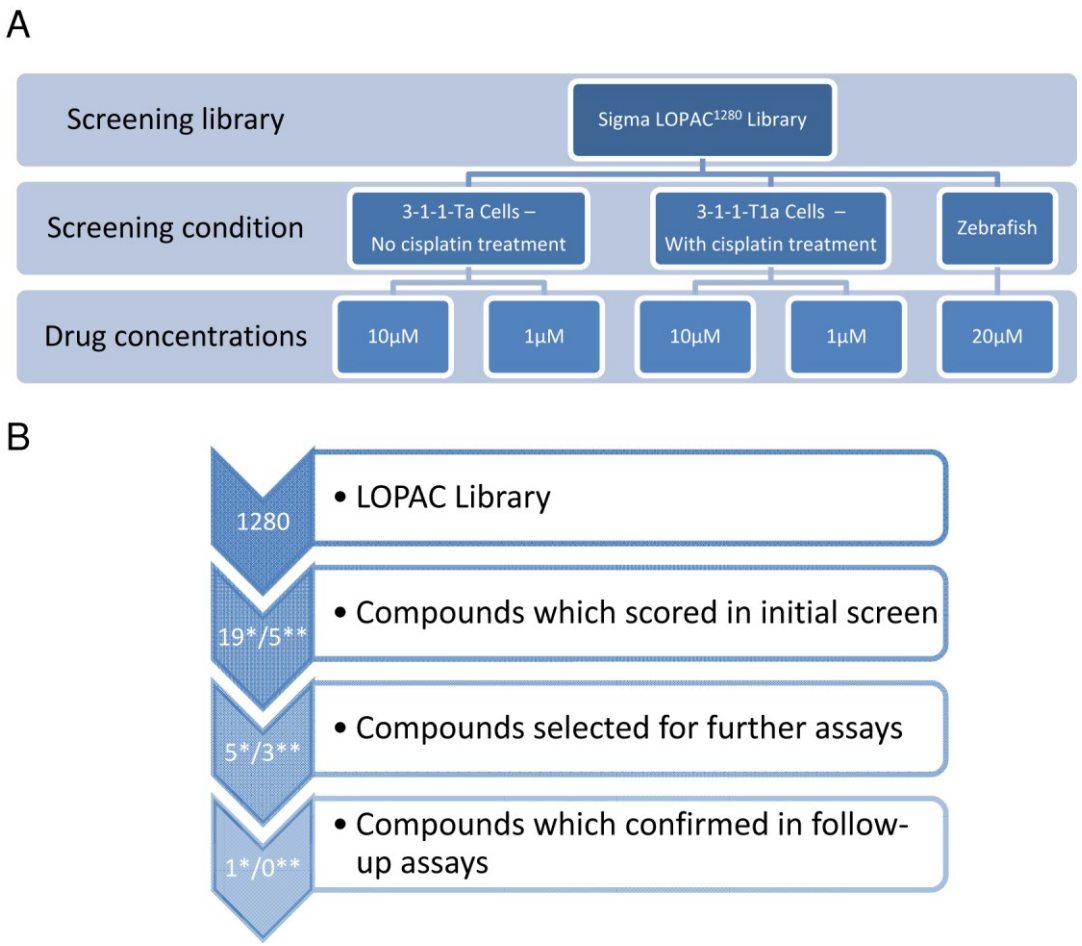

Figure 3.7: Schematic of drug screening approach and summary of results (A) Schematic of drug screening approach. The zebrafish screening arm was performed by a post-doctorate researcher of Dr Elizabeth Patton, Dr Nicholas Temperley (B) Summary of compound validation. * indicates compounds which demonstrated contracted, or less melanocytes in zebrafish and reduced growth of melanoma in cell culture. ** indicates compounds showing more than 50% enhancement of cisplatin toxicity in melanoma in cell culture.

To select compounds which were selectively active on melanocytes and thus may have activity against melanoma, we deemed compounds to be of interest if they met the following criteria; firstly they must have shown contracted or less melanocytes in the zebrafish screen; and secondly they must have shown toxicity in our cell culture screen as defined by <40% growth at either 1μM or 10μM. Using these selection criteria, we identified 19 compounds to be of interest. Subsequent

literature searches reduced this number to 5 compounds and these were then purchased for follow up validation. Compounds were deemed to be of interest in the literature search if activity against cancer, or on a pathway known to be active in melanoma had been published. Compounds of interest are shown in Table 3.1. The second selection criterion for compounds was those which enhanced the toxicity of cisplatin in our cells. Using this criterion, 5 compounds showed greater than a 50% increase in toxicity when combined with cisplatin. Following a literature search for activity against cancer, or activity on a pathway known to be active in melanoma, this was further reduced to 3 compounds and these were purchased for follow up validation. These compounds are shown in Table 3.2. The screening strategy is summarised in Figure 3.7B.

3.3.5 Compound validation

To validate compounds which showed specificity against melanocytes, we decided to perform two additional assays. The first was to determine the IC50 concentration on the 3-1-1-T1a cell line following a 6 day incubation with the compound. The results of this experiment are shown in Table 3.1. The second assay performed was to screen each compound in a panel of cell lines and determine if there was cell line specificity against melanocyte or melanoma cell lines as determined by a lower IC50 on melanoma/melanocytes than the other cell lines tested. The cell lines chosen were the human melanoma A375 cell line, the human SH5Y5Y neuroblastoma cell line, the human PEO4 ovarian cancer cell line and the human MRC5v1 fibroblast cell line. In addition, the Ercc1 proficient mouse melanocyte cell line (3-1-1-T1a), the mouse Melan A melanocyte cell line and finally the mouse PF20 fibroblast cell line were chosen.

Compound Name	IC50 (µM)	Cell line specificity?
Roscovitine	5.0	No
Chloro-APB hydrobromide	5.6	Yes
Doxycycline hydrochloride	5.8	No
Mephetyl tetrazole	30.2	No
Tyrphostin AG 528	2.8	No

Table 3.1: Summary of compounds showing melanocyte specificity in the compound screen. Summary of results from compounds selected for follow-up based upon selection criteria of contracted or less melanocytes in zebrafish and reduced growth of melanocytes in cell culture. IC50 calculated for 3-1-1-T1a cell line following 6 day drug treatment and growth assessed by SRB assay. Cell line specificity determined by plating against a panel of cell lines.

Of the compounds purchased for follow-up based upon showing melanocyte specificity, only one compound showed an indication of cell line specificity in our follow up assay. As shown in Table 3.1, Chloro-APB hydrobromide was the only compound to display any specificity against melanoma. As shown in Figure 3.8A, Chloro-APB hydrobromide is more potent on the human melanoma and neuroblastoma cell lines when compared to the human ovarian and fibroblast cell line. However, in mouse cell lines as shown in Figure 3.8B, this specificity was reversed and it was more potent on the mouse fibroblast than melanocyte cell lines. Based upon conflicting results between species, it was decided not to proceed further with this compound.

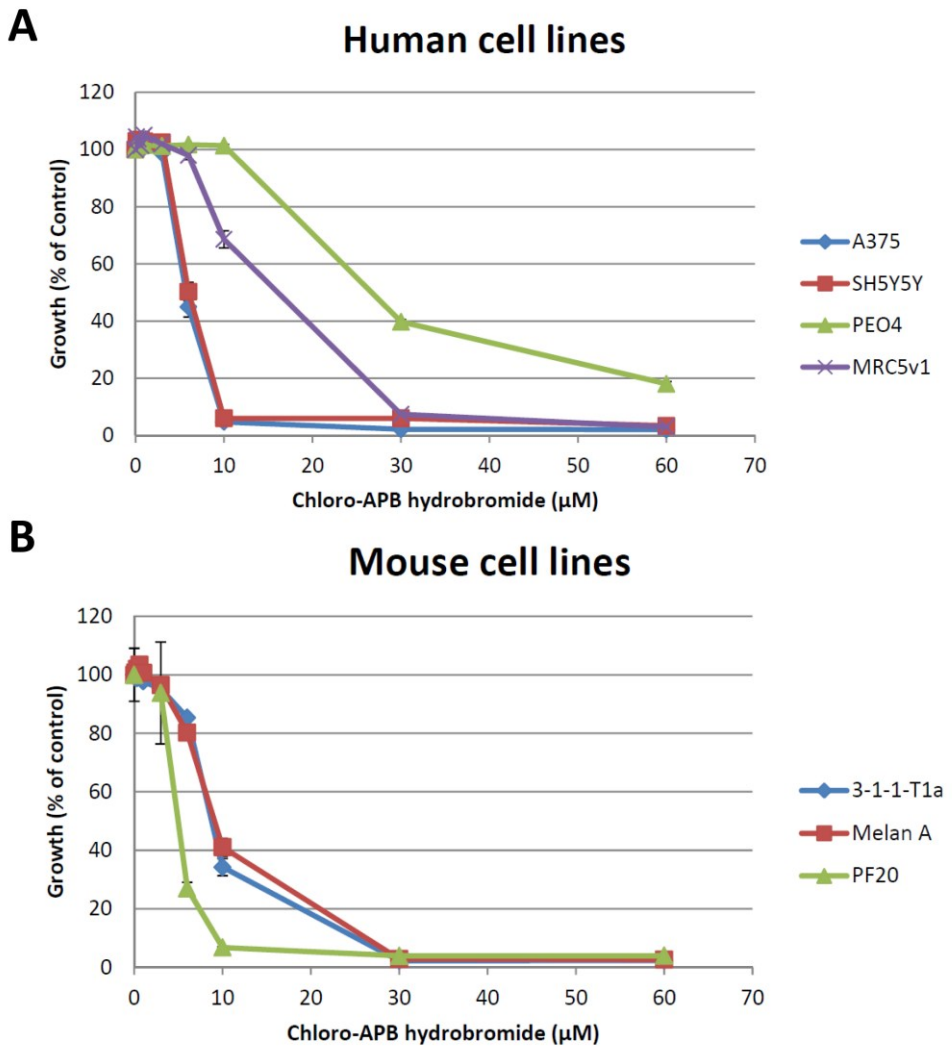

Figure 3.8: Cell line specificity of Chloro-APB hydrobromide. Toxicity curves of Chloro-APB hydrobromide on various cell lines. (A) Showing the effect of Chloro-APB hydrobromide on the growth of the human melanoma (A375), neuroblastoma (SH5Y5Y), ovarian cancer (PEO4) and fibroblast cell lines (MRC5v1). (B) Showing the effect of Chloro-APB hydrobromide on the growth of the mouse melanocyte (3-1-1-T1a and Melan A) and fibroblast cell lines (PF20). Growth values expressed as a percentage of the non-treated control ± SEM.

In order to validate compounds which enhanced the toxicity of cisplatin as shown in Table 3.2, we first generated IC50 values against the 3-1-1-T1a cell line. We then chose three concentrations of approximately IC10, IC30 and up to the IC50

concentrations and plated these with cells in the presence and absence of 10nM and 30nM cisplatin. At these cisplatin concentrations, we expected to observe an enhanced toxicity of the drugs. In these assays, no such enhanced toxicity was observed indicating these compounds were all false positives from the initial screen. No further work was carried out with these compounds.

Compound Name	IC50 (μM)	Enhanced toxicity of cisplatin?
Chlorprothixene hydrochloride	8.0	No
PD 169316	5.2	No
Terfenadine	2.5	No

Table 3.2: Summary table of compounds which showed enhanced toxicity with cisplatin in the compound screen. Summary of results selected for follow-up based upon a selection criterion of more than 50% enhancement of cisplatin toxicity in melanocytes. IC50 calculated for 3-1-1-T1a cell line following 6 day drug treatment and growth assessed by SRB assay. Enhancement of cisplatin toxicity assessed by co-treatment of compound with 10nM or 30nM cisplatin on 3-1-1-T1a cells. Enhanced toxicity quantified by reduction from control growth in cisplatin alone as measured by the SRB assay.

3.3.6 Bio1E7 is more potent than other nitrofurans

In parallel with screening the Sigma LOPAC[1280] Library, work was carried out on a previously identified nitrofuran identified by Dr Hironori Ishizaki and Dr Elizabeth Patton, termed Bio1E7. This had been identified in an earlier zebrafish screen and resulted in contracted melanocytes. Interestingly this compound also showed structural similarity to the antibiotic Nifurtimox used to treat Chagas disease and which is in clinical trials for neuroblastoma.

To characterise this nitrofuran compound, we first sought to determine its potency when compared to nifurtimox and other commercially available nitrofuran compounds. From Figure 3.9, it was clear that Bio1E7 is vastly more potent than the other nitrofurans tested. It was proposed that the common nitrofuran group is

essential for activity and that the difference in side chains represents the difference in potencies.

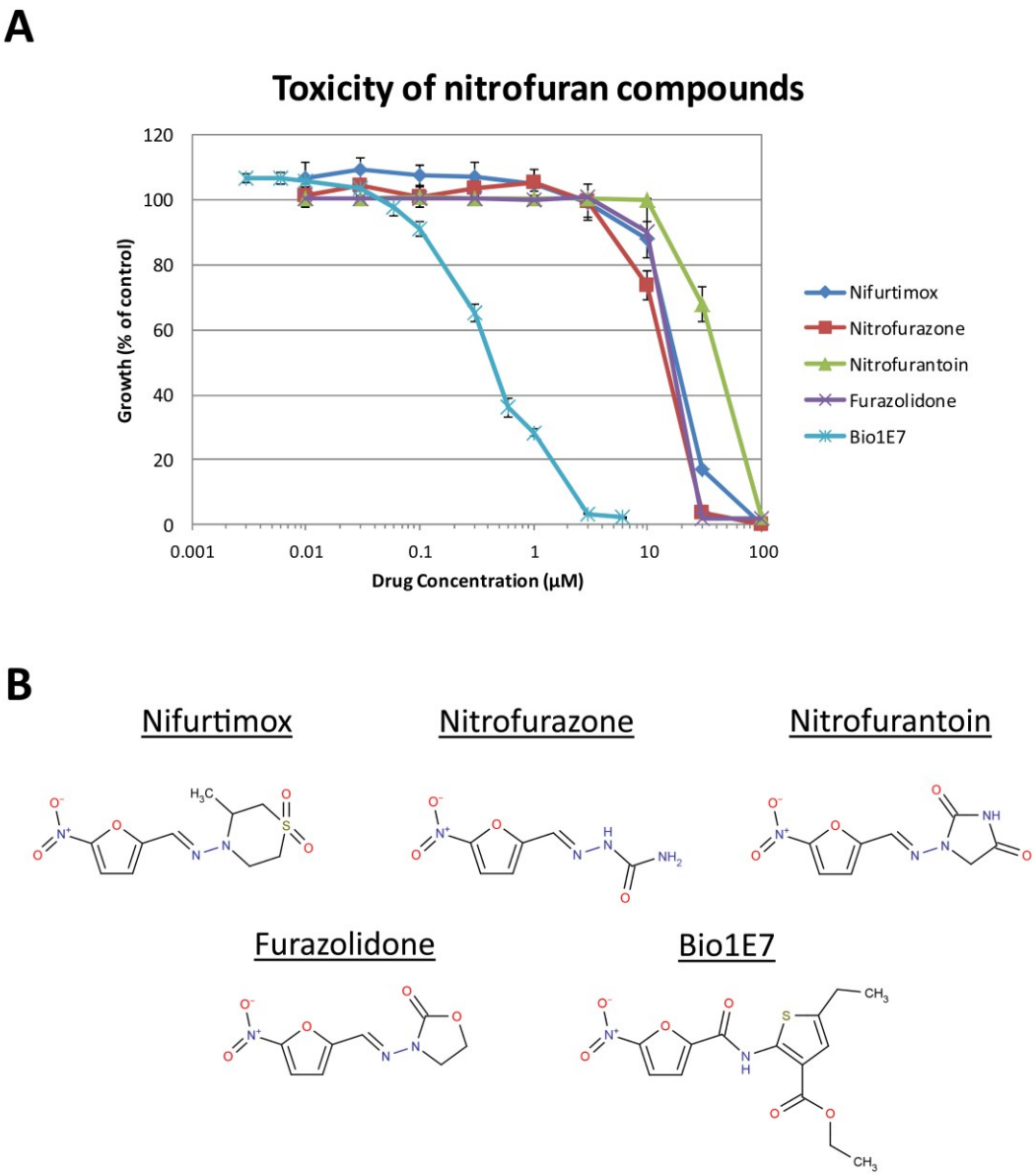

Figure 3.9: Toxicity of nitrofuran compounds on A375 cells. (A) Showing effect of increasing nitrofuran compound concentration upon growth of A375 cells following 5 day treatment. Growth values expressed as a percentage of the non-treated control ± SEM. (B) Structure of Bio1E7, nifurtimox and other commercially available nitrofuran compounds.

3.3.7 The nitrofuran group is essential for activity

To determine a structure activity relationship for Bio1E7, a collaboration with Linna Zhou from Dr Nicholas Westwood's group at the University of St Andrews was established with Dr Elizabeth Patton. Here, Linna Zhou created a series of Bio1E7 derivative compounds. Upon testing in cell culture upon A375 and SH5Y5Y cells, all compounds showed similar toxicity levels and enhanced the toxicity of cisplatin except for compound NFN1.1. As shown in Figure 3.10B, compound NFN1.1 had no activity on A375 cells (or SH5Y5Y cells, data not shown) even at 6µM, a concentration at which Bio1E7 is toxic. When considering the structural differences, NFN1.1 lacks the nitro group from the furan ring indicating that the intact nitrofuran functional group is essential for activity of these molecules.

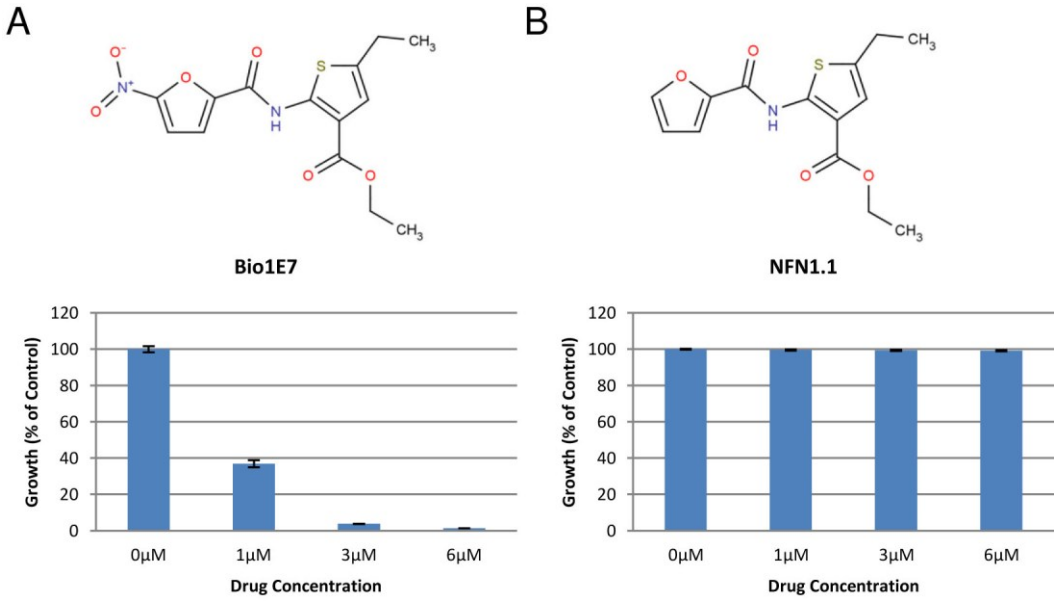

Figure 3.10: The nitrofuran group is essential for activity. (A) Showing the structure and activity of Bio1E7 on A375 melanoma cells. (B) Showing the structure and activity of NFN1.1 on A375 melanoma cells. Cell growth measured following 5 day drug treatment and analysed by the SRB assay. Values expressed relative to control growth +/- SEM.

3.3.8 Enhanced toxicity of Bio1E7 and cisplatin

It is thought that the mechanism of nitrofuran activity may involve production of superoxide resulting in DNA damage; as such we aimed to determine whether Bio1E7, would enhance the toxicity of cisplatin. To answer this, we chose to use the human melanoma cell line, A375, and the human neuroblastoma cell line, SH5Y5Y. Both cell lines showed similar toxicity to single agent treatment with either cisplatin or Bio1E7 (data not shown). As shown in Figure 3.11, growth values have been normalised to their respective cisplatin controls and thus account for the effect of cisplatin alone. Enhanced toxicity was observed with both cell lines. This corresponds to 31% and 32% enhancement (= growth reduction) at 0.1μM Bio1E7 for the A375 and SH5Y5Y cell lines respectively.

After confirming that Bio1E7 could enhance the toxicity of cisplatin, we next sought to determine whether DNA damage induced by Bio1E7 required an ERCC1-XPF dependent pathway for repair. To answer this, we utilised our Ercc1 proficient and Ercc1 deficient mouse melanocyte cell lines. As shown in Figure 3.12, a lower dose of cisplatin was used on the Ercc1 deficient cell line than the Ercc1 proficient cell line as Ercc1 deficient cells are hypersensitive to cisplatin. In addition, Figure 3.12 shows that Bio1E7 is similarly toxic to both the Ercc1 proficient and deficient cell line. Had Ercc1 been required for repair of Bio1E7 damage, it would be expected that Ercc1 deficient cell line would be hypersensitive to Bio1E7. Furthermore, enhanced cisplatin toxicity was observed for both Ercc1 proficient and Ercc1 deficient cells. Taken together, this shows that Bio1E7 toxicity and enhancement of cisplatin toxicity is independent of ERCC1-XPF and NER.

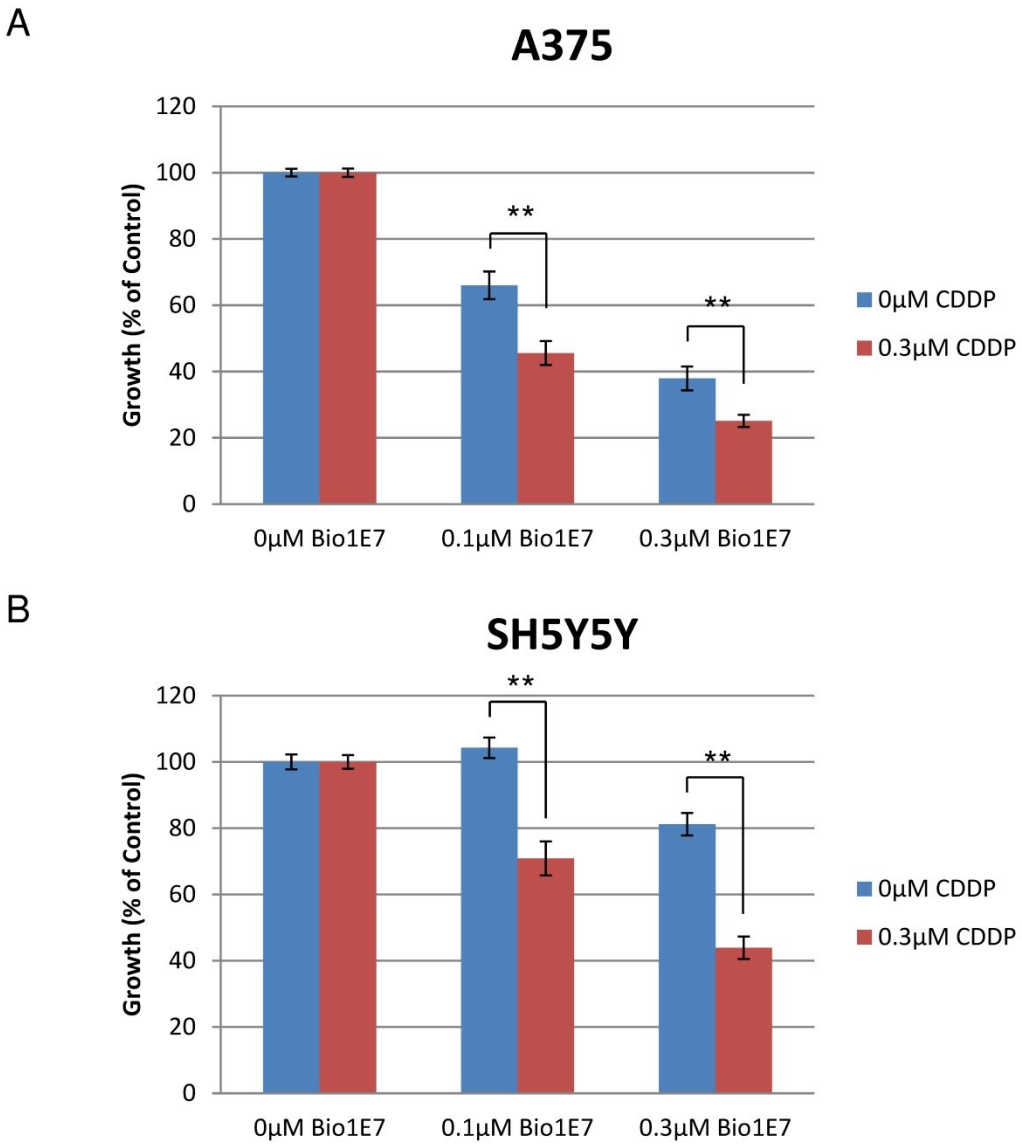

Figure 3.11: Enhanced toxicity of Bio1E7 and cisplatin on a melanoma and neuroblastoma cell line. (A) Enhanced toxicity of Bio1E7 and cisplatin on the A375 melanoma cell line. (B) Enhanced toxicity of Bio1E7 and cisplatin on the SH5Y5Y neuroblastoma cell line. Growth of cells after 5 days treatment was measured by SRB staining and is expressed relative to their respective cisplatin controls. Results calculated from average of three independent experiments (+/- SEM). Statistical significance calculated by Mann-Whitney U Test (**, $P<0.01$).

A

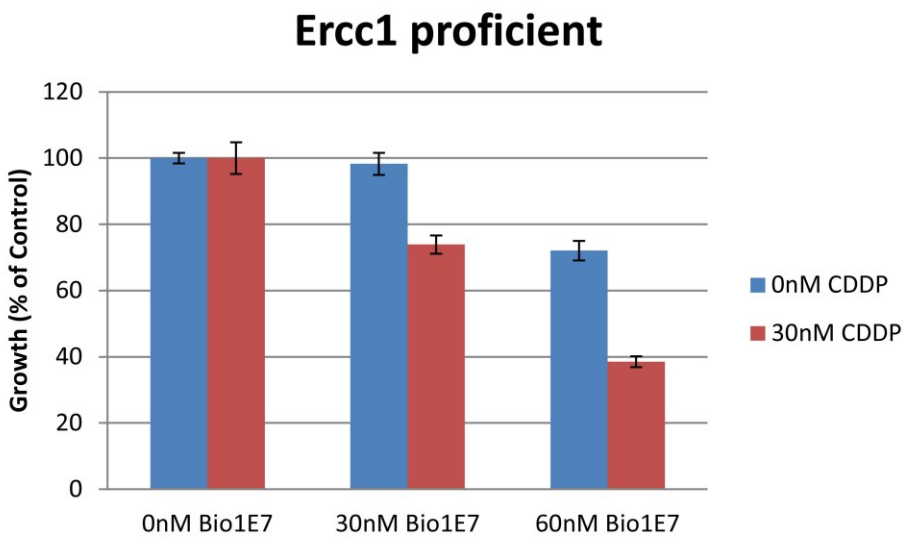

B

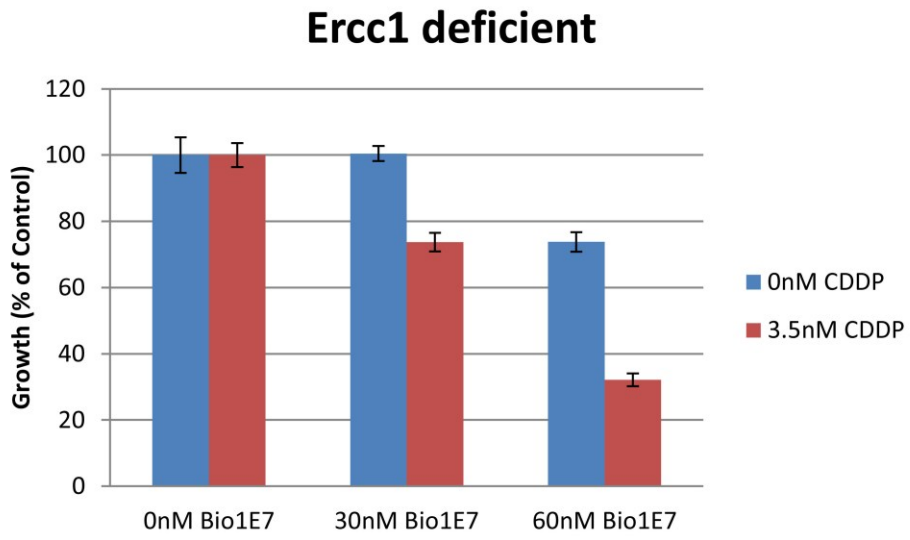

Figure 3.12: Enhanced toxicity of Bio1E7 and cisplatin on an Ercc1 proficient and Ercc1 deficient cell line. (A) Enhanced toxicity of Bio1E7 and cisplatin on an Ercc1 proficient (3-1-1-T1a) melanocyte cell line. (B) Enhanced toxicity of Bio1E7 and cisplatin on an Ercc1 deficient (3-1-1-T1a cre/neo #5) melanocyte cell line. Growth of cells after 6 days treatment was measured by SRB staining and expressed relative to their respective cisplatin treated controls ± SEM.

3.3.9 Cell line specificity of Bio1E7 toxicity

Although Bio1E7 appears to show a melanocyte effect in zebrafish, it is difficult to determine whether this is specific for melanocytes as only the pigmented cells can be observed. To investigate whether Bio1E7 displays cell line specificity in cell culture, we assayed Bio1E7 against a panel of cell lines. Although Bio1E7 was generally more potent against mouse cell lines compared to human cell lines, we noticed that the presence of pigmentation may be protective against Bio1E7 toxicity. As such, a larger panel of cell lines was screened to include a greater number of pigmented lines. As shown in Table 3.3, the presence of pigmentation correlated with protection against Bio1E7 toxicity however level of pigmentation was not predictive of the level of sensitivity. Attempts were made to reduce pigmentation levels in our cell lines by inhibiting tyrosinase and melanin synthesis with phenylthiourea (PTU) to determine if sensitivity could be restored, however the level of pigmentation was not sufficiently altered to enable any conclusion about the reduction of pigment levels on Bio1E7 sensitivity (data not shown).

Cell line	IC50 (µM)	95% CI	Cell Type	Origin	Pigment
MRC5v1	0.39	0.19 to 0.79	Fibroblast	Human	No
A375	0.71	0.50 to 1.02	Melanoma	Human	No
SH5Y5Y	1.30	0.69 to 2.45	Neuroblastoma	Human	No
PEO4	2.79	1.17 to 6.65	Ovarian Cancer	Human	No
HBL	6.58	2.73 to 15.90	Melanoma	Human	Black
3-1-1-T1a	0.08	0.05 to 0.13	Melanocyte	Mouse	No
PF20	0.34	0.16 to 0.72	Fibroblast	Mouse	No
SIB2W	1.21	0.60 to 2.43	Melanocyte	Mouse	V.Black
Melan A	1.91	1.23 to 2.95	Melanocyte	Mouse	Grey
13-4-1	2.40	1.59 to 3.64	Melanocyte	Mouse	Black
13-4-2	4.55	1.79 to 11.62	Melanocyte	Mouse	Grey

Table 3.3: Cell line specificity of Bio1E7 toxicity. Data shows Bio1E7 IC50 concentrations, 95% confidence intervals (CI), species origin and pigmentation status for each cell line. Table ordered by species then increasing IC50 value. Bio1E7 IC50 values calculated by SRB assay.

3.4 Discussion

In this chapter we aimed to characterise the sensitivity of melanoma cells to standard chemotherapeutic agents and the role of ERCC1 in repair of the DNA damage they cause. We show that dacarbazine which is the standard chemotherapeutic agent for melanoma is potent with an IC50 of 2.6µM however no significant difference exists when toxicity is compared between an Ercc1 proficient and deficient cell line. This observation was as predicted for this compound as dacarbazine is known to be an alkylating agent causing DNA adducts that would require base excision repair rather than NER (178). On the other hand, the

chemotherapeutic agents cisplatin and oxaliplatin are both known to cause monofunctional adducts, interstrand and intrastrand DNA crosslinks (157). Repair of monofunctional adducts and intrastrand crosslinks are known to involve NER whereas repair of interstrand cross links is by a different pathway. Both the NER and ICL DNA repair pathways involve ERCC1 thus the hypersensitivity of Ercc1 deficient cells is expected.

To confirm the effect of cisplatin on our cells we utilised propidium iodide cell cycle analysis and an Annexin V apoptosis assay. On A375 human melanoma cells, we observed S phase and G2 phase arrests following cisplatin treatment as has been previously published for other cell lines (179, 180). It is thought that this is due to accumulation of DNA damage preventing further DNA replication and allowing for a cisplatin induced change to the DNA repair pathways, thus enabling the cells to better cope with cisplatin induced damage (157, 181). In addition, an increased sub-G1 population was observed which we attribute to be as a result of apoptosis. Interestingly, the cell cycle profiles at 24 hours following cisplatin treatment showed an S phase and G2 phase arrest, but surprisingly by 48 hour and 72 hours of treatment this arrest was reduced. We hypothesise that this recovery is as a result of a coping strategy employed by the melanoma cell line. In this regard, cisplatin has previously been reported to induce an ERCC1 increase over the same period (176).

Our results confirm that ERCC1-XPF is required for the repair of DNA damage caused by cisplatin (182). Consequently, we considered whether ERCC1 was a suitable target for drug discovery. It is of note that testicular cancers have very low levels of ERCC1 and are effectively treated by cisplatin (183). High expression of ERCC1 has been linked with poor responses to chemotherapy in numerous cancer types, including non-small cell lung cancer, squamous cell carcinoma and ovarian cancer (184–191).

Increased levels of ERCC1 mRNA have been reported in melanoma and ovarian cancer cell lines in response to cisplatin-induced DNA damage (176, 192). In ovarian cancer cells, increased levels of the transcriptional activators, c-fos and c-jun, were involved in the cisplatin response (192). Treatment of melanoma cell lines with cisplatin resulted in increased phosphorylation of the extracellular signal-

regulated kinase (ERK) (193).The MAPK pathway also has an important role in the regulation of ERCC1 expression by epidermal growth factor in human hepatoma cells (194). Importantly, MAPK pathway-dependent increased levels of both ERCC1 and XPF proteins have been demonstrated after cisplatin treatment of melanoma cells (176).

We next sought to identify novel inhibitors through a small molecule drug screen. Two classes of compounds were initially sought, those which were selectively active in melanoma and those which enhanced toxicity of cisplatin. From our screen, 19 compounds were initially found to be selectively active on melanocytes when comparing the cell based and zebrafish screens. Of these, 5 were purchased for follow up and only Chloro-APB hydrobromide showed cell line specificity upon retesting. Although a high number of compounds did not confirm, this represents a false positive rate of 1.4% (18/1280) which is reasonable, particularly when considering this was based upon results from two very different screens being combined.

Although Chloro-APB hydrobromide showed some specificity on the human cell lines, no specificity was observed in the mouse cell lines. Chloro-APB hydrobromide is known to be a D1 dopamine receptor agonist. In published studies mouse melanoma, but not human melanoma was found to express dopamine D1 receptors (195). In D1 receptor deficient melanoma cells, a specific D1 receptor inhibitor was found to bind to cells, though this was thought to occur by non-specific binding to melanin (195). In a third study, dopamine was found to react with cell culture medium to form hydrogen peroxide and dopamine semiquinones/quinones (196).

In a structure search of the PubChem database, Chloro-APB hydrobromide was active in 31 of 497 bioassays tested (197). On the database, activity against D1 and D2 dopamine receptors was assessed to be 0.0055-1.3μM (197). Activities which were non-specific for dopamine receptors ranged from 3.5-39.8μM suggesting that the observed 5.6μM IC50 of Chloro-APB hydrobromide on our melanocytes was likely a nonspecific mechanism (197). Taken together, our decision was not to proceed any further with this compound.

In the second arm of the screen where compounds were selected for enhanced toxicity of cisplatin, 5 compounds were initially identified. Of these, three were purchased however no compound confirmed. This represented a false positive rate of 0.4% (5/1280). Although the cut-off for compounds being selected was initially set high with a 50% enhanced toxicity of cisplatin, this was appropriate based upon the observed results with Ercc1 proficient and deficient melanocytes. Although a lowered cut-off may have discovered a genuine hit compound, it would almost certainly have resulted in a compound with insufficient activity for further development and would have increased the false positive rate.

We then investigated the effect of the recently discovered nitrofuran compound, Bio1E7, on melanoma. This had been identified by Dr Hironori Ishizaki and Dr Elizabeth Patton in a previous small molecule screen and appeared to show contracted and less melanocytes in a zebrafish screen. Around this time, clinical efficacy of nifurtimox was being demonstrated against neuroblastoma (168). It was therefore tantalising that nifurtimox may also be active in melanoma, and that the recently discovered Bio1E7 may be a more potent analogue. In support, our results indicated that this nitrofuran compound was significantly more active on our melanoma cell lines than various commercially available derivatives including nifurtimox itself. Furthermore, structure activity relationships indicated that the nitro group attached to the furan ring was essential for Bio1E7 activity. This indicated that Bio1E7 was acting as a nitrofuran family member and activity was not due to an active group present in the side chain.

It is predicted that the mechanism of Bio1E7 was through production of superoxide during nitrofuran activation by cellular nitroreductases. In support of this Dr Hironori Ishizaki had shown that intracellular ROS levels were increased in A375 cells following Bio1E7 treatment. Furthermore, we showed that toxicity of Bio1E7 was enhanced by cisplatin treatment. In addition, this also occurred upon treatment with nifurtimox suggesting combinational therapy in patients may be beneficial. We propose that treatment with Bio1E7 or nifurtimox for neuroblastoma be combined with cisplatin to increase clinical efficacy.

Studies in the literature have suggested that the NER pathway was crucial to the survival of *E.coli* following nitrofuran treatment however this was conflicting with early research (167). Following this, we examined the effect of Bio1E7 on our Ercc1 proficient and Ercc1 deficient cells. We showed that Bio1E7 is equipotent on both cell lines and did not show hypersensitivity on the Ercc1 deficient cell line as might be expected for a compound where NER was essential for mitigating its toxicity. This indicates that contrary to Ona *et al.*, Bio1E7 and nitrofuran induced DNA damage does not require NER for its repair in human cells (167). It is hypothesised that in human cells, superoxide is formed as a result of nitrofuran activation leading to formation of DNA single strand breaks (164, 165, 198). That being said, DNA double strand breaks can also be formed when transcription machinery replicates past ROS-induced lesions or lesions occur in close proximity in opposite strands (198). In light of this, we wonder how nitrofurans may function in cancer harbouring defects in homologous recombination, such as BRCA1/2 deficient breast or ovarian cancer. Although in Table 3.3 we used PEO4 human ovarian cells carrying BRCA2 mutations, a secondary mutation is known to have occurred in this cell line reactivating the BRCA2 protein activity (199).

In a cell line specificity assay comparing the toxicity of Bio1E7 on a panel of cell lines, we noticed that Bio1E7 had less of an effect on cell lines which were pigmented. Upon addition of more pigmented cell lines to our panel, we showed that pigmentation appears to be protective over nitrofuran toxicity. This is likely to function by melanin absorbing the superoxide produced upon nitrofuran activation (171, 172). In the treatment of melanoma, we therefore propose that nitrofurans will be of limited benefit and greater clinical efficacy would be attained on amelanotic melanoma.

4 Chapter 4: Establishing *in vitro* endonuclease assays for screening ERCC1-XPF inhibitors

4.1 Aim of chapter

The aim of this chapter was to develop an *in vitro* endonuclease assay for ERCC1-XPF suitable for high throughput screening and compound validation following an *in silico* screen. In addition, we aimed to establish *in vitro* FEN1 and DNase1 assays suitable for compound screening and assessing compound specificity.

4.2 Introduction

4.2.1 ERCC1 is a target to overcome chemoresistance

As previously discussed in section 3.4, ERCC1-XPF has been linked with poor responses to chemotherapy in numerous cancer types, including non-small cell lung cancer, squamous cell carcinoma and ovarian cancer (184–191). Furthermore, it has been shown that a MAPK pathway-dependent increase occurs for both ERCC1 and XPF proteins levels following cisplatin treatment in melanoma cells (176). This increase is thought to partly account for the chemoresistance of melanoma to cisplatin treatment. This led us to propose that inhibition of ERCC1-XPF could be used to overcome chemoresistance in many cancers. To demonstrate this we used a mouse xenograft model of melanoma to show that, while ERCC1-proficient xenografts were resistant to cisplatin treatment, isogenic ERCC1-deficient melanoma xenografts could be cured by just two cisplatin treatments, this is shown in Figure 4.1 (149).

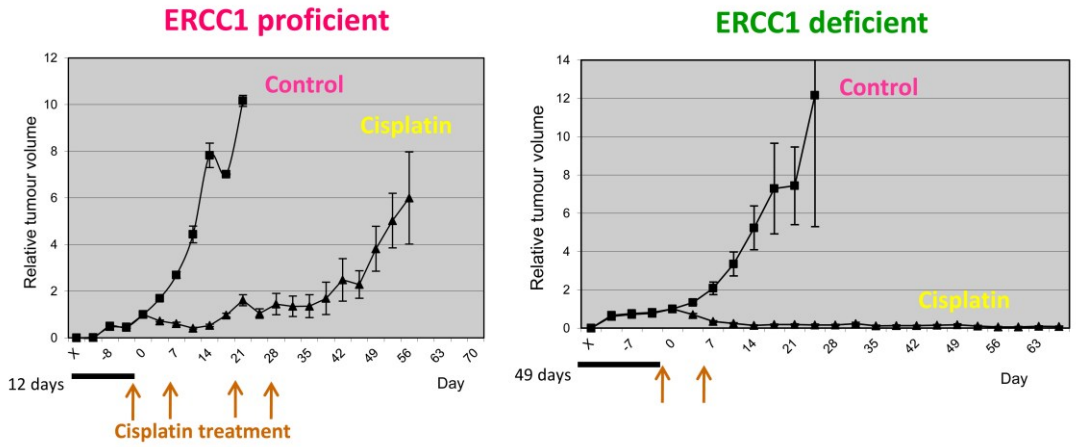

Figure 4.1: Response of Ercc1 proficient and deficient xenografts to cisplatin. 10^7 cells in 0.1ml of medium were injected subcutaneously into both flanks of 8- to 12-week-old female nude mice, together with 0.1ml matrigel (BD Biosciences, Oxford, UK) to facilitate xenograft establishment, on day X. Ten animals were injected with each cell line, and xenograft growth was monitored twice weekly. When the mean size of xenografts had reached $0.1cm^3$ (day 0), mice were randomized into two groups of five for each cell line. One group was untreated, while the other was treated on the days indicated (arrows) with 6mg/kg cisplatin i.p. The time taken from injection for xenografts to reach the threshold size to start treatment is indicated by the bar on the Days axis. The mean tumour volume for each group ± SEM is shown relative to the mean tumour volume at the start of treatment. Animals were culled when a tumour reached $1cm^3$. The SEM increases disproportionately as the experiment proceeds owing to culling of animals with the largest tumours. Figure adapted from Song *et al.* (149).

4.2.2 Published assays for ERCC1-XPF

An *in vitro* endonuclease assay for ERCC1 was first published in 1998 by de Laat *et al.* who utilized recombinant ERCC1-XPF and demonstrated *in vitro* structure specific cleavage (100). They showed that recombinant ERCC1-XPF is active on a range of radioactively labeled DNA substrates including stem-loop, splayed arm, flap, and structures with 3′ or 5′ overhangs; in all cases, structure specific cleavage occurs on the ds-DNA strand 5′ to the ds/ss-DNA junction (100). The stem-loop DNA substrate proposed by de Laat *et al.* has since become the standard assay for *in vitro* ERCC1-XPF activity (100, 102, 106, 112, 115). Until

recently, the assay was based upon radioactively labeled DNA substrates, however Bowles *et al.* modified this substrate to include 6-FAM on the 5′ end and the Dabcyl quencher on the 3′ end (102). While this modified assay was not published at the time of our work, this is a similar modification to that we developed independently and utilize herein. Furthermore de Laat *et al.,* and latterly Bowles *et al.* have shown that the minimum loop size required for cleavage is 6nt, but the preference is for larger, 22-40nt loops (100, 102).

Furthermore, de Laat *et al.* showed that the ERCC1-XPF endonuclease had a metal ion preference (100). They showed that the endonuclease is inactive at high magnesium concentrations of 10mM, and has greater activity around 1-2mM (100). Furthermore, they utilised the *in vitro* endonuclease assay to show that the favoured metal ion is not the biologically relevant magnesium, but manganese with an optimal concentration of 0.2-1mM (100). Interestingly, mutation of XPF residues Glu690 and Glu725 led to reduced nuclease activity in the presence of magnesium but not with manganese, suggesting an altered active site incompatible with the greater stringency requirements of magnesium binding, compared to those required for manganese binding (115). This suggests that *in vitro* the ERCC1-XPF endonuclease assay works better with manganese and not magnesium which is the biologically relevant metal cofactor (102, 106).

4.2.3 Production of recombinant ERCC1-XPF protein

For a drug discovery programme, significant quantities of recombinant ERCC1-XPF would be required. Expression of full-length ERCC1-XPF in *E.coli* leads to predominantly aggregated protein, while only small quantities of soluble protein can be purified from expression in Hela cells or baculovirus-infected Sf9 insect cells (106, 115). Bowles *et al.* have since published a modified purification protocol for full-length ERCC1-XPF protein resulting in a modest 100-150µg of purified ERCC1-XPF per 2 litres of *E.coli* culture (102). Expression of a truncated ERCC1-XPF complex in *E.coli* is possible in greater yields using $_{\Delta 95}$ERCC1-$_{\Delta 666}$XPF, lacking the ERCC1 N-terminus and the XPF helicase-like domain (106).

In our assays we opted to utilise the same truncated versions of ERCC1 and XPF as we found soluble complex to be expressed at good levels for purification (see Chapter 2 materials and methods for details of expression and purification) (106). These proteins have ERCC1 lacking the proposed nuclear localisation signal and XPF lacking the helicase-like domain. This truncated complex had previously been shown to be active by Tsodikov *et al.* and shown to have the same structure preference as full-length protein (106). Interestingly, a comparison of the enzyme kinetics between the truncated and full length ERCC1-XPF by Tsodikov *et al.* indicated Kcat values of 0.003min and 0.17min respectively, indicating the full length complex was ~60 fold more active (106). This was latterly confirmed by Bowles *et al.* who showed that full-length ERCC1-XPF has a Kcat of 0.19min (102). In addition, they expressed an alternative truncation of the ΔERCC1-XPF complex, but did not observe activity (102). They proposed that the slightly longer truncation that they produced may have acidic linkers on XPF which may inhibit the XPF active site or bind DNA (102). Alternatively, they proposed that the activity observed by Tsodikov *et al.* was due to non-specific nuclease activity (102).

4.2.4 Enzymes to investigate compound specificity

The ERCC4 endonuclease motif comprises of the ERCC4 endonuclease domain and the HhH_2 domain (200). In the ERCC1-XPF complex, the catalytic domain in ERCC1 is degenerate and lacks key residues for activity. This ERCC4 endonuclease motif is also present in other proteins including the MUS81-EME1/EME2 complex, the FANCM/FAAP24 complex and in the Archaeal Hef protein (Hef is the Archaeal homologue of FANCM) (200). Of the other ERCC4 family proteins, apart from XPF, only MUS81 and Archaeal Hef retain catalytic activity (200). This is shown in Figure 4.2.

The MUS81/EME1 complex is a Holliday junction resolvase and is known to perform bilateral cleavage on Holliday junction-like structures (201). *In vitro*, Mus81-Mms4 (yeast homologue of MUS81-EME1) from yeast has been shown to cleave a variety of DNA substrates including Holliday junction structures, DNA forks and DNA flap structures (202). Furthermore cleavage by Mus81-Mms4 has a

substrate preference distinct from Rad1-Rad10 (yeast homologues of ERCC1-XPF) (203). Although Mus81-Mms4 and Rad1-Rad10 are both structure specific endonucleases acting 5′ to the DNA damage lesions, the Mus81-Mms4 complex has a 100-fold greater preference for flap structures over DNA forks (203). This has also been demonstrated for human MUS81-EME1 (204). In addition Bastin-Shanower *et al.* showed that cleavage by Mus81-Mms4 occurs 5nt upstream of the DNA junction and that the gap in the ds-DNA must be 4nt or less for cleavage to occur (203).

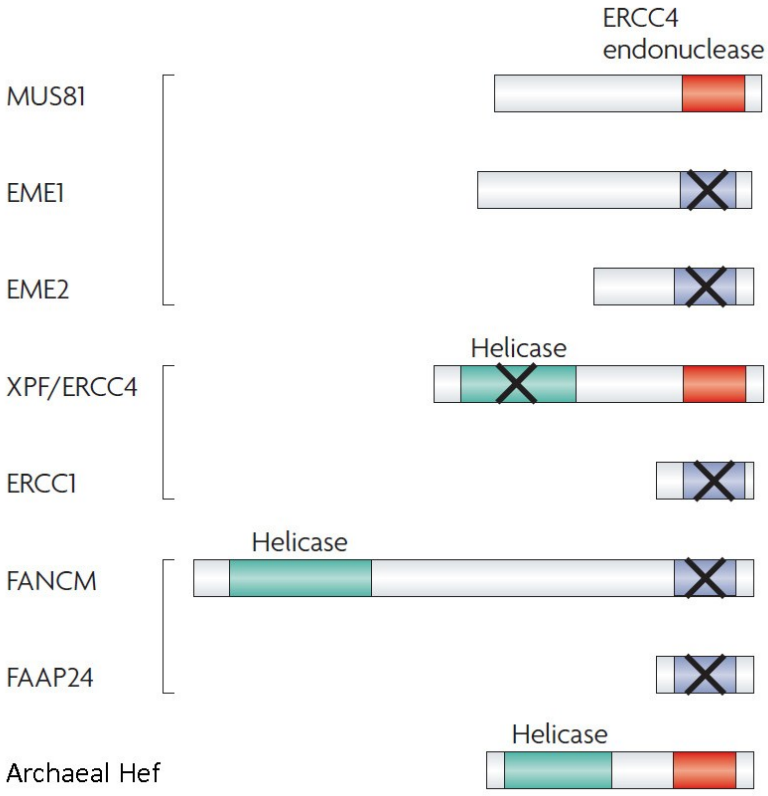

Figure 4.2: Figure showing ERCC4 endonuclease family members. Proteins which form heterodimer pairs are indicated by parenthesis. The active ERCC4-like domains are shown in red and ERCC4-like domains which lack essential residues and are catalytically inactive are shown in grey with crosses. Helicase-like domains are shown in green and inactive helicase-like domains are shown in green with crosses. Figure modified from (205).

While ERCC1-XPF and MUS81-EME act upon structures with 3′ overhangs or 3′ flaps, the flap endonuclease 1 (FEN1) family of proteins resolve the counterpart 5′ flap structures (200). The FEN1 family of proteins in addition to containing FEN1, also contains the XPG endonuclease which in NER acts with ERCC1-XPF to perform the dual incision and remove the damaged DNA (200). Although functioning in the same DNA damage pathways and containing a single helix-hairpin-helix motif, both FEN1 and XPG proteins share low homology to ERCC1-XPF (206).

4.2.5 FEN1 assay

The flap endonuclease 1 (FEN1) protein is a DNA endonuclease involved in DNA repair during the final ligation step of NER and BER (207–209) and is required for the repair of alkylating agents and UV induced DNA damage. In addition, FEN1 can function as a DNA exonuclease during DNA replication and is critical for the processing of Okazaki fragments (210).

Several *in vitro* FEN1 assays have been reported in literature however the majority of these are based upon radiolabeled substrates. In 2004, Tumey *et al.* developed a series of FEN1 inhibitors utilizing a fluorescent FEN1 assay (208, 209). This assay was proposed by Dorjsuren *et al.* to be unnecessarily complicated and they subsequently reported an alternative fluorescent based assay (207). This utilized three oligonucleotides annealed together with one labeled with TAMRA and another with the black hole quencher (BHQ-2) (207). Herein we utilize a modified version of the FEN1 assay as published by Dorjsuren *et al.* (See section 4.3.7).

In vitro, FEN1 is known to cut branched DNA substrates on the opposite strand to ERCC1-XPF, but has been shown not to cleave DNA substrates with closed loops (100). FEN1 typically cleaves structures containing flaps with 5′ tails and is capable of cleaving either DNA or RNA strands (211). Furthermore, cleavage is absent in structures which contain only single stranded overhangs (100).

4.2.6 DNase1 assay

To ensure compounds were not non-specific endonuclease inhibitors, we used an additional counter screen against the deoxyribonuclease I (DNase1) endonuclease. DNase1 is a waste management endonuclease expressed in cells in a cell-autonomous manner to degrade low molecular weight DNA following induction of apoptosis in differentiated cells (212). In addition, DNase1 is also secreted from cells to degrade DNA from necrotic cells and bacteria (212). This nuclease was chosen as DNase1 is known to display activity against a wide range of substrates including RNA, single stranded DNA, and chromatin bound DNA with a preference for double stranded DNA (213, 214).

DNase1 is known to function by cleaving phosphodiester bonds on one DNA strand at a time, acting from the minor grove of the DNA (213). This cleaves DNA to release 5′ phosphorylated di-, tr-, and oligonucleotide products (215). The catalytic efficiency of DNase1is then reduced on the small products formed as the preferred substrate size of DNase1 is structures of 4-6 bp or greater (213, 215). Furthermore, catalytic efficiency is shown to be DNA sequence dependent. Indeed, sequences containing AT repeats have a narrower minor grove than DNA of mixed sequence resulting in a lower catalytic efficiency (213).

4.2.7 Validation of screening assays

In order to assess the suitability of assays for high throughput screening and for compound validation, a statistical measure of the assay's performance must be utilized. In 1999, Zhang *et al.* reported a statistical measure known as the Z-factor (Z′) (216). This measure categorizes assays based upon their calculated Z′ value, whereby those achieving a value of 1 are an ideal assay, those between 1 and 0.5 are excellent, and those attaining less than 0.5 are only suitable as a second confirmation assay with another assay. The assay Z′ is calculated using the following equation:

$$Z' = 1 - \frac{3SD\ A + 3SD\ B}{mean\ A - mean\ B}$$

Whereby;

A = +'ve control samples

B = -'ve control samples

In addition to the assay Z′, assay robustness can also be quantified by a method published by Sittampalam *et al.* (217). This method relies on the SD of the controls and considers that compounds which have a signal of 3SD or greater from the control can be considered a hit (217). Herein, we utilize both measures for assay and compound validation.

4.3 Results

4.3.1 Developing an *in vitro* endonuclease assay for ERCC1-XPF

A well established *in vitro* endonuclease assay for ERCC1-XPF has been reported utilizing recombinant ERCC1-XPF and a short 46-mer DNA oligonucleotide that forms a stem-loop structure (100, 106, 112, 115). At the time of establishing this project, the assay was only radioactive based. As we were embarking on a drug screening project, it was necessary to develop an assay more amenable to high throughput screening, ideally based upon an analogous fluorescent substrate. We therefore decided to label the previously published 46-mer oligonucleotide with a fluorophore and a fluorescent quencher. As such, we had the 46-mer DNA oligonucleotide synthesized with 6-FAM on the 5′ end and a black hole quencher on the 3′ end. These were selected as 6-FAM has an excitation of 495nm and emission of 525nm whereas BHQ1 has a peak absorbance in the 480-580nm range (peak absorbance is at 534nm).

In the absence of ERCC1-XPF, the DNA oligonucleotide forms a stem-loop structure positioning the fluorophore and quencher in close proximity resulting in low levels of fluorescence. In the presence of ERCC1-XPF, this results in structure

specific cleavage of the DNA oligonucleotide and release of the fluorophore from the quencher. The resulting fluorescence can then be measured with a fluorimeter using 495nm excitation and 525nm emission filters. This is shown schematically in Figure 4.3.

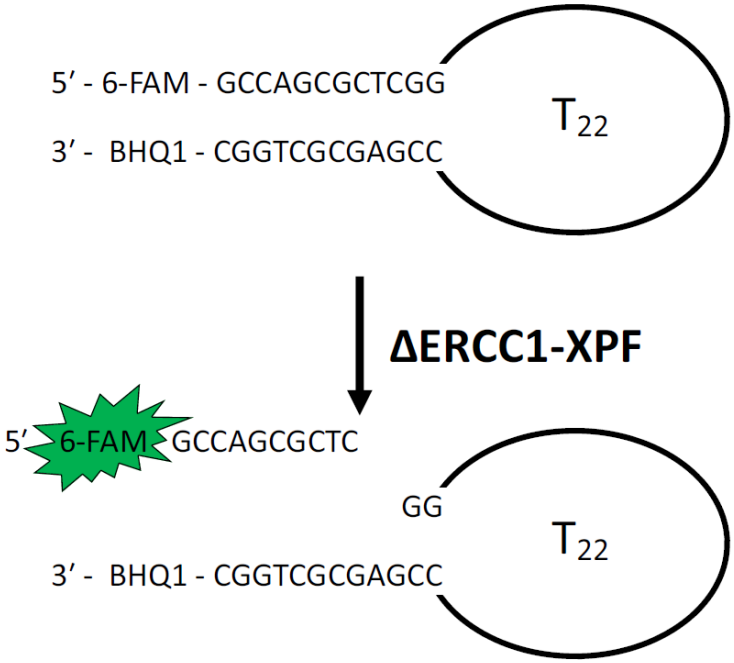

Figure 4.3: Schematic of the *in vitro* endonuclease assay for ERCC1-XPF. The 46-mer DNA oligonucleotide contains complementary DNA sequences at the 5′ and 3′ ends with a 22nt polythymine loop. The oligonucleotide has a fluorophore (6-FAM) on the 5′ end and a quencher (BHQ1) on the 3′ end. In the presence of ERCC1-XPF, this cleaves the DNA strand releasing the fluorophore and allowing fluorescence.

With regards to ERCC1-XPF, most of the previous assays were based upon using full length recombinant ERCC1-XPF. Unfortunately however, expression of full length ERCC1-XPF has been mostly performed in baculovirus infected insect cells. This is problematic as a screening project requires large quantities of protein that would not be practical based upon the published yields obtained for ERCC1-XPF using this expression system (115). Although it is possible to express full length ERCC1-XPF in a bacterial expression system, yields are low (106, 115). A truncated

$_{\Delta 95}$ERCC1-$_{\Delta 666}$XPF complex has also been published and shown to have activity in the analogous radioactive assay (106). This complex is expressed using an ERCC1 construct lacking the putative nuclear localisation signal and an XPF construct lacking the helicase-like domain. Although the helicase-like domain is not essential for activity, its presence results in greater activity (106). That being said, as we are seeking inhibitors of the XPF nuclease domain and ERCC1-XPF protein-protein interaction, the additional domains are surplus to our requirements.

4.3.2 Enzyme activity increases during long term pre-incubation

Optimization of the standard ΔERCC1-XPF assay had previously been published by Tsodikov *et al.* using 100nM ΔERCC1-XPF and 100nM of the radioactive DNA substrate (106). Upon adopting similar conditions, we observed similar levels of activity (see section 4.3.4) and a 3-4 fold assay window after 3 hours. This assay typically showed a Z′ of 0.6-0.8 and so was suitable to measure activity of inhibitors.

As the assay had low levels of activity, we wanted to see if activity was maintained over a long period of time. For this assay, we utilized the metal cofactors manganese, magnesium, cobalt and zinc. Here we found that manganese has more immediate activity in the endonuclease assay (and as such is the predominantly used metal ion in the literature), while magnesium, which is thought to be the biologically relevant metal ion, had a reduced activity. As shown in Figure 4.4, upon measuring the assay over a long period, manganese continued to result in a steady increase in fluorescence. Interestingly however, magnesium resulted in a large increase in activity at around 48-72 hours which did not occur with any of the other metal cofactors tested. This increased activity was unexpected and the reason for this increase was unknown.

Interested by the increased activity with magnesium, we set about developing an assay based around this observation. We found that if ΔERCC1-XPF protein was incubated at RT for 72 hours prior to the addition of substrate we would observe this higher activity level immediately after starting the reaction. We term this pre-incubation. Furthermore, conditions required for pre-incubation were independent of

protein concentration and could be performed in PBS with 5% glycerol, or in reaction buffer. This assay was setup as detailed in Chapter 2 materials and methods.

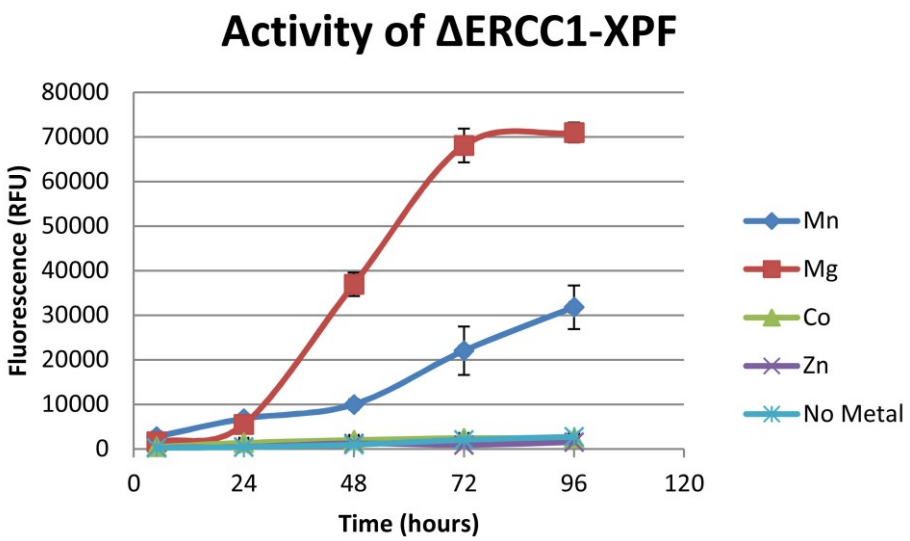

Figure 4.4: Long term fluorescence measurements of the ΔERCC1-XPF assay. The standard assay was setup using 0.5mM of $MnCl_2$, $MgCl_2$, $CoCl_2$, $ZnCl_2$ or no metal ion as a cofactor. The fluorescence was measured 5 hours after setup and then at every 24 hours thereafter. Data points show fluorescence after background subtraction ± SEM.

4.3.3 Metal ion specificity of the ΔERCC1-XPF assays

We then sought to determine what the optimal metal cofactor concentration was for each of the two ΔERCC1-XPF assays. Furthermore, high concentrations of metal cofactors are known to be inhibitory to ΔERCC1-XPF and as such the optimal concentration was likely to differ between cofactors. To determine the metal ion preference for the assays, we utilized the standard assay and the pre-incubated assay which had been pre-incubated for 72 hours and setup in the presence of $MnCl_2$, $MgCl_2$, $NiCl_2$, KCl, $CaCl_2$ or $ZnCl_2$ metal cofactors. Reactions were then started by addition of DNA substrate.

As shown in Figure 4.5A, for the standard ERCC1-XPF assay, there is a preference for low concentrations of the Mn^{2+} metal cofactor with the optimal concentration of 0.625mM. Although less activity is observed with Mg^{2+}, the optimal concentration of this was 2.5mM. The other metal cofactors tested did not show

activity. Interestingly, in a separate experiment (data not shown) Ni^{2+} was a potent inhibitor of the assay that also out competed Mn^{2+} in the assay.

In Figure 4.5B, we show an analogous experiment with the pre-incubated ΔERCC1-XPF assay. As we alluded to in Figure 4.4, following pre-incubation with Mg^{2+} we get enhanced activity, however this does not happen with Mn^{2+}. In Figure 4.5B, we show that the optimal Mg^{2+} concentration is 1.25mM and no other metal ions show activity in this assay. That being said, as the Mg^{2+} pre-incubated assay has significantly more activity (Figure 4.5B), this assay is measured at 30 minutes post substrate addition compared to the standard assay (Figure 4.5A) which is measured at 3 hours post substrate addition.

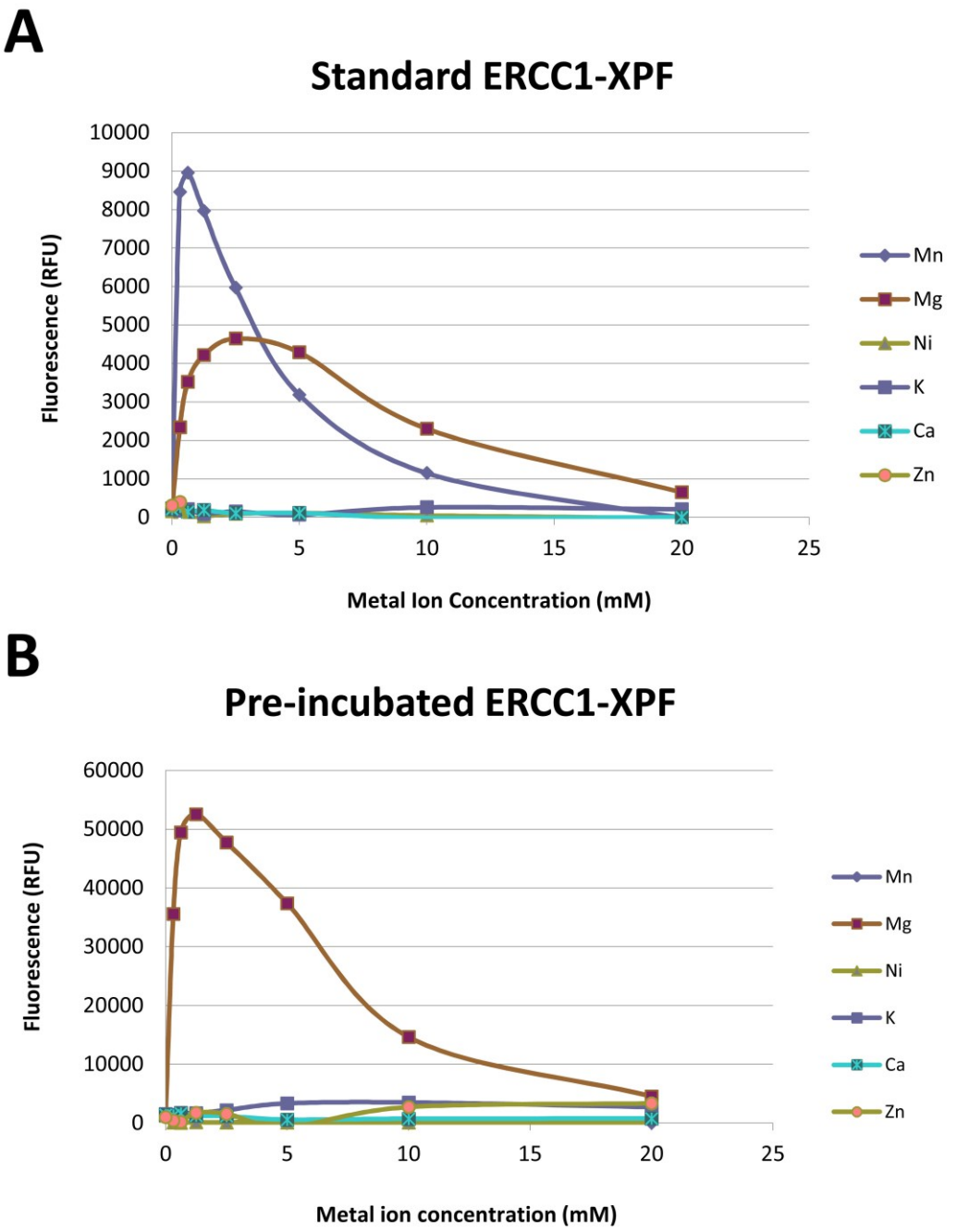

Figure 4.5: Metal ion preference of ΔERCC1-XPF assays. (A) The standard ERCC1-XPF assay was setup using 100nM recombinant ΔERCC1-XPF and 200nM substrate. The assay was performed with varying concentrations of metal cofactors as indicated. (B) The pre-incubated ERCC1-XPF assay was setup using 50nM recombinant ΔERCC1-XPF following 72 hours pre-incubation then the reactions were started by addition of 200nM substrate. Pre-incubated reactions were setup at varying concentrations of metal cofactors as indicated. The fluorescence was measured and background fluorescence was subtracted.

4.3.4 The pre-incubated ΔERCC1-XPF assay has greater activity

In order to quantify the increased activity that we observed between the standard ΔERCC1-XPF assay and the pre-incubated ΔERCC1-XPF assay, we performed enzyme kinetic assays. In Figure 4.6A, we show a Michaelis-Menton Plot for the standard ERCC1-XPF assay. Here we measure the Vmax to be 304fmol/min with a protein concentration of 100nM. Therefore, we calculate the Kcat of the enzyme to be 0.011min. Although the rate is low, it is similar to published kinetics for truncated ΔERCC1-XPF of 0.003min (106). Although we consider our measurement to be in line with Tsodikov *et al.*, this discrepancy may reflect our better preparation of ΔERCC1-XPF protein (106).

In Figure 4.6B we show a Michaelis-Menton plot for the pre-incubated ΔERCC1-XPF assay and calculate the activity to be approximately 200 fold higher than in the standard ERCC1-XPF assay. We show that the pre-incubated ERCC1-XPF assay has a Vmax of 34pmol/min at a protein concentration of 50nM. Therefore, we calculated the Kcat to be 2.448min. Interestingly, the published Kcat for full length ERCC1-XPF activity is 0.17-0.19min (106, 102). By pre-incubation, we achieve activity levels 13 fold greater than published for the full length ERCC1-XPF.

In addition, we show in Figure 4.6 that the KD for the stem-loop substrate differs between the two assays. The standard ΔERCC1-XPF assay shows a KD of 0.8μM whereas the pre-incubated ΔERCC1-XPF assay shows a KD of 28.9μM. This indicates that although the pre-incubated assay is 200 fold more active, it has a 35 fold reduced affinity for the DNA substrate.

Due to the small discrepancies in activity, we consider the activity of our standard ERCC1-XPF assay is in accordance with published data (106). Furthermore, this assay also shows a similar metal ion preference to published data. Interestingly, our pre-incubated assay is 200 fold more active. It is likely that this difference may be partly accounted for by the presence the magnesium cofactor rather than manganese as magnesium is the biologically relevant metal cofactor. The

reason for this increased activity and change in metal preference is unknown, but is investigated in a later section.

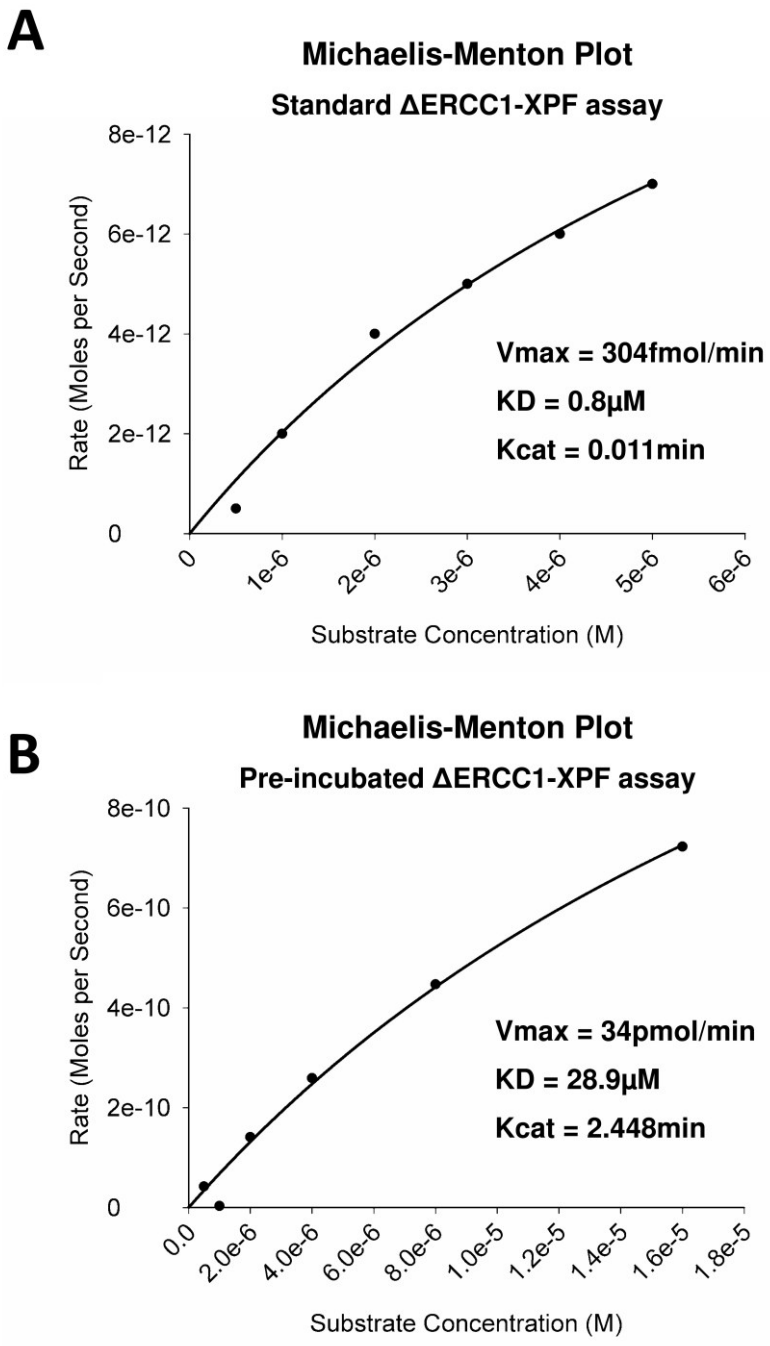

Figure 4.6: Michaelis-Menton plots for the standard ERCC1-XPF assay and the pre-incubated ERCC1-XPF assays. (A) Showing the Michaelis-Menton Plot obtained for the standard ERCC1-XPF assay using 100nM ΔERCC1-XPF. The insert shows the determined kinetic parameters (B) Showing the Michaelis-Menton Plot obtained for the pre-incubated assay using 50nM ΔERCC1-XPF. The ΔERCC1-XPF protein had been pre-incubated for 72

hours prior to assay. Insert shows the determined kinetic parameters. Kinetic parameters derived using the SigmaPlot v12.0 enzyme kinetics module.

4.3.5 Substrate cleavage specificity of the ΔERCC1-XPF assays

In section 4.3.2, we showed that there was increased activity of the pre-incubated ERCC1-XPF assay compared to the standard ERCC1-XPF assay. Therefore, we wanted to ensure that both ERCC1-XPF assays retained cleavage specificity. ERCC1-XPF is known to be a structure specific endonuclease that cleaves the stem-loop substrate 2nt upstream of the DNA junction on the 5′ ds-DNA strand. Based upon literature, the position of the expected cleavage site for the ERCC1-XPF assay is shown in Figure 4.7A (100, 102, 106).

Shown in Figure 4.7B is a DNA 'sequencing-like' gel, whereby the reaction products are run out on a 12% acrylamide/urea gel, and the relative positions of DNA bands are imaged due to their 6-FAM labels. Here we show that the standard ΔERCC1-XPF assay does indeed result in a major 10nt product as predicted with minor products at 9 and 11nt. To our surprise, the pre-incubated ΔERCC1-XPF assay showed an altered specificity and instead resulted in a product of 4nt. Additional minor cleavage products can also be observed in positions estimated to be 5nt, 7nt, 9nt and 11nt.

In addition, upon cleavage, only the pre-incubated ERCC1-XPF assay resulted in loss of the 46-mer DNA substrate band. This indicates that this assay had reached completion whereas the standard assay had not. Neither of the nuclease only, or metal cofactor only controls showed cleavage. These controls show that in the absence of the metal cofactor the enzyme is not active, and that in the absence of ERCC1-XPF protein there are no non-specific nucleases present in the buffer accounting for activity. Although Bowles *et al.* suggest cleavage by the truncated ΔERCC1-XPF protein is due to non-specific nuclease activity (102), the enzyme specificity in the standard assay as observed here, and the metal ion specificity observed in section 4.3.3 suggests this is not the case. We propose cleavage is due to specific activity of ΔERCC1-XPF and not due to non-specific cleavage from

contaminating proteins in the protein preparations or buffer. The purity of our standard ΔERCC1-XPF protein preparation is shown in Figure 4.8A.

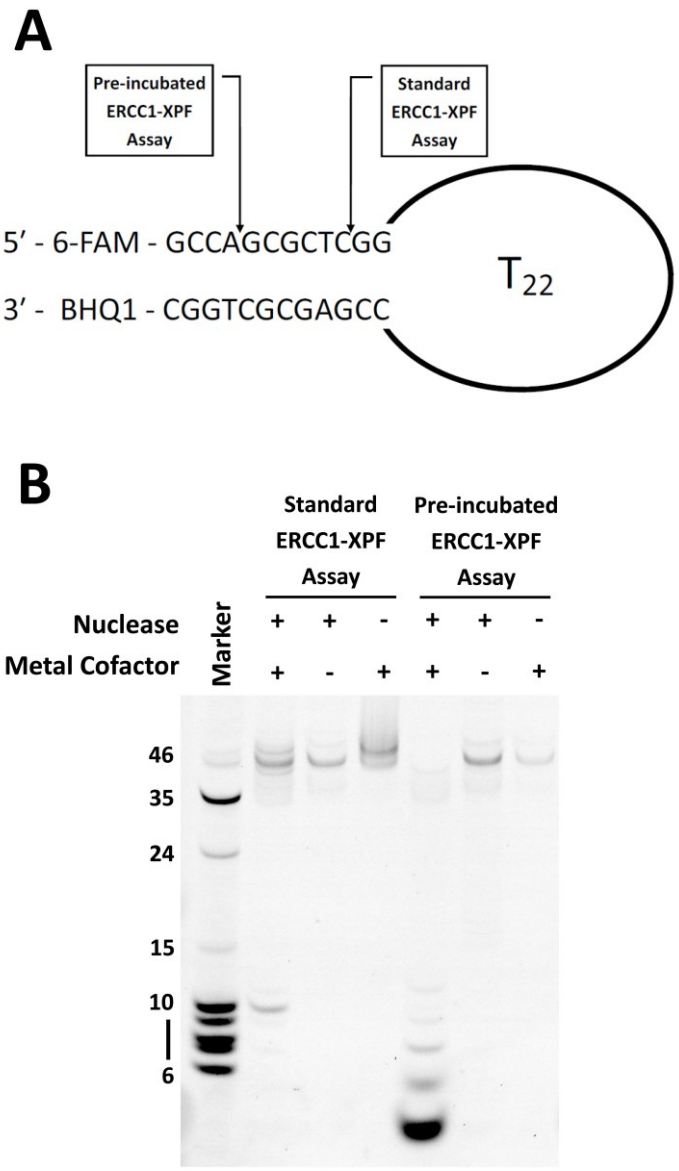

Figure 4.7: Gel based specificity assay of the standard ΔERCC1-XPF, and pre-incubated ΔERCC1-XPF assays. (A) Showing a schematic representation of the observed main cleavage sites in the stem-loop DNA oligonucleotide (B) Showing reaction products run out on a 'sequencing-like' gel and imaging of 6-FAM labels. Standard ERCC1-XPF assay performed using 200nM ΔERCC1-XPF and 200nM substrate for 3 hours and the pre-incubated assay was performed using 50nM ΔERCC1-XPF (72 hour pre-incubation) and 200nM substrate for 1 hour.

4.3.6 Protein breakdown during pre-incubation

To understand what molecular changes had occurred to ERCC1-XPF during this pre-incubation period to result in the greater activity, we ran a protein gel and stained it with coomassie protein stain. As shown in Figure 4.8A, we noticed a specific breakdown which occurred over the same period as the pre-incubation. This occurred in all protein batches tested and was characterized by an initial breakdown of ΔERCC1 and ΔXPF followed by a further breakdown to two doublet bands, one set just above 17kDa, and one set just below 17kDa. A smeared band was also characteristic of breakdown and was centered at 11kDa.

To identify which protein each of the fragments originated from, we performed Western blotting on the breakdown fragments. In Figure 4.8B, we performed a Western blot using the ERCC1 FL-297 polyclonal antibody which was raised against the entire sequence of ERCC1. In Figure 4.8C, we perform a Western Blot using the XPF Ab-5 monoclonal antibody with an undefined epitope. In order to directly visualize fragments from Western blots, and attribute each of the bands to either ΔERCC1 or ΔXPF, we overlaid the Western blots visualizing ERCC1 through the blue colour channel and XPF through the red channel. This is shown in Figure 4.8D.

As shown in Figure 4.8D, the ΔERCC1-XPF protein showed some initial breakdown without pre-incubation. This is typical of ERCC1-XPF when stored and typically occurred within 1-2 weeks after purification without affecting activity. At 48 hours we then begin to observe major breakdown of ΔERCC1-XPF occurring. At 72 hours, the XPF western (Figure 4.8C) clearly identifies the two doublets, one above 17kDa and one below 17kDa. Furthermore, ERCC1 breakdown products are also identified in the same region (Figure 4.8B), and in the merge appears to correspond to the lower band of the XPF doublets. An attempt by Dr Martin Wear from the University of Edinburgh to identify each of the fragments by Mass spectroscopy was unsuccessful due to the presence of ERCC1 and XPF peptides in all bands.

Although protein breakdown occurs during the same time scale as the ΔERCC1-XPF pre-incubation, it is unknown whether this is the cause of increased

activity, or whether increased activity is as a result of another factor occurring during the pre-incubation period.

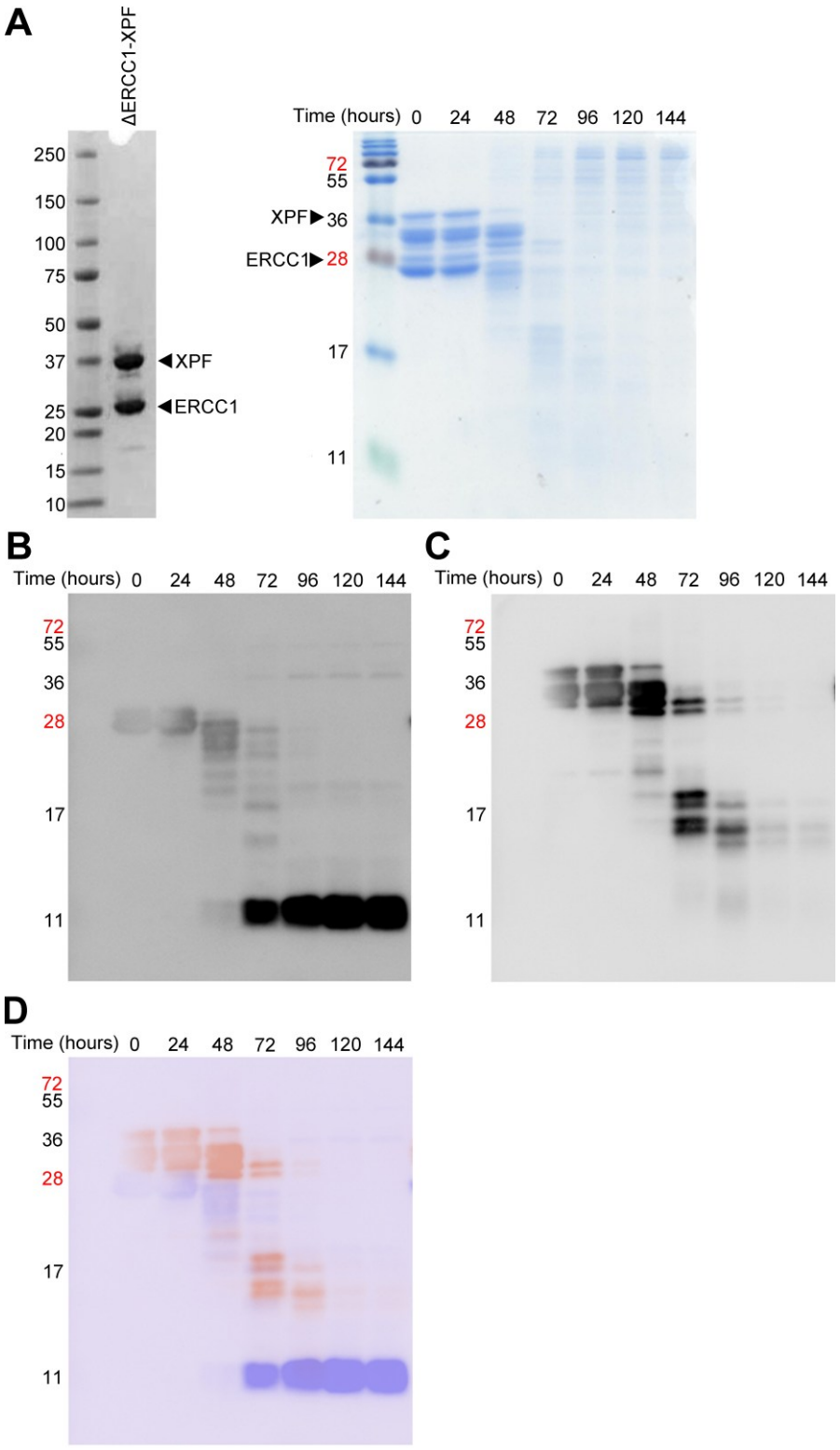

Figure 4.8: Identification of ΔERCC1-XPF breakdown during pre-incubation (A) Coomassie gel of ΔERCC1-XPF complex immediately after purification (left panel), and of breakdown fragments following pre-incubation (right panel). The length of pre-incubation is

indicated. (B) ERCC1 western blot of breakdown fragments (C) XPF western blot of breakdown fragments (D) Merged westerns of breakdown fragments, ERCC1 is shown in Blue, XPF is shown in Red. The positions of molecular weight markers are shown.

Although on the denaturing SDS-Page gel there was significant breakdown, we wanted to know whether this resulted in loss of fragments from the native complex. To answer this, we attempted to perform size-exclusion chromatography and native gels on the proteins however results were inconclusive..

In order to understand if these aberrations to the primary structure of the protein resulted in secondary structure change, our collaborators Dr Preeti Bakrania and Dr Barbara Saxty from MRC Technology performed circular dichroism and demonstrated an 11.3% loss in the α-helical structure following 72 hour pre-incubation. This is accompanied by a similar increase in random structures and no change (<1%) to either β-sheet or β-turn structures. Although it was unclear what regions of ΔERCC1 or ΔXPF are involved to cause this change, it corresponds to loss of structure in approximately 51 of the 452 residues. In addition, as the secondary structure is not radically changed following breakdown, this supports the notion that the ΔERCC1-XPF protein remained as a single complex following pre-incubation.

4.3.7 FEN1 assay

In order to assess the specificity of our ERCC1-XPF inhibitors, we sought to establish specificity assays. The first of these was a FEN1 assay. In the literature, there was a previously published assay using three oligonucleotides, one of which acted as a backbone, another was labeled with a quencher, a third which acted as a flap structure was labeled with a fluorophore (207). Once annealed, these three oligos would form a structure as shown in Figure 4.9A whereby the quencher and fluorophore would be in close proximity and result in low levels of fluorescence. The authors show that this assay reaches 3 fold activity over background after 30 minutes and that FEN1 cuts specifically in the position indicated in Figure 4.9A (207). For

our purposes, we opted to utilize a 6-FAM fluorophore and BHQ1 quencher instead of the TAMRA and BHQ2 as used by Dorjsuren *et al.* (207). We predict that this should not affect the assay but should facilitate compatibility with the filter set present on the fluorimeter.

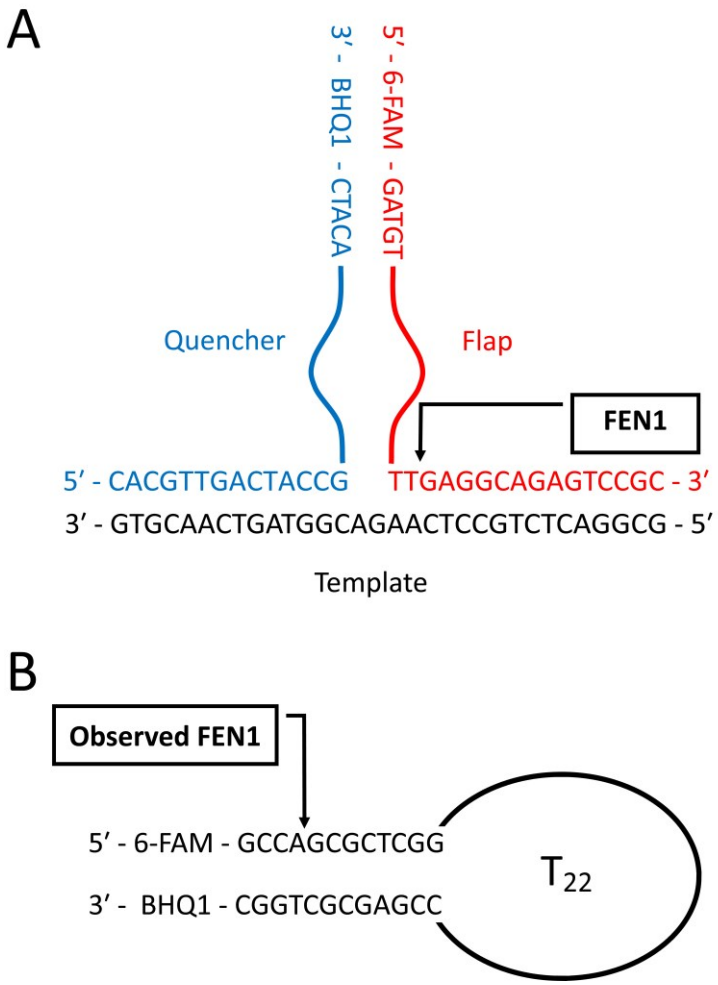

Figure 4.9: Schematic of FEN1 assay substrates. (A) The FEN1 assay oligos were annealed to form a structure as shown. This FEN1 assay is based upon an assay published by Dorjsuren *et al.* except for a change to the fluorophore and quencher (207). (B) Showing the DNA stem-loop substrate as used for the ERCC1-XPF assay. Indicated is the site where FEN1 was observed to cleave as demonstrated in Figure 4.11.

Upon testing the FEN1 assay using 20nM of recombinant FEN1 protein and 50nM of the annealed FEN1 substrates as published by Dorjsuren *et al.*, after 30 minutes we observed high levels of background fluorescence and only 1.25 fold activity over background levels (207). This is shown in Figure 4.10. In comparison, we also utilized the stem-loop from the ERCC1-XPF assay as although an unpublished observation by de Laat *et al.* stated it did not cut this radiolabelled structure (100), we had predicted that the addition of fluorophore and quencher may present as non-base paired bases. The observed cleavage site is indicated in Figure 4.9B. In the FEN1 assay with 20nM recombinant FEN1 protein and 50nM of the stem-loop DNA substrate (ERCC1 substrate), we achieved low levels of background and 5.2 fold activity after 30 minutes (see Figure 4.10). Furthermore, we showed that this assay had a Z' of 0.91 indicating highly reproducible results and a robust assay.

Additional attempts to anneal the standard FEN1 substrate were made however the increased fluorescence upon FEN1 addition indicates that a proportion of the substrate was correctly annealed. It is thought that the high background observed was either due to a proportion of un-annealed substrate, or poor quenching of annealed substrate. Furthermore, a DNA 'sequencing-like' gel performed on this substrate indicated cleavage of the flap strand was at the predicted position (data not shown). As the FEN1 assay performs better with the ERCC1-XPF stem-loop DNA substrate rather than the standard FEN1 substrate, this was selected for future assays.

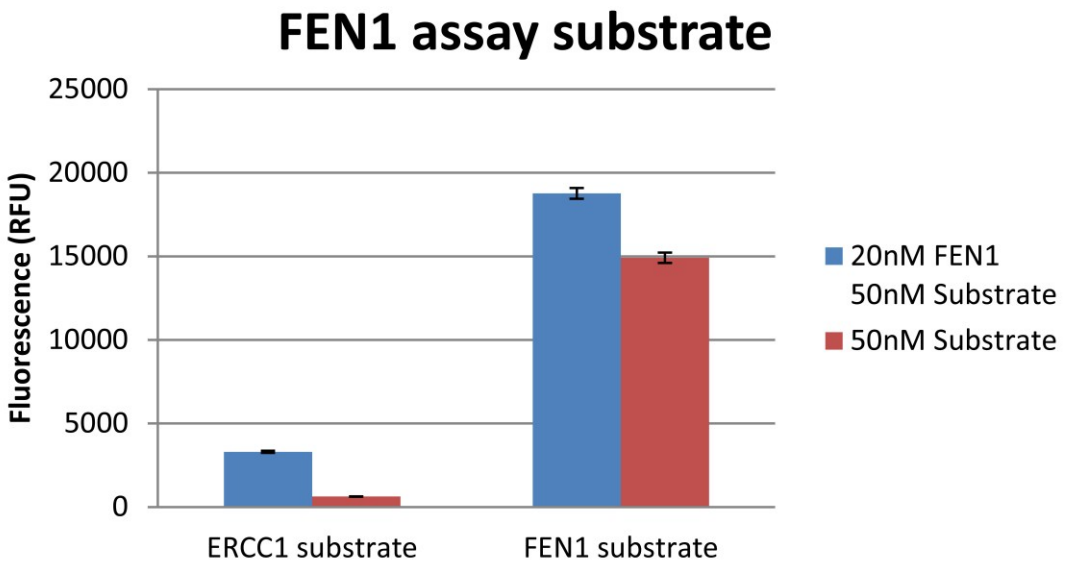

Figure 4.10: Substrate selection for the FEN1 assay. The FEN1 assay was setup at room temperature using 20nM FEN1 protein using either the stem-loop DNA structure (ERCC1 substrate) or the FEN1 specific substrate. The ERCC1 substrate achieves >4 fold activity over background in the assay with a Z′ of 0.91 after 30 minutes. The FEN1 substrate achieves 1.25 fold activity with a Z′ of 0.51 after 30 minutes. Fluorescence ± SEM shown.

4.3.8 DNase1 assay

A standard DNase1 (Deoxyribonuclease 1) assay was adopted from Dr Preeti Bakrania and Dr Barbara Saxty from MRC Technology. This assay utilized a 15 mer DNA oligonucleotide labeled with the 6FAM fluorophore on the 5′ end, and a BHQ1 quencher on the 3′ end. This assay uses 0.5ng Lyophilized DNase1 from bovine pancreas and 200nM of the DNase1 substrate. Furthermore, this assay reached 10 fold activity after 30 minutes and had a Z′ of 0.86. Optimisation of this assay was performed by Dr Preeti Bakrania. In addition, this assay also functioned on the ERCC1-XPF substrate with suitable fold activity and Z′ values for screening.

4.3.9 Substrate cleavage specificity of nucleases

In order to check the substrate cleavage specificity of the FEN1 and DNase1 assays, we once again utilized the DNA ‘sequencing-like’ gel using the stem-loop

DNA oligonucleotide. As shown in Figure 4.11B, the FEN1 assay resulted in a major product of 4nt indicating that FEN1 does recognize the fluorophore and quencher as non-base paired bases. This is also shown in the schematic of Figure 4.11A. In addition, minor cleavage products were observed at 5nt, 6nt, 7nt, 8nt and 9nt. Also shown in Figure 4.11 is the DNase1 assay which, as expected, resulted in multiple cleavage sites on the stem-loop DNA substrate. These cleavage sites were predominantly in the double stranded region of the DNA at positions 5-11nt. Furthermore, no cleavage occurred in the single stranded polythymine loop or occurred on DNA less than 4 nt in length however this was not surprising as DNase1 is known to have a preference for ds-DNA. In addition, cleavage was also observed to occur on the 3′ strand of the ds-DNA as shown by an increased fluorescence in the 35-46 nt region. The cleavage sites are schematically represented in Figure 4.11A. Figure 4.11B indicates that DNase1 is not dependent upon addition of metal cofactors though this is not the case as the DNase1 used was a crude preparation known to contain calcium chloride.

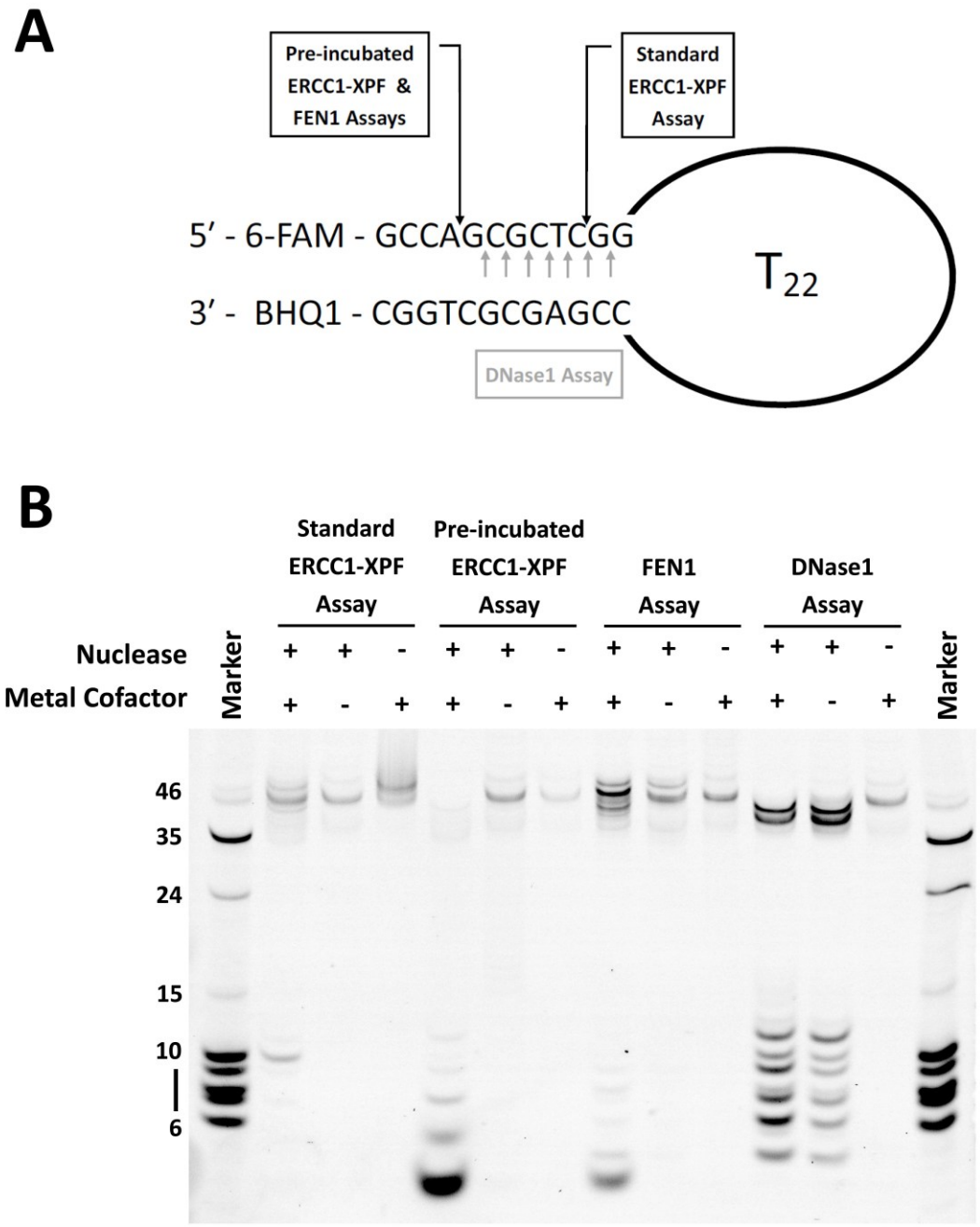

Figure 4.11: Substrate cleavage specificity of the standard ΔERCC1-XPF, pre-incubated ΔERCC1-XPF, FEN1 and DNase1 assays. (A) Schematic representation of the cleavage sites of the ΔERCC1-XPF, FEN1 and DNase1 assays. (B) The standard and pre-incubated assays were performed as documented in Figure 4.7B. The FEN1 assay was performed with 20nM FEN1 and 200nM stem-loop substrate for 3 hours. The DNase1 assay was performed with 0.5ng DNase1 and 200nM stem-loop substrate for 30 minutes.

4.3.10 Inhibition of the ERCC1-XPF, FEN1 and DNase1 assays by Aurintricarboxylic acid

To test the suitability of our assays to identify inhibitors, we screened all of the assays against the general nuclease inhibitor Aurintricarboxylic acid (ATA). This nuclease inhibitor is known to have a wide range of activities on targets including DNA helicases, DNA nucleases, RNA nucleases, DNA polymerases and kinesin proteins (218–221). Interestingly, we observed a difference in the IC50 for ATA between the standard ΔERCC1-XPF assay and the pre-incubated ΔERCC1-XPF assays. In Figure 4.12, we show that the IC50 in the standard ERCC1-XPF assay was 0.8μM. In the pre-incubated ERCC1-XPF assay, this increased to 15.1μM. The cause of this discrepancy is unknown. Furthermore, a similar increase was also observed for the binding affinity for the DNA substrate. In section 4.3.4, we showed the KD for the substrate to be 0.8μM and 28.9μM respectively.

The FEN1 assay also showed inhibition by Aurintricarboxylic acid. Here the IC50 was determined to be 0.2μM which was similar to Dorjsuren *et al.* who had previously shown this to be 0.59μM (222). This is considered to be equivalent as the IC50 values are within 3 fold. Importantly as we are using a different DNA substrate to Dorjsuren *et al.*, this supports the suggestion that our assay is acting similarly to the reported assay (222).

The DNase1 assay using the DNase1 specific substrate showed an ATA IC50 of 6.6μM. This was similar to that obtained using the ERCC1 substrate and to that obtained by Dr Preeti Bakrania and Dr Barbara Saxty from MRC Technology. Furthermore, previous publications have shown that ATA inhibits DNase1 with an IC50 of 5-9μM (220, 223). This indicates that the sensitivity to inhibition of our assay is in accordance with published literature.

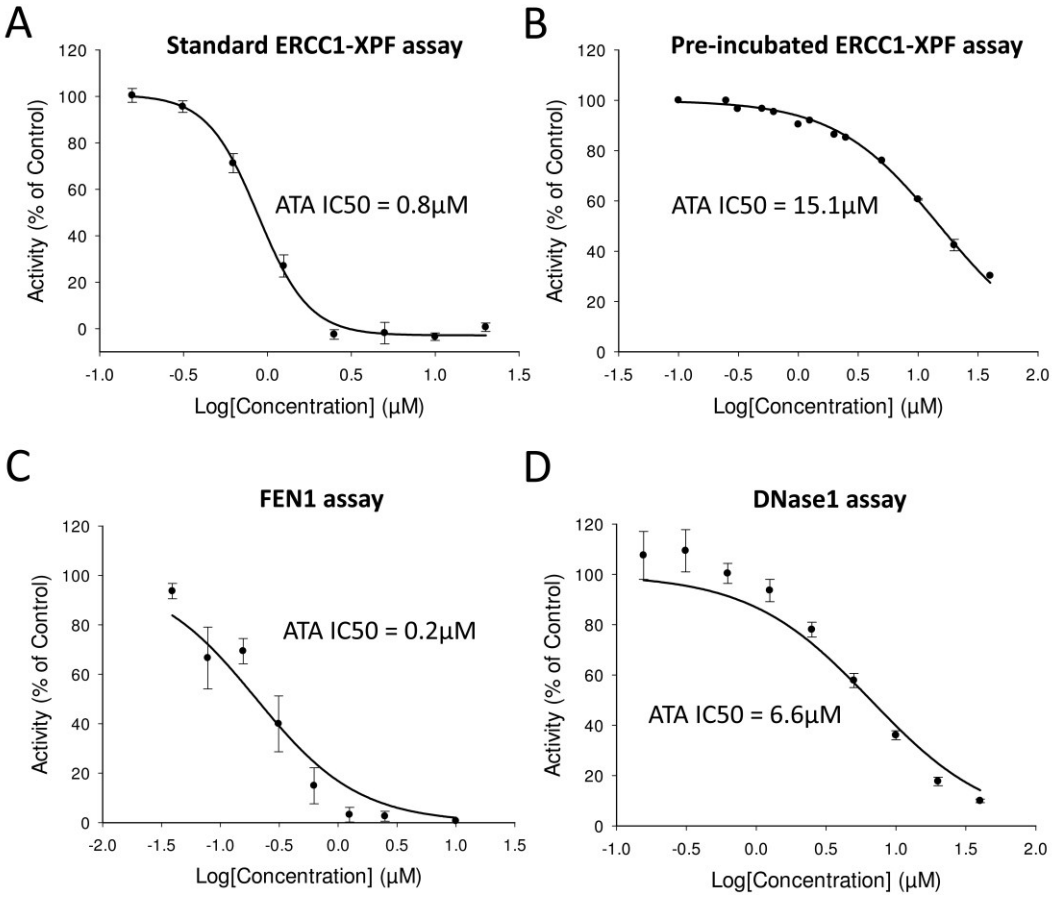

Figure 4.12: Inhibition of the ΔERCC1-XPF, FEN1 and DNase1 assays by Aurintricarboxylic acid (A) Inhibition of the standard ΔERCC1-XPF assay by Aurintricarboxylic acid (ATA) performed as documented in section 2.2.14. (B) Inhibition of the pre-incubated ΔERCC1-XPF assay by ATA performed as documented in section 2.2.15. (C) Inhibition of the FEN1 assay by ATA performed as documented in section 2.2.16. (D) Inhibition of the DNase1 assay by ATA performed as documented in section 2.2.17. Activity expressed as a percentage of the non-treated control ± SEM.

4.4 Discussion

The aim of this chapter was to develop an *in vitro* endonuclease assay for ERCC1-XPF suitable for high throughput screening. In order to do this, we utilised an existing assay based upon radioactively labelled substrates and converted it to a

fluorescent based assay. In addition, we sought to establish additional assays suitable for compound screening and to assess the specificity of ERCC1-XPF inhibitors.

While we decided to utilise a truncated complex of ΔERCC1 and ΔXPF due to more favourable expression characteristics, it had previously been reported that full length ERCC1-XPF had more activity (106). That being said, full length ERCC1-XPF protein also contained the putative ERCC1 nuclear localisation signal and the XPF helicase domain. In addition, since we are not targeting these domains, the favourable expression of the truncated ΔERCC1-XPF makes this more advantageous. The role of the putative ERCC1 nuclear localisation signal is unknown however it is thought that the XPF helicase like domain contributes to activity by binding to DNA. Bowles *et al.* propose that this domain binds at the ss- to ds-DNA junction inside the stem-loop. We believe this not to be the case as it is not required for cleavage specificity as proposed by Bowles *et al.* and because the domain is too large to fit into the stem-loop (102). Instead we propose this may contribute to activity by acting as a clamp, holding the DNA into the active site. This is shown in the model which we propose in section 1.4.5. Furthermore, as the expression constructs for full length ERCC1-XPF proteins were generated before the full XPF sequence was known, these proteins harbour an 11 amino acid truncation on the N-terminus. It is unknown whether these amino acids would contribute to the activity, or stability of the protein.

To our surprise, upon investigating the effect of changing the metal cofactor in the ERCC1-XPF assay, we noticed that after 48 hours the activity suddenly increased. Interestingly, this increase in activity seemed to be limited to magnesium and did not occur with manganese which is typically used in the assay. Furthermore, magnesium is the biologically relevant metal ion.

By utilising this phenomenon, we found that by pre-incubating the enzyme at room temperature for 72 hours prior to using it in the assay, we could achieve activity levels 200 fold higher than the standard ERCC1-XPF assay. Furthermore, when using the standard ERCC1-XPF assay, we achieved structure specific cleavage 2nt upstream of the DNA junction. When using the pre-incubated ERCC1-XPF assay we achieved significantly greater cleavage however the specificity had then changed. With this assay we still observed specific cleavage but the major cleavage product

now occurred 8nt upstream of the ds/ss-DNA junction. We therefore wonder whether this assay still represents structure specific cleavage recognising the DNA junction of the stem loop or whether this assay now recognises the ds-DNA end.

In order to understand what was happening to ERCC1-XPF during this pre-incubation period to result in these changes, we first ran SDS-Page gels and stained these with coomassie stain. Here we discovered that during this period, protein breakdown was occurring. Size exclusion analysis although inconclusive suggested that the native complex remained the same size. Circular dichroism performed by Dr Preeti Bakrania and Dr Barbara Saxty from MRC Technology on the pre-incubated ΔERCC1-XPF complex indicated an 11.3% loss in the α-helical structure to random structure. While inconclusive, we predict that the pre-incubated ERCC1-XPF represents a protein complex that has an altered protein secondary structure resulting from breakdown in the primary protein structure. We hypothesize that this results in either a greater flexibility, or a loss of a regulatory control within the complex to achieve greater levels of activity. Furthermore, as this occurs only with magnesium, it is likely that the greater flexibility may allow magnesium to bind in a more favorable conformation in the active site. This may account for the greater activity.

We documented two *in vitro* ΔERCC1-XPF assays with vastly different properties. We believe that the standard ΔERCC1-XPF complex is biologically more relevant to how ERCC1-XPF functions *in vivo* (though lacking the XPF helicase domain and ERCC1 nuclear localisation signal) than the pre-incubated ERCC1-XPF assay as it displays structure specific cleavage as predicted. From the literature, the published enzyme kinetics are 17 fold higher for full length ERCC1-XPF compared to our truncated ΔERCC1-XPF activity levels.

In order to screen compounds for specificity against ERCC1-XPF, we then set about establishing a FEN1 assay. This was chosen as FEN1 is a closely related enzyme, but with a different specificity to ERCC1-XPF. Furthermore, as an already established assay was published, and protein was commercially available, this best suited our requirements. Should additional assays be required for demonstrating compound specificity in the future, establishing an assay based upon MUS81-EME1 or XPG ought to be considered.

We first adopted a previously published FEN1 assay and adapted the fluorophore and quencher to meet our needs (222). Unfortunately however this assay had high background levels and a low fold activity window. We therefore considered that this was not of use for screening. It is thought that this was due to un-annealed substrate however as an increase in fluorescence was observed in the assay, this suggests that at least a proportion was correctly annealed. Another explanation might be that the base pairing at the fluorophore and quencher is insufficient to hold the modifications in close proximity so allowing fluorescence of the annealed substrate. Instead we investigated the possibility of using the ERCC1-XPF stem-loop substrate. Here much greater fold activity was observed. In contrast to previous literature (100), we did observe specific cleavage with this substrate. Here we observe cleavage of the DNA oligonucleotide on the ds-DNA end where the fluorophore and quencher are present rather than at the stem-loop end. In the literature, this assay was performed using radioactively labelled structures which would form a neat base-paired end; this is in contrast to our oligonucleotide whereby the fluorophore and quencher may present to FEN1 as non-paired bases. It is therefore thought that in our case, FEN1 recognises this region and specifically cleaves the 5′ strand 4nt downstream of the fluorophore.

The additional specificity assay that we chose for screening ERCC1-XPF inhibitors was for DNase1. This was a good choice of nucleases as DNase1 has activity on a wide range of substrates (213, 215) thus the specificity is not as tightly controlled compared to the nuclease activities of ERCC1-XPF or FEN1. In addition, cleavage specificity of DNase1 on the stem-loop DNA substrate was as expected based upon literature. We showed that cleavage occurred exclusively within the ds-DNA region and did not occur on DNA of less than 4 nt in length (213). No cleavage was observed in the ss-DNA region though it is unknown whether this is due to the lower activity on ss-DNA versus ds-DNA, or whether this is because of the polythymine sequence which is also known to cause a lower activity (213).

We then investigated the ability of the assays to be inhibited by the general nuclease inhibitor Aurintricarboxylic acid. As predicted this resulted in inhibition of all the assays. Of note, inhibition of FEN1 was similar to previously published by

Dorjsuren *et al.* (222). Potent inhibition of DNase1 was also observed. Furthermore, we showed that the IC50 of ATA against DNase1 is in accordance with previous literature (220, 223). Interestingly, the standard and pre-incubated ERCC1-XPF assays showed differences in ATA potency of 0.8μM and 15.1μM respectively. Furthermore, a similar difference also occurred in the binding affinity for the stem-loop substrate whereby the standard assay had a KD of 0.8μM and the pre-incubated assay had a KD of 28.9μM showing that although pre-incubated ERCC1-XPF has greater activity, it also has a lower binding affinity for DNA. It is likely that the differences in affinity for DNA and ATA may be due to different methodology to perform these assays or may be due to the changes occurring during pre-incubation. In addition, as pre-incubation only occurs with magnesium, it is likely that the greater flexibility may allow magnesium to bind in a more favorable conformation in the active site, and this alteration may result in the altered binding affinities.

5 Chapter 5: *In silico* screen and compound validation for inhibitors of ERCC1-XPF

5.1 Aim of chapter

The aim of this chapter was to identify an ERCC1-XPF HhH_2 domain inhibitor and an XPF endonuclease domain inhibitor through *in silico* screening. Here, we use biochemical, biophysical and cell based techniques to identify and characterise ERCC1-XPF inhibitors.

5.2 Introduction

5.2.1 ERCC1-XPF HhH_2 domain

ERCC1-XPF interaction through their HhH_2 domains is an obligate requirement for a stable ERCC1-XPF complex and so is essential for catalytic activity. Development of small molecule inhibitors of the HhH_2 domain interaction would be expected to sensitise cells to chemotherapeutics whose DNA-damaging effects are repaired by ERCC1-XPF-dependent pathways. Given the expected high affinity and the hydrophobic nature of this interaction, it will be considerably more difficult to block than an enzyme active site. However, the successful development of the p53/MDM2 interaction inhibitor, nutlin, demonstrates what can be achieved (224). Mutagenesis studies indicate that disruption of the ERCC1 Phe293 interaction with XPF is sufficient to prevent complex formation (93, 109). Furthermore, availability of an ERCC1-XPF HhH_2 domain crystal structure (PDB code 2A1J) (106) provides an attractive first step for rational drug design programmes.

5.2.2 XPF endonuclease domain

Inhibition of the XPF catalytic domain would inhibit all known functions of ERCC1-XPF in DNA repair. The presence of Mg^{2+} coordinated in the active site provides an ideal target for metal ion chelation with only weak DNA contacts being made by this domain. There is currently no crystal structure for the human XPF endonuclease domain, although the Archaebacterial XPF crystal structures (PDB code 2BGW) (126) has been used to generate a human homology model that could aid the search for active site inhibitors (see Figure 5.8). Inhibition of the nuclease

domain of XPF is however problematic, due to shared mechanistic activity with closely related nucleases, thus designing the necessary specificity into inhibitors will be challenging. It is of note that drug discovery programmes have been, or are currently being pursued for another structure-specific endonuclease, Flap Endonuclease 1 (FEN1), involved in the final ligation step of NER and base excision repair (BER) (207–209), for Apurinic/apyrimidinic Endonuclease (APE1) required for BER (225, 226) and the RAD51 recombinase, involved in HR (227).

5.2.3 Inhibition of the XPF helicase-like domain as a target for drug discovery

The helicase-like domain could be an attractive target for drug discovery, particularly when considering the single Arg153Pro substitution resulted in hypersensitivity to UV and ICL agents (95). It would also be anticipated that inhibition of this domain would result in decreased nuclease activity, since truncated $_{\Delta 95}$ERCC1-$_{\Delta 666}$XPF shows 60-fold reduced activity *in vitro* compared to the full-length complex (106). However, our current understanding of the DNA and protein-protein interactions is insufficient for a drug screening programme to target this region. In addition, no crystal structures exist for this domain and a homology model would be of only limited value due to insufficient sequence homology to other helicases with known crystal structures.

5.2.4 ERCC1/XPA interaction

The nonspecific PK-C and CHK1 inhibitor, UCN-01, inhibited NER by causing a reduction in ERCC1 binding to XPA (228). Upon DNA damage and UCN-01 treatment, an accumulation of DNA-bound XPA was observed, but there was a decrease in DNA-bound ERCC1. *In silico* modelling of UCN-01 binding to ERCC1 calculated a binding energy of -4.81 kcal/mol (123). UCN-01 was proposed to bind into the XPA interaction site on ERCC1, disrupting the interaction of Tyr145 and Tyr152 in ERCC1, with several hydrogen bonds stabilising the UCN-01/ERCC1 interaction (123). An *in silico* screen for potential inhibitors of the XPA interaction

site on ERCC1 was performed, but no compounds were investigated for *in vitro* or *in vivo* activity (123).

Inhibition of the ERCC1/XPA interaction is an attractive drug target due to the existence of crystal structures and known inhibitors. Inhibition of this site *in vitro* and *in vivo* has been shown with a synthetic XPA peptide and is also proposed for UCN-01 (112, 123). However, an inhibitor of this interaction would only disrupt NER and would not affect the role of ERCC1-XPF in ICL or DSB repair. Thus, synergistic use of an ERCC1/XPA inhibitor with a DNA crosslinking agent, such as cisplatin, would likely only be of limited benefit.

5.2.5 XPF/RPA interaction

Inhibition of the XPF/RPA interaction may prove to be an effective drug target as RPA has a role in both NER and ICL repair, thus inhibition could potentiate toxicity of a range of chemotherapeutic agents (69, 127, 128). However, not enough is known about the interaction site and no crystal structures of interaction exist, so a drug discovery programme based on this target would be premature.

5.2.6 XPF/SLX4 interaction

The XPF/SLX4 interaction is an emerging drug target (130, 131, 136). Disruption would sensitise cells to interstrand crosslinking agents without disrupting the role of ERCC1-XPF in NER. Currently, a drug discovery programme targeting this interaction would be challenging as the XPF/SLX4 interaction site awaits detailed mapping. Furthermore, the relevant crystal structures are unavailable and low SLX4 sequence conservation between species would hamper confidence in homology modelling.

5.2.7 ERCC1/FANCG interaction

If the interaction between ERCC1 and FANCG is confirmed it could represent an attractive and novel drug target that would specifically block the role of ERCC1-XPF in ICL repair (137, 139). Deletion of ERCC1 or FANCG interacting regions

results in sensitivity to crosslinking agents, but it is unknown whether mutation of specific interaction sites on either protein is sufficient to sensitise cells. Further mapping of the interaction site would be necessary before attempting to identify inhibitors of this interaction.

5.2.8 Effect of emodin on ERCC1 transcription

Emodin was first proposed to have activity against ERCC1 in 1999 when Chang *et al.* discovered that emodin resulted in an up regulation of ERCC1 expression and resulted in enhanced repair of UV and cisplatin induced DNA damage (229). In 2010 Ko *et al.* published a contrary observation (230). In this paper, they showed that protein and mRNA levels of ERCC1 and Rad51 were reduced following emodin treatment and that this occurs due to a MAPK pathway dependent mechanism (230). In a separate paper, they then showed that emodin decreased expression of ERCC1 protein and mRNA levels through transcriptional inhibition of ERCC1 (231). They then showed that emodin is capable of down regulating the expression of Rad51, ERCC1 and up-regulation of Thymidine phosphorylase (necessary for capecitabine activation as used in the paper) (232). From the data, a direct role of emodin in inhibiting ERCC1-XPF is not excluded. Furthermore, activity of emodin as an inhibitor of ERCC1 (transcriptional inhibitor or otherwise) remains to be corroborated by an independent lab. A recent paper published by Deloia *et al.* has shown that ERCC1 mRNA levels do not correlate with ERCC1 protein levels (233). It is likely this may partly explain the contradictory findings of emodin.

5.2.9 ERCC1-XPF as a target for a drug discovery

Developing inhibitors against the ERCC1-XPF complex will be challenging. The most tractable target is the XPF endonuclease site itself, due to lower affinity for the DNA substrate than the affinity of the various protein-protein interactions involved in the different repair roles of ERCC1-XPF. Inhibition of this site would block all the known functions of ERCC1-XPF needed for the repair of chemotherapy-induced DNA damage. However, the lack of a crystal structure for

this domain of human XPF and the existence of a number of endonucleases with similar divalent cation-based cleavage mechanisms will complicate the search for compounds of the desired specificity. The only other target whose inhibition would prevent all repair roles of ERCC1-XPF is the interaction domain needed for heterodimer formation. The large hydrophobic surface area of the interaction domain makes this a formidable target, but a single amino acid deletion in this region does completely block activity (93, 109).

Inhibition of other protein-protein interactions made by the complex could also be tractable to a drug discovery programme. For instance, if there is a requirement to enhance sensitivity to a chemotherapeutic that causes lesions repaired exclusively by NER, then targeting the ERCC1/XPA interaction site should be considered and has the advantage of existing crystal structures and drug and peptide inhibitors. If instead the requirement is to block repair of just ICLs then inhibitors of ERCC1/XPF interactions with SLX4 or RAD52 may also be effective therapies, but these interactions are not yet sufficiently well understood to be the direct focus of drug discovery programme. In this chapter, we opt to identify inhibitors for the ERCC1-XPF interaction domain and XPF endonuclease domain.

5.3 Results

5.3.1 Species differences between the ERCC1-XPF HhH_2 domains

The ERCC1 and XPF proteins show a high degree of conservation between eukaryotic species and form stable heterodimer complexes. In Archaebacteria, only XPF is present and forms stable homodimer complexes (126). While a lot is known about ERCC1-XPF, a large part of current knowledge is from species other than human. The HhH_2 domain of ERCC1 and XPF is essential for dimerization, we therefore sought to determine the similarity of the ERCC1 and XPF HhH_2 regions between species at a molecular level (106, 112). This has implications for our choice of cell lines, and for species to be utilized for future *in vivo* experiments.

The crystal structure of the human HhH_2 domain (PDB Code: 2A1J) (106) and the Archaeal XPF HhH_2 domain (PDB Code: 2BGW) (126) are available on the

Protein Data Bank (PDB). While mice have taught us a lot about ERCC1-XPF, no crystal structure exists for mouse ERCC1 or XPF. Furthermore, as future *in vivo* experiments will likely be performed on mice (and potentially zebrafish), we wanted to understand the level of structural similarity and so generated PHYRE^2 models (Protein Homology/Analogy Recognition Engine v2.0) of their ERCC1 and XPF (154). In addition, so that a comparison could be drawn between species and an estimate of the PHYRE^2 model accuracy could be established, PHYRE^2 models were generated for the human and *A. pernix* proteins.

In Figure 5.1, we show the protein-protein dimerization surfaces of the ERCC1 and XPF HhH_2 domains for human, archaebacteria, mouse and zebrafish. As expected, the PHYRE^2 models generated for both human and *A. pernix* were reported by the PHYRE^2 server to be 99.8-99.9% accurate and showed no discernible difference to the published crystal structures (106, 126). Furthermore, confidence in all models was reported to be greater than 99.8% as assessed by the PHYRE^2 server indicating a high degree of accuracy and confidence in all models.

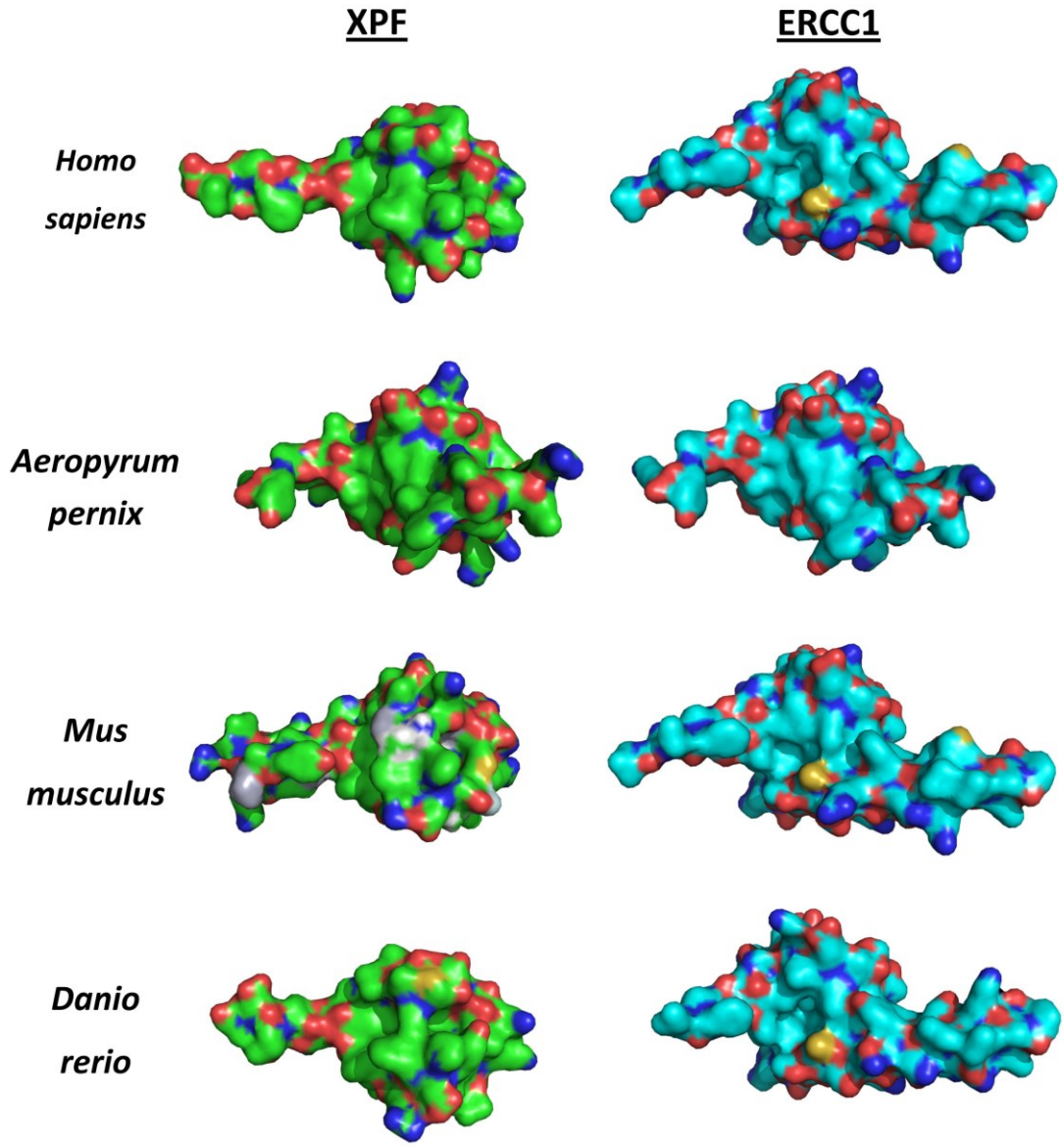

Figure 5.1: Showing the difference in HhH_2 domains of ERCC1 and XPF between species. Shown are the protein-protein dimerization surfaces of the HhH_2 domains for human, the Archaebacteria *A. pernix*, mouse and zebrafish. All models were generated using the PHYRE^2 server (154). *A. pernix* forms homodimer XPF structures. As a result, the XPF HhH_2 domain is represented instead of ERCC1 for *A. pernix*. This is aligned to the same orientation as the other ERCC1 proteins.

Based upon the PHYRE^2 prediction, all ERCC1 and XPF proteins adopt a HhH_2 fold motif characteristic of XPF protein family members (234). In the primary

amino acid sequence, differences between the proteins are revealed as shown in Figure 5.2. Consequently, as shown in Figure 5.1, this results in significant alterations to the tertiary protein structure and consequently the protein surface. The most diverse structures from human ERCC1 and XPF are for *A. pernix* though this is likely due to *A. pernix* forming XPF homodimers rather than the typical ERCC1-XPF heterodimer of eukaryotes. As predicted, the eukaryotic mouse and zebrafish structures show a high degree of similarity to human XPF.

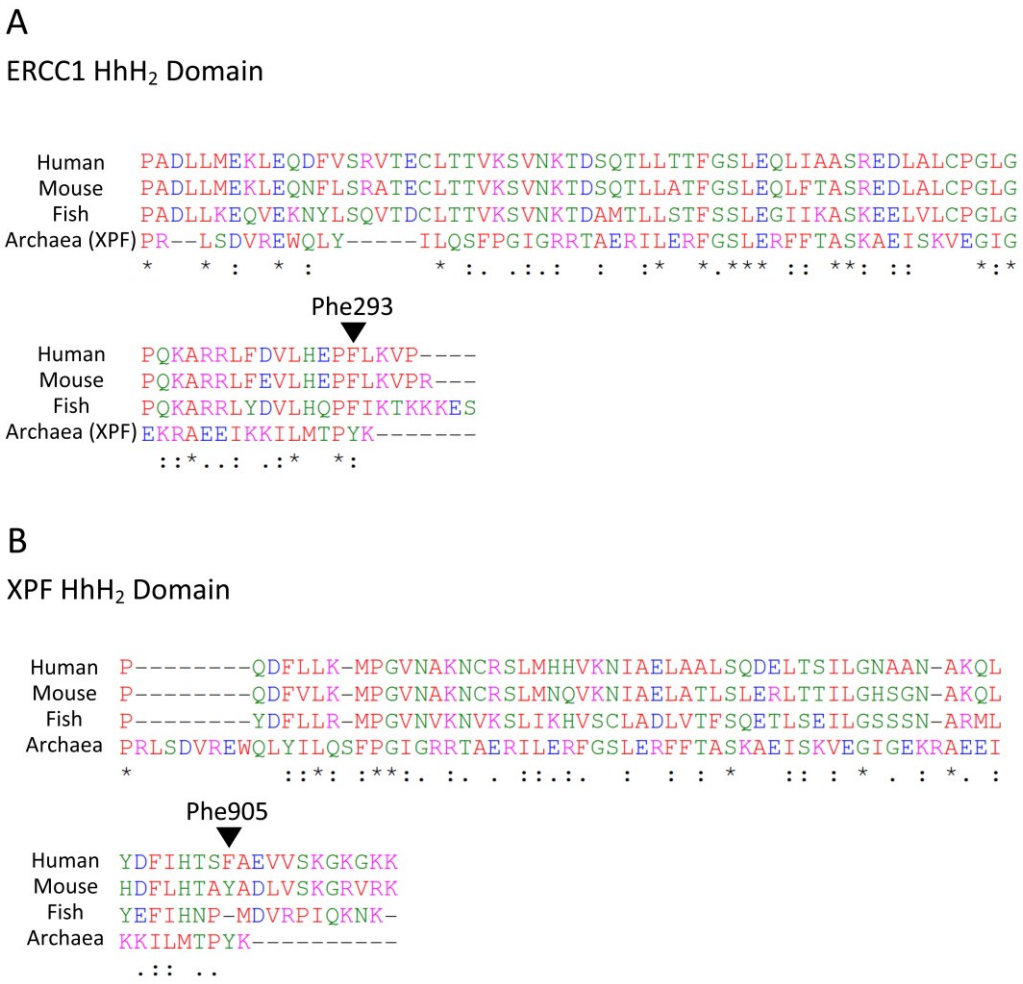

Figure 5.2: Sequence alignment of the ERCC1 and XPF sequences between species. Sequence alignment performed using ClustalW2 multiple sequence alignment tool. Amino acids are coloured so that small, hydrophobic, and aromatic residues are coloured red. Acidic residues are coloured blue. Basic residues are coloured magenta and hydroxyl, sulfhydryl or amine residues are coloured green. An asterisk indicates a conserved residue, a colon

indicates conservation with strongly similar properties, and a period indicates conservation with weakly similar properties.

The most significant difference between the HhH_2 domains between species were amino acid changes in positions equivalent to that of human ERCC1 Phe293 or XPF Phe905 as indicated in Figure 5.2. In the residue analogous to human XPF Phe905 of *A. pernix* and mice, this is substituted with a tyrosine residue. In zebrafish, the phenylalanine is absent and in the PHYRE^2 model is substituted with the adjacent methionine residue. Unlike a phenylalanine or tyrosine residue, the methionine lacks an aromatic side chain. Importantly, the residue analogous to human ERCC1 Phe293 is conserved in mouse and zebrafish and in the PHYRE^2 model all are positioned in the same spatial orientation as each other. Although *A. pernix* does not have ERCC1, the analogous tyrosine residue in XPF is in a similar orientation.

Additionally, in mouse there are substantial changes to the surface of XPF bridging the site of the binding pockets for ERCC1 Phe293 and Ile264 (see Figure 5.3). In this chapter, we aim to discover ERCC1-XPF interaction inhibitors which bridge multiple binding pockets; these are therefore likely to display species specific activity. This will be especially true for mouse. Furthermore, use of the Ercc1 proficient and deficient mouse cell lines for screening ERCC1-XPF HhH_2 interaction inhibitors designed against the human sequences will be unadvisable.

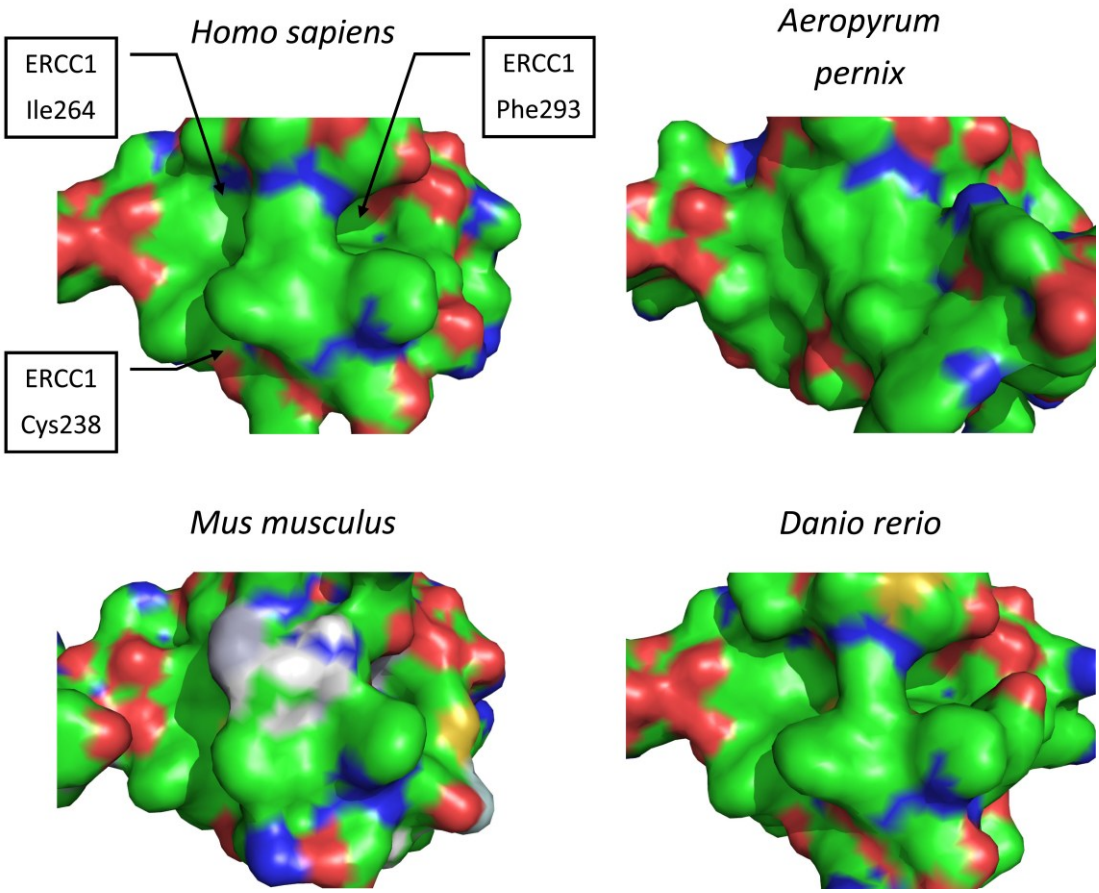

Figure 5.3: Figure showing the differences between the XPF protein surfaces between species. Showing the surface of XPF for each species as generated using a PHYRE^2 model (154). The ERCC1 binding pockets on human XPF are identified.

5.3.2 Target identification and *in silico* screening for inhibitors of the ERCC1-XPF HhH_2 domain

The human ERCC1-XPF HhH_2 domain is proposed as an *in silico* drug target as the crystal structure is available (106) and interaction is essential for the activity and stability of the ERCC1-XPF heterodimer (234). In this domain, the principal target site was identified as a pocket formed on XPF which the ERCC1 Phe293 residue binds to. This was proposed for a variety of reasons: ERCC1 Phe293 is conserved in eukaryotic species (103), ERCC1 binds into a large 280Å^2 pocket on the XPF protein surface (234) and finally, ERCC1 Phe293 is essential for interaction of the ERCC1 and XPF HhH_2 domains as deletion of this residue was sufficient to abrogate interaction (93, 109). The binding site for this residue on the XPF protein

surface is identified in Figure 5.4. To discover compounds with greater binding affinity and specificity, additional pockets on the XPF HhH_2 domain surface were sought. In collaboration with Professor Malcolm Walkinshaw and Dr Steven Shave from the University of Edinburgh, a surface triplet propensities (STP) program was utilized to predict additional, and unique protein binding sites (235). Two additional pockets on the XPF surface where the ERCC1 Ile264 and Cys238 residues bound were chosen. The locations of these binding sites are shown in Figure 5.4. Neither of these additional pockets have been previously reported in the literature.

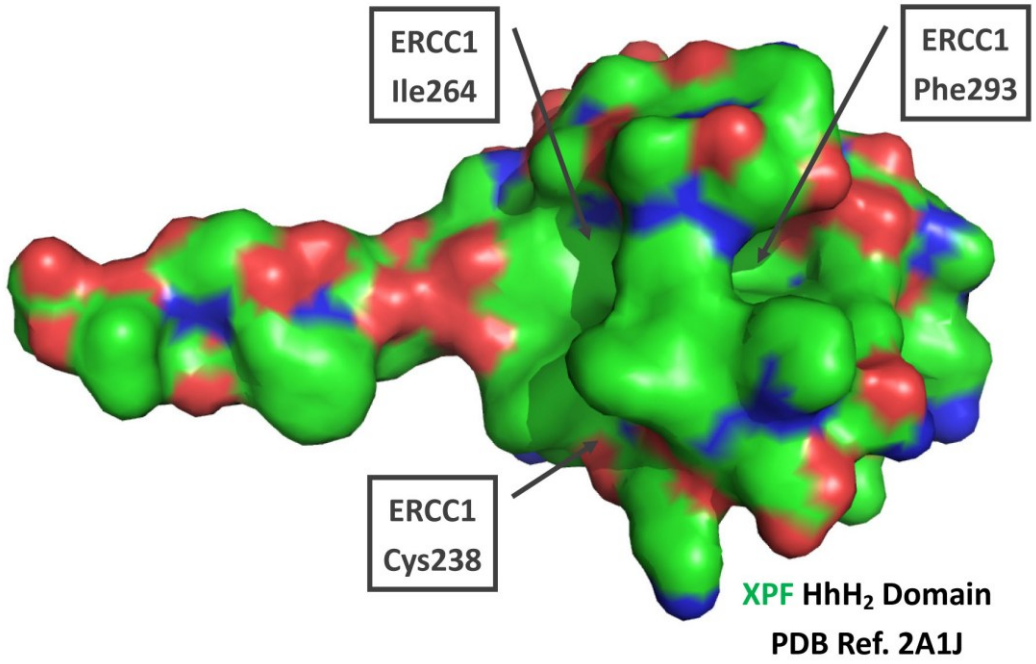

Figure 5.4: Showing the drug targets on the XPF HhH_2 surface. Showing the XPF HhH_2 domain surface following removal of ERCC1. Drug target sites are indicated by arrows and are identified by the corresponding ERCC1 amino acid which interact with this region. Figure created in PYMOL v0.99 using the ERCC1-XPF HhH_2 domain crystal structure 2A1J (106).

This is a protein-protein interaction and there is widespread scepticism about their suitability as drug targets, due to the strong protein-protein interactions that would need to be disrupted. The strength of interaction between ERCC1 and XPF

has not been reported. To determine the strength of their interaction, we used a BIAcore SPR assay in collaboration with Dr Martin Wear from the University of Edinburgh. In Figure 5.5, we used recombinant ΔXPF covalently bound to the BIAcore SPR surface and directly measured the interaction with ΔERCC1. We calculated the binding affinity to be 4.6nM demonstrating a tight interaction. Furthermore, with a fast on-rate, and slow off-rate, this indicates formation of a stable ΔERCC1-XPF complex on the BIAcore SPR surface. While such a strong interaction is unfavourable for inhibitor design, published mutagenesis suggests that only the Phe293 pocket needs to be inhibited to disrupt the formation of ERCC1-XPF complex. Inhibiting *de novo* complex formation *in vivo* may be more achievable than inhibiting preformed ERCC1-XPF complex. In practice this may mean the binding affinity required of inhibitors to achieve complex disruption will be reduced.

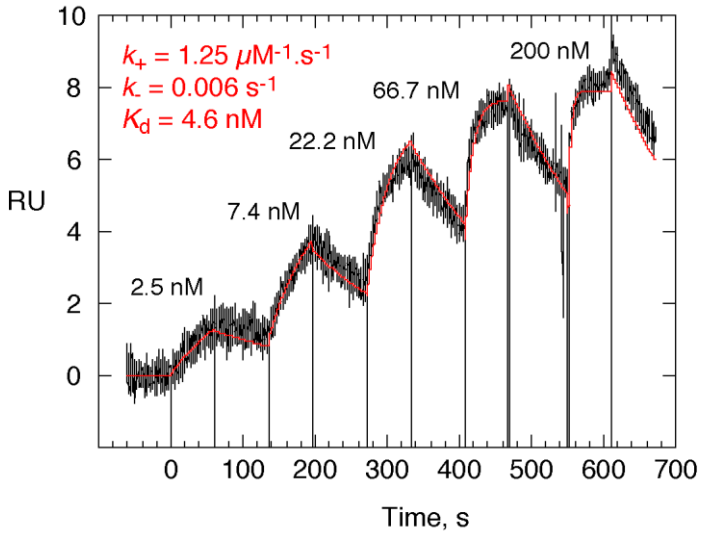

Figure 5.5: BIAcore SPR analysis of ERCC1 binding to XPF. Characterisation of the interaction of ΔXPF with ΔERCC1 using BIAcore T100. Reference corrected single cycle kinetic titration SPR binding curves (black), monitored on a surface of 276 response units (RU) of covalently stabilized ΔXPF, for various concentrations of ΔERCC1. Graph shows change in response against time. A three-fold dilution series from 2.5nM to 200nM of ΔERCC1was injected over the ΔXPF bound surface and the apparent on- and off-rate constants and KD (inset) were determined by globally fitting (red) a 1:1 kinetic binding model, with mass transport considerations, to the sensorgrams using the instrument analysis software. Assay performed by Dr Martin Wear.

Following target site identification, an *in silico* screen was performed by Dr Steven Shave as described in Chapter 2 materials and methods. Here Dr Steven Shave virtually screened the Chembridge, Maybridge and Specs dataset (subset of the 5 million compound EDULISS database) for compounds which bound to either single, or a combination of pockets (156). The combination of pockets chosen to screen were the F&C, F&I, I, F and I&C pockets. Screening to detect compounds which bound to all three pockets was not performed as only three compounds capable of binding to both the F&C pockets had been detected. Theoretical binding affinities were calculated and the compounds were ranked by their theoretical ligand efficiencies. This is a measure of binding affinity and is calculated by the Gibbs free energy as a ratio to the number of non-hydrogen atoms (236). The top scoring compounds purchased for follow up validation are shown in Table 5.1. Compound structures are searchable online from the EDULISS database (http://eduliss.bch.ed.ac.uk/test/index.jsp) via their Compound ID's (156).

Compound ID	Docked Affinity	Ligand Efficiency	F	I	C
(#1) SPH1-130-234	9.44μM	0.152	1		1
(#2) SPH1-101-765	51.80μM	0.107	1		1
SPH1-170-932	96.87μM	0.093	1		1
SPH1-162-759	38.12nM	0.256	1	1	
SPH1-113-609	2.07μM	0.196	1	1	
SPH1-018-583	3.08μM	0.172	1	1	
SPH1-184-504	18.47μM	0.158	1	1	
SPH1-224-925	5.08μM	0.151	1	1	
SPH1-202-698	17.70μM	0.149	1	1	
SPH1-016-259	7.24μM	0.198		1	
SPH1-106-348	47.37μM	0.197		1	
SPH1-139-256	12.82μM	0.196		1	
SPH1-127-198	45.89μM	0.189		1	
SPH1-141-032	19.65μM	0.174		1	
SPH1-004-620	119.72μM	0.163		1	
SPH1-029-060	9.02μM	0.360	1		
SPH1-227-152	45.19μM	0.290	1		
(#18) SPH1-078-651	16.32μM	0.282	1		
SPH1-113-000	21.44μM	0.275	1		
SPH1-054-528	21.34μM	0.259	1		
SPH1-125-714	4.07μM	0.257	1		
SPH1-011-687	4.27μM	0.256	1		
SPH1-067-405	22.80μM	0.202		1	1
SPH1-144-543	20.99μM	0.187		1	1
SPH1-168-516	2.08μM	0.167		1	1
SPH1-015-081	21.03μM	0.167		1	1
(#26) SPH1-173-203	5.63μM	0.164		1	1
SPH1-060-277	13.19μM	0.163		1	1

Table 5.1: Compounds from the ERCC1-XPF HhH_2 domain *in silico* screen selected for further investigation. Showing the Compound ID, theoretical docked affinity, theoretical ligand efficiency and target site of inhibitors. Compounds were targeted to either a single, or combination of Phe293, Ile264 or Cys238 pockets on XPF as indicated.

In Figure 5.6, we show the structure and docking poses for four of the *in silico* compounds which herein we demonstrate to display activity against ERCC1-XPF. Furthermore, we show the structure of three control compounds which are proposed to have activity against ERCC1-XPF. UCN-01 (Figure 5.7A) is proposed to be an inhibitor of the ERCC1/XPA interaction. Emodin (Figure 5.7B) is reported to be a transcriptional inhibitor of ERCC1, though our evidence suggests this to be an

endonuclease domain inhibitor (see section 5.3.4). Aurintricarboxylic acid (Figure 5.7C) is known to be a general nuclease inhibitor, though no activity against ERCC1-XPF has previously been demonstrated.

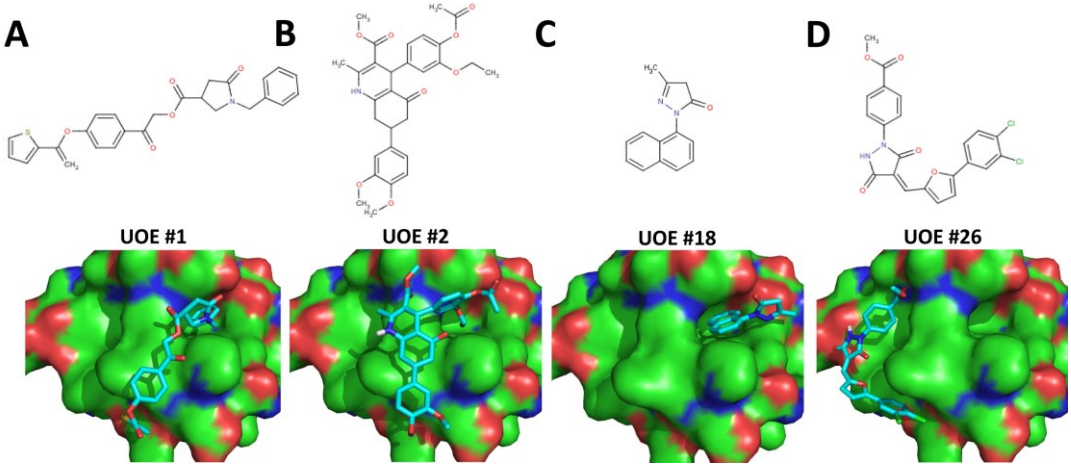

Figure 5.6: Showing structure and docking pose of the proposed ERCC1-XPF HhH_2 domain inhibitors. Compound structures were generated using ChemAxon Marvin Sketch. Docking poses were generated using the *in silico* docking file in PyMOL v0.99.

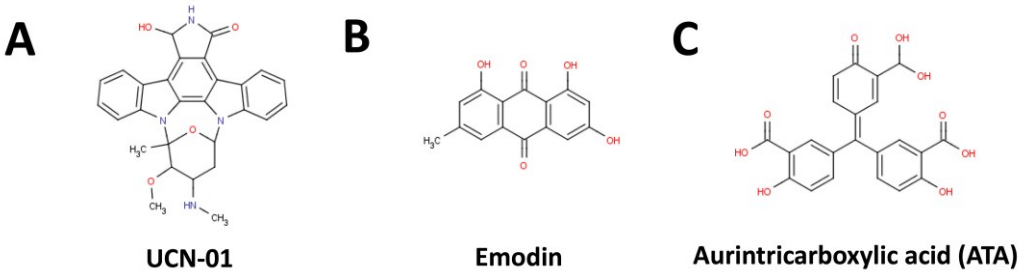

Figure 5.7: Showing the structures of control compounds. (A) Showing the structure of UCN-01 which inhibits the ERCC1/XPA interaction. (B) Showing the structure of Emodin which we propose to inhibit the XPF endonuclease domain. (C) Showing the structure of the known general nuclease inhibitor, Aurintricarboxylic acid. Compound structures were generated using ChemAxon Marvin Sketch.

5.3.3 Target identification and an *in silico* screen of the XPF endonuclease domain

In addition to developing an ERCC1-XPF HhH_2 interaction domain inhibitor, we also sought to develop an inhibitor of the XPF endonuclease domain. This had the advantage over the HhH_2 interaction domain inhibitors in that protein-DNA interactions were likely to be lower affinity than the 4.6nM ERCC1-XPF interaction.

The main problem with this target site is the lack of published human XPF endonuclease domain crystal structure thus posing a technical problem for *in silico* design. Instead a crystal structure for the Archaebacteria *A. pernix* was available. Unlike the HhH_2 domains, this region does show a high degree of similarity between species and the essential amino acids required for catalysis are conserved. The same is true for other species including mouse and zebrafish. As such, a PHYRE model was generated by Dr Steven Shave and energy minimalisation performed to refine the structure and allow *in silico* screening to be performed. A comparison of the PHYRE model and the *A. pernix* crystal structure of the XPF endonuclease domain is shown in Figure 5.8A and 5.8B.

The *in silico* screen of the EDULISS database was then performed by Dr Steven Shave as detailed in Chapter 2 materials and methods (156). As the reliability of a PHYRE model for *in silico* screening is limited by the quality of the model, the *in silico* screen was performed independently on both the *A. pernix* XPF crystal structure and the human XPF PHYRE model. For this screen, the newly available Autodock Vina program was used (237). This program has a more sophisticated and rigorous docking process and had not been available for use at the time of the ERCC1-XPF HhH_2 screen. For this reason compounds were ranked according to their Vina score upon binding to the target rather than the previously used ligand efficiency.

The top scoring 200 compounds were ranked and those with a Vina score less than -7.5 were subsequently purchased for validation. These are shown in Table 5.2. One of these compounds termed compound #44 shows activity against ERCC1-XPF and its structure and docking pose are shown in Figure 5.8C and 5.8D. Herein, we show the data which lead us to conclude that this is an inhibitor of ERCC1-XPF.

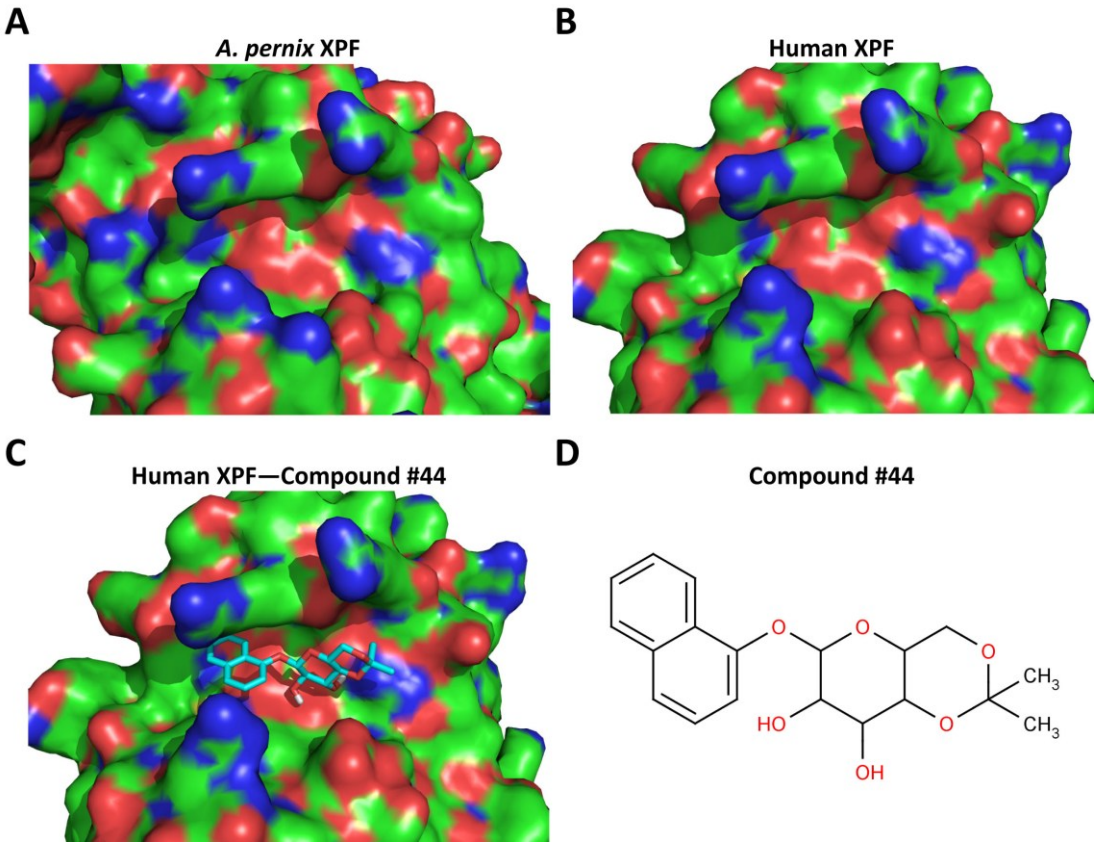

Figure 5.8: Showing the structures of the XPF nuclease domain from A. pernix and human XPF as used for in silico screening. (A) Showing the nuclease domain from *A. pernix* (PDB Code: 2BGW) (126). (B) Showing the nuclease domain of a PHYRE generated model of human XPF (154). (C-D) Showing the structure and docking pose for the proposed XPF endonuclease domain inhibitor Compound #44. Compound structures were generated using ChemAxon Marvin Sketch. Docking poses were generated using the *in silico* docking file in PyMOL v0.99.

Compound ID	Vina Score	*A. pernix*	Human XPF
SPH1-260-417	-8.8	1	
SPH1-147-013	-8.6	1	
SPH1-022-074	-8.6	1	
SPH1-345-548	-8.5	1	
SPH1-147-741	-8.4	1	1
SPH1-226-541	-8.3	1	
SPH1-361-517	-8.2	1	
SPH1-190-808	-8.2	1	
SPH1-349-340	-8.2		1
SPH1-365-118	-8.2		1
SPH1-221-020	-8.1		1
SPH1-420-478	-8		1
SPH1-457-453	-7.8		1
SPH1-016-324	-7.7		1
(#44) SPH1-218-855	-7.7		1
(#45) SPH1-080-022	-7.7		1
(#46) SPH1-071-868	-7.5		1

Table 5.2: Table of compounds selected from the XPF endonuclease domain *in silico* screen for further investigation. Showing the Compound ID, Vina Score and Screening model used for compound identification. Compounds were identified by an *in silico* screen performed against the Archaeal XPF crystal structure from *A. pernix* (PDB Code: 2BGW) (126), or a PHYRE generated model of human XPF (154).

5.3.4 Screening ERCC1-XPF inhibitors in the ERCC1-XPF, FEN1 and DNase1 assays

To determine whether the compounds were inhibitory against ERCC1-XPF and, if so, whether they also had activity in the counter screening assays, compounds in Table 5.1 and 5.2 were plated into a 96 well format. From this, the standard ERCC1-XPF assay, the pre-incubated ERCC1-XPF assay, and the DNase1 assays were screened at 100µM. If compounds showed activity, then they were followed up with a concentration series to determine the IC50 values. The FEN1 assay was then performed on selected compounds which showed favourable ERCC1-XPF activity. Results for compounds which either inhibited the *in vitro* ERCC1-XPF endonuclease assay, or were identified in the BIAcore SPR assays (see section 5.3.5) are shown in Table 5.3.

Compound ID	Binding site	Compound IC50			
		Standard ERCC1-XPF Assay	Pre-incubated ERCC1-XPF Assay	FEN1 Assay	DNase1 Assay
UOE #1	ERCC1-XPF interaction (F-C pockets)	*see note	NA	NA	NA
UOE #2	ERCC1-XPF interaction (F-C pockets)	*see note	NA	NA	NA
UOE #18	ERCC1-XPF interaction (F pocket)	158.4µM (124.3-203.5)	612.7µM (417.7-898.6)	NA	NA
UOE #26	ERCC1-XPF interaction (I-C pockets)	4.3µM (3.4-5.5)	87.7µM (63.0-122.2)	73.0µM (61.5-86.8)	70.2µM (60.4-85.3)
UOE #44	XPF endonuclease domain	NA	NA	NA	NA
UOE #45	XPF endonuclease domain	320.1µM (125.4-817.6)	150.9µM (87.1-261.4)	ND	NA
UOE #46	XPF endonuclease domain	198.1µM (167.5-234.2)	305.5µM (187.3-498.4)	ND	NA
UCN-01	ERCC1/XPA interaction domain	NA	ND	NA	NA
Emodin	Proposed endonuclease domain	6.1µM (4.3-8.6)	254.5µM (210.6-307.7)	NA	23.8µM (19.7-28.7)
ATA	Non-specific nuclease	0.8µM (0.63-1.03)	15.2µM (14.3-16.1)	0.2µM (0.15-0.28)	6.6µM (5.7-7.7)

Table 5.3: Activity of ERCC1-XPF inhibitors in the ERCC1-XPF, FEN1 or DNase1 assays. Showing the compound IC50 and 95% confidence intervals indicated in parenthesis. Assays performed as documented in Chapter 2 materials and methods. *Compounds UOE #1 and UOE #2 resulted in an apparent increased activity in the standard ERCC1-XPF assay however this was unreliable (see text). NA indicates compounds which show no activity, ND indicates compounds whose activity has not been determined. ATA denotes compound Aurintricarboxylic acid. Dose-response curves for active compounds are shown in Figure 4.12 or in Sections 10.2 to 10.5 of the Appendix.

In Figure 4.12 we observed the IC50 for ATA on the pre-incubated ERCC1-XPF to be higher than that for the standard ERCC1-XPF assay, the majority of IC50s

for other compounds were also higher in this assay. This included emodin, which we propose to directly inhibit ERCC1-XPF, which had a low (6.1μM) IC50 on the standard ERCC1-XPF, but a much greater (254.5μM) IC50 on pre-incubated ERCC1-XPF.

In the standard, but not the pre-incubated ERCC1-XPF assays, compounds UOE #1 and UOE #2 consistently resulted in an increased activity of the protein. The magnitude of this increase was unreliable and thus could not be quantified. The reason for this increase is unknown, but it is possible that these compounds are weakly fluorescent in the presence of protein.

The ERCC1-XPF interaction inhibitor compounds UOE #18 and UOE #26 showed activity in the ERCC1-XPF assays. Furthermore, compound UOE #18 was specific for ERCC1-XPF, had a 4-fold higher IC50 for the pre-incubated assay, and showed no activity on either FEN1 or DNase1. Compound UOE #26 on the other hand showed ~20-fold higher IC50 values for the pre-incubated ERCC1-XPF, FEN1 and DNase1 assays. This indicates that this compound has specificity for the standard ERCC1-XPF assay.

Although it is difficult to determine the reason for the differences in the inhibitor performances between the standard and pre-incubated ERCC1-XPF assays, it is anticipated this may be due to the protein breakdown known to have taken place in this protein. If this breakdown facilitates greater flexibility within the ERCC1-XPF protein, it might be anticipated that some drugs will have weaker binding affinities. If breakdown is the reason for the difference between the ERCC1-XPF assays, this is unfavourable for UOE #18 and UOE #26 binding. It is likely that breakdown may result in loss, or a change to the binding sites as it is already known there is an 11.3% loss in α-helical structure (see section 4.3.6).

Of the XPF endonuclease domain inhibitors, UOE #44 showed no activity for ERCC1-XPF *in vitro*. This was disappointing and in contradiction to results obtained in the BIAcore SPR assay (see next section). UOE #45 and UOE #46 on the other hand did show activity against ERCC1-XPF. However, as the IC50s were high, and non-specific binding had previously been demonstrated by BIAcore SPR analysis for these compounds, no further action was taken with these compounds.

5.3.5 Biophysical binding of ERCC1-XPF inhibitors can be demonstrated in a BIAcore SPR assay to ERCC1-XPF proteins

To directly measure whether our inhibitors biophysically interacted with ERCC1-XPF, a BIAcore SPR assay was performed. For interaction inhibitors recombinant ΔXPF was used, whereas for endonuclease inhibitors, recombinant ΔERCC1-XPF complex was used. This was because interaction inhibitors may not be able to disrupt preformed ERCC1-XPF complex on the BIAcore SPR surface. Initially all compounds were screened at a single concentration of 200μM. Compounds which showed indication of specific interaction to ERCC1-XPF were carried forward to a concentration assay. Here, a concentration series was performed from a maximum concentration of 500μM. The control compound aurintricarboxylic acid (ATA) was excluded from the concentration series at this stage as super-stoichiometric binding of 1:40 was observed and once bound, the compound did not dissociate. Two additional compounds were excluded from the screen of endonuclease domain inhibitors for similar reasons as detailed in Table 5.4.

In Table 5.4, we show the summary of results obtained from screening both the ERCC1-XPF HhH_2 interaction domain inhibitors and the XPF endonuclease domain compounds. Of the endonuclease domain compounds, most showed super-stoichiometric binding resulting in unrealistic binding kinetics. These were therefore classed as non-specific inhibitors. Of the ERCC1-XPF HhH_2 interaction domain inhibitors, compounds UOE #1, #2 and #18 were confirmed as specific inhibitors. Of the XPF endonuclease domain compounds, only compound UOE #44 was confirmed as a specific inhibitor.

Compound ID	Target site	Result	KD (M)	Rmax (RU)
(#1) SPH1-130-234	ERCC1-XPF Interaction (IC)	Hit	1.78E-05	26.66
(#2) SPH1-101-765	ERCC1-XPF Interaction (IC)	Hit	2.76E-04	48.88
(#18) SPH1-078-651	ERCC1-XPF Interaction (F)	Hit	5.37E-04	68.06
SPH1-147-741	Endonuclease domain (*A.pernix + Human)*	*Non-specific binding		
SPH1-226-541	Endonuclease domain (*A.pernix)*	Non-specific binding	1.73E+00	1.69E+05
SPH1-361-517	Endonuclease domain (*A.pernix)*	**Non-specific binding		
SPH1-190-808	Endonuclease domain (*A.pernix)*	Non-specific binding	4.61E-03	385.7
SPH1-420-478	Endonuclease domain (Human)	Non-specific binding	9.52E-03	555.1
SPH1-457-453	Endonuclease domain (Human)	Non-specific binding	1.41E+02	1.14E+07
SPH1-016-324	Endonuclease domain (Human)	Non-specific binding	3.04E-03	336.7
(#44) SPH1-218-855	Endonuclease domain (Human)	Hit	8.16E-04	42.04
Emodin	Putative endonuclease domain inhibitor	Hit	6.63E-05	19.6
ATA	Endonuclease domain	***Non-specific binding		
UCN-01	ERCC1/XPA Interaction domain	Hit	3.23E-05	76.53

*Binds to reference and active flowcell but does not dissociate

**Binds specifically to active flowcell but with nonspecific binding kinetics and does not dissociate

***Binds specifically to active flowcell but has a stoichiometry of 1:40 and does not dissociate

Table 5.4: BIAcore SPR Results. Showing kinetic parameters following single concentration and subsequent concentration series screen. Results for all ERCC1-XPF HhH_2, XPF endonuclease domain and control compounds which showed activity on the BIAcore surface are shown. Table shows the Compound ID, proposed Target site, result from BIAcore SPR assay including the KD (M) and Rmax (RU). Three compounds with unfavourable activity on the surface are indicated with asterisks and were excluded from the concentration screen.ERCC1-XPF interaction domain inhibitors bound to ΔXPF protein. XPF endonuclease domain inhibitors and control compounds bound to ΔERCC1-XPF protein.

The control compounds emodin and UCN-01 also showed specific binding to ΔERCC1-XPF protein. This was interesting as, although UCN-01 had previously been proposed to inhibit the ERCC1-XPA interaction, direct biophysical evidence had not been demonstrated. This confirms interaction with ERCC1-XPF and supports the notion of inhibiting the ERCC1-XPA interaction. The other control compound emodin was also interesting. Literature suggests that this compound inhibits ERCC1-XPF through transcriptional regulation. We show for the first time that this may instead act by directly inhibiting ERCC1-XPF. That being said, although physical interaction has been demonstrated to ΔERCC1-XPF protein indicating direct

inhibition, an additional indirect mechanism of inhibition as has previously been reported cannot be excluded (230, 231). As an additional control, we attempted to bind the ERCC1-XPF stem-loop DNA substrate to ERCC1-XPF on the BIAcore. This was unsuccessful with no evidence of binding. It is thought that this is due to ERCC1-XPF being immobilised on the BIAcore chip in a conformation unfavourable to the DNA being slotted over the complex. As proposed by our model of ERCC1-XPF in Figure 1.5, DNA binding would require significant flexibility in both the DNA structure and the ERCC1-XPF proteins.

In Figure 5.9, we show the obtained concentration series profiles for the ERCC1-XPF interaction inhibitor compound UOE #18 binding to recombinant ΔXPF protein. In Figure 5.9A, the sensogram plot shows a concentration dependent increase in response (the green line indicates the observed binding for 500μM compound and the subsequent lower lines indicate responses following two-fold drug dilutions). At steady state, the response was measured and was plotted against concentration. This is shown in Figure 5.9B. From this graph the maximum achievable response (Rmax) was projected and the KD calculated. In Figure 5.9B, the red line indicates an observed KD of 537.2μM. The Rmax was estimated to be 68.06RU indicating near-stoichiometric binding of 1:2. As UOE #18 has a Mr of 224.3 and is therefore considered almost fragment-like, near-stoichiometric binding is common for compound fragments and so UOE #18 is not excluded as a useful inhibitor solely upon this observation.

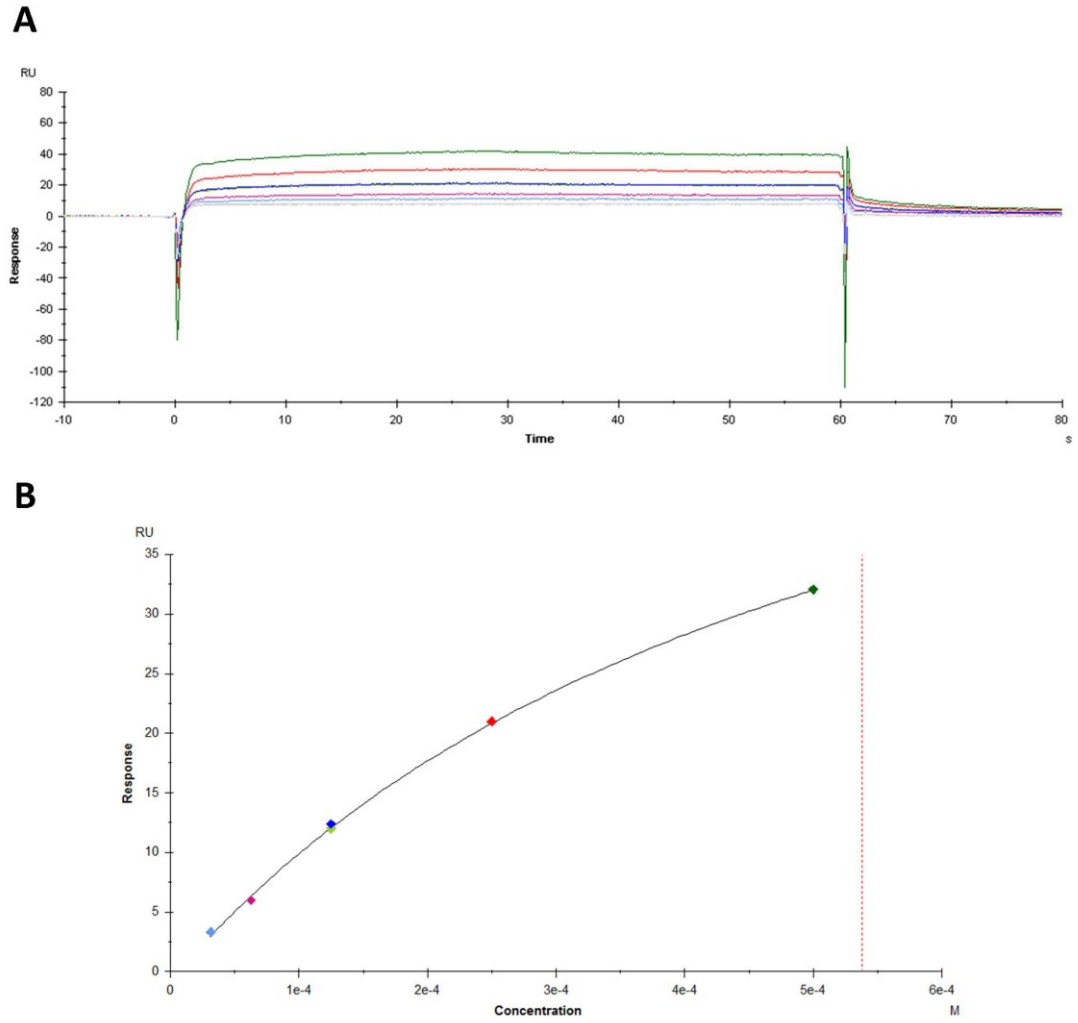

Figure 5.9: BIAcore SPR Results for UOE #18. (A) Showing the sensogram profile of increasing UOE #18 drug concentrations plotted with response (RU) versus time (seconds). (B) Showing response (RU) plotted against UOE #18 drug concentrations (M). The green line and data point represents 500µM UOE #18 and subsequent concentrations are 2-fold dilutions thereof. Determining kinetic parameters are shown in Table 5.4.

5.3.6 Binding of inhibitors to ΔERCC1-XPF results in protein stabilization

A thermal denaturation assay was utilised as an additional biophysical method to demonstrate interaction of compounds that had shown specific binding in the BIAcore SPR assay with ERCC1-XPF. This assay, although more subjective than the BIAcore SPR assay, has the advantage of proteins being in solution rather than constrained by being bound to the sensor chip. In this assay, ΔERCC1-XPF protein

was thermally denatured in the presence of the environmentally sensitive SYPRO Orange dye. SYPRO Orange is a fluorescent dye whereby its fluorescence is quenched in an aqueous solution With increasing temperature, hydrophobic regions of ERCC1-XPF become exposed allowing SYPRO Orange to bind to the protein and become unquenched thus allowing a direct readout of protein denaturation. Upon interaction of inhibitor compounds, binding could stabilize the ΔERCC1-XPF protein resulting in a positive shift in the melting temperature. Alternatively, ERCC1-XPF interaction inhibitors may be able to break apart the ERCC1-XPF heterodimers; this could destabilize the individual proteins and manifest as a decrease in melting temperature.

To validate the assay with inhibitors, we utilised UCN-01 (ERCC1/XPA inhibitor), DNA (ERCC1-XPF substrate) and UOE #18 (shows activity in all other assays) as control compounds and a positive Tm shift was observed for all. ATA was a poor control for this assay as in the BIAcore SPR assay, it bound at superstoichiometric ratios. In addition, three randomly selected compounds which do not show activity in the other assays were also selected and were inactive in this assay. We then screened compounds UOE #1, #2, #26 and #44 as these had shown activity against ΔERCC1-XPF in the endonuclease or BIAcore SPR assays. Initially all of the proposed inhibitors were screened at a single concentration of 500μM. Although higher than concentrations used for previous experiments, such as the BIAcore SPR analysis, affinity decreases with temperature (anecdotal evidence suggests that for every 10 degrees above 20°C, there is a four-fold reduced binding affinity). It was therefore imperative that, unless drug precipitation was observed, higher concentrations were used in order to maximise the possibility of observing a temperature shift. In this assay, we observed a stabilisation of the ΔERCC1-XPF complex with compounds UOE #18, #26, UCN-01 and emodin resulting in a Tm increase of +1.7°C, +2.5°C, +1.1°C and +3.2°C respectively. Results are shown in Table 5.7.

To validate the observed ΔTm of +1.7°C for compound UOE #18 at 500μM, a concentration assay was performed. In Figure 5.10A, we show the relative fluorescence units (RFU) of the SYPRO Orange dye plotted against temperature. We

show that in the absence of ΔERCC1-XPF, there is no auto-fluorescence of the compound, or of the buffer and that the dye is not affected by either. In the presence of ΔERCC1-XPF, typical thermal denaturation profiles are observed with a single transition temperature. Upon addition of UOE #18, a concentration dependent positive shift is observed. This is better visualized in Figure 5.10B where the inverse of the ΔRFU relative to the ΔT (-ΔRFU/ΔT) is plotted against temperature. These minima therefore represent the inflection point on the lines of Figure 5.10A. This represents the Tm value for each condition. As shown in Figure 5.10B, a concentration dependent increase in Tm is observed with compound UOE #18. This is graphically represented in Figure 5.11B where Tm is plotted against concentration.

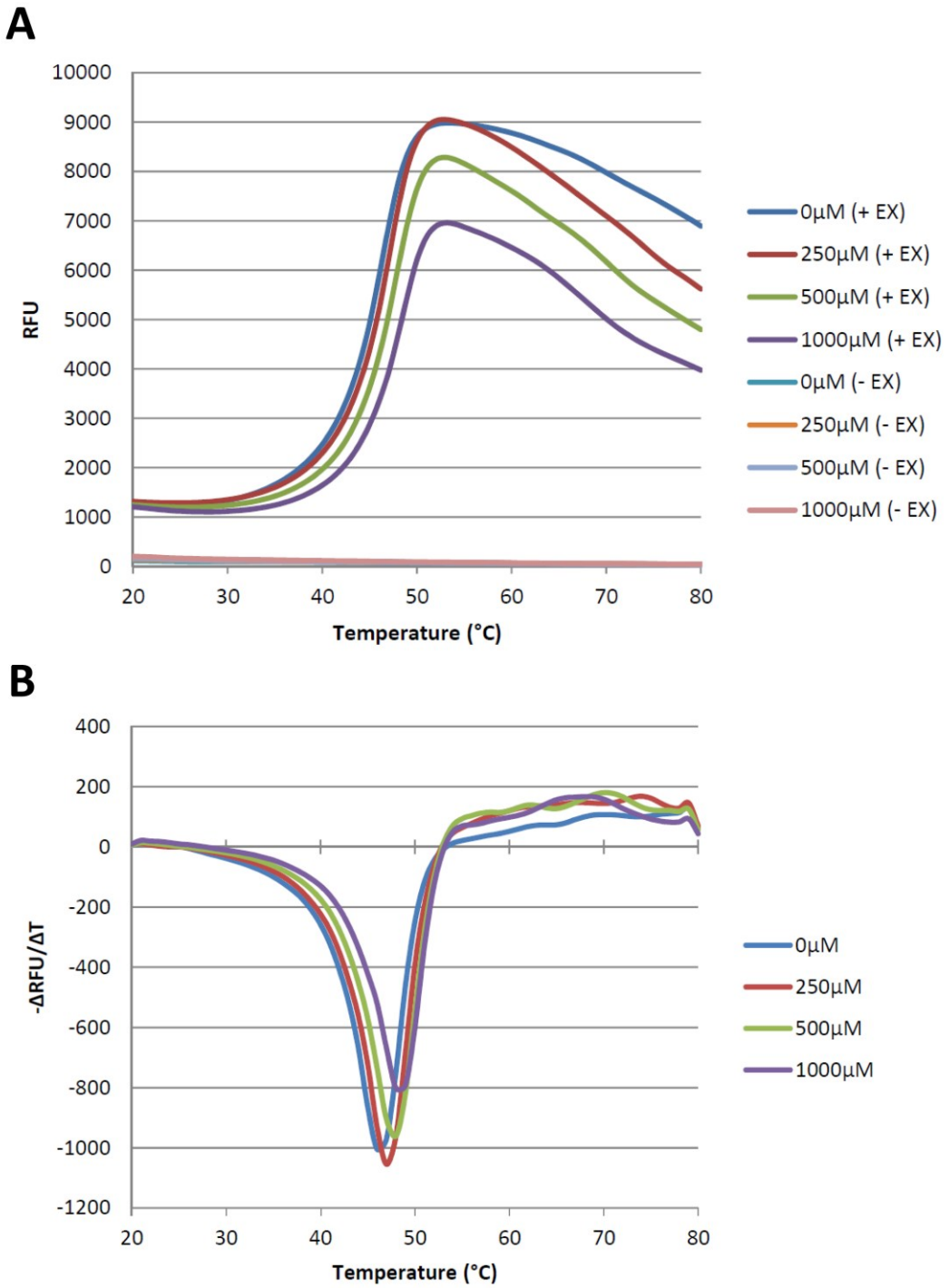

Figure 5.10: Showing thermal denaturation profiles of compound UOE #18 against the ΔERCC1-XPF protein. (A) Showing the thermal denaturation profiles of compound #18 against 5µM ΔERCC1-XPF (+ EX) including compound only controls (- EX). Assay performed from 20°C to 80°C with 30 second 1°C intervals. Data measured by relative fluorescence units of the SYPRO Orange dye. (B) Plot of –ΔRFU/ΔT versus temperature to determine the change of transition temperature (Tm) of ΔERCC1-XPF due to UOE #18.

To validate this result with a known binder to ERCC1-XPF, we decided to utilize the ERCC1-XPF stem-loop DNA substrate. In a solution based assay, as opposed to the surface of a BIAcore chip, it is anticipated that the DNA substrate would bind to ERCC1-XPF. We show in Figure 5.11A that with 5μM ΔERCC1-XPF used, we observe a concentration dependent increase in ΔTm which plateaus at around 5μM DNA. This supports interaction of DNA and ΔERCC1-XPF at a stoichiometric ratio of 1:1. In addition, this suggests that the majority of the recombinant ΔERCC1-XPF protein in the preparation is properly folded and capable of specifically binding to DNA.

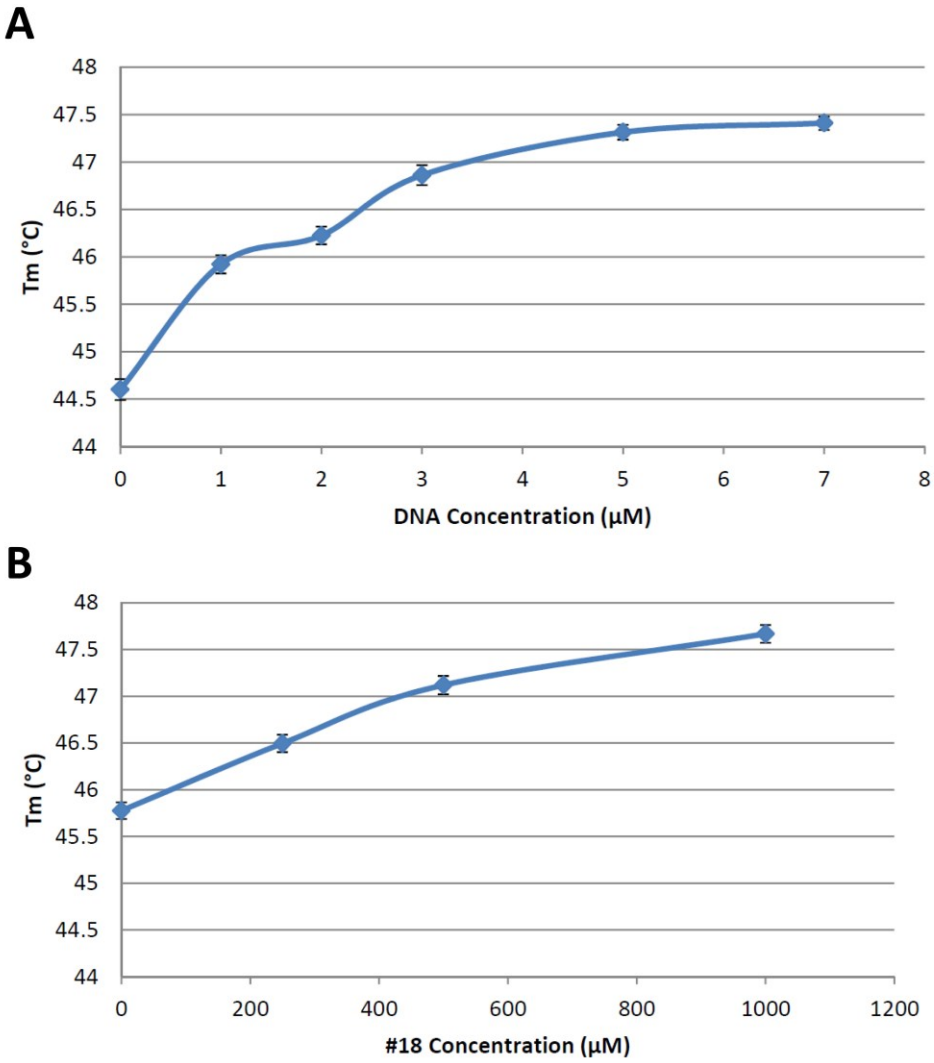

Figure 5.11: Showing the change in transition temperature (Tm) caused by DNA and compound UOE #18 in a ΔERCC1-XPF thermal denaturation assay. (A) Showing the effect of the ERCC1-XPF DNA stem-loop substrate on the stability of ΔERCC1-XPF. Protein concentration was 5µM indicating 1:1 binding of DNA to ΔERCC1-XPF protein. Values ± SEM (n=3) (B) Showing the effect of compound UOE #18 plotted with Tm versus drug concentration. Tm values derived from Figure 5.10B ± SEM (n=3).

5.3.7 Activity of ERCC1-XPF inhibitors in a cell based assay

In addition to the biophysical and biochemical techniques, we sought to validate ERCC1-XPF inhibitor compounds in a cell based assay. The reason for this was that for an ERCC1-XPF inhibitor to be used therapeutically it must show activity

in cells. In addition, as we sought to discover inhibitors of the tight ERCC1-XPF interaction, these may not be able to disrupt preformed ERCC1-XPF complex. As such, the *in vitro* endonuclease assay may not be able to identify ERCC1-XPF inhibitors that could only disrupt *de novo* ERCC1-XPF protein synthesis. The principle behind this assay was to determine whether we could recreate the hypersensitivity of cells to cisplatin using molecular inhibitors of ERCC1-XPF, analogous to the effects of genetic deletion in the Ercc1 deficient melanocytes described in section 3.3.2 Although this is an indirect measure of ERCC1-XPF inhibition, activity in this assay would be supportive of on-target activity and necessary for compounds to be progressed as potential ERCC1-XPF inhibitors.

The initial assay was an IC50 curve for each compound performed on the A375 human melanoma cell line. This allows us to gauge the toxicity of each compound and select an appropriate concentration for use in the enhancement of cisplatin sensitivity assay. While a majority of compounds had high IC50 values on their own, this is expected for an ERCC1-XPF inhibitor compound as cells deficient in ERCC1 grow equally well as ERCC1 proficient cells *in vitro* in the absence of exogenous genotoxic stress (Table 5.5 and Table 5.6).

To assess the ability of compounds to overcome cisplatin resistance, compounds were plated with human A375 melanoma cells at varying concentrations against cells treated with, and without cisplatin. Compounds were assessed against two concentrations of cisplatin, 0.3μM cisplatin and 0.6μM cisplatin. These were chosen as 0.3μM is below the cisplatin IC50 concentration, and 0.6μM was chosen to be around the IC50 value. Cells were treated for 5 days then growth was measured by the SRB assay. Obtained OD values were normalized to their respective compound, and cisplatin only controls. Enhanced toxicity was assessed by a reduced growth rate following normalization. In this assay, 60% of the compounds showed greater than 10% enhancement of cisplatin toxicity. Results obtained for the different compounds are shown in Table 5.5 and Table 5.6.

Compound ID	F	I	C	A375 IC50 (μM)	Enhancement of cisplatin sensitivity (%)
(#1) SPH1-130-234	1		1	>80	18
(#2) SPH1-101-765	1		1	37.6	34
SPH1-170-932	1		1	15.4	24
SPH1-162-759	1	1		26.4	29
SPH1-113-609	1	1		44.9	21
SPH1-018-583	1	1		29.8	51
SPH1-184-504	1	1		43.6	NA
SPH1-224-925	1	1		91.5	24
SPH1-202-698	1	1		52.1	21
SPH1-016-259		1		>100	21
SPH1-106-348		1		83	22
SPH1-139-256		1		43.1	30
SPH1-127-198		1		>100	NA
SPH1-141-032		1		>100	NA
SPH1-004-620		1		>100	NA
SPH1-029-060	1			>100	NA
SPH1-227-152	1			>100	25
(#18) SPH1-078-651	1			66	34
SPH1-113-000	1			>100	34
SPH1-054-528	1			>100	NA
SPH1-125-714	1			>100	NA
SPH1-011-687	1			>100	NA
SPH1-067-405		1	1	11.2	18
SPH1-144-543		1	1	87.7	30
SPH1-168-516		1	1	46.7	18
SPH1-015-081		1	1	>100	NA
(#26) SPH1-173-203		1	1	40.7	NA
SPH1-060-277		1	1	78.7	NA

Table 5.5: Showing activity of ERCC1-XPF interaction inhibitors in cell culture. Table shows the ERCC1-XPF inhibitors and their designed target pockets. For each compound, the IC50 in A375 cells and their enhancement of cisplatin sensitivity are shown. Dose response curves for UOE #1, UOE #2, UOE #18 and UOE #26 are shown in Section 10.1 of the Appendix.

Compound ID	*A. pernix*	Human XPF	A375 IC50 (μM)	Enhancement of cisplatin sensitivity (%)
SPH1-260-417	1		>100	NA
SPH1-147-013	1		>100	17
SPH1-022-074	1		>100	NA
SPH1-345-548	1		67	NA
SPH1-147-741	1	1	42.3	12
SPH1-226-541	1		16.5	17
SPH1-361-517	1		83.7	NA
SPH1-190-808	1		43.1	20
(#38) SPH1-349-340		1	2.3	31
SPH1-365-118		1	>100	NA
SPH1-221-020		1	16.2	33
SPH1-420-478		1	34.1	15
SPH1-457-453		1	91.4	NA
SPH1-016-324		1	64	29
(#44) SPH1-218-855		1	61.5	24
SPH1-080-022		1	15.1	26
(#46) SPH1-071-868		1	>100	NA

Table 5.6: Showing activity of XPF endonuclease domain inhibitors in cell culture. Table shows the XPF endonuclease domain inhibitors and whether they were designed against the Archaeal XPF structure or the human PHYRE XPF model. For each compound, the IC50 in A375 cells and their enhancement of cisplatin sensitivity are shown. Dose response curves for UOE #38, UOE #44 and UOE #46 are shown in Section 10.1 of the Appendix.

A more elaborate experiment was subsequently performed on compounds UOE #1, #2 and #18 to quantify their ability to shift the IC50 value of cisplatin. Here cisplatin toxicity curves were performed in the presence and absence of a fixed concentration of ERCC1-XPF inhibitors. Two concentrations of ERCC1-XPF inhibitor were chosen based upon the IC50 in cell culture and the concentration which enhanced the toxicity of cisplatin in the previous experiment. Concentrations of compounds did not exceed their IC50 values. Cell growth was assessed by SRB

staining and values were normalized to their respective compound only control values meaning the effect on the cisplatin IC50 can be directly measured. As shown in Figure 5.12, compounds UOE #1, #2 and #18 all shift the IC50 of cisplatin. The shift in IC50 was deemed to be 1.38, 1.27 and 1.26-fold respectively for these three compounds.

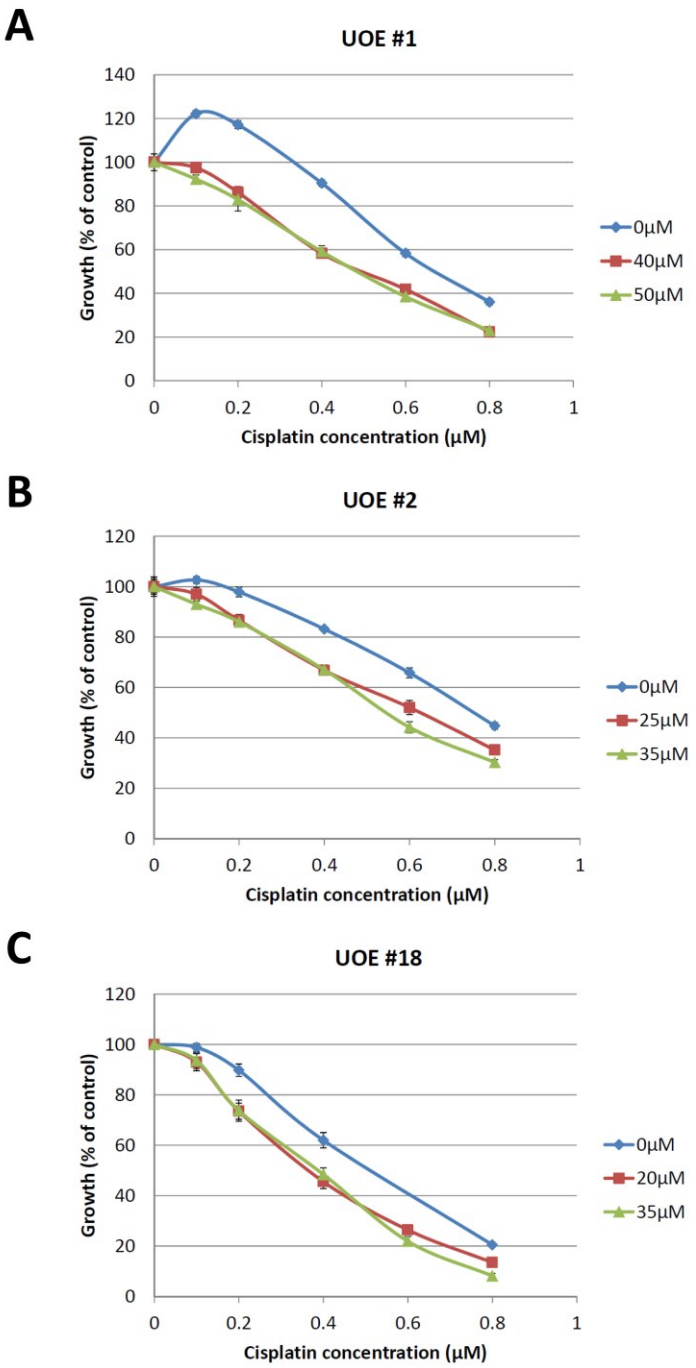

Figure 5.12: Showing activity of ERCC1-XPF HhH_2 interaction inhibitors on the A375 human melanoma cells. (A-C) Showing the ability of UOE #1, #2 and #18 to enhance the toxicity of cisplatin. Growth of A375 cells assessed following 5 day drug treatment by SRB assay. Growth values normalised to no-cisplatin treated control for each drug concentration. Data show values ± SEM. Data obtained by Ashley Whitham.

5.3.8 Summary of ERCC1-XPF inhibitors

In summary, through the *in silico* screening that was performed in collaboration with Dr Steven Shave and Professor Malcolm Walkinshaw, we have identified a number of ERCC1-XPF inhibitor compounds. In this chapter we identified UOE #1, #2, #18, #26 and #44 and demonstrate activity in a range of assays.

UOE #1 and #2 for instance both show enhancement of cisplatin sensitivity in cell culture, and show biophysical binding to ΔXPF in a BIAcore SPR assay. These compounds are not able to inhibit the *in vitro* endonuclease assay, however this is likely because interaction inhibitors spanning the interaction surface are unable to prise apart the preformed complex. We therefore present these compounds as inhibitors of *de novo* ERCC1-XPF complex formation.

UOE #26 on the other hand was designed as an ERCC1-XPF interaction inhibitor spanning the Ile264 and Cys238 pockets on XPF. With this compound, although we observed no enhanced activity with cisplatin in cell culture, or binding to XPF in the BIacore SPR analysis however interaction with the complex was demonstrated in the thermal denaturation assay. Furthermore, this compound was potent in the *in vitro* endonuclease assay and was specific for ERCC1-XPF.

UOE #18 is our favored compound from the *in silico* screening hits as activity was observed in all of the assays. In the *in vitro* endonuclease assay, a high IC50 was observed against ERCC1-XPF. In cell culture, this compound was active at a much lower concentration and showed an enhancement of cisplatin toxicity. Furthermore, physical binding was demonstrated by the BIAcore SPR assay to XPF and interaction was demonstrated to ERCC1-XPF complex in the thermal denaturation assay. We predict that the lower IC50 in cell culture may be due to the ability of this compound to inhibit *de novo* complex formation.

UOE #44 was designed by the *in silico* screening to be an inhibitor of the XPF endonuclease domain. While activity was observed in cell culture, and biophysical binding to ERCC1-XPF was demonstrated in the BIAcore SPR assay and the thermal denaturation assay, we did not observe activity in the *in vitro* endonuclease assay.

We are therefore unsure of how this compound may be acting, and if it is an ERCC1-XPF inhibitor.

Taking the results summarized in Table 5.7 into consideration, we propose UOE #1, #2 and #18 to be specific inhibitors of the ERCC1-XPF interaction domain.

Compound ID	Binding site	ERCC1-XPF assay	FEN1 assay	DNase1 assay	Biacore SPR Assay	TDA assay	Synergistic enhancement of cisplatin sensitivity	Cisplatin IC50 Shift
UOE #1	ERCC1-XPF interaction inhibitor (F-C pockets)	NA	NA	NA	KD=17.8μM Rmax=26.66RU	Precipitated protein	18%	1.38-fold
UOE #2	ERCC1-XPF interaction inhibitor (F-C pockets)	NA	NA	NA	KD=275.5μM Rmax=48.88RU	Fluorescent	34%	1.27-fold
UOE #18	ERCC1-XPF interaction inhibitor (F pocket)	158.4μM	NA	NA	KD=537.2μM Rmax=68.06RU Stoichiometry of 1:2	Tm = +1.7°C	34%	1.26-fold
UOE #26	ERCC1-XPF interaction inhibitor (I-C pockets)	4.3μM	73.0μM	70.2μM	NA	Tm = +2.5°C	NA	ND
UOE #44	XPF endonuclease domain inhibitor (Human XPF)	NA	NA	NA	KD=815.9μM Rmax=42.04RU	NA	24%	ND
UCN-01	ERCC1/XPA interaction domain inhibitor	NA	NA	NA	KD=32.3μM Rmax=76.53RU Stoichiometry of 1:2	Tm = +1.1°C	37%	ND
Emodin	Proposed XPF endonuclease domain inhibitor	6.1μM	NA	23.8μM	KD=66.3μM Rmax=19.60RU	Tm = +3.2°C	NA	ND
ATA	Non-specific nuclease inhibitor	0.8μM	0.2μM	6.6μM	Excluded*	Precipitated protein	ND	ND

Table 5.7: Summary of results attained for proposed ERCC1-XPF inhibitor compounds. Table shows the proposed binding site of inhibitors, activity on A375 cells when combined with cisplatin, their activity in a BIAcore SPR assay and activity in a thermal denaturation assay. *Aurintricarboxylic acid (ATA) was excluded as it bound with 1:40 stoichiometry and did not disasociate, see section 5.3.5.

5.4 Discussion

In this chapter, we aimed to identify inhibitors of the ERCC1-XPF DNA repair endonuclease. Here, we utilised a rational *in silico* based screening approach and sought to identify inhibitors of the ERCC1-XPF HhH_2 interaction domain, and the XPF endonuclease domain.

In a review of the protein-protein and protein-DNA interactions, three principal target sites were identified. The first of these was the interaction between ERCC1 and XPA. This interaction is known to be required to recruit the ERCC1-XPF complex to sites of DNA damage to allow the incision step of the NER DNA repair pathway to proceed (112). Should this interaction be blocked, NER would be inhibited. Furthermore, previous work in this area has led to the development of a peptide inhibitor of this region and the drug UCN-01 being proposed as a non-specific inhibitor of this site (123, 228). In addition, Barakat *et al.* have already performed an *in silico* screen targeting this region (123). A patent protecting the ERCC1/XPA crystal structure has also been filed (238). In order to overcome cisplatin resistance however, this interaction is not required for all forms of cisplatin induced DNA damage. It is for these reasons that we chose not to pursue this interaction further.

The second interaction that we identified was the ERCC1 HhH_2 domain. This interaction has the advantage over the ERCC1-XPA interaction in that it is required for repair of all forms of cisplatin DNA damage. It is therefore anticipated that if this region could be inhibited, the obligate interaction required for protein stability would be disrupted destabilising both ERCC1 and XPF.

In the protein-protein interaction domain, we identified two amino acids which lock into the reciprocal partner protein: ERCC1 Phe293 and XPF Phe905. It has previously been shown that the ERCC1 Phe293 is required for interaction between ERCC1 and XPF and deletion of this residue abrogates interaction (93, 109). Based upon a crystal structure of this region, this residue is situated in a deep $280Å^2$ pocket on the XPF surface (106). The analogous XPF Phe905 residue on the other hand has not been demonstrated to be essential for interaction and the pocket on ERCC1 is only $220Å^2$ (234). This pocket is also less structurally defined and therefore less

tractable to *in silico* screening. We therefore favoured an *in silico* screen for compounds targeting the pocket on XPF occupied by the ERCC1 Phe293.

In addition to the XPF Phe293 pocket for *in silico* based drug design, it was important to select additional pockets on the XPF surface. This would not only increase the binding affinity of compounds to the target protein, but could also engineer specificity into the small molecule. For these reasons, the additional Ile264 and Cys238 pockets were identified.

As our knowledge of the ERCC1-XPF complex comes from a variety of species, we wanted to understand the molecular similarity. In addition, it is planned that we would perform xenograft experiments should a high potency lead compound be discovered. These would either be performed in mice or in zebrafish. Although unconventional, xenografting in zebrafish is an emerging tool as has the advantage of being rapid and higher throughput than mouse models, and also requires less compound. Understanding the species differences between the HhH_2 domains was therefore necessary to influence our choice in cell culture and xenograft models.

Interestingly, the crystal structures and our PHYRE^2 generated models revealed that there are substantial differences between the HhH_2 domains, particularly between human and *A. pernix* (106, 126, 154). Although they both adopt an HhH_2 fold motif, the surfaces of the domains are considerably different. This is likely due to *A. pernix* forming XPF homodimers and thus the surfaces must be different to facilitate this. The HhH_2 domains between the eukaryotic species are more similar, but still with notable differences. Interestingly, the zebrafish structure is more similar to human than mouse as mouse XPF has an enlarged bridge between the Phe293 and Ile264 pockets. It is therefore important that for *in vivo* and cell culture models that the appropriate species are chosen. Importantly, for interaction inhibitors which span multiple binding sites, mouse models must be used with caution.

As the protein-protein interaction surface in the ERCC1-XPF complex is large and predominantly hydrophobic, identification of small molecules able to inhibit this region will be formidable task. Furthermore, the binding affinity of ERCC1 for XPF interaction has not previously been published. We therefore used BIAcore SPR

analysis and demonstrated the KD of this interaction to be 4.6nM, confirming the expected strong interaction. On the other hand, mutational studies of ERCC1 Phe293 have shown that deletion of this residue is sufficient to abrogate interaction of the two proteins (93, 109). We therefore predict that inhibitors of the Phe293 binding pocket on XPF may be sufficient to inhibit complex formation, or at the very least, disrupt key DNA interactions made by the HhH_2 domains.

The third interaction that we identified was the XPF endonuclease domain. Like the ERCC1-XPF interaction domain, this is also required for the repair of all forms of cisplatin induced DNA damage. This target is more straightforward compared to the previous target however it does have its own challenges. One challenge faced with this region is that no crystal structure is published. Instead, a PHYRE model was utilised in addition to the crystal structure for the nuclease domain of *A. pernix.* In this region, there is a high degree of conservation and key active site residues are conserved. Therefore the PHYRE model was assessed to be suitable for *in silico* screening. An additional challenge faced by the drug discovery programme on this region is designing specificity into compounds as the mechanism of action is expected to be similar to other nucleases.

In order to discover inhibitors of our chosen target domains, we decided to use an *in silico* screening approach. This was chosen as we had already identified specific target domains on our protein. The benefit of *in silico* screening means that compounds purchased for follow up validation already have predicted affinity for the target, thus higher hit rates compared to the high throughput approach are expected. Furthermore, due to the tight ERCC1-XPF interaction, inhibitors of this region may not be able to disrupt preformed ERCC1-XPF complex. As such, a high throughput screening approach based around an *in vitro* endonuclease assay may not be able to identify ERCC1-XPF inhibitors that could only disrupt *de novo* ERCC1-XPF protein synthesis.

Following the *in silico* screen, we purchased a number of the proposed compounds for follow up validation. We show in Table 5.7 a summary of the results obtained for active compounds. We propose compounds UOE #1, #2, #18 and #26 to inhibit the interaction domain of ERCC1-XPF and UOE #44 to inhibit the

endonuclease domain of XPF. Furthermore, we show direct biophysical evidence that the control compounds UCN-01, Emodin and ATA bind to ERCC1-XPF.

In the *in silico* screen only 3 compounds were proposed to bind to both the Phe293 and Cys238 binding pockets on XPF. Interestingly, two of the three compounds, UOE #1 and #2, were discovered to have activity. As shown in Table 5.7, both of these compounds enhance the toxicity of cisplatin with a 1.38-fold and 1.27-fold shift in the IC50 of cisplatin, respectively. Furthermore, these compounds both bind to XPF in the BIAcore SPR assay with KD of 17.8μM and 275.5μM respectively. In the thermal denaturation assay there was immediate protein precipitation with UOE #1. This may be explained by UOE #1 disrupting complex stability thus resulting in protein precipitation, or alternatively by non-specific binding to ΔERCC1-XPF as is believed to be the case for the non-specific inhibitor ATA. UOE #2 was fluorescent and prevented thermal denaturation measurements. In the *in vitro* endonuclease assay, neither of these compounds showed inhibition of ΔERCC1-XPF however this might be expected as they are proposed to inhibit the Phe293 and Cys238 pockets on XPF which would be inaccessible with ERCC1 bound. These compounds may be more suited to inhibiting *de novo* ERCC1-XPF complex formation.

Through the *in silico* screen, we also identified one compound which inhibits the Phe293 pocket. As summarised in Table 5.7 we show that UOE #18 is also able to enhance the toxicity of cisplatin in cell culture and results in a 1.26-fold shift in the IC50 of cisplatin. This showed binding to XPF in the BIAcore SPR assay with a KD of 537.2μM. In confirmation of this, we show that in thermal denaturation, we observe a concentration dependent increase in the Tm. This indicated UOE #18 binds to ERCC1-XPF and increases complex stability. Although this is an interaction inhibitor, this could be explained by UOE #18 dislodging the ERCC1 Phe293 from the XPF pocket and inhibiting ERCC1-XPF activity without breaking the heterodimer apart. Furthermore, this could explain why a high IC50 is observed in the *in vitro* endonuclease assay. Activity against *de novo* ERCC1-XPF complex formation is therefore expected to be greater than *in vitro*.

In Table 5.7, we show compound UOE #26 is an interaction domain inhibitor binding to the Ile264 and Cys238 pockets on XPF. While this compound showed no

binding to XPF in the BIAcore assay, we observed a positive Tm shift in the thermal denaturation experiment with this compound and showed that it also displayed specific activity against ERCC1-XPF in an *in vitro* endonuclease assay. Furthermore no activity was observed in cell culture with this compound. The lack of activity in the BIAcore SPR assay could be for various reasons. One of these is that XPF was immobilised and the protein was cross-linked to the chip. It is possible that immobilisation may be in an unfavourable conformation for inhibitors which bind to the Ile264 pocket on XPF.

Of the compounds purchased for follow up validation from the endonuclease screen, only one, UOE #44, showed specific binding to ERCC1-XPF in the BIAcore SPR assay. Interestingly 7 of the 17 endonuclease domain inhibitor compounds showed non-specific binding kinetics to ERCC1-XPF in the BIAcore SPR assay. In cell culture, UOE #44 also showed enhanced toxicity of cisplatin however no change in Tm was observed in the thermal denaturation assay. In addition, no activity was observed in the *in vitro* endonuclease assay as would be expected for this compound. Based upon this data, it is inconclusive whether UOE #44 is an ERCC1-XPF inhibitor.

6 Chapter 6: Iterative screening for ERCC1-XPF inhibitors of greater potency

6.1 Aim of chapter

Following successful identification of ERCC1-XPF inhibitors in Chapter 5, we sought to identify additional ERCC1-XPF inhibitors which were of greater potency. This chapter is based around an ERCC1-XPF drug development project in collaboration with Professor Malcolm Walkinshaw from the University of Edinburgh and Dr Barbara Saxty from MRC Technology, London. Herein we present inhibitors discovered through an additional *in silico* screen and a high-throughput ERCC1-XPF inhibitor screen.

6.2 Introduction

6.2.1 Crystal structures of ERCC1-XPF

The ERCC1-XPF complex in its entirety has not yet been crystallised. Currently crystal structures only exist for the ERCC1 central domain and the ERCC1-XPF HhH_2 domains as summarised in Table 6.1 (106). During overexpression of the truncated ΔERCC1-XPF protein analogous to our protein, Tsodikov *et al.* noticed a protein fragment spanning the ERCC1 central domain was produced by proteolytic degradation (106). Upon size exclusion chromatography, this fragment eluted separately (106). Tsodikov *et al.* crystallised this ERCC1 fragment which consisted of ERCC1 residues 96-214 (106). They propose that the ERCC1 linker ($ERCC1_{215\text{-}219}$) is unstructured and flexible to allow the ERCC1 central domain and HhH_2 domain to adopt different orientations (106). Consequently, this results in the linker region being exposed and proteolytically sensitive (106). The ERCC1 central domain crystals grew in 3-5 days in a hanging drop format (using 1:1 protein:reservoir solution) (106). Crystallisation of the ERCC1-XPF HhH_2 domains was also performed using co-expressed $\Delta ERCC1_{220\text{-}297}$ and $\Delta XPF_{848\text{-}916}$ proteins (106). The ERCC1-XPF HhH_2 crystals grew in 5-10 days in the same hanging drop format (106).

Although not human ERCC1-XPF, the crystal structure of the XPF homodimer from *Aeropyrum pernix* gives valuable insight into the structure of the human XPF

endonuclease domain and shows how the domains might associate in the human complex (126). To generate crystals of ApeXPF, Newman *et al.* used a truncated protein consisting of residues ApeXPF$_{19-231}$ (full length protein is 248 amino acids) (126). In addition, Newman *et al.* crystallised the ApeXPF complex with a 15 mer DNA duplex (126). These crystals were generated using a protocol developed by Lally *et al.* and crystals grew in a sitting drop format appearing after 6-10 weeks (126, 239).

PDB Code	Structure method	Description	Ref
2A1I	X-Ray Diffraction with resolution of 1.90 Å	Crystal Structure of the Central Domain of Human ERCC1	(106)
2A1J	X-Ray Diffraction with resolution of 2.70 Å	Crystal Structure of the Complex between the C-Terminal Domains of Human XPF and ERCC1	(106)
2BHN	X-Ray Diffraction with resolution of 3.20 Å	XPF from Aeropyrum pernix	(126)
2BHN	X-Ray Diffraction with resolution of 2.80 Å	XPF from Aeropyrum pernix, complex with DNA	(126)
2JNW	Solution NMR	Solution structure of a ERCC1-XPA heterodimer	(112)
2KN7	Solution NMR	Structure of the XPF-single strand DNA complex	(111)

Table 6.1: Summary of structures available for the ERCC1 and XPF proteins in the protein data bank (PDB). Solution structures which duplicate a crystal structure have been excluded.

6.3 Results

6.3.1 Structure activity relationship for compound UOE #18

In Chapter 5, we showed that compound UOE #18 shows specific inhibition of recombinant ΔERCC1-XPF in an *in vitro* endonuclease assay, showed specific binding to ΔERCC1-XPF in a BIAcore SPR assay, stabilised ΔERCC1-XPF in a

thermal denaturation assay and enhanced the toxicity of cisplatin in a cell culture assay. We therefore sought to investigate whether analogues of this compound would show greater potency *in vitro* and whether structural modifications of UOE #18 would disrupt activity.

Based upon the predicted *in silico* binding pose of UOE #18 into the Phe293 binding pocket on XPF shown in Figure 6.1A, we predicted that the naphthalene ring is critical for binding into the pocket. Attached to the naphthalene ring is a pyrazolone ring substituted with a methyl group which is also likely to confer specificity to this inhibitor. We therefore purchased commercially available analogues of UOE #18 which contained modifications to these groups.

Following purchase, we tested *in vitro* activity in the ΔERCC1-XPF, FEN1 and DNase1 assays. We show in Figure 6.1 that derivative UOE #18_6 has been modified with a naphthalene ring substituted for a benzene ring. Based upon the *in silico* docking pose of UOE #18, a modification of this nature would abolish binding. A PubChem search of this compound showed it had previously been demonstrated to be active in 27 of the 920 screens. Unconfirmed or undefined activity was reported in a further 77 of the screens. In the *in vitro* endonuclease activity, UOE #18_6 confirmed our prediction and showed no activity against ERCC1-XPF.

Compound UOE #18_7 was selected as this showed activity in a range of other screens in the PubChem search similar to UOE #18_6. This was documented to be active in 13 of the 573 screens tested and was unconfirmed or undefined in a further 19 screens. This compound differed from UOE #18 in that it had an additional functional group off the pyrazole ring. We predicted that the additional functional group may be responsible for the non-specific activity in the PubChem screens. In our assays, this compound was fluorescent, which may account for the compound scoring as a false positive in many of the published screens, and so we were unable to determine whether it had any inhibitory activity.

Compound UOE #18_8 was purchased to investigate the effect of rotating the pyrazolone ring. In addition to the ring rotation, the carbonyl group on this molecule had been replaced by a hydroxyl group and the methyl group had been used to link this to the naphthalene ring. In a PubChem search no published screens using this

compound had been identified. When tested in the *in vitro* endonuclease assays, although an increased potency against ΔERCC1-XPF was observed, this compound also showed activity against FEN1 indicating a loss in specificity. This is therefore deemed an unfavourable modification.

Compounds UOE #18_9 and UOE #18_10 were both purchased as the pyrazolone ring was attached to the naphthalene ring from a different position to that of UOE #18. In addition, both of these compounds contain additional functional groups. No specificity data were found in a PubChem search for either of these compounds. It was unknown whether the change in the compound backbone or whether the additional side chains would be advantageous to binding. In the *in vitro* endonuclease assays, no additional increase in potency against ΔERCC1-XPF was observed with #18_9 however a decreased IC50 from 158.4μM to 59.6μM was observed with UOE #18_10. Furthermore, both compounds retained specificity against FEN1 and DNase1.

Compound UOE #18_11 was purchased in order to test whether a modification to the naphthalene ring would be tolerable. Based upon the naphthalene ring binding into the hydrophobic Phe293 pocket on XPF, it might be expected that the hydrophilic hydroxyl group would be incompatible with binding. A nitrogen atom was also inserted into this ring. As expected in the endonuclease assay, no activity was observed against ΔERCC1-XPF however interestingly, activity was observed against DNase1 with an IC50 of 491μM.

A

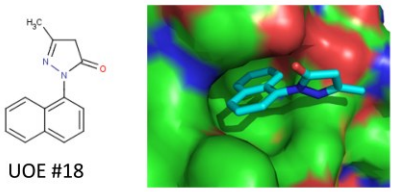

UOE #18

B

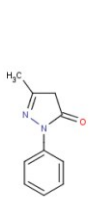

UOE #18_6

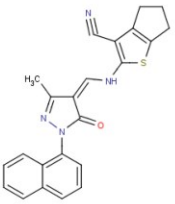

UOE #18_7

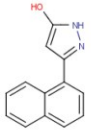

UOE #18_8

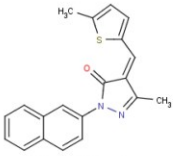

UOE #18_9

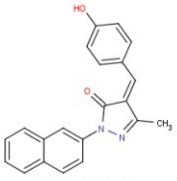

UOE #18_10

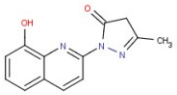

UOE #18_11

C

Compound	ERCC1-XPF Assay	FEN1 Assay	DNase1 Assay
UOE #18	158.4μM (124.3-203.5)	NA	NA
UOE #18_6	NA	NA	NA
UOE #18_7	Fluorescent	Fluorescent	Fluorescent
UOE #18_8	111.9μM (85.0-147.4)	92.2μM (72.9-116.7)	NA
UOE #18_9	157.5μM (114.2-217.3)	NA	NA
UOE #18_10	59.6μM (44.5-79.7)	NA	NA
UOE #18_11	NA	NA	491μM (248.6-691.7)

Figure 6.1: Structure activity relationship between UOE #18 and its compound derivatives. (A) Showing the structure and docking pose of UOE #18 which is predicted to inhibit the ERCC1 Phe293 pocket on XPF. (B) Structures of compound UOE #18 derivatives. (C) Activity of compound UOE #18 and its derivatives in the standard ΔERCC1-XPF, FEN1 and DNase1 assays. Showing the compound IC50 and 95% confidence interval indicated in parenthesis. The standard ERCC1-XPF assay was performed as documented in Chapter 2 materials and methods. The FEN1 and DNase1 assays were performed by Vera Lúcia Freitas Rodrigues as documented in Chapter 2 materials and methods.

6.3.2 Second *in silico* screen for ERCC1-XPF inhibitors

In order to discover new compounds with an increased potency, a second high throughput screen was performed by Dr Doug Houston and Professor Malcolm Walkinshaw from the University of Edinburgh. This screen principally differed from the previous *in silico* screen in two ways: firstly a more sophisticated docking protocol was utilized (discussed in Chapter 2 materials and methods), and secondly the ERCC1 protein surface in the ERCC1-XPF interaction domain was also targeted.

From the compounds identified through *in silico* screening, 100 from each of the target sites were purchased for validation in the ΔERCC1-XPF, FEN1 and DNase1 assays. Of these, 5 compounds (1C3, 1D6, 1F7, 2C5, 2E11) showed activity in the endonuclease assay as shown in Table 6.2. An additional three compounds were detected from an analogous screen by Dr Preeti Bakrania and Dr Barbara Saxty from MRC Technology, but these either did not confirm, or had a high IC50 meaning no further development was appropriate. In comparison to the previous *in silico* screen, the hit rate is similar. In the first screen as documented in Chapter 5, one compound out of 58 was observed to have an IC50 less than 50μM indicating a hit rate of 1.7%. In this second *in silico* screen, 5 compounds had an IC50 less than 50μM, also indicating a hit rate of 1.7%. Furthermore, as 4 of these compounds were XPF endonuclease domain inhibitors, the hit rate for this screen was much greater (4%: 4/100 compounds).

Additional *in silico* screening was performed around the 5 *in silico* hit compounds by Dr Doug Houston and Professor Malcolm Walkinshaw. Here they generated site points for the 5 hit compounds binding to ERCC1-XPF and screened the Edinburgh University Ligand Selection System (EDULISS) database for new compounds sharing similar molecular properties. The 6 compounds from each screen with the greatest theoretical binding affinity were purchased for screening and we identified two additional hits, UOE #2C5_2 and UOE #2E11_1. Unfortunately however, when repurchased from a different source compounds 1F7 and 2E11 failed to show activity. These were subsequently dropped from further investigation.

Compound ID	Target site	ERCC1-XPF Assay (µM)	FEN1 Assay (µM)	DNase1 Assay (µM)
1C3	XPF Endonuclease domain	35.4 (28.6-43.8)	NA	NA
1D6	ERCC1-XPF interaction (XPF surface)	14.9 (11.0-20.2)	NA	NA
1F7*	XPF Endonuclease domain	9.2 (6.5-13.0)	NA	NA
2C5	XPF Endonuclease domain	18.3 (14.1-26.0)	NA	NA
2C5_2	XPF Endonuclease domain	24.2 (19.0-30.9)	272.7 (179-392)	72.2 (43.8-119)
2E11*	XPF Endonuclease domain	48.8 (36.4-65.4)	NA	NA
2E11_1	XPF Endonuclease domain	62.3 (42.9-83.6)	NA	218 (133-356)

Table 6.2: Activity of ERCC1-XPF inhibitors discovered by the second *in silico* screen. Compounds screened in the standard ERCC1-XPF assay, FEN1 assay and DNase1 assay as documented in Chapter 2 materials and methods. Showing the compound IC50 and the 95% confidence intervals indicated in parentheses. NA indicates compounds which showed no activity. *Repurchased compounds failed to show activity.

6.3.3 High throughput screen and validation of ERCC1-XPF inhibitors

In addition to the second *in silico* screen a high throughput compound screen was performed by Dr Preeti Bakrania and Dr Barbara Saxty from MRC Technology. This was performed using the standard ΔERCC1-XPF assay in 384 well format with 100nM substrate and 100nM ΔERCC1-XPF in 20µl reaction volumes. The protein used was supplied by Dr Martin Wear from the University of Edinburgh in weekly batches to negate issues surrounding protein breakdown which occurs between 1-2 weeks post purification.

The MRC Technology compound library consisting of 101,440 compounds was screened at 20µM. From this, 384 compounds were identified by a 3x SD cut-off and compounds displaying <70% residual activity. In follow up assays, 87

compounds repeated signifying a 23% hit conformation rate. Of these 49 had an IC50 value <200μM and these were further reduced to 30 compounds following structural triage to remove frequent hitters and unfavorable structural motifs. Finally the IC50 was confirmed for 24 of these compounds. In the DNase1 counter screen, only 1 compound showed activity. A summary of compounds discovered through the *in silico* screening and the high throughput screen are shown in Table 6.3.

In Table 6.3, hit compounds from both *in silico* and high throughput screens were clustered by Dr Tim Chapman from MRC Technology into groups of structural similarity. It is expected that compounds in each groupings will have similar mechanisms of action. One cluster of note is cluster 2 as compound MRCT_9 was observed to have a similar structure to a previously published FEN1 inhibitor which utilized metal ion chelation of the FEN1 active site. A second compound MRCT_9 MOD was identified by Dr Tim Chapman. This is also shown in Table 6.3.

A selection of the compounds from Table 6.3 was then purchased for follow up validation. Techniques documented in Chapter 5 were employed to characterize potential ERCC1-XPF inhibitors. For each of the compounds, we gained FEN1 IC50 data, thermal denaturation data, PubChem search data and BIAcore SPR data for binding to the ΔERCC1-XPF complex in collaboration with Dr Martin Wear. Compounds which showed favourable activity in these assays were also subjected to cell culture assays. Results for these compounds are documented in Table 6.3.

(A) ID	(B) Cluster	(C) ERCC1 DNase1 FEN1 IC50 (μM)	(D) Cell CDDP IC50	(E) TDA Tm Shift (°C)	(F) BIAcore SPR Assay KD	(G) Pub Chem
MRCT_16	1	48.36 NA NA	2.1 @4μM	+3.1	390μM n~1:4	n=7 A=0
MRCT_9	2	1.71 NA 68.9	1.2 @3μM	+1.3	NA	n=75 A=14
MRCT_9 MOD	2	94.13 148.2 115.0	1.4 @3μM	+1.7	ND	n=82 A=16
MRCT_1	3	21.82 NA NA	NA	+2.0	10μM n~1:0.2	n=0 A=0
MRCT_19	3	28.08 NA NA	1.4 @1μM	+2.4	NA	n=0 A=0
MRCT_20	3	21.45 NA NA	2.1 @3μM	+2.0	160μM n~1:3/4	No Record
UOE2C5_2	3	24.2 72.2 272.7	2.8 @3μM	+3.4	NA	n=0 A=0
MRCT_13	4	4.27 NA ND	ND	ND	500μM n~1:4/5	n=0 A=0
MRCT_15	4	14.03 NA ND	ND	ND	NA	n=196 A=20 U=14
MRCT_18	4	33.05 NA NA	NA	+1.2	NA	No Record
MRCT_25	4	26.68 NA NA	NA	NA	NA	n=0 A=0
MRCT_22	5	63.95 NA ND	ND	ND	NA	n=0 A=0
UOE2C5	5	18.26 NA NA	NA	+3.0	650μM n~1:5	n=0 A=0
UOE2E11_1	5	62.3 218 NA	1.9 @2.5μM	+1.0	NA	n=0 A=0
MRCT_14	6	23.58 83 ND	ND	ND	NA	n=1 A=0
UOE1D6	6	14.92 NA NA	1.1 @40μM	NA	200μM n~1:3	No Record
MRCT_8	7	57.72 NA NA	1.3 @15μM	NA	NA	n=0 A=0
MRCT_29	7	70.54 NA NA	1.3 @50μM	+1.0	NA	n=0 A=0
UOE1C3	8	35.37 NA NA	1.3 @1.5μM	+3.0	NA	n=0 A=0
MRCT_7	9	60.77 NA ND	ND	ND	NA	n=348 A=23 U=14
MRCT_5	10	8.98 NA NA	NA	+1.7	50-150μM	n=0 A=0
MRCT_10	10	160.9 NA	ND	ND	NA	n=7 A=0

(A) ID	(B) Cluster	(C) ERCC1 DNase1 FEN1 IC50 (μM)	(D) Cell CDDP IC50	(E) TDA Tm Shift (°C)	(F) BIAcore SPR Assay KD	(G) Pub Chem
		ND				
MRCT_21	10	27.89 NA NA	NA	+2.0	50-150μM	n=0 A=0
MRCT_6	11	14.37 NA ND	ND	ND	NA	n=6 A=0
MRCT_24	11	97.14 NA ND	ND	ND	NA	n=0 A=0
MRCT_26	11	112.11 NA ND	ND	ND	NA	n=0 A=0
MRCT_27	11	124.69 NA ND	ND	ND	NA	n=0 A=0
MRCT_28	11	259.17 NA ND	ND	ND	NA	n=0 A=0
MRCT_30	11	153.85 NA ND	ND	ND	NA	n=1 A=0
UOE18	11	158.4 NA NA	1.7 @45μM	+1.7	103μM N~1:2	n=7 A=0
UOE18_6		NA NA NA	ND	ND	ND	n=920 A=27 U=77
UOE18_7		FLU FLU FLU	ND	ND	ND	n=573 A=13 U=19
UOE18_8		111.9 NA 92.2	ND	+0.6	ND	n=0 A=0
UOE18_9		157.5 NA NA	ND	+1.4	ND	n=0 A=0
UOE18_10		59.6 NA NA	ND	+3.7	ND	No record
UOE18_11		NA 491 NA	ND	ND	ND	n=1 A=0
MRCT_17	12	326.25 NA ND	ND	ND	NA	n=0 A=0
ATA	Control compound	0.81 6.60 0.199	ND	Protein precipitation before run @500μM	Binds irreversibly to chip n~1:40	n=352 A=102

Table 6.3: Results table of ERCC1-XPF inhibitor compounds. (A) Showing the working ID for each compound. (B) Showing the compound cluster. Compound clustering performed by Dr Tim Chapman from MRC Technology, London. (C) IC50 data generated from the standard ΔERCC1-XPF, DNase1 and FEN1 assays. Assays were performed either by Dr Preeti Bakrania and Dr Barbara Saxty from MRC Technology, or Ewan McNeil. FEN1 assays were performed by Ewan McNeil. NA denotes non-activity, ND denotes not determined, FLU denotes a fluorescent compound. (D) Enhancement of sensitivity to cisplatin in A375 human melanoma cells. The control IC50 for cisplatin (CDDP) is 570nM.

The IC50 for CDDP in the presence of the different inhibitors was determined. Values given are for the fold enhancement of sensitivity to CDDP, calculated from the ratio of control/treated IC50s, in the presence of the stated inhibitor concentration. Cell culture assays were performed by Ann-Marie Ritchie. (E) Showing the change in thermal stability of ΔERCC1-XPF protein in the presence of each compound. Assay performed using 5μM ΔERCC1-XPF and 500μM compound. A positive Tm shift of 0.5°C or greater indicates an increase in protein stability. (F) BIAcore SPR analysis of compounds binding to ΔERCC1-XPF protein. A single concentration screen was performed then a concentration series screen was performed on those which displayed specific binding. BIAcore SPR assay performed in collaboration with Martin Wear from the University of Edinburgh. (G) PubChem database search showing activity in previously published assays. N denotes the number of screens published using each compound, A denotes the number of screens the compound was active in, and U denotes screens whereby activity was inconclusive or an IC50 was not determined.

6.3.4 Crystallisation trials of ΔERCC1-XPF

In order to determine the mechanism of compounds binding to ERCC1-XPF and direct compound development, it is favourable to generate protein crystals in the presence of the inhibitors. We therefore started crystallisation trials on the ΔERCC1-XPF protein in collaboration with Dr Jacqueline Dornan and Professor Malcolm Walkinshaw. For these trials, we opted to use the truncated ΔERCC1-XPF protein shown in Figure 6.2 by the red bars. This was chosen for several reasons, firstly inhibition and biophysical binding of compounds to this protein had already been demonstrated. Secondly this protein could be expressed in significant quantities which would be necessary for crystallisation trials, and finally it contained the XPF endonuclease and ERCC1-XPF interaction domains which were being targeted in our screening attempts. Of note, no crystals have been published for the XPF endonuclease domain and therefore crystals would be greatly beneficial to the drug screening project.

Before attempts to crystallise the complex with inhibitors, we first sought to crystallise the ΔERCC1-XPF complex on its own. To perform this, a number of conditions surrounding previously published ERCC1-XPF crystallisation conditions were set up as per Chapter 2 materials and methods (106). In addition crystallisation

screens were setup at 5°C and 19°C using protein within 4 days of purification as breakdown is known to occur at 1-2 weeks at 5°C, and quicker at higher temperatures. Initial attempts were unsuccessful; therefore, a batch of ΔERCC1-XPF was prepared by Dr Martin Wear whereby the His-tags had been cleaved off by a thrombin digestion and subsequent purification. This crystallisation attempt was also unsuccessful. Although some of the wells showed crystals forming, upon X-Ray diffraction a characteristic salt profile was observed and was thought to be due to metal ions in the crystallisation solution forming phosphate crystals with the PBS 5% glycerol protein buffer.

The reason for failure of crystals to form is likely due to the instability of the ΔERCC1-XPF protein. That being said, published crystals of the ERCC1-XPF HhH_2 domains were generated from a breakdown product though this was formed during purification rather than protein storage (106). For the progression of this project and as the majority of ERCC1-XPF inhibitors discovered are likely XPF endonuclease domain inhibitors, it is thought that production of a truncated XPF endonuclease domain protein may have more success. The proposed protein is shown in Figure 6.2 by the blue bar. It is thought that this may have greater stability due to the absence of the HhH_2 domains. We predict greater success may be achieved with this truncated protein if it could be stably expressed in sufficient yields.

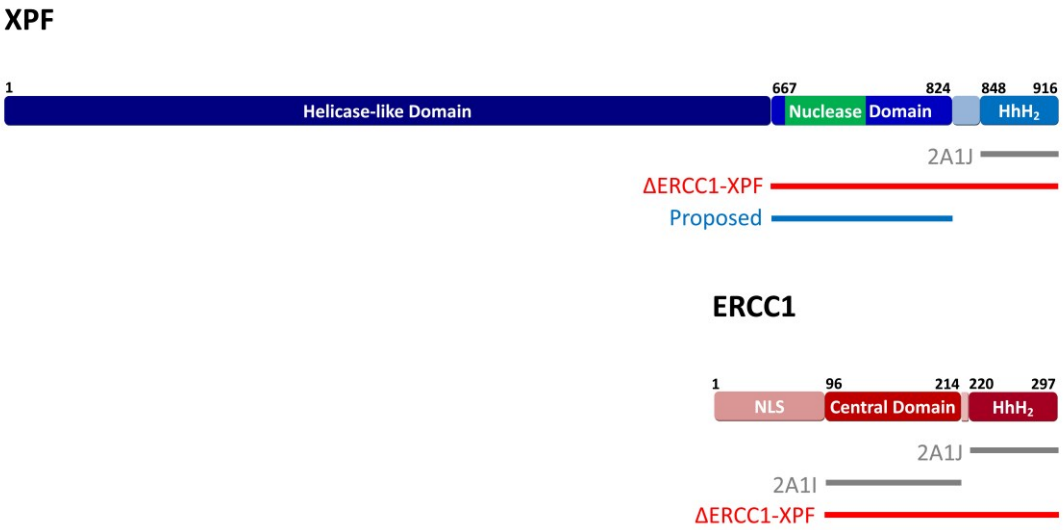

Figure 6.2: Schematic figure of ERCC1-XPF complex used for crystallisation. Shown in red is the ΔERCC1-XPF protein that we utilised for crystallisation attempts. Indicated by grey bars are the regions of ERCC1-XPF that have previously been crystallised (106). Indicated by a blue bar is the region of XPF protein that is proposed to be expressed for future crystallisation trials.

6.4 Discussion

In the previous chapter, we identified UOE #18 through an *in silico* screening approach which was proposed to disrupt the ERCC1-XPF interaction domain by binding to the Phe293 pocket. We had previously shown in Chapter 5 that this compound showed specific inhibition of ΔERCC1-XPF and bound biophysically to the ΔXPF protein. Furthermore, we also showed that this compound had activity in cell culture. In order to better understand the mechanism of inhibition of this compound, and to investigate whether we could discover a more potent analogue of UOE #18, we purchased several analogues with significant structural modifications.

Of these modifications, two had structural modifications to the naphthalene ring which was proposed by the *in silico* docking to bind into the ERCC1 Phe293 pocket on XPF; these were UOE #18_7 and UOE #18_11. Compound UOE #18_7 had a benzene ring substituted for the naphthalene ring, and as a result did not inhibit ΔERCC1-XPF. Compound UOE #18_11 had a hydroxyl and nitrogen added into the

naphthalene ring. This was predicted to add a hydrophilic charge and be incompatible with binding to the hydrophobic pocket. As expected, this compound also did not inhibit ΔERCC1-XPF.

One of the compounds, UOE #18_8 had a modification to the pyrazole ring whereby the ring was rotated and the carbonyl replaced with a hydroxyl. With this modification, although a slight improvement was observed over the parent compound against ERCC1-XPF, a loss in specificity indicated an unfavourable modification.

Compounds UOE #18_7, UOE #18_9 and UOE #18_10 all possessed the naphthalene and pyrazole rings but had additional side-chain modifications off the pyrazole group. UOE #18_9 and UOE #18_10 also had the pyrazole ring attached to the naphthalene ring at a different point to the parent compound. Although a compound possessing this drug backbone change and without the additional side-chain was not available as a direct comparison to UOE #18, it appears that this modification does not make a significant difference to activity. With regards to the side-chains, one was fluorescent, one showed no activity, and one showed an improved activity. We therefore predict that further exploration of different side chains or further changes to the pyrazole ring may result in a more potent inhibitor.

Following identification of additional ERCC1-XPF inhibitors through the second *in silico* screen and the high-throughput screen, we performed experiments to validate these as inhibitors. Initially these were clustered by Dr Tim Chapman from MRC Technology into 12 groups containing compounds with similar chemical structure and properties. One of these clusters in particular was clustering 2 in which Dr Tim Chapman noticed structural similarity of MRCT_9 to a published FEN1 inhibitor. Although the published inhibitor was not available, a closely related analogue was purchased. In Table 6.3, we showed that MRCT_9 and MRCT_9 MOD (FEN1 analogue) were both active against FEN1 and ΔERCC1-XPF. Furthermore, compound MRCT_9 identified from the high throughput screen had a significant increase in specificity for ERCC1-XPF compared to FEN1 and showed no activity against DNase1.

Of the 31 compounds identified as ERCC1-XPF inhibitors in Table 6.3 (excluding UOE #18 analogues and control compounds), 18 were purchased for

follow-up validation. Of these 6 showed no activity in cell based assays, though this could be due to low cell permeability with two of these, MRCT_5 and MRCT_21 possessing a similar chemical structure. In the thermal denaturation assay, only 3 of the 18 compounds showed no activity. Of these only 1 bound to ERCC1-XPF on the BIAcore SPR analysis indicating that the other 2 compounds may inhibit ERCC1-XPF through a non-direct mechanism. In the BIAcore SPR assay, 9 of the 31 compounds showed binding to ΔERCC1-XPF protein. Although this is low, the lack of a positive control for the SPR surface means that a stringent cut-off for binders versus non-binders had to be used. It is therefore possible that weak binding by some of these inhibitors was missed and so excluded from the concentration screen.

To conclude, 3 of the 18 compounds are active in all of the assays tested. These are MRCT_16, MRCT_20 and UOE_#18. In addition, a further 9 compounds showed specific inhibition of ERCC1-XPF and were active in the cell based assay. Interaction of these compounds with ERCC1-XPF was observed for 8 of the 9 compounds in one of the two biophysical techniques used. We therefore present 11 compounds as ERCC1-XPF inhibitors and have a further 13 that may also be inhibitors following additional validation experiments.

Finally we attempted to generate crystals of ΔERCC1-XPF protein so that we could crystallise our compounds in the presence of ERCC1-XPF and determine their mechanism of binding. Although crystallisation screens are not generally expected to produce crystals that diffract well, their benefit and use is in informing us whether a protein is likely to produce a crystal or not, and guide further screening (240). Furthermore, it is considered that screening 300 crystallisation conditions is sufficient to answer this (240, 241). In addition, following a review of success rates following crystallisation trials, Segelke considers that given there is a wide range of success rates for crystallisation trials (2-68%), the problem with crystallisation is not with arriving at the appropriate conditions, rather "finding a protein that crystallises" (241). Once conditions suitable for crystallisation are determined, optimisation of precipitant, buffer, protein concentration, pH, additives and seeding are necessary to optimise crystal formation (242). Given the number of crystallisation screens that were performed on both His-tagged, and non-His-tagged ΔERCC1-XPF protein at

both 5°C and 19°C, we suggest that this complex is not crystallisable, possibly due to its poor stability. For future crystallisation trials, we suggest that expression of the XPF nuclease domain on its own might have a greater chance of success.

7 Chapter 7: Discussion

7.1 Malignant melanoma

Malignant melanoma is a major problem in the UK with 11,877 cases diagnosed and 2,203 deaths recorded in the year 2009. Interestingly, although it is not the most common form of skin cancer, it results in more cancer deaths. Furthermore, malignant melanoma is the sixth most common cancer in the UK and is the second most common cancer in young people aged 15-34. Worryingly, although incidence rates continue to rise faster than that of any other cancer, the standard therapy for metastatic disease is ineffective (33). Furthermore, although targeted therapies are beginning to emerge, no substantial long term benefit (i.e. improved 5 year survival) has yet been observed (45, 51).

The work presented in this thesis aimed to partly address this problem. In Chapter 3, we performed a phenotypic drug screen to identify compounds that were active against melanoma. Through this, we characterised a series of nitrofuran compounds demonstrating that these are active in melanoma and enhanced the toxicity of existing chemotherapeutics. In subsequent chapters, we identified the ERCC1-XPF structure specific endonuclease as a target to overcome chemoresistance in metastatic melanoma. We established *in vitro* specificity assays and performed *in silico* and high throughput screens for ERCC1-XPF inhibitors. In this thesis, we identified and characterised ERCC1-XPF inhibitor compounds and showed activity *in vitro* and in cell culture.

7.2 Screen for compounds active against melanoma

In Chapter 3, we compared the effect of standard chemotherapeutic agents on melanoma and melanocyte cell lines. We showed that the alkylating agent dacarbazine, which is the standard chemotherapeutic for melanoma, does not require ERCC1 for its repair. In contrast, the chemotherapeutics cisplatin and oxaliplatin which both cause monofunctional, inter- and intrastrand crosslinks require ERCC1 for repair. We then showed using propidium iodide FACS cell cycle analysis in melanocyte cells that cisplatin treatment results in a characteristic S phase and G2

phase arrest. This also resulted in an increase in the sub-G1 population and in Annexin-V staining, this was shown to be the result of apoptosis. In the human melanoma A375 cell line, we observed an S phase and G2 phase arrest after 24 hours of treatment however by 48 and 72 hours of treatment, this was reduced. Although this result was surprising, we proposed this may be due to a coping strategy employed by the cells to permit continued growth in the presence of cisplatin.

7.3 Nitrofurans

We then performed a phenotypic drug screen in collaboration with Dr Elizabeth Patton and identified a number of compounds which showed activity against melanocytes or enhanced the toxicity of cisplatin. In validation experiments, compounds either did not repeat or results obtained did not justify further investigation. We then investigated a nitrofuran compound termed Bio1E7 that had been identified by Dr Hironori Ishizaki and Dr Elizabeth Patton in a previous small molecule screen. This compound showed structural similarity to another nitrofuran compound called nifurtimox that is currently used for the treatment of the African Trypanosomal Chagas disease (164). In addition, this compound is also used in cancer therapy and is in clinical trials for the treatment of neuroblastoma (168, 169). These compounds were proposed to act by being metabolised to generate superoxide formation (164). Some reports suggest that these compounds required an NER dependent DNA repair mechanism (167), using our ERCC1 proficient and deficient cell lines we showed that this was not the case. As superoxide formation is known to result in single and double stranded DNA breaks (198), we expect the homologous recombination pathway to be involved in nitrofuran induced DNA damage. Our future experiments include determining if cells harbouring BRCA1/2 mutations are hypersensitive to nitrofuran compounds as these are expected to be hypersensitive to nitrofuran induced double strand breaks. Finally, we showed that the toxicity of these compounds was abrogated by the presence of melanin pigment in our cell lines. Although pigmentation levels were not experimentally altered, we wonder whether future induction of pigmentation could protect cells from nitrofuran toxicity. Future

experiments could also include determining whether cell lines expressing either eumelanin or pheomelanin will have a differential toxicity to nitrofuran compounds.

7.4 ERCC1-XPF

We then investigated the role of ERCC1-XPF in DNA repair and showed this to be required for the repair of cisplatin induced DNA damage. Interestingly, as malignant melanoma has elevated expression of DNA repair protein in response to chemotherapy, we wondered whether this is the cause of the chemoresistance of melanoma to cisplatin therapy. A xenograft experiment in our lab had previously shown that deletion of ERCC1 from melanoma resulted in susceptibility of tumours to cisplatin treatment (149). We therefore proposed the ERCC1-XPF endonuclease as a drug target to overcome chemoresistance.

In order to develop inhibitors of ERCC1-XPF we established a fluorescence based *in vitro* endonuclease assay using recombinant ΔERCC1-XPF. While we utilised a truncated ΔERCC1-XPF which is known to have a reduced activity compared to full length ERCC1-XPF, the expression yields were greater favouring this protein for a drug discovery programme. Interestingly, during our optimisation, we observed a phenomenon whereby pre-incubating our protein at room temperature prior to the assay resulted in 200-fold greater activity levels. Furthermore, this activity was now greater than that reported for full length protein. Although the reason for this is unknown, importantly this increased activity only occurs with the biologically relevant metal ion and not manganese which is used in the standard assay and all other published assays (100, 102, 106, 112, 115). When investigating the cleavage specificity of our proteins, we confirmed that the standard assay had specificity as previously published (100, 106). The pre-incubated protein however had an altered specificity. We therefore favoured the standard ΔERCC1-XPF assay for future screening.

7.5 In silico screening

In order to identify an ERCC1-XPF inhibitor compound, initially we opted to use an *in silico* drug screening approach in collaboration with Professor Malcolm Walkinshaw from the University of Edinburgh. Here we identified the ERCC1-XPF interaction domain and the XPF endonuclease domain as our principal drug targets. Our collaborators then performed the *in silico* screen and compounds were selected for *in vitro* validation. Although one of our target sites was a protein-protein interaction, a precedent for targeting such domains has been established for MDM2/p53 interaction by Nutin compounds (224). Similarly to XPF, MDM2 also possesses a deep hydrophobic pocket tractable to drug design (224). Using a range of biochemical, biophysical and cell culture assays, we screened the compounds and characterised their activity. In addition, we utilised *in vitro* FEN1 and DNase1 assays to demonstrate that these compounds were specific.

One compound in particular, UOE #18 was of particular interest to us. This compound was designed to be an ERCC1-XPF interaction inhibitor binding to the Phe293 pocket on XPF. We demonstrated this compound to show specificity against ERCC1-XPF in the *in vitro* endonuclease assay and showed no activity against either FEN1 or DNase1. Furthermore, we demonstrated biophysical binding of this compound to recombinant ΔXPF protein in a BIAcore SPR assay and showed a stabilisation of the ΔERCC1-XPF complex in a thermal denaturation assay. In cell culture, using a human melanoma cell line we showed that this compound does enhance the toxicity of cisplatin, and was able to shift the IC50 of cisplatin.

We then purchased analogues of UOE #18 to perform basic structure activity studies with this compound. We showed that the compound predicted to have no activity based upon the *in silico* docking pose indeed lacked activity. Compounds with minor modifications to the compound backbone either had no change in activity, or resulted in a loss of specificity. We show that compounds with particular side chains were able to increase potency. Based upon the information gained, we recommend investigating these compounds further to determine whether a further increase in potency could be observed. Using the *in vitro* endonuclease assay to identify interaction inhibitors is problematic as it requires an inhibitor to disrupt the

protein-protein interaction between ERCC1-XPF for it to be able to bind. Although inhibition of this assay by UOE #18 suggests that it is able accomplish this, the resultant IC50 is much greater than that observed for cell culture assays where UOE #18 is able to inhibit *de novo* complex formation. Interestingly, identification of nutlin as a MDM2/p53 inhibitor was performed by BIAcore SPR analysis and confirmed in cell culture (224). It will be interesting to see if the UOE #18 derivatives also have greater activity in cell culture compared to UOE #18.

7.6 High throughput screen

In collaboration with Dr Barbara Saxty from MRC Technology London a high throughput drug screen was performed using our standard ΔERCC1-XPF assay. In addition, in collaboration with Professor Malcolm Walkinshaw from the University of Edinburgh a more sophisticated *in silico* screen was performed. Through a combination of these screens, and the aforementioned screening, a list of 31 ERCC1-XPF inhibitors was documented in Chapter 6. Using the biochemical, biophysical and cell culture techniques described in Chapter 5, we showed that 11 of the 18 compounds investigated are ERCC1-XPF inhibitor compounds. We now need to purchase analogues of these compounds to perform structure activity relationships on each of the compound classifications.

7.7 Crystallisation

To determine the mechanism of binding of inhibitors to ERCC1-XPF and to direct further screening efforts, we performed protein crystallisation trials using our ΔERCC1-XPF protein. Unfortunately however these trials were unsuccessful and this was likely due to protein instability when stored for a long period of time. We therefore recommend attempting to express the XPF endonuclease on its own as this may be more stable and have a greater chance of success. Preliminary expression trials are currently underway in our lab. For ERCC1-XPF interaction inhibitors it will be necessary to express the ERCC1-XPF HhH_2 interaction domain and crystallise

this in the presence of inhibitors. Although this complex has previously been crystallised, it would rely on compounds being able to disrupt the preformed complex. Therefore it might be necessary to express and crystallise the XPF HhH_2 domain in the absence of ERCC1. That being said, if this could be purified as a monodisperse protein, it is likely that there will be issues with protein stability which may hamper crystallisation attempts.

7.8 Future plans

In order to further the project it will be nessesary to develop compounds with greater potency for ERCC1-XPF. As we have already identified numerous inhibitors of ERCC1-XPF the most likely method will be to perform structure activity relationship experiments on each of the compound clusters. These efforts however will likely be limited by the activity of the *in vitro* endonuclease assay which would primarily be used to perform this screening. As this assay uses 100nM protein per reaction detection of compounds in this concentration range would need to inhibit at stoichiometric concentrations. Another option will be to express full length ERCC1-XPF proteins as these have been shown to have more activity and are active at lower protein concentrations (102, 106). Furthermore, anecdotal evidence suggests that storage of these proteins is more stable than ΔERCC1-XPF. Attempts are currently underway to express the full length protein using a modified purification protocol as published by Bowles *et al.* (102). If successful, it will also be interesting to see whether the pre-incubation phenomenon is an artefact of the truncated ΔERCC1-XPF, or whether it also occurs to full length ERCC1-XPF.

In addition, while the *in vitro* endonuclease assay is particularly suitable to endonuclease domain inhibitors, demonstrating inhibition by interaction domain inhibitors with this assay is problematic. This is because interaction inhibitors are designed primarily to disrupt *de novo* complex formation and are likely to be unable to disrupt the tight protein-protein interaction formed by ERCC1 and XPF. In order to optimise interaction inhibitors, a cell culture assay will need to be utilised. This may be based upon fluorescently tagging ERCC1- XPF to directly monitor protein

levels, or by using either standard or in-cell Western blotting techniques to detect ERCC1 and XPF protein levels.

The next main step for our ERCC1-XPF inhibitor compounds will be to demonstrate direct inhibition of DNA repair in cells. Attempts to demonstrate this are currently underway by others in our lab. It is anticipated that this will either be demonstrated using a COMET assay, or by the repair of a reporter plasmid introduced into cells following DNA damage.

In addition, we are also interested in demonstrating *in vivo* activity of our inhibitors. We therefore plan to perform xenograft experiments in either zebrafish or mice. While xenografting in zebrafish is not commonplace, it is an emerging tool for compound screening and has the advantage of being higher throughput when compared to mouse modelling.

8 Chapter 8: References

1. Cancer Research UK (2012) Skin cancer statistics - UK. Available from: http://info.cancerresearchuk.org/cancerstats/types/skin/

2. Gandini,S., Sera,F., Cattaruzza,M.S., Pasquini,P., Abeni,D., Boyle,P. and Melchi,C.F. (2005) Meta-analysis of risk factors for cutaneous melanoma: I. Common and atypical naevi. *Eur. J. Cancer*, **41**, 28–44.

3. Arana,A., Wentworth,C.E., Fernández-Vidaurre,C., Schlienger,R.G., Conde,E. and Arellano,F.M. (2010) Incidence of cancer in the general population and in patients with or without atopic dermatitis in the U.K. *Br. J. Dermatol.*, **163**, 1036–1043.

4. Bertoni,J.M., Arlette,J.P., Fernandez,H.H., Fitzer-Attas,C., Frei,K., Hassan,M.N., Isaacson,S.H., Lew,M.F., Molho,E., Ondo,W.G., et al. (2010) Increased melanoma risk in Parkinson disease: a prospective clinicopathological study. *Arch. Neurol.*, **67**, 347–352.

5. Herrero Hernández,E. (2009) Pigmentation genes link Parkinson's disease to melanoma, opening a window on both etiologies. *Med. Hypotheses*, **72**, 280–284.

6. Zanetti,R., Rosso,S. and Loria,D.I. (2007) Parkinson's Disease and Cancer. *Cancer Epidemiol Biomarkers Prev*, **16**, 1081–1081.

7. Raimondi,S., Sera,F., Gandini,S., Iodice,S., Caini,S., Maisonneuve,P. and Fargnoli,M.C. (2008) MC1R variants, melanoma and red hair color phenotype: a meta-analysis. *Int. J. Cancer*, **122**, 2753–2760.

8. Hayward,N.K. (2003) Genetics of melanoma predisposition. *Oncogene*, **22**, 3053–3062.

9. Nasir,J. (2001) Sunburn in childhood linked to melanoma. *The Lancet Oncology*, **2**, 653–653.

10. Noonan,F.P., Recio,J.A., Takayama,H., Duray,P., Anver,M.R., Rush,W.L., Fabo,E.C.D. and Merlino,G. (2001) Neonatal sunburn and melanoma in mice. *Nature*, **413**, 271–272.

11. Rosso,S., Zanetti,R., Pippione,M. and Sancho-Garnier,H. (1998) Parallel risk assessment of melanoma and basal cell carcinoma: skin characteristics and sun exposure. *Melanoma Res.*, **8**, 573–583.

12. Gandini,S., Autier,P. and Boniol,M. (2011) Reviews on sun exposure and artificial light and melanoma. *Prog. Biophys. Mol. Biol.*, **107**, 362–366.

13. Boniol,M., Autier,P., Boyle,P. and Gandini,S. (2012) Cutaneous melanoma attributable to sunbed use: systematic review and meta-analysis. *BMJ*, **345**, e4757–e4757.

14. Green,A.C., Williams,G.M., Logan,V. and Strutton,G.M. (2011) Reduced melanoma after regular sunscreen use: randomized trial follow-up. *J. Clin. Oncol.*, **29**, 257–263.

15. Lazovich,D., Vogel,R.I., Berwick,M., Weinstock,M.A., Warshaw,E.M. and Anderson,K.E. (2011) Melanoma risk in relation to use of sunscreen or other sun protection methods. *Cancer Epidemiol. Biomarkers Prev.*, **20**, 2583–2593.

16. Mercer,K.E. and Pritchard,C.A. (2003) Raf proteins and cancer: B-Raf is identified as a mutational target. *Biochimica et Biophysica Acta (BBA) - Reviews on Cancer*, **1653**, 25–40.

17. Tran,M.A., Gowda,R., Sharma,A., Park,E.-J., Adair,J., Kester,M., Smith,N.B. and Robertson,G.P. (2008) Targeting V600EB-Raf and Akt3 using nanoliposomal-small interfering RNA inhibits cutaneous melanocytic lesion development. *Cancer Res*, **68**, 7638–7649.

18. Flaherty,K.T., Puzanov,I., Kim,K.B., Ribas,A., McArthur,G.A., Sosman,J.A., O'Dwyer,P.J., Lee,R.J., Grippo,J.F., Nolop,K., et al. (2010) Inhibition of mutated, activated BRAF in metastatic melanoma. *N. Engl. J. Med.*, **363**, 809–819.

19. Cheung,M., Sharma,A., Madhunapantula,S.V. and Robertson,G.P. (2008) Akt3 and mutant V600E B-Raf cooperate to promote early melanoma development. *Cancer Res*, **68**, 3429–3439.

20. Curtin,J.A., Fridlyand,J., Kageshita,T., Patel,H.N., Busam,K.J., Kutzner,H., Cho,K.-H., Aiba,S., Bröcker,E.-B., LeBoit,P.E., et al. (2005) Distinct sets of genetic alterations in melanoma. *N. Engl. J. Med*, **353**, 2135–2147.

21. Walker,G.J., Flores,J.F., Glendening,J.M., Lin,A.H., Markl,I.D. and Fountain,J.W. (1998) Virtually 100% of melanoma cell lines harbor alterations at the DNA level within CDKN2A, CDKN2B, or one of their downstream targets. *Genes Chromosomes Cancer*, **22**, 157–163.

22. Freedberg,D.E., Rigas,S.H., Russak,J., Gai,W., Kaplow,M., Osman,I., Turner,F., Randerson-Moor,J.A., Houghton,A., Busam,K., et al. (2008) Frequent p16-independent inactivation of p14ARF in human melanoma. *J. Natl. Cancer Inst*, **100**, 784–795.

23. Piepkorn,M. (2000) Melanoma genetics: an update with focus on the CDKN2A(p16)/ARF tumor suppressors. *J. Am. Acad. Dermatol.*, **42**, 705–722; quiz 723–726.

24. Widlund,H.R. and Fisher,D.E. (2007) Potent p53-independent tumor suppressor activity of ARF in melanoma-genesis. *Pigment Cell Res*, **20**, 339–340.

25. Hanahan,D. and Weinberg,R.A. (2011) Hallmarks of cancer: the next generation. *Cell*, **144**, 646–674.

26. Hoeijmakers,J.H.J. (2009) DNA damage, aging, and cancer. *N. Engl. J. Med.*, **361**, 1475–1485.

27. Broberg,K., Höglund,M., Gustafsson,C., Björk,J., Ingvar,C., Albin,M. and Olsson,H. (2007) Genetic variant of the human homologous recombination-associated gene RMI1 (S455N) impacts the risk of AML/MDS and malignant melanoma. *Cancer Lett.*, **258**, 38–44.

28. Tomescu,D., Kavanagh,G., Ha,T., Campbell,H. and Melton,D.W. (2001) Nucleotide excision repair gene XPD polymorphisms and genetic predisposition to melanoma. *Carcinogenesis*, **22**, 403–408.

29. Zhang,M., Qureshi,A.A., Guo,Q. and Han,J. (2011) Genetic variation in DNA repair pathway genes and melanoma risk. *DNA Repair (Amst.)*, **10**, 111–116.

30. Kauffmann,A., Rosselli,F., Lazar,V., Winnepenninckx,V., Mansuet-Lupo,A., Dessen,P., Van den Oord,J.J., Spatz,A. and Sarasin,A. (2008) High expression of DNA repair pathways is associated with metastasis in melanoma patients. *Oncogene*, **27**, 565–573.

31. Jewell,R., Conway,C., Mitra,A., Randerson-Moor,J., Lobo,S., Nsengimana,J., Harland,M., Marples,M., Edward,S., Cook,M., et al. (2010) Patterns of expression of DNA repair genes and relapse from melanoma. *Clin. Cancer Res*, **16**, 5211–5221.

32. Song,L., Robson,T., Doig,T., Brenn,T., Mathers,M., Brown,E.R.S., Doherty,V., Bartlett,J.M.S., Anderson,N. and Melton,D.W. (2012) DNA repair proteins as prognostic and predictive markers in melanoma. *Histopathology*, **IN PRESS**.

33. Eggermont,A.M.M. and Kirkwood,J.M. (2004) Re-evaluating the role of dacarbazine in metastatic melanoma: what have we learned in 30 years? *Eur. J. Cancer*, **40**, 1825–1836.

34. Chapman,P.B., Hauschild,A., Robert,C., Haanen,J.B., Ascierto,P., Larkin,J., Dummer,R., Garbe,C., Testori,A., Maio,M., et al. (2011) Improved survival with vemurafenib in melanoma with BRAF V600E mutation. *N. Engl. J. Med.*, **364**, 2507–2516.

35. Chapman,P.B., Einhorn,L.H., Meyers,M.L., Saxman,S., Destro,A.N., Panageas,K.S., Begg,C.B., Agarwala,S.S., Schuchter,L.M., Ernstoff,M.S., et al. (1999) Phase III multicenter randomized trial of the Dartmouth regimen versus dacarbazine in patients with metastatic melanoma. *J. Clin. Oncol.*, **17**, 2745–2751.

36. Bedikian,A.Y., Millward,M., Pehamberger,H., Conry,R., Gore,M., Trefzer,U., Pavlick,A.C., DeConti,R., Hersh,E.M., Hersey,P., et al. (2006) Bcl-2

antisense (oblimersen sodium) plus dacarbazine in patients with advanced melanoma: the Oblimersen Melanoma Study Group. *J. Clin. Oncol.*, **24**, 4738–4745.

37. Gajewski,T.F., Sosman,J., Gerson,S.L., Liu,L., Dolan,E., Lin,S. and Vokes,E.E. (2005) Phase II trial of the O6-alkylguanine DNA alkyltransferase inhibitor O6-benzylguanine and 1,3-bis(2-chloroethyl)-1-nitrosourea in advanced melanoma. *Clin. Cancer Res*, **11**, 7861–7865.

38. Dolan,M.E., Mitchell,R.B., Mummert,C., Moschel,R.C. and Pegg,A.E. (1991) Effect of O6-benzylguanine analogues on sensitivity of human tumor cells to the cytotoxic effects of alkylating agents. *Cancer Res.*, **51**, 3367–3372.

39. Middleton,M.R., Kelly,J., Thatcher,N., Donnelly,D.J., McElhinney,R.S., McMurry,T.B., McCormick,J.E. and Margison,G.P. (2000) O(6)-(4-bromothenyl)guanine improves the therapeutic index of temozolomide against A375M melanoma xenografts. *Int. J. Cancer*, **85**, 248–252.

40. Al-Sarraf,M., Fletcher,W., Oishi,N., Pugh,R., Hewlett,J.S., Balducci,L., McCracken,J. and Padilla,F. (1982) Cisplatin hydration with and without mannitol diuresis in refractory disseminated malignant melanoma: a southwest oncology group study. *Cancer Treat Rep*, **66**, 31–35.

41. Luger,S.M., Kirkwood,J.M., Ernstoff,M.S. and Vlock,D.R. (1990) High-dose cisplatin and dacarbazine in the treatment of metastatic melanoma. *J. Natl. Cancer Inst.*, **82**, 1934–1937.

42. Glover,D., Grabelsky,S., Fox,K., Weiler,C., Cannon,L. and Glick,J. (1989) Clinical trials of WR-2721 and cis-platinum. *Int. J. Radiat. Oncol. Biol. Phys.*, **16**, 1201–1204.

43. Gradishar,W.J., Stephenson,P., Glover,D.J., Neuberg,D.S., Moore,M.R., Windschitl,H.E., Piel,I. and Abeloff,M.D. (2001) A Phase II trial of cisplatin plus WR-2721 (amifostine) for metastatic breast carcinoma. *Cancer*, **92**, 2517–2522.

44. Glover,D., Ibrahim,J., Kirkwood,J., Glick,J., Karp,D., Stewart,J., Ewell,M. and Borden,E. (2003) Phase II randomized trial of cisplatin and WR-2721 versus cisplatin alone for metastatic melanoma: an Eastern Cooperative Oncology Group Study (E1686). *Melanoma Res.*, **13**, 619–626.

45. Sosman,J.A., Kim,K.B., Schuchter,L., Gonzalez,R., Pavlick,A.C., Weber,J.S., McArthur,G.A., Hutson,T.E., Moschos,S.J., Flaherty,K.T., et al. (2012) Survival in BRAF V600-mutant advanced melanoma treated with vemurafenib. *N. Engl. J. Med.*, **366**, 707–714.

46. Su,F., Bradley,W.D., Wang,Q., Yang,H., Xu,L., Higgins,B., Kolinsky,K., Packman,K., Kim,M.J., Trunzer,K., et al. (2012) Resistance to selective

BRAF inhibition can be mediated by modest upstream pathway activation. *Cancer Res.*, **72**, 969–978.

47. Poulikakos,P.I., Persaud,Y., Janakiraman,M., Kong,X., Ng,C., Moriceau,G., Shi,H., Atefi,M., Titz,B., Gabay,M.T., et al. (2011) RAF inhibitor resistance is mediated by dimerization of aberrantly spliced BRAF(V600E). *Nature*, **480**, 387–390.

48. Hanaizi,Z., Van Zwieten-Boot,B., Calvo,G., Lopez,A.S., Van Dartel,M., Camarero,J., Abadie,E. and Pignatti,F. (2012) The European Medicines Agency review of ipilimumab (Yervoy) for the treatment of advanced (unresectable or metastatic) melanoma in adults who have received prior therapy: summary of the scientific assessment of the Committee for Medicinal Products for Human Use. *Eur. J. Cancer*, **48**, 237–242.

49. Robert,C., Thomas,L., Bondarenko,I., O'Day,S., M D,J.W., Garbe,C., Lebbe,C., Baurain,J.-F., Testori,A., Grob,J.-J., et al. (2011) Ipilimumab plus dacarbazine for previously untreated metastatic melanoma. *N. Engl. J. Med.*, **364**, 2517–2526.

50. Ledford,H. (2011) Melanoma drug wins US approval. *Nature*, **471**, 561.

51. Hodi,F.S., O'Day,S.J., McDermott,D.F., Weber,R.W., Sosman,J.A., Haanen,J.B., Gonzalez,R., Robert,C., Schadendorf,D., Hassel,J.C., et al. (2010) Improved survival with ipilimumab in patients with metastatic melanoma. *N. Engl. J. Med.*, **363**, 711–723.

52. Rosenberg,S.A., Yang,J.C. and Restifo,N.P. (2004) Cancer immunotherapy: moving beyond current vaccines. *Nat Med*, **10**, 909–915.

53. Schwartzentruber,D.J., Lawson,D.H., Richards,J.M., Conry,R.M., Miller,D.M., Treisman,J., Gailani,F., Riley,L., Conlon,K., Pockaj,B., et al. (2011) gp100 peptide vaccine and interleukin-2 in patients with advanced melanoma. *N. Engl. J. Med.*, **364**, 2119–2127.

54. O'Day,S.J., Maio,M., Chiarion-Sileni,V., Gajewski,T.F., Pehamberger,H., Bondarenko,I.N., Queirolo,P., Lundgren,L., Mikhailov,S., Roman,L., et al. (2010) Efficacy and safety of ipilimumab monotherapy in patients with pretreated advanced melanoma: a multicenter single-arm phase II study. *Ann. Oncol.*, **21**, 1712–1717.

55. Flaherty,K.T., Schiller,J., Schuchter,L.M., Liu,G., Tuveson,D.A., Redlinger,M., Lathia,C., Xia,C., Petrenciuc,O., Hingorani,S.R., et al. (2008) A phase I trial of the oral, multikinase inhibitor sorafenib in combination with carboplatin and paclitaxel. *Clin. Cancer Res.*, **14**, 4836–4842.

56. Eisen,T., Ahmad,T., Flaherty,K.T., Gore,M., Kaye,S., Marais,R., Gibbens,I., Hackett,S., James,M., Schuchter,L.M., et al. (2006) Sorafenib in advanced

melanoma: a Phase II randomised discontinuation trial analysis. *Br. J. Cancer*, **95**, 581–586.

57. McDermott,D.F., Sosman,J.A., Gonzalez,R., Hodi,F.S., Linette,G.P., Richards,J., Jakub,J.W., Beeram,M., Tarantolo,S., Agarwala,S., et al. (2008) Double-blind randomized phase II study of the combination of sorafenib and dacarbazine in patients with advanced melanoma: a report from the 11715 Study Group. *J. Clin. Oncol.*, **26**, 2178–2185.

58. Eisen,T., Marais,R., Affolter,A., Lorigan,P., Robert,C., Corrie,P., Ottensmeier,C., Chevreau,C., Chao,D., Nathan,P.D., et al. (2011) Sorafenib and dacarbazine as first-line therapy for advanced melanoma: phase I and open-label phase II studies. *Br. J. Cancer*, **105**, 353–359.

59. Hauschild,A., Agarwala,S.S., Trefzer,U., Hogg,D., Robert,C., Hersey,P., Eggermont,A., Grabbe,S., Gonzalez,R., Gille,J., et al. (2009) Results of a phase III, randomized, placebo-controlled study of sorafenib in combination with carboplatin and paclitaxel as second-line treatment in patients with unresectable stage III or stage IV melanoma. *J. Clin. Oncol.*, **27**, 2823–2830.

60. Jhappan,C., Noonan,F.P. and Merlino,G. (2003) Ultraviolet radiation and cutaneous malignant melanoma. *Oncogene*, **22**, 3099–3112.

61. Sinha,R.P. and Häder,D.P. (2002) UV-induced DNA damage and repair: a review. *Photochem. Photobiol. Sci*, **1**, 225–236.

62. Diderich,K., Alanazi,M. and Hoeijmakers,J.H.J. (2011) Premature aging and cancer in nucleotide excision repair-disorders. *DNA Repair (Amst.)*, **10**, 772–780.

63. Friedberg,E.C., Walker,G.C., Siede,W., Wood,R.D., Schultz,R.A. and Ellenberger,T. (2006) DNA Repair and Mutagenesis 2nd ed. ASM Press.

64. Aboussekhra,A., Biggerstaff,M., Shivji,M.K., Vilpo,J.A., Moncollin,V., Podust,V.N., Protić,M., Hübscher,U., Egly,J.M. and Wood,R.D. (1995) Mammalian DNA nucleotide excision repair reconstituted with purified protein components. *Cell*, **80**, 859–868.

65. Naegeli,H. and Sugasawa,K. (2011) The xeroderma pigmentosum pathway: decision tree analysis of DNA quality. *DNA Repair (Amst.)*, **10**, 673–683.

66. Hanawalt,P.C. and Spivak,G. (2008) Transcription-coupled DNA repair: two decades of progress and surprises. *Nat. Rev. Mol. Cell Biol.*, **9**, 958–970.

67. Camenisch,U., Dip,R., Schumacher,S.B., Schuler,B. and Naegeli,H. (2006) Recognition of helical kinks by xeroderma pigmentosum group A protein triggers DNA excision repair. *Nat. Struct. Mol. Biol.*, **13**, 278–284.

68. Li,L., Elledge,S.J., Peterson,C.A., Bales,E.S. and Legerski,R.J. (1994) Specific association between the human DNA repair proteins XPA and ERCC1. *Proc. Natl. Acad. Sci. U.S.A.*, **91**, 5012–5016.

69. Bessho,T., Sancar,A., Thompson,L.H. and Thelen,M.P. (1997) Reconstitution of human excision nuclease with recombinant XPF-ERCC1 complex. *J. Biol. Chem.*, **272**, 3833–3837.

70. Fagbemi,A.F., Orelli,B. and Schärer,O.D. (2011) Regulation of endonuclease activity in human nucleotide excision repair. *DNA Repair (Amst.)*, **10**, 722–729.

71. Schiestl,R.H. and Prakash,S. (1990) RAD10, an excision repair gene of Saccharomyces cerevisiae, is involved in the RAD1 pathway of mitotic recombination. *Mol. Cell. Biol.*, **10**, 2485–2491.

72. Ahmad,A., Robinson,A.R., Duensing,A., Van Drunen,E., Beverloo,H.B., Weisberg,D.B., Hasty,P., Hoeijmakers,J.H.J. and Niedernhofer,L.J. (2008) ERCC1-XPF endonuclease facilitates DNA double-strand break repair. *Mol. Cell. Biol.*, **28**, 5082–5092.

73. Sargent,R.G., Rolig,R.L., Kilburn,A.E., Adair,G.M., Wilson,J.H. and Nairn,R.S. (1997) Recombination-dependent deletion formation in mammalian cells deficient in the nucleotide excision repair gene ERCC1. *Proc. Natl. Acad. Sci. U.S.A.*, **94**, 13122–13127.

74. Niedernhofer,L.J., Essers,J., Weeda,G., Beverloo,B., De Wit,J., Muijtjens,M., Odijk,H., Hoeijmakers,J.H. and Kanaar,R. (2001) The structure-specific endonuclease Ercc1-Xpf is required for targeted gene replacement in embryonic stem cells. *EMBO J.*, **20**, 6540–6549.

75. Al-Minawi,A.Z., Saleh-Gohari,N. and Helleday,T. (2008) The ERCC1/XPF endonuclease is required for efficient single-strand annealing and gene conversion in mammalian cells. *Nucleic Acids Res.*, **36**, 1–9.

76. Fishman-Lobell,J. and Haber,J.E. (1992) Removal of nonhomologous DNA ends in double-strand break recombination: the role of the yeast ultraviolet repair gene RAD1. *Science*, **258**, 480–484.

77. Prado,F. and Aguilera,A. (1995) Role of reciprocal exchange, one-ended invasion crossover and single-strand annealing on inverted and direct repeat recombination in yeast: different requirements for the RAD1, RAD10, and RAD52 genes. *Genetics*, **139**, 109–123.

78. McVey,M. and Lee,S.E. (2008) MMEJ repair of double-strand breaks (director's cut): deleted sequences and alternative endings. *Trends Genet.*, **24**, 529–538.

79. Ma,J.-L., Kim,E.M., Haber,J.E. and Lee,S.E. (2003) Yeast Mre11 and Rad1 proteins define a Ku-independent mechanism to repair double-strand breaks lacking overlapping end sequences. *Mol. Cell. Biol.*, **23**, 8820–8828.

80. Wood,R.D. (2010) Mammalian nucleotide excision repair proteins and interstrand crosslink repair. *Environ. Mol. Mutagen*, **51**, 520–526.

81. Deans,A.J. and West,S.C. (2011) DNA interstrand crosslink repair and cancer. *Nat Rev Cancer*, **11**, 467–480.

82. Niedernhofer,L.J., Lalai,A.S. and Hoeijmakers,J.H.J. (2005) Fanconi anemia (cross)linked to DNA repair. *Cell*, **123**, 1191–1198.

83. Kuraoka,I., Kobertz,W.R., Ariza,R.R., Biggerstaff,M., Essigmann,J.M. and Wood,R.D. (2000) Repair of an interstrand DNA cross-link initiated by ERCC1-XPF repair/recombination nuclease. *J. Biol. Chem*, **275**, 26632–26636.

84. Niedernhofer,L.J., Odijk,H., Budzowska,M., Van Drunen,E., Maas,A., Theil,A.F., De Wit,J., Jaspers,N.G.J., Beverloo,H.B., Hoeijmakers,J.H.J., et al. (2004) The structure-specific endonuclease Ercc1-Xpf is required to resolve DNA interstrand cross-link-induced double-strand breaks. *Mol. Cell. Biol.*, **24**, 5776–5787.

85. Bhagwat,N., Olsen,A.L., Wang,A.T., Hanada,K., Stuckert,P., Kanaar,R., D'Andrea,A., Niedernhofer,L.J. and McHugh,P.J. (2009) XPF-ERCC1 participates in the Fanconi anemia pathway of cross-link repair. *Mol. Cell. Biol.*, **29**, 6427–6437.

86. Rageul,J., Frëmin,C., Ezan,F., Baffet,G. and Langouët,S. (2011) The knock-down of ERCC1 but not of XPF causes multinucleation. *DNA Repair (Amst.)*, **10**, 978–990.

87. McWhir,J., Selfridge,J., Harrison,D.J., Squires,S. and Melton,D.W. (1993) Mice with DNA repair gene (ERCC-1) deficiency have elevated levels of p53, liver nuclear abnormalities and die before weaning. *Nat. Genet*, **5**, 217–224.

88. Tian,M., Shinkura,R., Shinkura,N. and Alt,F.W. (2004) Growth retardation, early death, and DNA repair defects in mice deficient for the nucleotide excision repair enzyme XPF. *Mol. Cell. Biol.*, **24**, 1200–1205.

89. Tan,L.J., Saijo,M., Kuraoka,I., Narita,T., Takahata,C., Iwai,S. and Tanaka,K. (2012) Xeroderma pigmentosum group F protein binds to Eg5 and is required for proper mitosis: implications for XP-F and XFE. *Genes Cells*, **17**, 173–185.

90. Kamileri,I., Karakasilioti,I., Sideri,A., Kosteas,T., Tatarakis,A., Talianidis,I. and Garinis,G.A. (2012) Defective transcription initiation causes postnatal growth

failure in a mouse model of nucleotide excision repair (NER) progeria. *PNAS*, 10.1073/pnas.1114941109.

91. Le May,N., Fradin,D., Iltis,I., Bougnères,P. and Egly,J.-M. (2012) XPG and XPF Endonucleases Trigger Chromatin Looping and DNA Demethylation for Accurate Expression of Activated Genes. *Molecular cell*, 10.1016/j.molcel.2012.05.050.

92. Van Duin,M., De Wit,J., Odijk,H., Westerveld,A., Yasui,A., Koken,M.H., Hoeijmakers,J.H. and Bootsma,D. (1986) Molecular characterization of the human excision repair gene ERCC-1: cDNA cloning and amino acid homology with the yeast DNA repair gene RAD10. *Cell*, **44**, 913–923.

93. Sijbers,A.M., Van der Spek,P.J., Odijk,H., Van den Berg,J., Van Duin,M., Westerveld,A., Jaspers,N.G., Bootsma,D. and Hoeijmakers,J.H. (1996) Mutational analysis of the human nucleotide excision repair gene ERCC1. *Nucleic Acids Res.*, **24**, 3370–3380.

94. Brookman,K.W., Lamerdin,J.E., Thelen,M.P., Hwang,M., Reardon,J.T., Sancar,A., Zhou,Z.Q., Walter,C.A., Parris,C.N. and Thompson,L.H. (1996) ERCC4 (XPF) encodes a human nucleotide excision repair protein with eukaryotic recombination homologs. *Mol. Cell. Biol.*, **16**, 6553–6562.

95. Niedernhofer,L.J., Garinis,G.A., Raams,A., Lalai,A.S., Robinson,A.R., Appeldoorn,E., Odijk,H., Oostendorp,R., Ahmad,A., Van Leeuwen,W., et al. (2006) A new progeroid syndrome reveals that genotoxic stress suppresses the somatotroph axis. *Nature*, **444**, 1038–1043.

96. Gregg,S.Q., Robinson,A.R. and Niedernhofer,L.J. (2011) Physiological consequences of defects in ERCC1–XPF DNA repair endonuclease. *DNA Repair*, **10**, 781–791.

97. Jaspers,N.G.J., Raams,A., Silengo,M.C., Wijgers,N., Niedernhofer,L.J., Robinson,A.R., Giglia-Mari,G., Hoogstraten,D., Kleijer,W.J., Hoeijmakers,J.H.J., et al. (2007) First reported patient with human ERCC1 deficiency has cerebro-oculo-facio-skeletal syndrome with a mild defect in nucleotide excision repair and severe developmental failure. *Am. J. Hum. Genet*, **80**, 457–466.

98. Nishino,T., Komori,K., Ishino,Y. and Morikawa,K. (2003) X-ray and biochemical anatomy of an archaeal XPF/Rad1/Mus81 family nuclease: similarity between its endonuclease domain and restriction enzymes. *Structure*, **11**, 445–457.

99. Ahmad,A., Enzlin,J.H., Bhagwat,N.R., Wijgers,N., Raams,A., Appledoorn,E., Theil,A.F., J Hoeijmakers,J.H., Vermeulen,W., J Jaspers,N.G., et al. (2010) Mislocalization of XPF-ERCC1 nuclease contributes to reduced DNA repair in XP-F patients. *PLoS Genet*, **6**, e1000871.

100. De Laat,W.L., Appeldoorn,E., Jaspers,N.G. and Hoeijmakers,J.H. (1998) DNA structural elements required for ERCC1-XPF endonuclease activity. *J. Biol. Chem*, **273**, 7835–7842.

101. Bardwell,A.J., Bardwell,L., Tomkinson,A.E. and Friedberg,E.C. (1994) Specific cleavage of model recombination and repair intermediates by the yeast Rad1-Rad10 DNA endonuclease. *Science*, **265**, 2082–2085.

102. Bowles,M., Lally,J., Fadden,A.J., Mouilleron,S., Hammonds,T. and McDonald,N.Q. (2012) Fluorescence-based incision assay for human XPF-ERCC1 activity identifies important elements of DNA junction recognition. *Nucleic Acids Research*, 10.1093/nar/gks284.

103. Gaillard,P.H. and Wood,R.D. (2001) Activity of individual ERCC1 and XPF subunits in DNA nucleotide excision repair. *Nucleic Acids Res*, **29**, 872–879.

104. Sgouros,J., Gaillard,P.H. and Wood,R.D. (1999) A relationship betweena DNA-repair/recombination nuclease family and archaeal helicases. *Trends Biochem. Sci.*, **24**, 95–97.

105. Tripsianes,K., Folkers,G., Ab,E., Das,D., Odijk,H., Jaspers,N.G.J., Hoeijmakers,J.H.J., Kaptein,R. and Boelens,R. (2005) The structure of the human ERCC1/XPF interaction domains reveals a complementary role for the two proteins in nucleotide excision repair. *Structure*, **13**, 1849–1858.

106. Tsodikov,O.V., Enzlin,J.H., Schärer,O.D. and Ellenberger,T. (2005) Crystal structure and DNA binding functions of ERCC1, a subunit of the DNA structure-specific endonuclease XPF-ERCC1. *Proc. Natl. Acad. Sci. U.S.A*, **102**, 11236–11241.

107. Choi,Y.-J., Ryu,K.-S., Ko,Y.-M., Chae,Y.-K., Pelton,J.G., Wemmer,D.E. and Choi,B.-S. (2005) Biophysical characterization of the interaction domains and mapping of the contact residues in the XPF-ERCC1 complex. *J. Biol. Chem*, **280**, 28644–28652.

108. Arora,S., Kothandapani,A., Tillison,K., Kalman-Maltese,V. and Patrick,S.M. (2010) Downregulation of XPF-ERCC1 enhances cisplatin efficacy in cancer cells. *DNA Repair (Amst.)*, **9**, 745–753.

109. De Laat,W.L., Sijbers,A.M., Odijk,H., Jaspers,N.G. and Hoeijmakers,J.H. (1998) Mapping of interaction domains between human repair proteins ERCC1 and XPF. *Nucleic Acids Res.*, **26**, 4146–4152.

110. Su,Y., Orelli,B., Madireddy,A., Niedernhofer,L.J. and Schärer,O.D. (2012) Multiple DNA Binding Domains Mediate the Function of the ERCC1-XPF Protein in Nucleotide Excision Repair. *J. Biol. Chem.*, **287**, 21846–21855.

111. Das,D., Folkers,G.E., Van Dijk,M., Jaspers,N.G.J., Hoeijmakers,J.H.J., Kaptein,R. and Boelens,R. (2012) The Structure of the XPF-ssDNA Complex

Underscores the Distinct Roles of the XPF and ERCC1 Helix- Hairpin-Helix Domains in ss/ds DNA Recognition. *Structure*, **20**, 667–675.

112. Tsodikov,O.V., Ivanov,D., Orelli,B., Staresincic,L., Shoshani,I., Oberman,R., Schärer,O.D., Wagner,G. and Ellenberger,T. (2007) Structural basis for the recruitment of ERCC1-XPF to nucleotide excision repair complexes by XPA. *EMBO J*, **26**, 4768–4776.

113. McNeil,E.M. and Melton,D.W. (2012) DNA repair endonuclease ERCC1–XPF as a novel therapeutic target to overcome chemoresistance in cancer therapy. *Nucl. Acids Res.*, **40**, 9990–10004.

114. Das,D., Tripsianes,K., Jaspers,N.G.J., Hoeijmakers,J.H.J., Kaptein,R., Boelens,R. and Folkers,G.E. (2008) The HhH domain of the human DNA repair protein XPF forms stable homodimers. *Proteins*, **70**, 1551–1563.

115. Enzlin,J.H. and Schärer,O.D. (2002) The active site of the DNA repair endonuclease XPF-ERCC1 forms a highly conserved nuclease motif. *EMBO J.*, **21**, 2045–2053.

116. Nishino,T., Komori,K., Tsuchiya,D., Ishino,Y. and Morikawa,K. (2005) Crystal structure and functional implications of Pyrococcus furiosus hef helicase domain involved in branched DNA processing. *Structure*, **13**, 143–153.

117. Caruthers,J.M. and McKay,D.B. (2002) Helicase structure and mechanism. *Curr. Opin. Struct. Biol.*, **12**, 123–133.

118. Schneider,R. and Schweiger,M. (1991) The yeast DNA repair proteins RAD1 and RAD7 share similar putative functional domains. *FEBS Lett.*, **283**, 203–206.

119. Sijbers,A.M., De Laat,W.L., Ariza,R.R., Biggerstaff,M., Wei,Y.F., Moggs,J.G., Carter,K.C., Shell,B.K., Evans,E., De Jong,M.C., et al. (1996) Xeroderma pigmentosum group F caused by a defect in a structure-specific DNA repair endonuclease. *Cell*, **86**, 811–822.

120. Tripsianes,K., Folkers,G.E., Zheng,C., Das,D., Grinstead,J.S., Kaptein,R. and Boelens,R. (2007) Analysis of the XPA and ssDNA-binding surfaces on the central domain of human ERCC1 reveals evidence for subfunctionalization. *Nucleic Acids Res.*, **35**, 5789–5798.

121. Li,L., Peterson,C.A., Lu,X. and Legerski,R.J. (1995) Mutations in XPA that prevent association with ERCC1 are defective in nucleotide excision repair. *Mol. Cell. Biol*, **15**, 1993–1998.

122. Orelli,B., McClendon,T.B., Tsodikov,O.V., Ellenberger,T., Niedernhofer,L.J. and Schärer,O.D. (2010) The XPA-binding domain of ERCC1 is required for nucleotide excision repair but not other DNA repair pathways. *J. Biol. Chem.*, **285**, 3705–3712.

123. Barakat,K.H., Torin Huzil,J., Luchko,T., Jordheim,L., Dumontet,C. and Tuszynski,J. (2009) Characterization of an inhibitory dynamic pharmacophore for the ERCC1-XPA interaction using a combined molecular dynamics and virtual screening approach. *J. Mol. Graph. Model*, **28**, 113–130.

124. Krasikova,Y.S., Rechkunova,N.I., Maltseva,E.A., Petruseva,I.O. and Lavrik,O.I. (2010) Localization of xeroderma pigmentosum group A protein and replication protein A on damaged DNA in nucleotide excision repair. *Nucleic Acids Res.*, **38**, 8083–8094.

125. Shell,S.M. and Chazin,W.J. (2012) XPF-ERCC1: On the Bubble. *Structure*, **20**, 566–568.

126. Newman,M., Murray-Rust,J., Lally,J., Rudolf,J., Fadden,A., Knowles,P.P., White,M.F. and McDonald,N.Q. (2005) Structure of an XPF endonuclease with and without DNA suggests a model for substrate recognition. *EMBO J*, **24**, 895–905.

127. Matsunaga,T., Park,C.H., Bessho,T., Mu,D. and Sancar,A. (1996) Replication protein A confers structure-specific endonuclease activities to the XPF-ERCC1 and XPG subunits of human DNA repair excision nuclease. *J. Biol. Chem.*, **271**, 11047–11050.

128. Fisher,L.A., Bessho,M., Wakasugi,M., Matsunaga,T. and Bessho,T. (2011) Role of interaction of XPF with RPA in nucleotide excision repair. *J. Mol. Biol.*, **413**, 337–346.

129. De Laat,W.L., Appeldoorn,E., Sugasawa,K., Weterings,E., Jaspers,N.G. and Hoeijmakers,J.H. (1998) DNA-binding polarity of human replication protein A positions nucleases in nucleotide excision repair. *Genes Dev.*, **12**, 2598–2609.

130. Muñoz,I.M., Hain,K., Déclais,A.-C., Gardiner,M., Toh,G.W., Sanchez-Pulido,L., Heuckmann,J.M., Toth,R., Macartney,T., Eppink,B., et al. (2009) Coordination of structure-specific nucleases by human SLX4/BTBD12 is required for DNA repair. *Mol. Cell*, **35**, 116–127.

131. Svendsen,J.M., Smogorzewska,A., Sowa,M.E., O'Connell,B.C., Gygi,S.P., Elledge,S.J. and Harper,J.W. (2009) Mammalian BTBD12/SLX4 assembles a Holliday junction resolvase and is required for DNA repair. *Cell*, **138**, 63–77.

132. Fekairi,S., Scaglione,S., Chahwan,C., Taylor,E.R., Tissier,A., Coulon,S., Dong,M.-Q., Ruse,C., Yates,J.R.,3rd, Russell,P., et al. (2009) Human SLX4 is a Holliday junction resolvase subunit that binds multiple DNA repair/recombination endonucleases. *Cell*, **138**, 78–89.

133. Andersen,S.L., Bergstralh,D.T., Kohl,K.P., LaRocque,J.R., Moore,C.B. and Sekelsky,J. (2009) Drosophila MUS312 and the vertebrate ortholog BTBD12

interact with DNA structure-specific endonucleases in DNA repair and recombination. *Mol. Cell*, **35**, 128–135.

134. Kim,Y., Lach,F.P., Desetty,R., Hanenberg,H., Auerbach,A.D. and Smogorzewska,A. (2011) Mutations of the SLX4 gene in Fanconi anemia. *Nat. Genet.*, **43**, 142–146.

135. Stoepker,C., Hain,K., Schuster,B., Hilhorst-Hofstee,Y., Rooimans,M.A., Steltenpool,J., Oostra,A.B., Eirich,K., Korthof,E.T., Nieuwint,A.W.M., et al. (2011) SLX4, a coordinator of structure-specific endonucleases, is mutated in a new Fanconi anemia subtype. *Nat. Genet.*, **43**, 138–141.

136. Crossan,G.P., Van der Weyden,L., Rosado,I.V., Langevin,F., Gaillard,P.-H.L., McIntyre,R.E., Gallagher,F., Kettunen,M.I., Lewis,D.Y., Brindle,K., et al. (2011) Disruption of mouse Slx4, a regulator of structure-specific nucleases, phenocopies Fanconi anemia. *Nat. Genet.*, **43**, 147–152.

137. Wang,C. and Lambert,M.W. (2010) The Fanconi anemia protein, FANCG, binds to the ERCC1-XPF endonuclease via its tetratricopeptide repeats and the central domain of ERCC1. *Biochemistry*, **49**, 5560–5569.

138. Sridharan,D., Brown,M., Lambert,W.C., McMahon,L.W. and Lambert,M.W. (2003) Nonerythroid alphaII spectrin is required for recruitment of FANCA and XPF to nuclear foci induced by DNA interstrand cross-links. *J. Cell. Sci.*, **116**, 823–835.

139. Blom,E., Van de Vrugt,H.J., De Vries,Y., De Winter,J.P., Arwert,F. and Joenje,H. (2004) Multiple TPR motifs characterize the Fanconi anemia FANCG protein. *DNA Repair (Amst.)*, **3**, 77–84.

140. Bertrand,P., Tishkoff,D.X., Filosi,N., Dasgupta,R. and Kolodner,R.D. (1998) Physical interaction between components of DNA mismatch repair and nucleotide excision repair. *Proc. Natl. Acad. Sci. U.S.A.*, **95**, 14278–14283.

141. Zhang,N., Lu,X., Zhang,X., Peterson,C.A. and Legerski,R.J. (2002) hMutSbeta is required for the recognition and uncoupling of psoralen interstrand cross-links in vitro. *Mol. Cell. Biol.*, **22**, 2388–2397.

142. Lan,L., Hayashi,T., Rabeya,R.M., Nakajima,S., Kanno,S.I., Takao,M., Matsunaga,T., Yoshino,M., Ichikawa,M., Riele,H. te, et al. (2004) Functional and physical interactions between ERCC1 and MSH2 complexes for resistance to cis-diamminedichloroplatinum(II) in mammalian cells. *DNA Repair (Amst.)*, **3**, 135–143.

143. Bennardo,N., Cheng,A., Huang,N. and Stark,J.M. (2008) Alternative-NHEJ is a mechanistically distinct pathway of mammalian chromosome break repair. *PLoS Genet.*, **4**, e1000110.

144. Motycka,T.A., Bessho,T., Post,S.M., Sung,P. and Tomkinson,A.E. (2004) Physical and functional interaction between the XPF/ERCC1 endonuclease and hRad52. *J. Biol. Chem.*, **279**, 13634–13639.

145. Zhu,X.-D., Niedernhofer,L., Kuster,B., Mann,M., Hoeijmakers,J.H.J. and De Lange,T. (2003) ERCC1/XPF removes the 3' overhang from uncapped telomeres and represses formation of telomeric DNA-containing double minute chromosomes. *Mol. Cell*, **12**, 1489–1498.

146. Muñoz,P., Blanco,R., Flores,J.M. and Blasco,M.A. (2005) XPF nuclease-dependent telomere loss and increased DNA damage in mice overexpressing TRF2 result in premature aging and cancer. *Nat. Genet.*, **37**, 1063–1071.

147. Wu,Y., Zacal,N.J., Rainbow,A.J. and Zhu,X.-D. (2007) XPF with mutations in its conserved nuclease domain is defective in DNA repair but functions in TRF2-mediated telomere shortening. *DNA Repair (Amst.)*, **6**, 157–166.

148. Wu,Y., Mitchell,T.R.H. and Zhu,X.-D. (2008) Human XPF controls TRF2 and telomere length maintenance through distinctive mechanisms. *Mech. Ageing Dev.*, **129**, 602–610.

149. Song,L., Ritchie,A.-M., McNeil,E.M., Li,W. and Melton,D.W. (2011) Identification of DNA repair gene Ercc1 as a novel target in melanoma. *Pigment Cell Melanoma Res*, **24**, 966–971.

150. Melton,D.W., Ketchen,A.M., Núñez,F., Bonatti-Abbondandolo,S., Abbondandolo,A., Squires,S. and Johnson,R.T. (1998) Cells from ERCC1-deficient mice show increased genome instability and a reduced frequency of S-phase-dependent illegitimate chromosome exchange but a normal frequency of homologous recombination. *J. Cell. Sci.*, **111 (Pt 3)**, 395–404.

151. Towbin,H., Staehelin,T. and Gordon,J. (1979) Electrophoretic transfer of proteins from polyacrylamide gels to nitrocellulose sheets: procedure and some applications. *Proc. Natl. Acad. Sci. U.S.A.*, **76**, 4350–4354.

152. Vindeløv,L.L., Christensen,I.J. and Nissen,N.I. (1983) A detergent-trypsin method for the preparation of nuclei for flow cytometric DNA analysis. *Cytometry*, **3**, 323–327.

153. Wear,M.A. and Walkinshaw,M.D. (2006) Thermodynamics of the cyclophilin-A/cyclosporin-A interaction: a direct comparison of parameters determined by surface plasmon resonance using Biacore T100 and isothermal titration calorimetry. *Anal. Biochem.*, **359**, 285–287.

154. Kelley,L.A. and Sternberg,M.J.E. (2009) Protein structure prediction on the Web: a case study using the Phyre server. *Nat Protoc*, **4**, 363–371.

155. Taylor,P., Blackburn,E., Sheng,Y.G., Harding,S., Hsin,K.-Y., Kan,D., Shave,S. and Walkinshaw,M.D. (2008) Ligand discovery and virtual screening using the program LIDAEUS. *Br. J. Pharmacol.*, **153 Suppl 1**, S55–67.

156. Hsin,K.-Y., Morgan,H.P., Shave,S.R., Hinton,A.C., Taylor,P. and Walkinshaw,M.D. (2011) EDULISS: a small-molecule database with data-mining and pharmacophore searching capabilities. *Nucleic Acids Res.*, **39**, D1042–1048.

157. Galluzzi,L., Senovilla,L., Vitale,I., Michels,J., Martins,I., Kepp,O., Castedo,M. and Kroemer,G. (2012) Molecular mechanisms of cisplatin resistance. *Oncogene*, **31**, 1869–1883.

158. Shen,D.-W., Pouliot,L.M., Hall,M.D. and Gottesman,M.M. (2012) Cisplatin Resistance: A Cellular Self-Defense Mechanism Resulting from Multiple Epigenetic and Genetic Changes. *Pharmacological reviews*, 10.1124/pr.111.005637.

159. Larson,C.A., Adams,P.L., Blair,B.G., Safaei,R. and Howell,S.B. (2010) The role of the methionines and histidines in the transmembrane domain of mammalian copper transporter 1 in the cellular accumulation of cisplatin. *Mol. Pharmacol.*, **78**, 333–339.

160. Sun,N., Sun,X., Chen,B., Cheng,H., Feng,J., Cheng,L. and Lu,Z. (2010) MRP2 and GSTP1 polymorphisms and chemotherapy response in advanced non-small cell lung cancer. *Cancer Chemother. Pharmacol.*, **65**, 437–446.

161. More,S.S., Akil,O., Ianculescu,A.G., Geier,E.G., Lustig,L.R. and Giacomini,K.M. (2010) Role of the copper transporter, CTR1, in platinum-induced ototoxicity. *J. Neurosci.*, **30**, 9500–9509.

162. Ishida,S., McCormick,F., Smith-McCune,K. and Hanahan,D. (2010) Enhancing tumor-specific uptake of the anticancer drug cisplatin with a copper chelator. *Cancer Cell*, **17**, 574–583.

163. Yamasaki,M., Makino,T., Masuzawa,T., Kurokawa,Y., Miyata,H., Takiguchi,S., Nakajima,K., Fujiwara,Y., Matsuura,N., Mori,M., et al. (2011) Role of multidrug resistance protein 2 (MRP2) in chemoresistance and clinical outcome in oesophageal squamous cell carcinoma. *Br. J. Cancer*, **104**, 707–713.

164. Wilkinson,S.R., Taylor,M.C., Horn,D., Kelly,J.M. and Cheeseman,I. (2008) A mechanism for cross-resistance to nifurtimox and benznidazole in trypanosomes. *Proc. Natl. Acad. Sci. U.S.A.*, **105**, 5022–5027.

165. Oliveira,I.M., Bonatto,D. and Henriques,J.A. (2010) Nitroreductases: enzymes with environmental, biotechnological and clinical importance. *Current Research, Technology and Education Topics in Applied Microbiology and Microbial Biotechnology.*, **2**, 1008–1019.

166. Jin,X., Tang,S., Chen,Q., Zou,J., Zhang,T., Liu,F., Zhang,S., Sun,C. and Xiao,X. (2011) Furazolidone induced oxidative DNA damage via up-regulating ROS that caused cell cycle arrest in human hepatoma G2 cells. *Toxicol. Lett.*, **201**, 205–212.

167. Ona,K.R., Courcelle,C.T. and Courcelle,J. (2009) Nucleotide excision repair is a predominant mechanism for processing nitrofurazone-induced DNA damage in Escherichia coli. *J. Bacteriol.*, **191**, 4959–4965.

168. Saulnier Sholler,G.L., Kalkunte,S., Greenlaw,C., McCarten,K. and Forman,E. (2006) Antitumor activity of nifurtimox observed in a patient with neuroblastoma. *J. Pediatr. Hematol. Oncol.*, **28**, 693–695.

169. Saulnier Sholler,G.L., Bergendahl,G.M., Brard,L., Singh,A.P., Heath,B.W., Bingham,P.M., Ashikaga,T., Kamen,B.A., Homans,A.C., Slavik,M.A., et al. (2011) A phase 1 study of nifurtimox in patients with relapsed/refractory neuroblastoma. *J. Pediatr. Hematol. Oncol.*, **33**, 25–30.

170. Koto,K.S., Lescault,P., Brard,L., Kim,K., Singh,R.K., Bond,J., Illenye,S., Slavik,M.A., Ashikaga,T. and Saulnier Sholler,G.L. (2011) Antitumor activity of nifurtimox is enhanced with tetrathiomolybdate in medulloblastoma. *Int. J. Oncol.*, **38**, 1329–1341.

171. Tada,M., Kohno,M. and Niwano,Y. (2010) Scavenging or quenching effect of melanin on superoxide anion and singlet oxygen. *J Clin Biochem Nutr*, **46**, 224–228.

172. Takeuchi,S., Zhang,W., Wakamatsu,K., Ito,S., Hearing,V.J., Kraemer,K.H. and Brash,D.E. (2004) Melanin acts as a potent UVB photosensitizer to cause an atypical mode of cell death in murine skin. *Proc. Natl. Acad. Sci. U.S.A.*, **101**, 15076–15081.

173. Skehan,P., Storeng,R., Scudiero,D., Monks,A., McMahon,J., Vistica,D., Warren,J.T., Bokesch,H., Kenney,S. and Boyd,M.R. (1990) New colorimetric cytotoxicity assay for anticancer-drug screening. *J. Natl. Cancer Inst.*, **82**, 1107–1112.

174. Selfridge,J., Song,L., Brownstein,D.G. and Melton,D.W. (2010) Mice with DNA repair gene Ercc1 deficiency in a neural crest lineage are a model for late-onset Hirschsprung disease. *DNA Repair (Amst.)*, **9**, 653–660.

175. Papazisis,K.T., Geromichalos,G.D., Dimitriadis,K.A. and Kortsaris,A.H. (1997) Optimization of the sulforhodamine B colorimetric assay. *J. Immunol. Methods*, **208**, 151–158.

176. Li,W. and Melton,D.W. (2012) Cisplatin regulates the MAPK kinase pathway to induce increased expression of DNA repair gene ERCC1 and increase melanoma chemoresistance. *Oncogene*, **31**, 2412–2422.

177. Taylor,K.L., Grant,N.J., Temperley,N.D. and Patton,E.E. (2010) Small molecule screening in zebrafish: an in vivo approach to identifying new chemical tools and drug leads. *Cell Commun. Signal*, **8**, 11.

178. Mudipalli,A., Nadadur,S.S., Maccubbin,A.E. and Gurtoo,H.L. (1995) Mutations induced by dacarbazine activated with cytochrome P-450. *Mutat. Res*, **327**, 113–120.

179. Zhang,P., Zhang,Z., Zhou,X., Qiu,W., Chen,F. and Chen,W. (2006) Identification of genes associated with cisplatin resistance in human oral squamous cell carcinoma cell line. *BMC Cancer*, **6**, 224.

180. Baldassarre,G., Belletti,B., Battista,S., Nicoloso,M.S., Pentimalli,F., Fedele,M., Croce,C.M. and Fusco,A. (2005) HMGA1 protein expression sensitizes cells to cisplatin-induced cell death. *Oncogene*, **24**, 6809–6819.

181. Links,M., Ribeiro,J., Jackson,P., Friedlander,M. and Russell,P.J. (1998) Regulation and deregulation of G2 checkpoint proteins with cisplatin. *Anticancer Res.*, **18**, 4057–4066.

182. Kirschner,K. and Melton,D.W. (2010) Multiple roles of the ERCC1-XPF endonuclease in DNA repair and resistance to anticancer drugs. *Anticancer Res.*, **30**, 3223–3232.

183. Usanova,S., Piée-Staffa,A., Sied,U., Thomale,J., Schneider,A., Kaina,B. and Köberle,B. (2010) Cisplatin sensitivity of testis tumour cells is due to deficiency in interstrand-crosslink repair and low ERCC1-XPF expression. *Mol. Cancer*, **9**, 248.

184. Simon,G.R., Sharma,S., Cantor,A., Smith,P. and Bepler,G. (2005) ERCC1 expression is a predictor of survival in resected patients with non-small cell lung cancer. *Chest*, **127**, 978–983.

185. Olaussen,K.A., Dunant,A., Fouret,P., Brambilla,E., André,F., Haddad,V., Taranchon,E., Filipits,M., Pirker,R., Popper,H.H., et al. (2006) DNA repair by ERCC1 in non-small-cell lung cancer and cisplatin-based adjuvant chemotherapy. *N. Engl. J. Med.*, **355**, 983–991.

186. Wang,L., Wei,J., Qian,X., Yin,H., Zhao,Y., Yu,L., Wang,T. and Liu,B. (2008) ERCC1 and BRCA1 mRNA expression levels in metastatic malignant effusions is associated with chemosensitivity to cisplatin and/or docetaxel. *BMC Cancer*, **8**, 97.

187. Jun,H.J., Ahn,M.J., Kim,H.S., Yi,S.Y., Han,J., Lee,S.K., Ahn,Y.C., Jeong,H.-S., Son,Y.-I., Baek,J.-H., et al. (2008) ERCC1 expression as a predictive marker of squamous cell carcinoma of the head and neck treated with cisplatin-based concurrent chemoradiation. *Br. J. Cancer*, **99**, 167–172.

188. Kwon,H.-C., Roh,M.S., Oh,S.Y., Kim,S.-H., Kim,M.C., Kim,J.-S. and Kim,H.-J. (2007) Prognostic value of expression of ERCC1, thymidylate synthase, and glutathione S-transferase P1 for 5-fluorouracil/oxaliplatin chemotherapy in advanced gastric cancer. *Ann. Oncol.*, **18**, 504–509.

189. Matsubara,J., Nishina,T., Yamada,Y., Moriwaki,T., Shimoda,T., Kajiwara,T., Nakajima,T.E., Kato,K., Hamaguchi,T., Shimada,Y., et al. (2008) Impacts of excision repair cross-complementing gene 1 (ERCC1), dihydropyrimidine dehydrogenase, and epidermal growth factor receptor on the outcomes of patients with advanced gastric cancer. *Br. J. Cancer*, **98**, 832–839.

190. Bellmunt,J., Paz-Ares,L., Cuello,M., Cecere,F.L., Albiol,S., Guillem,V., Gallardo,E., Carles,J., Mendez,P., De la Cruz,J.J., et al. (2007) Gene expression of ERCC1 as a novel prognostic marker in advanced bladder cancer patients receiving cisplatin-based chemotherapy. *Ann. Oncol.*, **18**, 522–528.

191. Kim,M.K., Cho,K.-J., Kwon,G.Y., Park,S.-I., Kim,Y.H., Kim,J.H., Song,H.-Y., Shin,J.H., Jung,H.Y., Lee,G.H., et al. (2008) ERCC1 predicting chemoradiation resistance and poor outcome in oesophageal cancer. *Eur. J. Cancer*, **44**, 54–60.

192. Li,Q., Gardner,K., Zhang,L., Tsang,B., Bostick-Bruton,F. and Reed,E. (1998) Cisplatin induction of ERCC-1 mRNA expression in A2780/CP70 human ovarian cancer cells. *J. Biol. Chem.*, **273**, 23419–23425.

193. Mirmohammadsadegh,A., Mota,R., Gustrau,A., Hassan,M., Nambiar,S., Marini,A., Bojar,H., Tannapfel,A. and Hengge,U.R. (2007) ERK1/2 is highly phosphorylated in melanoma metastases and protects melanoma cells from cisplatin-mediated apoptosis. *J. Invest. Dermatol.*, **127**, 2207–2215.

194. Andrieux,L.O., Fautrel,A., Bessard,A., Guillouzo,A., Baffet,G. and Langouët,S. (2007) GATA-1 is essential in EGF-mediated induction of nucleotide excision repair activity and ERCC1 expression through ERK2 in human hepatoma cells. *Cancer Res.*, **67**, 2114–2123.

195. Böni,R., Lichtensteiger,W., Steinert,H.C., Böni,R.A., Früh,H., Dummer,R., Hartmann,D.G., Laine,E. and Burg,G. (1997) D1 dopamine receptors are not expressed in human melanoma. *Melanoma Res.*, **7**, 117–119.

196. Clement,M.-V., Long,L.H., Ramalingam,J. and Halliwell,B. (2002) The cytotoxicity of dopamine may be an artefact of cell culture. *J. Neurochem.*, **81**, 414–421.

197. Wang,Y., Xiao,J., Suzek,T.O., Zhang,J., Wang,J., Zhou,Z., Han,L., Karapetyan,K., Dracheva,S., Shoemaker,B.A., et al. (2012) PubChem's BioAssay Database. *Nucleic Acids Res.*, **40**, D400–412.

198. Woodbine,L., Brunton,H., Goodarzi,A.A., Shibata,A. and Jeggo,P.A. (2011) Endogenously induced DNA double strand breaks arise in heterochromatic DNA regions and require ataxia telangiectasia mutated and Artemis for their repair. *Nucleic Acids Res.*, **39**, 6986–6997.

199. Sakai,W., Swisher,E.M., Jacquemont,C., Chandramohan,K.V., Couch,F.J., Langdon,S.P., Wurz,K., Higgins,J., Villegas,E. and Taniguchi,T. (2009) Functional restoration of BRCA2 protein by secondary BRCA2 mutations in BRCA2-mutated ovarian carcinoma. *Cancer Res*, **69**, 6381–6386.

200. Ciccia,A., McDonald,N. and West,S.C. (2008) Structural and functional relationships of the XPF/MUS81 family of proteins. *Annu. Rev. Biochem*, **77**, 259–287.

201. Taylor,E.R. and McGowan,C.H. (2008) Cleavage mechanism of human Mus81-Eme1 acting on Holliday-junction structures. *Proc. Natl. Acad. Sci. U.S.A.*, **105**, 3757–3762.

202. Fricke,W.M., Bastin-Shanower,S.A. and Brill,S.J. (2005) Substrate specificity of the Saccharomyces cerevisiae Mus81-Mms4 endonuclease. *DNA Repair (Amst.)*, **4**, 243–251.

203. Bastin-Shanower,S.A., Fricke,W.M., Mullen,J.R. and Brill,S.J. (2003) The mechanism of Mus81-Mms4 cleavage site selection distinguishes it from the homologous endonuclease Rad1-Rad10. *Mol. Cell. Biol.*, **23**, 3487–3496.

204. Ciccia,A., Constantinou,A. and West,S.C. (2003) Identification and characterization of the human mus81-eme1 endonuclease. *J. Biol. Chem.*, **278**, 25172–25178.

205. Wang,W. (2007) Emergence of a DNA-damage response network consisting of Fanconi anaemia and BRCA proteins. *Nature Reviews Genetics*, **8**, 735–748.

206. Doherty,A.J., Serpell,L.C. and Ponting,C.P. (1996) The helix-hairpin-helix DNA-binding motif: a structural basis for non-sequence-specific recognition of DNA. *Nucleic Acids Res.*, **24**, 2488–2497.

207. Dorjsuren,D., Kim,D., Maloney,D.J., Wilson,D.M. and Simeonov,A. (2011) Complementary non-radioactive assays for investigation of human flap endonuclease 1 activity. *Nucleic Acids Res*, **39**, e11.

208. Tumey,L.N., Bom,D., Huck,B., Gleason,E., Wang,J., Silver,D., Brunden,K., Boozer,S., Rundlett,S., Sherf,B., et al. (2005) The identification and optimization of a N-hydroxy urea series of flap endonuclease 1 inhibitors. *Bioorg. Med. Chem. Lett*, **15**, 277–281.

209. Tumey,L.N., Huck,B., Gleason,E., Wang,J., Silver,D., Brunden,K., Boozer,S., Rundlett,S., Sherf,B., Murphy,S., et al. (2004) The identification and

optimization of 2,4-diketobutyric acids as flap endonuclease 1 inhibitors. *Bioorg. Med. Chem. Lett.*, **14**, 4915–4918.

210. Hosfield,D.J., Mol,C.D., Shen,B. and Tainer,J.A. (1998) Structure of the DNA Repair and Replication Endonuclease and Exonuclease FEN-1. *Cell*, **95**, 135–146.

211. Murante,R.S., Rumbaugh,J.A., Barnes,C.J., Norton,J.R. and Bambara,R.A. (1996) Calf RTH-1 nuclease can remove the initiator RNAs of Okazaki fragments by endonuclease activity. *J. Biol. Chem.*, **271**, 25888–25897.

212. Samejima,K. and Earnshaw,W.C. (2005) Trashing the genome: the role of nucleases during apoptosis. *Nature Reviews Molecular Cell Biology*, **6**, 677–688.

213. Sutton,D.H., Conn,G.L., Brown,T. and Lane,A.N. (1997) The dependence of DNase I activity on the conformation of oligodeoxynucleotides. *Biochem. J.*, **321 (Pt 2)**, 481–486.

214. Schmidt,E.R. (1977) Digestion of insect chromatin with micrococcal nuclease, DNase I and DNase I combined with single-strand specific nuclease S1. *Nucleic Acids Res*, **4**, 2169–2180.

203. Vanecko,S. and Laskowski,M. (1961) Studies of the Specificity of Deoxyribonu clease I III. Hydrolysis of chains carrying a monoesterified phosphate on carb on 5'. *J. Biol. Chem.*, **236**, 3312–3316.

216. Zhang, Chung and Oldenburg (1999) A Simple Statistical Parameter for Use in Evaluation and Validation of High Throughput Screening Assays. *J Biomol Screen*, **4**, 67–73.

217. Sittampalam,G.S., Iversen,P.W., Boadt,J.A., Kahl,S.D., Bright,S., Zock,J.M., Janzen,W.P. and Lister,M.D. (1997) Design of Signal Windows in High Throughput Screening Assays for Drug Discovery. *J Biomol Screen*, **2**, 159–169.

218. Mukherjee,S., Hanson,A.M., Shadrick,W.R., Ndjomou,J., Sweeney,N.L., Hernandez,J.J., Bartczak,D., Li,K., Frankowski,K.J., Heck,J.A., et al. (2012) Identification and analysis of hepatitis C virus NS3 helicase inhibitors using nucleic acid binding assays. *Nucleic acids research*, 10.1093/nar/gks623.

219. Milanovic,M., Radtke,S., Peel,N., Howell,M., Carrière,V., Joffre,C., Kermorgant,S. and Parker,P.J. (2012) Anomalous inhibition of c-Met by the kinesin inhibitor aurintricarboxylic acid. *Int. J. Cancer*, **130**, 1060–1070.

220. Ghosh,U., Giri,K. and Bhattacharyya,N.P. (2009) Interaction of aurintricarboxylic acid (ATA) with four nucleic acid binding proteins DNase I, RNase A, reverse transcriptase and Taq polymerase. *Spectrochim Acta A Mol Biomol Spectrosc*, **74**, 1145–1151.

221. Chen,Y., Bopda-Waffo,A., Basu,A., Krishnan,R., Silberstein,E., Taylor,D.R., Talele,T.T., Arora,P. and Kaushik-Basu,N. (2009) Characterization of aurintricarboxylic acid as a potent hepatitis C virus replicase inhibitor. *Antivir. Chem. Chemother.*, **20**, 19–36.

222. Dorjsuren,D., Kim,D., Maloney,D.J., Wilson,D.M. and Simeonov,A. (2011) Complementary non-radioactive assays for investigation of human flap endonuclease 1 activity. *Nucleic Acids Research*, **39**, e11.

223. Hallick,R.B., Chelm,B.K., Gray,P.W. and Orozco,E.M.,Jr (1977) Use of aurintricarboxylic acid as an inhibitor of nucleases during nucleic acid isolation. *Nucleic Acids Res.*, **4**, 3055–3064.

224. Vassilev,L.T., Vu,B.T., Graves,B., Carvajal,D., Podlaski,F., Filipovic,Z., Kong,N., Kammlott,U., Lukacs,C., Klein,C., et al. (2004) In vivo activation of the p53 pathway by small-molecule antagonists of MDM2. *Science*, **303**, 844–848.

225. Rai,G., Vyjayanti,V.N., Dorjsuren,D., Simeonov,A., Jadhav,A., Wilson,D.M.,3rd and Maloney,D.J. (2012) Synthesis, Biological Evaluation, and Structure-Activity Relationships of a Novel Class of Apurinic/Apyrimidinic Endonuclease 1 Inhibitors. *Journal of Medicinal Chemistry*, 10.1021/jm201537d.

226. Manvilla,B.A., Wauchope,O., Seley-Radtke,K.L. and Drohat,A.C. (2011) NMR studies reveal an unexpected binding site for a redox inhibitor of AP endonuclease 1. *Biochemistry*, **50**, 10540–10549.

227. Huang,F., Motlekar,N.A., Burgwin,C.M., Napper,A.D., Diamond,S.L. and Mazin,A.V. (2011) Identification of Specific Inhibitors of Human RAD51 Recombinase Using High-Throughput Screening. *ACS Chem Biol*, 10.1021/cb100428c.

228. Jiang,H. and Yang,L.Y. (1999) Cell cycle checkpoint abrogator UCN-01 inhibits DNA repair: association with attenuation of the interaction of XPA and ERCC1 nucleotide excision repair proteins. *Cancer Res.*, **59**, 4529–4534.

229. Chang,L.C., Sheu,H.M., Huang,Y.S., Tsai,T.R. and Kuo,K.W. (1999) A novel function of emodin: enhancement of the nucleotide excision repair of UV- and cisplatin-induced DNA damage in human cells. *Biochem. Pharmacol*, **58**, 49–57.

230. Ko,J.-C., Su,Y.-J., Lin,S.-T., Jhan,J.-Y., Ciou,S.-C., Cheng,C.-M. and Lin,Y.-W. (2010) Suppression of ERCC1 and Rad51 expression through ERK1/2 inactivation is essential in emodin-mediated cytotoxicity in human non-small cell lung cancer cells. *Biochem. Pharmacol.*, **79**, 655–664.

231. Ko,J.-C., Su,Y.-J., Lin,S.-T., Jhan,J.-Y., Ciou,S.-C., Cheng,C.-M., Chiu,Y.-F., Kuo,Y.-H., Tsai,M.-S. and Lin,Y.-W. (2010) Emodin enhances cisplatin-

induced cytotoxicity via down-regulation of ERCC1 and inactivation of ERK1/2. *Lung Cancer*, **69**, 155–164.

232. Ko,J.-C., Tsai,M.-S., Kuo,Y.-H., Chiu,Y.-F., Weng,S.-H., Su,Y.-C. and Lin,Y.-W. (2011) Modulation of Rad51, ERCC1, and thymidine phosphorylase by emodin result in synergistic cytotoxic effect in combination with capecitabine. *Biochem. Pharmacol*, **81**, 680–690.

233. Deloia,J.A., Bhagwat,N.R., Darcy,K.M., Strange,M., Tian,C., Nuttall,K., Krivak,T.C. and Niedernhofer,L.J. (2012) Comparison of ERCC1/XPF genetic variation, mRNA and protein levels in women with advanced stage ovarian cancer treated with intraperitoneal platinum. *Gynecologic oncology*, 10.1016/j.ygyno.2012.05.006.

234. Tripsianes,K., Folkers,G., Ab,E., Das,D., Odijk,H., Jaspers,N.G.J., Hoeijmakers,J.H.J., Kaptein,R. and Boelens,R. (2005) The structure of the human ERCC1/XPF interaction domains reveals a complementary role for the two proteins in nucleotide excision repair. *Structure*, **13**, 1849–1858.

235. Mehio,W., Kemp,G.J.L., Taylor,P. and Walkinshaw,M.D. (2010) Identification of protein binding surfaces using surface triplet propensities. *Bioinformatics*, **26**, 2549–2555.

236. Hopkins,A.L., Groom,C.R. and Alex,A. (2004) Ligand efficiency: a useful metric for lead selection. *Drug Discovery Today*, **9**, 430–431.

237. Trott,O. and Olson,A.J. (2010) AutoDock Vina: improving the speed and accuracy of docking with a new scoring function, efficient optimization, and multithreading. *J Comput Chem*, **31**, 455–461.

226. Schärer,O., Ellenberger,T. and Tsodikov,O. (2009) Crystal of XPA and ERCC1 complex and uses thereof. International Patent WO/2009/045541

239. Lally,J., Newman,M., Murray-Rust,J., Fadden,A., Kawarabayasi,Y. and McDonald,N. (2004) Crystallization of the xeroderma pigmentosum group F endonuclease from Aeropyrum pernix. *Acta Crystallogr. D Biol. Crystallogr.*, **60**, 1658–1661.

240. Bergfors,T. (2009) The Rapid Crystallization Strategy for Structure-Based Inhibitor Design. In Sussman,J.L., Spadon,P. (eds), *From Molecules to Medicines*. Springer Netherlands, Dordrecht, pp. 11–19.

241. Segelke,B.W. (2001) Efficiency analysis of sampling protocols used in protein crystallization screening. *Journal of Crystal Growth*, **232**, 553–562.

242. Bergfors,T. (2003) Seeds to crystals. *J. Struct. Biol.*, **142**, 66–76.

9 Chapter 9: Papers by the candidate

Pigment Cell Melanoma Res. **24**; 966–971

SHORT COMMUNICATION

Identification of DNA repair gene *Ercc1* as a novel target in melanoma

Liang Song, Ann-Marie Ritchie, Ewan M. McNeil, Weiling Li and David W. Melton

Institute of Genetics and Molecular Medicine, University of Edinburgh, Edinburgh, UK

CORRESPONDENCE D. W. Melton, e-mail: David.Melton@ed.ac.uk

KEYWORDS chemotherapy/cisplatin/DNA damage/ERCC1/XPF/melanoma/nucleotide excision repair

PUBLICATION DATA Received 15 March 2011, revised and accepted for publication 23 June 2011, published online 2 July 2011

doi: 10.1111/j.1755-148X.2011.00882.x

Summary

Increased expression of DNA repair genes contributes to the extreme resistance shown by melanoma to conventional DNA-damaging chemotherapeutics. One such chemotherapeutic effective against a range of other cancers, but not melanoma, is cisplatin. The DNA repair protein, ERCC1, is needed to remove cisplatin-induced DNA damage. We have shown that ERCC1 is essential for melanoma growth and resistance to cisplatin in a mouse xenograft model. Untreated xenografts of our transformed *Ercc1*-proficient melanocyte cell line grew very rapidly as malignant melanoma. Cisplatin treatment caused initial shrinkage of xenografts, but cisplatin-resistant regrowth soon followed. Cells reisolated into culture had twofold elevated levels of ERCC1 compared to both input cells and cells reisolated from untreated xenografts. An isogenic *Ercc1*-deficient derivative grew equally well in vitro as the *Ercc1*-proficient melanocyte cell line. However, in xenografts, the *Ercc1*-deficient melanomas were much slower to establish and were completely cured by just two cisplatin treatments.

The incidence of malignant melanoma is increasing globally faster than for any other form of cancer. Worldwide, around 197 000 people were diagnosed with malignant melanoma in 2008. It is now the second most common cancer among young adults (aged 15–34) in the United Kingdom (Cancer Research UK cancer statistics, 2011). Although early-stage primary melanomas are often cured by surgery, up to 20% of patients go on to develop metastatic disease. Conventional chemotherapy using DNA-damaging agents has a proven record of success against many different cancers, but such agents have consistently proven ineffective against metastatic melanoma. A meta-analysis concluded that the standard treatment for metastatic melanoma, the alkylating agent dacarbazine, generally produces poor outcomes (Tsao et al., 2004), while combinations of chemotherapeutics have shown only marginally higher response rates (Chapman et al., 1999). These studies highlight the unmet need for effective therapy for melanoma.

Elevated expression of DNA repair genes has been reported in primary melanomas that subsequently went on to metastasize when compared to non-recurrent pri-

Significance

The incidence of malignant melanoma is growing rapidly worldwide, and there is still no effective therapy for metastatic disease. Increased expression of a number of DNA repair genes contributes to the extreme resistance shown by melanoma to conventional DNA-damaging chemotherapeutics. One such chemotherapeutic effective against a range of other cancers, but not melanoma, is cisplatin. We have shown that the DNA repair protein, ERCC1, which is needed to remove cisplatin-induced DNA damage, is a novel target in a mouse model of melanoma. This raises the possibility that an ERCC1 inhibitor in combination with cisplatin could be effective against melanoma.

mary tumours (Kauffmann et al., 2008). This increased expression could contribute to the extreme resistance shown by melanoma to conventional DNA-damaging chemotherapeutics.

In addition to causing DNA lesions that are repaired by nucleotide excision repair (NER), platinum compounds also generate interstrand crosslinks that require different pathways for their repair. The ERCC1 protein in combination with the XPF protein constitutes an endonuclease essential for NER (Petit and Sancar, 1999), but unlike other NER proteins, ERCC1 and XPF are also involved in repair of interstrand crosslinks (Kuraoka et al., 2000), double-strand DNA breaks (Ahmad et al., 2008) and recombination repair pathways (Sargent et al., 1997). High *ERCC1* expression has been associated with an inferior outcome following platinum-based chemotherapy in a number of solid tumours, including ovarian and non-small-cell lung cancer, and cisplatin has been found to enhance *ERCC1* expression, but such induction has not yet been reported for melanoma (for review, see Kirschner and Melton, 2010).

We are investigating the role of DNA repair in melanoma chemoresistance and decided to start with the NER gene, *ERCC1*, because of the availability of a good model system comprising transformed isogenic *Ercc1*-proficient and *Ercc1*-deficient mouse melanocytes (Selfridge et al., 2010) that grow as malignant melanoma in mouse xenografts.

We have previously described the production of a mouse line with *loxP* sites inserted into the *Ercc1* gene. The floxed *Ercc1* gene remains fully functional, but is marked for subsequent Cre-recombinase-mediated inactivation (Doig et al., 2006) (Figure 1B). Primary melanocytes were isolated from the skin of a newborn albino $Ercc1^{flox/flox}$ mouse (Figure 1A), and after prolonged culture, an immortalized melanocyte cell line was derived. When xenografted into nude mice, 30% of the xenografts grew, but only after a latent period of >12 weeks. The transformed *Ercc1*-proficient mouse melanocyte line used here was derived by reisolating cells from one of these xenografts. Transformed *Ercc1*-proficient mouse melanocytes retained their characteristic morphology and stained positively for the melanocyte markers MITF (Figure 1C), S100 and melan-A. When the transformed *Ercc1*-proficient melanocytes were regrafted into mice, the xenografts grew rapidly with no latent period and with the histological characteristics of amelanotic malignant melanoma (Figure 1C). An isogenic *Ercc1*-deficient derivative was obtained by transiently expressing Cre recombinase and screening for recombination of the $Ercc1^{flox}$ allele (Figure 1B). *Ercc1* deficiency was confirmed by western blotting (Figure 4A).

Before the responses to cisplatin of the transformed *Ercc1*-proficient and *Ercc1*-deficient mouse melanocytes were compared in xenografts, the in vitro growth rates and responses to cisplatin were first determined (Figure 2). Untreated cell lines grew at the same rapid rate following low-density plating, with a generation time of around 24 h. Thus, any growth differences subsequently observed in vivo could not be due to intrinsic differences in growth rates of the untreated transformed *Ercc1*-proficient and *Ercc1*-deficient mouse melanocytes. However, the *Ercc1*-deficient melanocytes were around 20-fold more sensitive to cisplatin, with an IC_{50} of 3.4 ± 0.7 nM, compared to 56.5 ± 3.5 nM for *Ercc1*-proficient melanocytes. As predicted, *Ercc1* deficiency also conferred increased sensitivity on our melanocytes to another platinum compound, oxaliplatin (*Ercc1*-proficient IC_{50} 740 nM, *Ercc1*-deficient IC_{50} 26 nM), but not to the standard chemotherapeutic for melanoma, dacarbazine, which causes alkylating DNA damage that is repaired by ERCC1-independent pathways (*Ercc1*-proficient IC_{50} 2.6 μM, *Ercc1*-deficient IC_{50} 2.4 μM; Figure S1). Exposure of *Ercc1*-proficient melanocytes to 100 nM cisplatin for 48 h triggered a G2 arrest, while 300 nM cisplatin caused a more pronounced arrest and the appearance of a sub-G1 nuclear DNA content peak (Figure S2 and Table S1). Flow cytometry on Annexin V– and propidium iodide–stained cells confirmed that the sub-G1 peak was attributable to apoptosis (Figure S3). A similar G2 arrest followed by apoptosis was also observed in *Ercc1*-deficient melanocytes, albeit at tenfold lower cisplatin concentrations (Figures S2 and S3 and Table S1). Thus, *Ercc1*-deficient melanocytes do not show a general sensitivity to chemotherapeutics, only sensitivity to drugs that cause lesions that ERCC1 is involved in removing. In the case of cisplatin, both *Ercc1*-proficient and *Ercc1*-deficient mouse melanocytes respond with a G2 arrest and the induction of apoptosis.

Transformed *Ercc1*-proficient and *Ercc1*-deficient melanocytes were then used as input cells for xenografts into immunocompromised mice, and the growth of control xenografts and of xenografts growing in mice treated with cisplatin was monitored. When xenografts reached their maximum permitted size, animals were culled, xenografts were removed, macerated and trypsinized, and output cells were reisolated into culture for analysis (Figure 1D). *Ercc1*-proficient xenografts grew very rapidly, taking only 12 days from injection (on day X) to reach the threshold size of 0.1 cm^3 (on day 0) when mice were randomized into two groups and cisplatin treatment was begun (Figure 3A). Despite growing at the same rate in vitro, transformed *Ercc1*-deficient xenografts took four times longer (49 days) to reach the same threshold size before cisplatin treatment could start (Figure 4B).

Untreated *Ercc1*-proficient xenografts continued to grow very rapidly, taking only 21 days for the mean tumour volume of the group to increase a further tenfold. At this stage, all mice contained xenografts that had reached the maximum permitted size (1 cm^3), and the animals were culled and output cells were reisolated

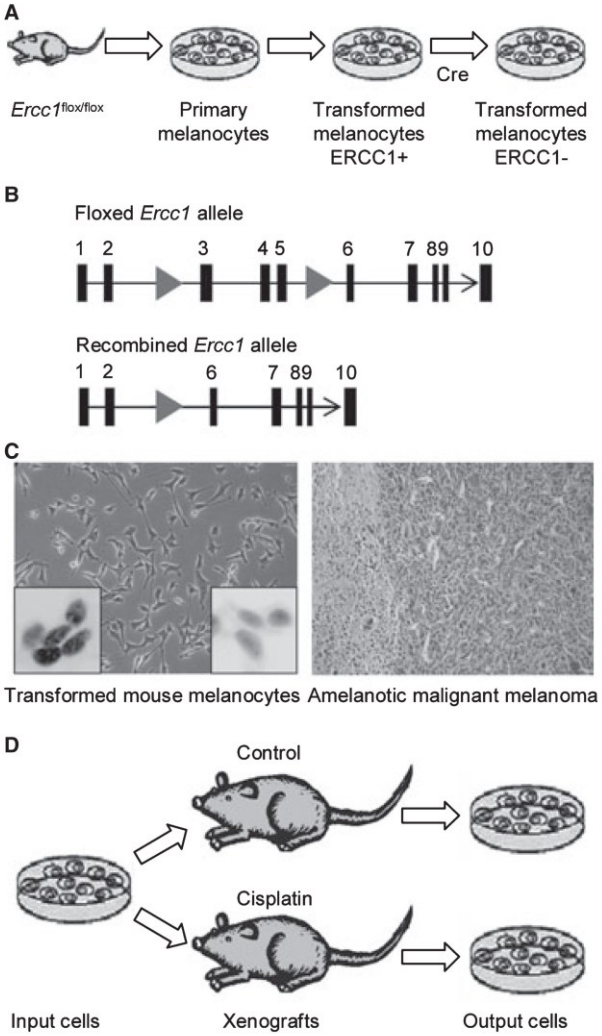

Figure 1. Experimental materials and strategy. (A) Origin of transformed mouse melanocytes. Primary melanocytes were isolated from the skin of a newborn albino *Ercc1*$^{flox/flox}$ mouse as described (Selfridge et al., 2010). After prolonged culture and xenografting, a transformed *Ercc1*-proficient mouse melanocyte line was derived by reisolating cells from one of the xenografts. The isogenic *Ercc1*-deficient derivative was obtained by transiently transfecting the transformed *Ercc1*-proficient mouse melanocytes with the pMC-CreN plasmid (Gu et al., 1993) to express Cre recombinase. Following low-density plating, resulting colonies were screened for recombination of the *Ercc1*^{flox} allele as described (Doig et al., 2006) to identify *Ercc1*-deficient derivatives. (B) Structure of the *Ercc1*-floxed allele and its Cre-mediated recombination product. The structure of the floxed *Ercc1* gene is shown schematically, with *loxP* sites located in introns 2 and 5. The floxed allele is fully functional, but recombination between *loxP* sites removes exons 3–5 to generate a non-functional allele. (C) Transformed mouse melanocytes and melanoma. A phase-contrast micrograph of transformed *Ercc1*-proficient mouse melanocytes is shown. The two higher-power insets show immunocytochemical staining for MITF in cell nuclei (left inset) and the no primary antibody control (right inset). For immunocytochemistry, methanol-fixed cells were stained with a mouse monoclonal antibody against MITF (VP-M650, 1:20 dilution, 1 h at room temperature, VECTOR Labs) and then detected with VECTASTAIN Elite ABC system and DAB+ (DAKO, Dako Ltd., Ely, UK) according to the manufacturers' instructions. The transformed *Ercc1*-proficient mouse melanocytes grow rapidly as xenografts with the histological characteristics of amelanotic malignant melanoma (see image of haematoxylin and eosin-stained section through a xenograft). (D) Response of xenografts to cisplatin. Transformed *Ercc1*-proficient and *Ercc1*-deficient melanocytes were used as input cells for xenografts into nude mice, and the growth of control xenografts and of xenografts growing in mice treated with cisplatin was monitored. When xenografts reached their maximum permitted size, animals were culled, xenografts were removed, macerated and trypsinized, and output cells were reisolated into culture for analysis. All melanocytes were cultured in RPMI1640 medium supplemented with 10% foetal calf serum at 37°C in 5% CO_2.

into culture for analysis. The treated group of *Ercc1*-proficient xenografts received cisplatin on days 0 and 7. This resulted in initial shrinkage of tumours, but this was followed by rapid regrowth that could not be prevented by two further cisplatin injections on days 21 and 28. All the animals in the treated group had

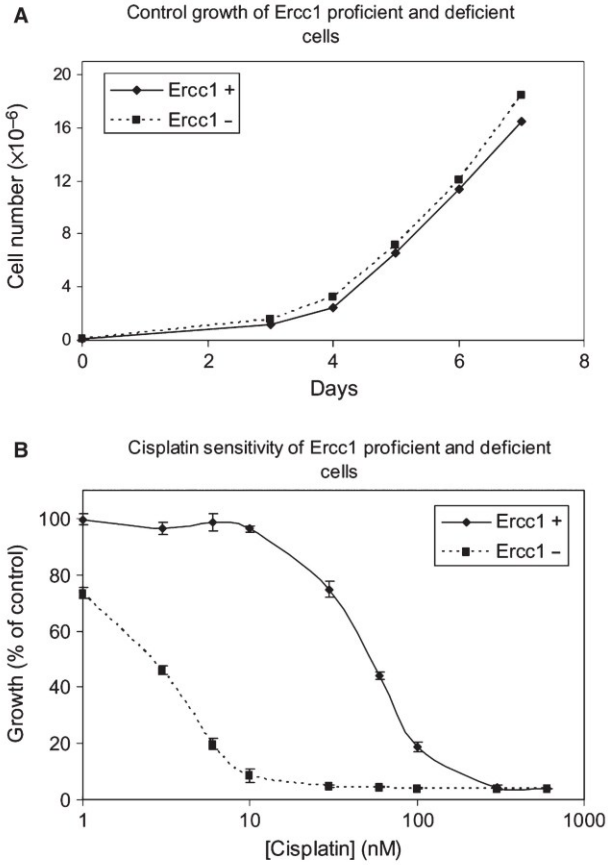

Figure 2. In vitro growth and cisplatin sensitivity of transformed *Ercc1*-proficient and *Ercc1*-deficient melanocytes. (A) Growth assay. For each cell line, 5×10^4 cells were plated into 25-cm^2 flasks and grown in control medium. Flasks were harvested on days 3–7, and the cells were counted. The cell number at each time point is the mean of duplicate flasks. *Ercc1*+, *Ercc1*-proficient melanocytes; *Ercc1*-, *Ercc1*-deficient melanocytes. (B) Cisplatin sensitivity. The sensitivity to cisplatin was determined using the sulforhodamine B (SRB) colorimetric growth assay (Vichai and Kirtikara, 2006). One thousand cells were plated/well in 96-well plates directly into medium containing varying concentrations of cisplatin. Plates were incubated for 6 days until control wells were nearly confluent and then fixed, stained and assayed. For each cell line, growth is expressed as a percentage of growth in control untreated wells. Each point is the mean% growth ± SEM from eight individual wells.

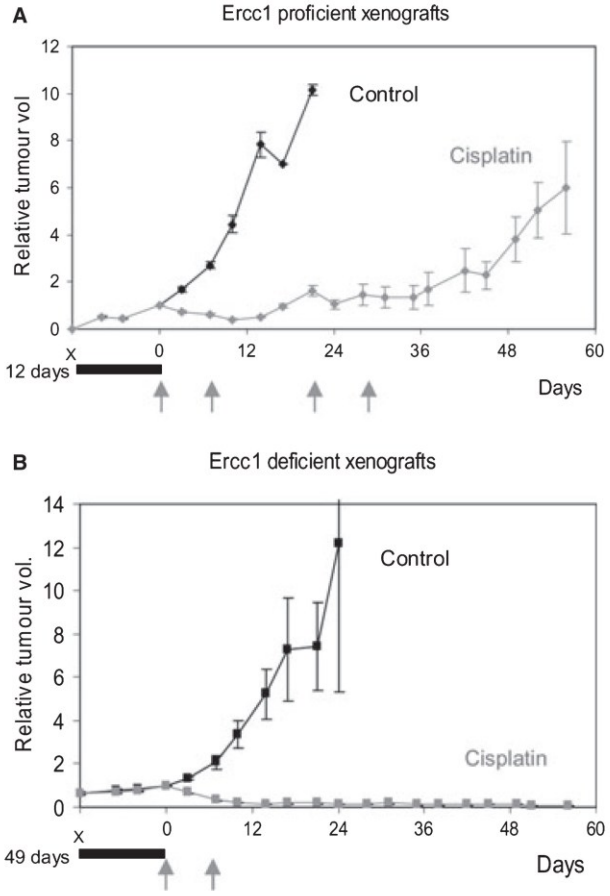

Figure 3. Response to cisplatin of transformed *Ercc1*-proficient and *Ercc1*-deficient melanocyte xenografts. (A) *Ercc1*-proficient and (B) *Ercc1*-deficient melanocyte xenografts. 10^7 transformed melanocytes in 0.1 ml of medium were injected subcutaneously into both flanks of 8- to 12-week-old female *nude* mice, together with 0.1 ml matrigel (BD Biosciences, Oxford, UK) to facilitate xenograft establishment, on day X. Ten animals were injected with each melanocyte line, and xenograft growth was monitored twice weekly. When the mean size of xenografts had reached 0.1 cm^3 (day 0), mice were randomized into two groups of five for each cell line. One group was untreated, while the other was treated on the days indicated (arrows) with 6 mg/kg cisplatin i.p. The time taken from injection for xenografts to reach the threshold size to start treatment is indicated by the bar on the Days axis. The mean tumour volume for each group ± SEM is shown relative to the mean tumour volume at the start of treatment. Animals were culled when a tumour reached 1 cm^3. The SEM increases disproportionately as the experiment proceeds owing to culling of animals with the largest tumours.

tumours that had reached the maximum permitted size and were culled by day 56, and output cells were reisolated.

Despite having been very slow to establish, untreated *Ercc1*-deficient xenografts then grew rapidly taking only 24 days for the mean tumour volume of the group to increase a further 12-fold. By this stage, all mice contained xenografts that had reached the maximum permitted size, and the animals were culled, and output cells were reisolated. The treated group of *Ercc1*-deficient xenografts received cisplatin on days 0 and 7, and this was sufficient to cause a rapid, complete shrinkage of the tumours, and the experiment was terminated on Day 108. The cisplatin dose used in these experiments (6 mg/kg) is our standard dose to demonstrate the cisplatin sensitivity/resistance of a range of human cancers growing as xenografts. Xenografts of human melanoma are resistant to this dose, so it enables a realistic assessment of the cisplatin response of our tumourigenic mouse melanocyte model compared to human melanoma.

Output cells were cultured from the different xenografts (no cisplatin was used in the culture medium),

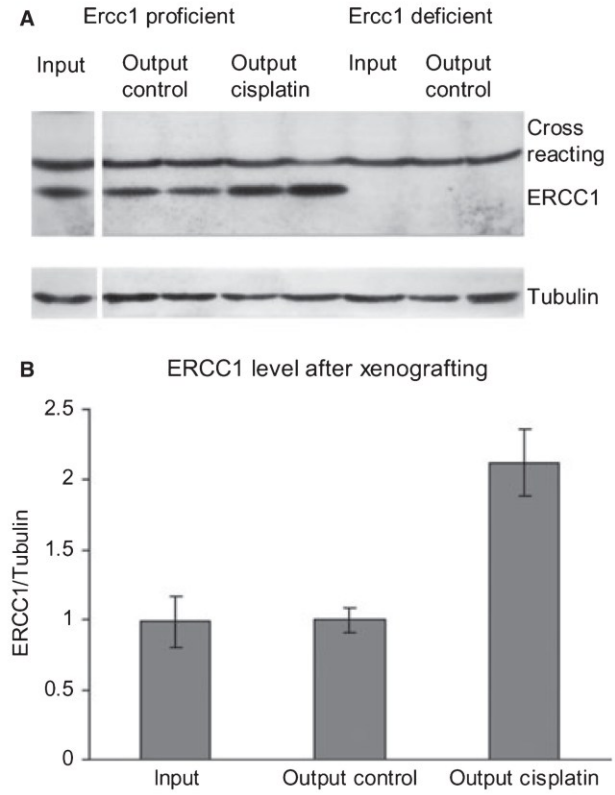

Figure 4. *Ercc1* expression in melanocytes retrieved from xenografts. (A) Western blots on *Ercc1*-proficient and *Ercc1*-deficient melanocytes used as input cells for xenografts and independent isolates of output cells from control and cisplatin-treated xenografts. Western blotting was carried out as described (Selfridge et al., 2010). ERCC1 was detected using goat polyclonal antibody SC-10157 (Santa Cruz Biotechnology Inc., Santa Cruz, CA, USA); for a loading control, β-tubulin was detected with rabbit polyclonal antibody ab6046-200 (Abcam). Upper panel, the positions of the 33-kDa ERCC1 and a 40-kDa cross-reacting band, also detected by the antibody to ERCC1, are indicated. The ERCC1 band is absent in both input and output *Ercc1*-deficient melanocytes. Lower panel, 50-kDa β-tubulin is indicated. (B) Histogram showing mean ERCC1 protein level ± SEM in input *Ercc1*-proficient melanocytes and output cells retrieved from control and cisplatin-treated xenografts. ERCC1 levels are standardized against β-tubulin and normalized to the mean ERCC1/tubulin ratio in the input group. Input, n = 4 independent cultures; Output control, n = 4 independent xenografts; Output cisplatin-treated, n = 8 independent xenografts.

and ERCC1 protein levels were determined by western blotting and standardized against β-tubulin (Figure 4). As expected, ERCC1 was undetectable in both input and output *Ercc1*-deficient melanocytes. The level of ERCC1 expression in the group of output *Ercc1*-proficient melanocytes isolated from untreated xenografts was equivalent to that of the input cells. However, the mean ERCC1/tubulin ratio of the group of output *Ercc1*-proficient melanocytes isolated from cisplatin-treated xenografts was 2.1-fold higher than that of the input cells ($P = 0.004$, by Mann–Whitney U test). This demonstrates in a direct functional assay in a mouse melanoma model that resistance to cisplatin results from increased levels of ERCC1.

Western blotting (Figure S4) and TaqMan assays on cisplatin-treated input *Ercc1*-proficient melanocytes showed no evidence for rapid transcriptional induction of *Ercc1*. This is contrary to the situation in human melanoma cells where cisplatin results in a threefold increase in both ERCC1 and XPF protein and mRNA levels in 48 h (Li, W. and Melton, D.W., submitted). We were unable to detect mouse XPF by western blotting and so could not investigate whether there was also a corresponding increase in XPF protein levels in output cells from transformed *Ercc1*-proficient melanocyte xenografts. Previous reports have suggested that neither ERCC1 nor XPF was stable in cells in the absence of the other protein. However, a recent study (Arora et al., 2010) in human cancer cells found that while XPF was unstable in the absence of ERCC1, ERCC1 levels were largely unaffected by the absence of XPF.

Transformed *Ercc1*-proficient melanocytes grew very rapidly as xenografts with no latent period. Why did it take four times longer for isogenic transformed *Ercc1*-deficient melanocyte xenografts to establish, despite having an equivalent growth rate in vitro? The requirement to accumulate additional mutations is one possible explanation. Another explanation is that it is a direct in vivo consequence of the DNA repair deficiency. During tumour growth, a highly heterogeneous microenvironment, characterized by oxygen depletion, extracellular acidosis, elevated lactate levels, glucose deprivation, low energy status and interstitial hypertension can develop (Vaupel, 2004). During the initial growth of xenografts, the vascular density will be very low, the blood supply to the tumour could be critical and the oxygen level low. With the establishment of the blood supply, the oxygen level in the tumour cells could increase rapidly, resulting in elevated levels of oxidative DNA damage. Such a hostile microenvironment could result in increased levels of a variety of different forms of endogenous DNA damage that would normally be repaired by one or more of the key DNA repair pathways requiring ERCC1. Such unrepaired DNA damage would inevitably slow proliferation and could result in cell death. Transformed *Ercc1*-deficient melanocytes growing in vitro are evidently not exposed to the same growth constraints. A similar explanation, involving unrepaired endogenous DNA damage, has been put forward to explain the progeroid phenotype observed in the liver and brain of *Ercc1*-deficient mice (McWhir et al., 1993; Niedernhofer et al., 2006).

Once established, the *Ercc1*-deficient xenografts grew as rapidly as their *Ercc1*-proficient counterparts. However, they were exquisitely sensitive to cisplatin and were cured by just two treatments, while *Ercc1*-proficient xenografts were resistant. These results demonstrate that, in this mouse melanoma xenograft model, ERCC1 is important for early melanoma growth and is

essential for resistance to cisplatin. This raises the possibility that an ERCC1 inhibitor could be used to enhance the effectiveness of cisplatin treatment in melanoma. The melanoma xenograft system that we have developed could be used to identify and test such inhibitors.

Acknowledgements

DWM is grateful to Morwenna Muir and Michael Dodds for excellent technical assistance with the xenograft work. LS was supported by a PhD scholarship from the College of Medicine and Veterinary Medicine, University of Edinburgh. EMM was supported by a PhD scholarship from Cancer Research UK. WL was supported by a China Scholarship Council/University of Edinburgh Scholarship. This work was supported by The Charon Fund.

References

Ahmad, A., Robinson, A.R., Duensing, A., van Drunen, E., Beverloo, H.B., Weisberg, D.B., Hasty, P., Hoeijmakers, J.H., and Niedernhofer, L.J. (2008). ERCC1-XPF endonuclease facilitates DNA double-strand break repair. Mol. Cell. Biol. *28*, 5082–5092.

Arora, S., Kothandapani, A., Tillison, K., Kalman-Maltese, V., and Patrick, S.M. (2010). Downregulation of XPF–ERCC1 enhances cisplatin efficacy in cancer cells. DNA Repair *9*, 745–753.

Cancer Research UK cancer statistics. (2011). http://info.cancerresearchuk.org/cancerstats.

Chapman, P.B.L., Einhorn, H., Meyers, M.L. et al. (1999). Phase III multicenter randomized trial of the Dartmouth regimen versus dacarbazine in patients with metastatic melanoma. J. Clin. Oncol. *17*, 2745–2751.

Doig, J., Anderson, C., Lawrence, N.J., Selfridge, J., Brownstein, D.G., and Melton, D.W. (2006). Mice with skin-specific DNA repair gene (Ercc1) inactivation are hypersensitive to ultraviolet irradiation-induced skin cancer and show more rapid actinic progression. Oncogene *25*, 6229–6238.

Gu, H., Zou, Y.R., and Rajewsky, K. (1993). Independent control of immunoglobulin switch recombination at individual switch regions evidenced through Cre-loxP-mediated gene targeting. Cell *73*, 1155–1164.

Kauffmann, A., Rosselli, F., Lazar, V., Winnepenninckx, V., Mansuet-Lupo, A., Dessen, P., van den Oord, J.J., Spatz, A., and Sarasin, A. (2008). High expression of DNA repair pathways is associated with metastasis in melanoma patients. Oncogene *27*, 565–573.

Kirschner, K., and Melton, D.W. (2010). Multiple roles of the ERCC1-XPF endonuclease in DNA repair and resistance to anticancer drugs. Anticancer Res. *30*, 3223–3232.

Kuraoka, I., Kobertz, W.R., Ariza, R.R., Biggerstaff, M., Essigmann, J.M., and Wood, R.D. (2000). Repair of interstrand DNA crosslink initiated by ERCC1-XPF repair/recombination nuclease. J. Biol. Chem. *275*, 26632–26636.

McWhir, J., Selfridge, J., Harrison, D.J., Squires, S., and Melton, D.W. (1993). Mice with DNA repair gene (ERCC-1) deficiency have elevated levels of p53, liver nuclear abnormalities and die before weaning. Nat. Genet. *5*, 217–224.

Niedernhofer, L.J., Garinis, G.A., Raams, A. et al. (2006). A new progeroid syndrome reveals that genotoxic stress suppresses the somatotroph axis. Nature *444*, 1038–1043.

Petit, C., and Sancar, A. (1999). Nucleotide excision repair: from *E. coli* to man. Biochimie *81*, 15–25.

Sargent, R.G., Brenneman, M.A., and Wilson, J.H. (1997). Repair of site-specific double-strand breaks in a mammalian chromosome by homologous and illegitimate recombination. Mol. Cell. Biol. *17*, 267–277.

Selfridge, J., Song, L., Brownstein, D.G., and Melton, D.W. (2010). Mice with DNA repair gene Ercc1 deficiency in a neural crest lineage are a model for late-onset Hirschsprung disease. DNA Repair *9*, 653–660.

Tsao, H., Atkins, M.B., and Sober, A.J. (2004). Management of cutaneous melanoma. N. Engl. J. Med. *351*, 998–1012.

Vaupel, P. (2004). Tumor microenvironmental physiology and its implications for radiation oncology. Semin. Radiat. Oncol. *14*, 198–206.

Vichai, V., and Kirtikara, K. (2006). Sulforhodamine B colorimetric assay for cytotoxicity screening. Nat. Protoc. *1*, 1112–1116.

Supporting information

Additional Supporting Information may be found in the online version of this article:

Appendix S1. Full figure legends for the below.

Figure S1. Sensitivity of transformed *Ercc1*-proficient and *Ercc1*-deficient melanocytes to chemotherapeutics.

Figure S2. DNA content of cisplatin-treated transformed *Ercc1*-proficient and *Ercc1*-deficient melanocytes.

Figure S3. Cisplatin-induced apoptosis in transformed *Ercc1*-proficient and *Ercc1*-deficient melanocytes.

Figure S4. *Ercc1* expression in transformed *Ercc1*-proficient melanocytes following cisplatin treatment.

Table S1. Cell cycle analysis of cisplatin-treated transformed *Ercc1*-proficient and *Ercc1*-deficient melanocytes.

Please note: Wiley-Blackwell are not responsible for the content or functionality of any supporting materials supplied by the authors. Any queries (other than missing material) should be directed to the corresponding author for the article.

Chemistry & Biology
Article

ALDH2 Mediates 5-Nitrofuran Activity in Multiple Species

Linna Zhou,[1,8] Hironori Ishizaki,[2,3,4,8] Michaela Spitzer,[5] Kerrie L. Taylor,[2,3] Nicholas D. Temperley,[2,4] Stephen L. Johnson,[6] Paul Brear,[4] Philippe Gautier,[2,3] Zhiqiang Zeng,[2,3] Amy Mitchell,[2,4] Vikram Narayan,[2,4] Ewan M. McNeil,[2,4] David W. Melton,[2,4] Terry K. Smith,[1,7] Mike Tyers,[5] Nicholas J. Westwood,[1,*] and E. Elizabeth Patton[2,3,4,*]

[1]School of Chemistry and Biomedical Sciences Research Complex, University of St. Andrews and EaStCHEM, St. Andrews, Fife, Scotland KY16 9ST, UK
[2]Institute of Genetics and Molecular Medicine
[3]MRC Human Genetics Unit
[4]Edinburgh Cancer Research Centre
The University of Edinburgh, Crewe Road South, Edinburgh, EH4 2XR, Scotland, UK
[5]Wellcome Trust Centre for Cell Biology, University of Edinburgh, Michael Swann Building, King's Buildings, Mayfield Road, Edinburgh, EH9 3JR, UK
[6]Department of Genetics, Washington University Medical School, 4566 Scott Avenue, St. Louis, MO 63110, USA
[7]School of Biology, University of St. Andrews, Fife, Scotland KY16 9ST, UK
[8]These authors contributed equally to this work
*Correspondence: njw3@st-andrews.ac.uk (N.J.W.), e.patton@igmm.ed.ac.uk (E.E.P.)
http://dx.doi.org/10.1016/j.chembiol.2012.05.017

SUMMARY

Understanding how drugs work in vivo is critical for drug design and for maximizing the potential of currently available drugs. 5-nitrofurans are a class of prodrugs widely used to treat bacterial and trypanosome infections, but despite relative specificity, 5-nitrofurans often cause serious toxic side effects in people. Here, we use yeast and zebrafish, as well as human in vitro systems, to assess the biological activity of 5-nitrofurans, and we identify a conserved interaction between aldehyde dehydrogenase (ALDH) 2 and 5-nitrofurans across these species. In addition, we show that the activity of nifurtimox, a 5-nitrofuran anti-trypanosome prodrug, is dependent on zebrafish Aldh2 and is a substrate for human ALDH2. This study reveals a conserved and biologically relevant ALDH2-5-nitrofuran interaction that may have important implications for managing the toxicity of 5-nitrofuran treatment.

INTRODUCTION

Drugs often have multiple targets in vivo that can lead to unintended side effects. Identifying unintended drug targets and their in vivo relevance is a fundamental challenge in chemical biology. 5-Nitrofurans are a class of drugs that save thousands of lives as front-line treatments for parasitic trypanosome infections in Latin America and Africa, and they are also effective antibiotics in human and veterinary medicine (Castro et al., 2006; Coura and Viñas, 2010; Nussbaum et al., 2010; Priotto et al., 2009). 5-Nitrofurans are of such importance to human health that the World Heath Organization deems the 5-nitrofuran, nifurtimox, an essential medicine and Bayer HealthCare provides nifurtimox free of charge for trypanosome infections. 5-Nitrofurans are prodrugs, and their relative specificity comes from parasitic and bacteria-specific nitroreductases (NTRs) that reduce the 5-NO_2 functional group to a toxic anion radical, thereby generating reactive oxygen species and inducing cell death. Despite their widespread use, 5-nitrofurans have serious toxic side effects (Castro et al., 2006). For nifurtimox, toxic side effects lead to treatment cessation in over 30% of patients with Chagas disease, which is caused by *Trypanosoma cruzi* infection (Castro et al., 2006). Clinical side effects are complex and can vary between populations, but they include polyneuropathy, depression, forgetfulness, alcohol intolerance, and headaches, as well as gastrointestinal complications. There is currently no treatment strategy available to reduce the off-target toxic side effects of 5-nitrofurans.

Over decades of research, scientists have identified multiple human enzymes capable of 5-nitrofuran reduction in vitro, in cells or tissues (Dubuisson et al., 2001; Rao et al., 1987; Rao and Mason, 1987). However, the question of whether these enzymes are relevant to 5-nitrofuran side-effect activity and the potential for therapeutic intervention to inhibit their off-target activity in vivo is unanswered. Drug mechanism of action is readily examined in the zebrafish model system, in which clinically active compounds can be directly assayed in the transparent embryo (Zon and Peterson, 2005). Within 2 to 5 days of development in zebrafish, most tissues and organs have formed, thereby enabling the identification of tissue-specific drug activities and/or bioactivation. These features allow facile phenotypic chemical screens within the whole animal. Phenotypic small-molecule screens in zebrafish have enabled the identification of new biological pathways, novel bioactive chemicals, and unexpected potential for known drugs (Taylor et al., 2010). Drugs often have multiple targets in vivo, and examining the effects of small molecules on the developing zebrafish can also identify unintended drug targets (Ishizaki et al., 2010; Ito et al., 2010; Laggner et al., 2012; Rihel et al., 2010).

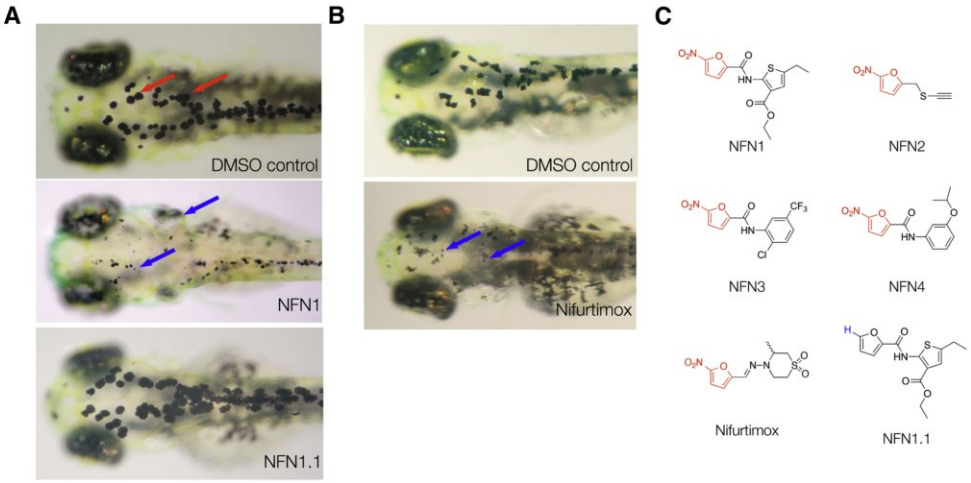

Figure 1. 5-Nitrofurans Promote Melanocytotoxicity in Zebrafish

(A and B) Examples of zebrafish embryos treated at 2 dpf for 48 hr with DMSO as a control, plus 5 μM NFN1 and 5 μM NFN1.1 (A) or 50 μM nifurtimox (B). Black melanocytes (red arrows) and melanocyte detritus (blue arrows) are indicated.

(C) Chemical structures of the four 5-nitrofurans (NFN1–4 [Maybridge compounds BTB05727, SEW00138, BTB13657, and BR00087]) identified in a chemical screen for modulators of melanocyte development. The 5-NO_2-furan functional group shared between the 5-nitrofurans, including nifurtimox, is indicated in red. The chemical structure of NFN1.1. is identical to that of NFN1 but lacks the 5-NO_2 functional group required for activity (blue).

See also Figure S1 and Movie S1.

Here, we use a multispecies approach to identify ALDH2 as a mediator of 5-nitrofuran toxicity in yeast and zebrafish, and we show that 5-nitrofurans are substrates for human ALDH2 in vitro. In a zebrafish phenotypic screen, we found that 5-nitrofurans are melanocytotoxic. We exploited this highly visible in vivo activity to generate a 5-nitrofuran probe, identify ALDH2 as a 5-nitrofuran target, and validate the interaction in vivo. This interaction is conserved from yeast to human, and is also relevant for the clinically active 5-nitrofuran nifurtimox. We propose that this new interaction may be relevant to some of the 5-nitrofuran toxicity observed in the clinic.

RESULTS

5-Nitrofurans Are Active in Zebrafish

Melanocytes are pigment-producing cells that generate black melanin, and pigmented melanocytes are clearly visible in the developing zebrafish beginning at 28 hr postfertilization (hpf; Figure 1A). We identified four 5-nitrofuran compounds, NFN1 (Maybridge BTB05727), NFN2 (SEW00138), NFN3 (BTB13657), and NFN4 (BR00087), in a chemical screen for modulators of melanocyte development in zebrafish embryos (Figures 1A and 1C; see Methods). We also found that zebrafish were sensitive to the clinically active 5-nitrofuran nifurtimox (Figures 1B and 1C). 5-Nitrofuran treatment directly affected the melanocyte and melanocyte progenitor viability in a dose-dependent manner and was independent of tyrosinase activity (Figure S1 available online; Movie S1). Thus, 5-nitrofurans are melanocytotoxic in zebrafish, and unlike prodrugs that are bioactivated by pigmentation enzymes (Jawaid et al., 2009; Yang and Johnson, 2006), their activity is independent of tyrosinase. Altered pigmentation is not a feature of 5-nitrofuran toxicity in humans, but melanocyte specificity in zebrafish provided a rapid, convenient, and highly visible assay to study 5-nitrofuran activity in an animal model, independent of trypanosome infection.

5-Nitrofuran Activity Requires the 5-NO_2 Moiety

5-Nitrofurans are prodrugs, and the 5-NO_2 moiety is essential for bioactivation in parasites and bacteria (Maya et al., 2007). We modified NFN1 by replacing the NO_2 moiety with a hydrogen atom (Figure 1C, NFN1.1; Table 1; Supplemental Information). In contrast to treatment with NFN1, NFN1.1 had no effect on zebrafish melanocytes, and the melanocyte remained pigmented and intact (Figure 1A; Table 1). Nitrofuran activity in melanocytes is therefore dependent upon the 5-NO_2 functional group. As in humans, zebrafish do not have NTRs (which are present in trypanosomes) to process the 5-NO_2 functional group, and thus, the effects of NFN1 on zebrafish melanocytes may

Table 1. Derivatives of 5-Nitrofurans and Their Activity in Zebrafish

Compound	0.2 μM	0.4 μM	0.8 μM	1.6 μM
NFN1	No activity	No activity	+	+++
NFN1.1	No activity	No activity	No activity	No activity
NFN5	No activity	+	++	++++
NFN5.1	No activity	+	++	++
NFN5.2	No activity	+	++	++++[a]

+Some melanocytes become dendritic, few are fragmented.
++Some punctate and fragmented melanocytes.
+++All melanocytes are punctate, many clearly fragmented, pigment remains in eye.
++++All melanocytes are fragmented, with almost complete loss of pigment in body and eye.
[a]Additional nonspecific toxicity.

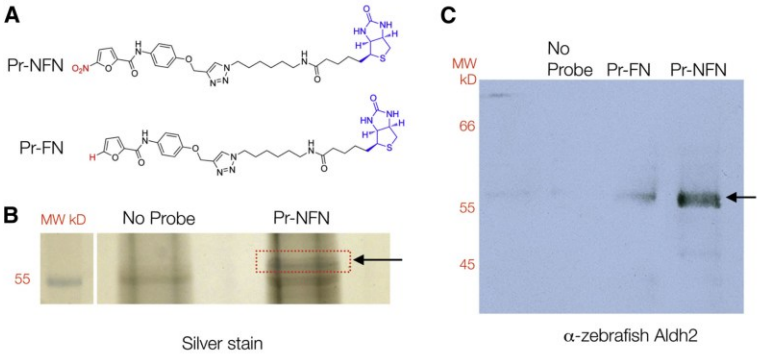

Figure 2. 5-Nitrofurans Bind Aldh2 in Zebrafish

(A) Biotinylated probes linked to a 5-nitrofuran (Pr-NFN) and a control furan (Pr-FN). Biotin is labeled in blue and the 5-nitro or modification moiety in red.

(B) Silver stain of protein bands identified using Pr-NFN probe, or streptavidin beads alone as a control (No Probe). The red box indicates the region of the gel that was isolated for mass spectrometry analysis (arrow) at 57 kD.

(C) Western blot of zebrafish protein bound to the no-probe control, the furan (Pr-FN) control, or the 5-nitrofuran probe (Pr-NFN), and probed with zebrafish anti-Aldh2 antibodies. A band corresponding to 57 kDa is indicated (arrow). MW, molecular weight.

See also Figure S2 and Table S1.

provide information about alternative methods of 5-nitrofuran processing.

Nitrofurans Bind ALDH2 in Zebrafish

To identify the possible targets of the 5-nitrofurans, we performed affinity purification to capture 5-nitrofuran interacting proteins in zebrafish extracts. First, we generated a series of 5-nitrofuran derivatives and tested their activity in zebrafish (Table 1; Supplemental Information). Importantly, 5-nitrofuran derivatives containing a phenyl ring (NFN5, NFN5.1, NFN5.2) effectively targeted zebrafish melanocytes (Table 1). As substitution at the *para* position of the phenyl ring in NFN5.1 and NFN5.2 was tolerated, a 5-nitrofuran probe was generated by linking to biotin through the *para* position of the phenyl ring (Pr-NFN; Figure 2A). Next, the 5-nitrofuran probe was bound to streptavidin beads, and protein complexes captured from zebrafish extract derived from 3-day embryos were subjected to tandem mass spectrometry. A 57-kD binding protein was identified as aldehyde dehydrogenase (Aldh) 2b (Figure 2B; Table S1). Zebrafish have two *aldh2* (Lassen et al., 2005; Song et al., 2006) genes (*a* and *b*) that are orthologs of human ALDH2 (Figure S2); *aldh2b* is expressed in neural crest derived cells, including presumptive melanocytes (Thisse et al., 2001). To confirm the identity of the 57-kD protein, we repeated our affinity purification protocol and performed western blotting with anti-Aldh2 zebrafish antibodies raised against both a and b forms of Aldh2 (Lassen et al., 2005) (Figure 2C). As a control, we generated a furan probe that was identical to the nitrofuran probe except that it lacked the 5-NO_2 functional group (Pr-FN; Figure 2A). Aldh2 (either a or b) bound more strongly to the 5-nitrofuran probe than to the control probe, and not to streptavidin beads alone (Figure 2C). These experiments validate Aldh2 as a 5-nitrofuran binding protein.

Aldh2 Is Required for 5-Nitrofuran Activity in Zebrafish

Aldh2 catabolizes toxic aldehydes in the liver after alcohol consumption (Druesne-Pecollo et al., 2009), in the heart after ischemia (Chen et al., 2008), and in dopamine metabolism (Yao et al., 2010). We asked if 5-nitrofuran toxicity was dependent on Aldh2 in zebrafish. The natural product daidzin, found in the Kudzu vine (*Pueraria lobata*), is a potent and specific inhibitor of human ALDH2 and has long been used in traditional medicines as an antidipsotropic (Keung and Vallee, 1993a, 1993b; Lowe et al., 2008). More recently, ALDH2 inhibitors have been shown to reduce anxiety associated with treatment of cocaine and alcohol addiction (Arolfo et al., 2009; Yao et al., 2010). We reasoned that ALDH2 inhibitors were likely to prevent the toxicity of 5-nitrofurans in zebrafish because (1) human ALDH2 is closely related to zebrafish Aldh2 (a and b forms) (Figure S2), and (2) computational modeling of zebrafish Aldh2b bound to daidzin suggests that critical drug-protein interactions are conserved between species (Figure 3A). Treatment of zebrafish embryos with daidzin protected melanocytes from the cytotoxicity of the coadministered 5-nitrofuran NFN1 (Figure 3B), as well as the clinically active 5-nitrofuran nifurtimox (Figure 3C). Thus, coadministration of the Aldh2 inhibitor daidzin abrogates the activity of NFN1 and nifurtimox in zebrafish.

To provide additional evidence that the action of daidzin was by inhibition of Aldh2 and not an additional unintended target, zebrafish embryos were cotreated with NFN1 and a second ALDH1/2 inhibitor, disulfiram (DSF). DSF, also called Antabuse and Antabus, is used to treat chronic alcoholism by preventing the ALDH2-dependent metabolism of alcohol and producing enhanced sensitivity to alcohol. DSF also chelates copper, and we and others have found that DSF prevents pigmentation of zebrafish melanocytes prior to melaninization, most likely due to inhibition of copper-dependent pigmentation enzymes (Figure S3; O'Reilly-Pol and Johnson, 2008). DSF treatment of embryos 3 days postfertilization (dpf) that had fully pigmented melanocytes had no effect on melanocyte integrity, while DSF prevented melanocyte toxicity upon cotreatment with NFN1 (Figure 3B). Taken together, these experiments with two chemically independent ALDH2 inhibitors support a biological role for Aldh2 in the bioactivation of 5-nitrofuran melanocytotoxicity in zebrafish.

ALDH2 is regulated in a tissue-specific manner, and in particular, εPKC can directly modulate ALDH2 during ischemic preconditioning in the heart (Chen et al., 2008, 2010). We identified the PKC inhibitors PKC412 and Ro318220 as chemical suppressors of 5-nitrofuran activity in zebrafish by screening a library of 80 known kinase inhibitors. Treatment of 3 dpf zebrafish embryos with PKC412 or Ro318220 had no effect on melanocyte viability (Figure 3B). However, treatment with PKC412 or Ro318220 prevented NFN1 activity in melanocytes (Figure 3B). We tested a third PKC inhibitor, GF109203X, that can inhibit ethanol or dopamine D2 receptor agonist NPA-induced intracellular translocation of εPKC (Yao et al., 2008). GFX109203X had no effect on melanocytes alone, but we found that it could also

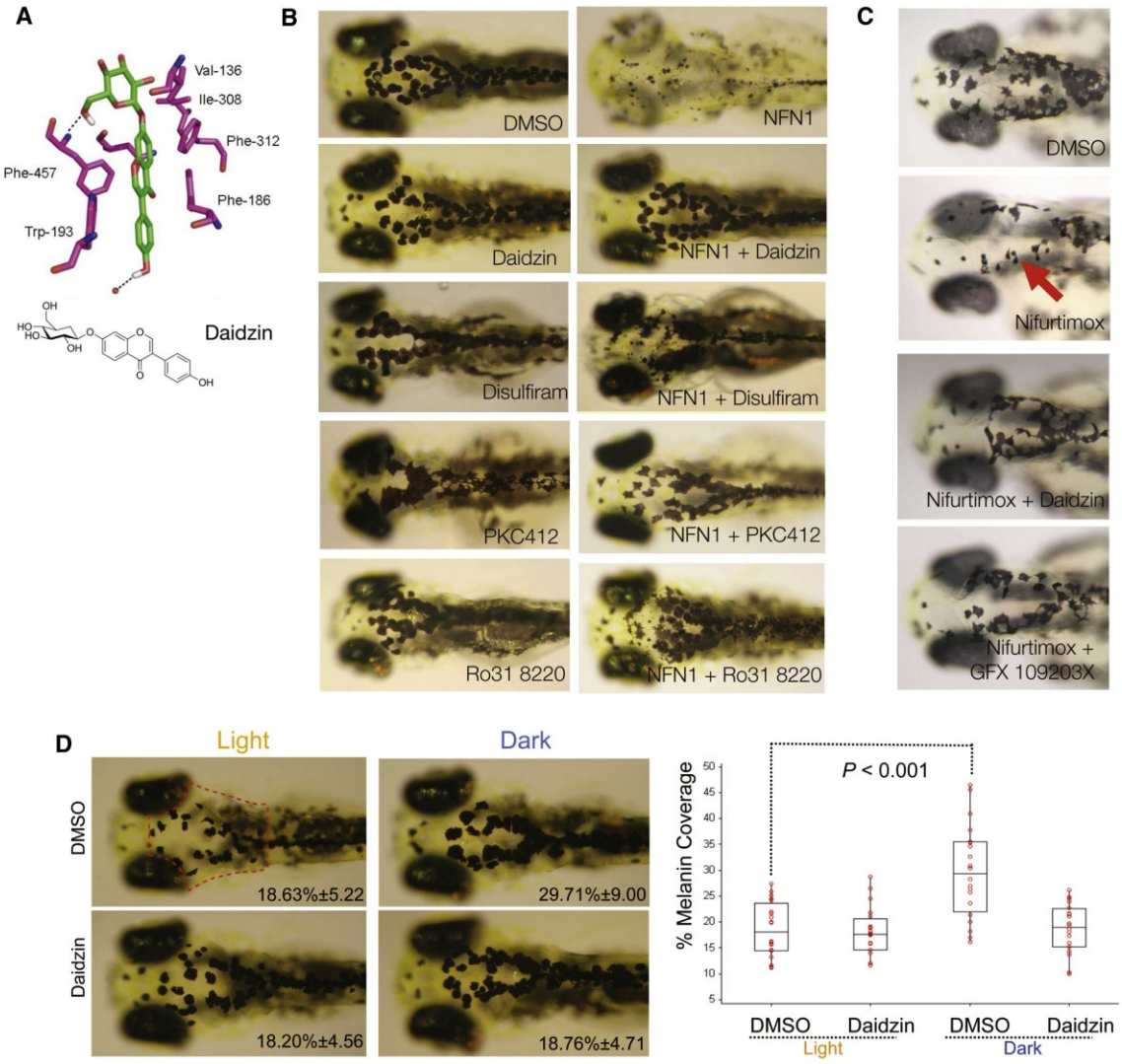

Figure 3. Aldh2 Is Responsible for 5-Nitrofuran Activity in Zebrafish

(A) A predicted model of daidzin binding to zebrafish ALDH2b, based on key residues involved in the human ALDH2-daidzin (PDB 2vle) protein-ligand interaction (Lowe et al., 2008). The equivalent residues in zebrafish Aldh2b are shown. Human ALDH2→Zebrafish Aldh2 2b (Phe-459→Phe-457; Phe-170→Phe-186; Trp-177→Trp-193; Val-120→Val-136; Phe-296→Phe-312; Phe-292→Ile-308; Asp-457→Asn-473; Cys-303→Cys-319).

(B) Aldh2 and PKC inhibitors prevent 5-nitrofuran activity in zebrafish. Examples of zebrafish embryos treated at 2 dpf with 20 μM of the ALDH inhibitors daidzin or DSF for 1 hr, or with 20 μM of the PKC inhibitors PKC412 or Ro318220, and then treated with 5 μM NFN1 or 0.1% DMSO alone for 2 days. Experiments were repeated at least three times, with n > 10 embryos per condition.

(C) Examples of 2 dpf zebrafish embryos pretreated with DMSO, 30 μM of daidzin, or the PKC inhibitor GFX 109203X for 1 hr, and then treated with 50 μM nifurtimox for 7 hr. Punctate melanocytes are indicated. Experiments were repeated at least three times (n = 5–10 embryos per condition) and treatment-condition cohorts blind scored.

(D) Daidzin alters background adaptation in zebrafish embryos. (Left) Images of fixed zebrafish embryos (5 dpf) treated with 0.1% DMSO or 10 μM daidzin, and shifted from a dark environment to a light environment (light), or vice versa (dark). The average percentage of melanin coverage (within the area indicated by the red dotted outline) for each treatment condition ± SD is indicated. (Right) Box plot of melanin coverage (y axis) for each embryo in different treatment conditions (x axis). Individual values taken from one of three experiments are shown as red circles. The box depicts the lower quartile and the upper quartile, with the median depicted by the intersecting line. Whiskers extend between the minimum and maximum of all the data. In DMSO-treated embryos, melanocytes are significantly contracted in the light and expanded in the dark ($p < 0.001$, n = 20 for each condition; ANOVA, 95% confidence interval [CI] 11.081[5.966, 16.195]). Zebrafish treated with daidzin contract their melanin in response to light environment but do not significantly expand their melanin in response to dark environments (95% CI 0.563[−4.552, 5.677]). The experiment was repeated three separate times with embryos at 5 dpf (n = 5–20 embryos per condition) and once with embryos at 4 dpf (n = 10 embryos per condition).

See also Figure S3.

suppress NFN1 melanocytotoxicity (Figure S3). GFX109203X was also effective at preventing the activity of nifurtimox in zebrafish melanocytes (Figure 3C). Although we do not know if PKC directly enhances Aldh2b activity or expression in zebrafish, these results suggest that PKC activity is important for 5-nitrofuran cytotoxicity within the melanocyte.

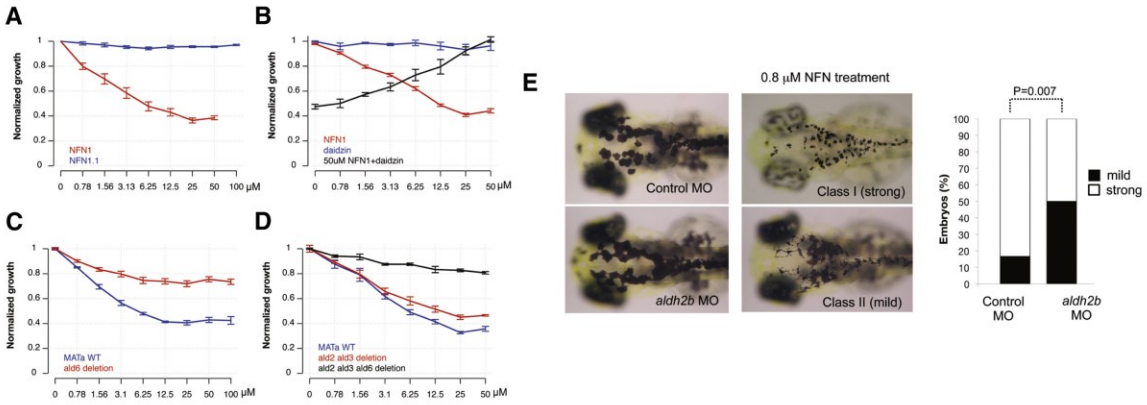

Figure 4. Cross-Species Conservation of 5-Nitrofuran-ALDH2 Interaction in Yeast

(A) Yeast cultures were treated with NFN1 (red) or NFN1.1 (blue). OD values were normalized against DMSO-treated controls. The mean of two experiments with three replicates is shown; error bars represent the SE.

(B) Daidzin-NFN1 drug interaction was assessed by combination matrix assays in 96 well plates. Cultures were treated with NFN1 (red) or with daidzin in the absence (blue) or presence (black) of 50 μM NFN1. The average normalized growth of three experiments is shown; error bars represent the SE.

(C) Normalized growth in the presence of NFN1 was determined for wild-type (blue) and the *Δald6* strain (red). Data points are the mean of four replicates; error bars represent the SE.

(D) NFN1 dose response curves for Δ*ald2*Δ*ald3* (red) and the Δ*ald2*Δ*ald3*Δ*ald6* (black) strains, as well as wild-type control (blue), were generated and normalized against DMSO-treated controls. The average of three replicates is shown; error bars represent the SE.

(E) Control (n = 24) or *aldh2b* splice-site morphants (n = 62) at 3 dpf without NFN1 treatment (left) or with 0.8 μM NFN1 treatment (right). Embryos were scored as class I (strong) or class II (mild) sensitivity to NFN1 (bar graph). *aldh2b* morphant embryos were less sensitive to NFN1 treatment compared to control morphants ($p = 0.007$; 95% CI [0.139, 0.528]; Fisher's exact test).

See also Figure S4.

ALDH2 Contributes to Background Adaptation in Zebrafish Melanocytes

We wanted to understand why zebrafish melanocytes were sensitive to 5-nitrofuran treatment, when this is not a feature of 5-nitrofuran toxicity in patients. Unlike human melanocytes, zebrafish melanocytes respond to environmental conditions by concentrating or dispersing their melanosomes in light or dark conditions, respectively (Logan et al., 2006). This effect is termed background adaptation and is a dopaminergic response (Logan et al., 2006). A role of Aldh2 in zebrafish background adaptation has not been previously identified, but *aldh2b* is specifically expressed in developing pigment cells (Thisse et al., 2001), and ALDH2 is required for dopamine metabolism in mammals (Chen et al., 2010). We tested the effects of ALDH2 inhibition on background adapation in zebrafish and found that daidzin treatment blocked dispersal of melanin in zebrafish melanocytes in the dark (Figure 3D). These observations suggest that Aldh2 activity is required for regulation of zebrafish background adaptation, and they may explain the sensitivity of zebrafish melanocytes to 5-nitrofurans.

Multispecies Conservation of the 5-Nitrofuran-ALDH Interaction

Chemical-genetic and chemical-chemical interactions identified in yeast are often conserved in multicellular species including zebrafish and mammals (Ishizaki et al., 2010). Budding yeast have five ALDH genes (*ALD2–6*) that all share 42%–48% similarity with human *ALDH 1/2* (Figure S2). Yeast also have two fungal-specific nitroreductase-like proteins, but these share little similarity with the nitroreductases that are known to reduce nitrofurans (de Oliveira et al., 2007). To establish that 5-nitrofurans also showed activity in yeast, liquid cultures were treated with increasing concentrations of NFN1 (Figure 4A). Yeast were highly sensitive to NFN1, which inhibited growth even at submicromolar concentrations. In contrast, treatment with the control furan compound, NFN1.1, had no effect on yeast growth, even at 100 μM. These data indicate that the toxicity of 5-nitrofurans in yeast is dependent on the 5-NO_2 moiety. To test whether NFN1 toxicity was dependent on ALDH activity, we tested drug combinations in yeast cultures. Increasing concentrations of daidzin rescued the effects of 50 μM NFN1 on the yeast growth rate in a dose-dependent fashion, whereas daidzin alone had no effect on growth (Figure 4B).

Mutations that render yeast resistant to a specific compound can provide direct links to the target pathway (Ishizaki et al., 2010). We determined whether yeast strains bearing deletions in each of the *ALD* genes (orthologs of human and zebrafish *ALDH1/2*) were resistant to 5-nitrofuran treatment. The *ald2*Δ, *ald3*Δ, *ald4*Δ, and *ald5*Δ deletion strains each exhibited the same sensitivity to NFN1 as wild-type (data not shown). In contrast, an *ald6*Δ strain was significantly less sensitive to NFN1 treatment, as was an *ald2*Δ*ald3*Δ double-deletion strain (Figures 4C and 4D). These effects of different *ald* mutations appeared to be additive, as a triple *ald2*Δ*ald3*Δ*ald6*Δ deletion strain was almost completely resistant to 50 μM NFN1 treatment (Figure 4D). Once activated, 5-nitrofurans cause DNA damage, and consistent with this observation, we find that chemical-genetic profiles in yeast indicate that disruption of DNA damage repair pathways causes hypersensitivity to 5-nitrofurans (Figure S4).

To further validate the genetic dependence of 5-nitrofuran bioactivity on Aldh2, we used morpholino oligonucleotides (MOs) to knockdown *aldh2b* in zebrafish. Single-cell embryos

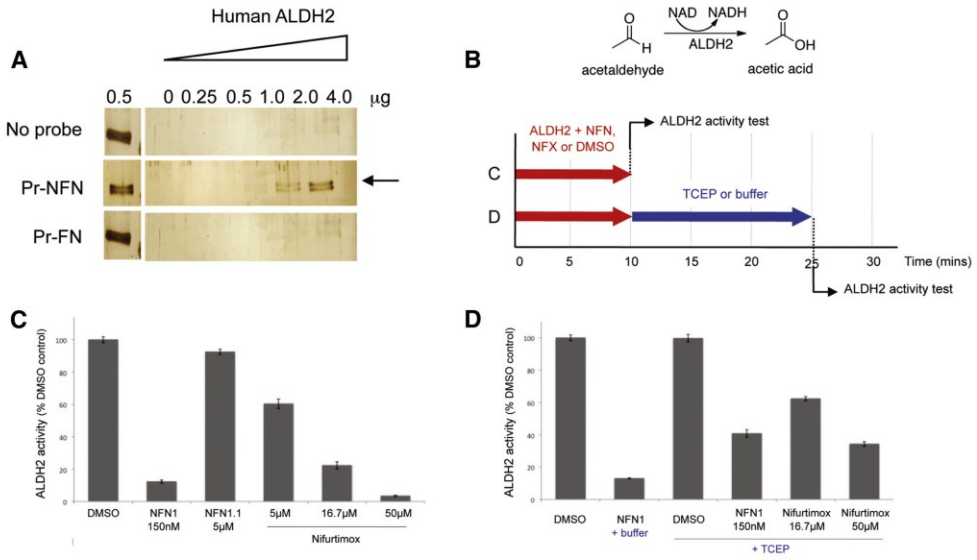

Figure 5. 5-Nitrofurans Bind and Are Substrates for Human ALDH2 In Vitro

(A) Binding of purified human ALDH2 by 5-nitrofuran probe (Pr-NFN), a furan control probe (Pr-FN), or streptavidin beads alone (No Probe). Arrow indicates ALDH2 protein, ALDH2 input lane (0.5 μg).

(B) Schematic overview of chemical reaction used to monitor recombinant human ALDH2 activity and experimental design. In experiment C (red arrow), ALDH2 was incubated with 1% DMSO, NFN1, and NFN1.1 or Nifurtimox for 10 min., and then ALDH2 activity was assessed. In experiment D (red + blue arrows), ALDH2 was incubated with 1% DMSO, NFN1, or Nifurtimox for 10 min., incubated with 0.5 mM TCEP or buffer alone for a further 15 min., and then ALDH2 activity was assessed.

(C) Bar graph of spectrophotometric analysis of the rate of production of NADH (monitored at 341 nm) by ALDH2 (expressed as a percentage of DMSO control treatment) with DMSO, NFN1, NFN1.1, and Nifurtimox.

(D) Bar graph of spectrophotometric analysis of the rate of production of NADH by ALDH2 after combined treatment of DMSO, NFN1, and Nifurtimox with TCEP or buffer. Enzyme buffer = 50 mM sodium phosphate (pH 7.4). Error bars are SD; experiments were repeated in triplicate.

were injected with a splice-site-blocking *aldh2b* MO and at 2 dpf were treated with NFN1. PCR analysis of the splice-site MO indicated that *aldh2b* morphants had reduced levels of correctly spliced *aldh2b* transcript in addition to a missplined transcript, indicating that the *aldh2b* morphants are hypomorphic for *aldh2b* (Figure S4). We consistently found that the splice-site-blocking *aldh2b* MO conferred partial resistance to a low treatment dose (0.8 μM) of NFN1 melanocytotoxicity (Figure 4E). An *aldh2b*-translation-block MO also conferred partial resistance to a short NFN1 treatment (Figure S4). We conclude that there is a genetic dependence on Aldh2b for 5-nitrofuran activation in zebrafish, in line with genetic studies in yeast.

5-Nitrofurans Are Substrates for Human ALDH2

There are 19 ALDH enzymes in humans, each with specific targets and additional activities (Marchitti et al., 2008). To determine whether the 5-nitrofuran-ALDH2 interaction is conserved in humans we asked whether human ALDH2 could bind 5-nitrofurans directly. Purified human ALDH2 was added to the 5-nitrofuran probe (Pr-NFN), a furan control probe (Pr-FN), or streptavidin beads alone. In an analogous manner to the experiments using zebrafish extracts, human ALDH2 binding was strongly enriched in association with the 5-nitrofuran, while the control furan and the streptavidin beads alone did not bind ALDH2 (Figure 5A).

Given our results with daidzin in yeast and zebrafish, we proposed that NFN1 was probably a substrate of ALDH enzymes. ALDH2 enzymes have reducing potential as well as dehydrogenase activity (Chen et al., 2002; Marchitti et al., 2008), and it has been shown that in the absence of a reducing agent, ALDH2 inactivates itself during the bioactivation of substrates such as nitroglycerine (GTN) (Chen et al., 2010; Wenzel et al., 2007). Consistent with this, we found that in the absence of a reducing agent, NFN1, but not the no-nitro NFN1.1, inactivated recombinant human ALDH2 in vitro (Figures 5B–5D). Likewise, we found that ALDH2 activity was reduced by 39.6%, 77.6%, and 96.5% following 10 min incubation with 5 μM nifurtimox, 16.7 μM nifurtimox, and 50 μM nifurtimox, respectively (Figure 5C). Importantly, as with the zebrafish studies, these experiments were performed with nifurtimox at concentrations that are within the range of those recorded in the serum of nifurtimox-treated patients (Paulos et al., 1989; Saulnier Sholler et al., 2011). For both NFN1- and nifurtimox-inactivated ALDH2, the subsequent addition of a reducing agent (TCEP) led to partial reactivation of the enzyme, in line with literature studies using the accepted substrate, GTN (Figure 5D). We observe that the NFN1-ALDH2 interaction is stronger than the nifurtimox-ALDH2 in zebrafish and in our biochemical assay. This raises the possibility that the mechanism of action of nifurtimox is more complex than that of NFN1, or that NFN1 may in fact be a more effective 5-nitrofuran substrate of ALDH2 than nifurtimox.

Daidzin Does Not Affect Nifurtimox Trypanocidal Activity

In an attempt to develop a clinically testable hypothesis, we examined the genome sequence of the trypanosomatids to

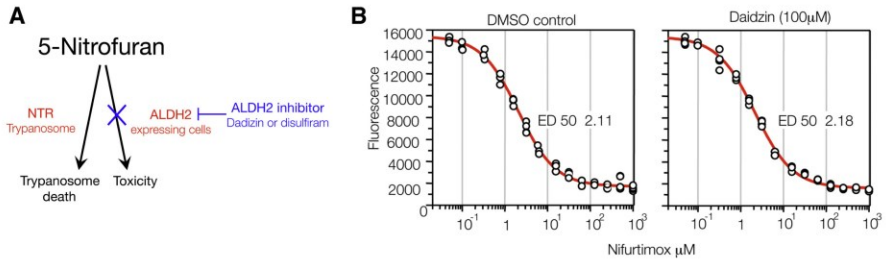

Figure 6. ALDH2 in Trypanosomes

(A) Schematic of a 5-nitrofuran-daidzin combination-treatment strategy. ALDH2 can cause 5-nitrofuran bioactivtion in ALDH2-expressing cells (e.g., zebrafish melanocytes), but not in trypanosomes because they lack ALDH2 (see also Figure S2). We propose that cotreatment with an ALDH2 inhibitor such as daidzin could limit 5-nitrofuran toxicity without interfering with anti-trypanosome activity.

(B) Viability of *Trypanosoma brucei* (bloodstream form) at 37°C after 72 hr treatment with increasing concentrations of nifurtimox in the absence or presence of daidzin (100 μM). Experiments were conducted twice in replicates of four; a representative set of data from one experiment containing four replicates is shown. ED, effective dose.

identify possible ALDH enzymes in *T. brucei*, *T. cruzi* and *Leishmania* (Figure S2) (Aslett et al., 2010; Cross, 2005; Lowe et al., 2008; Marchitti et al., 2008; Sobreira et al., 2011). Given the absence of an obvious ALDH2 in *Trypanosoma* we hypothesized that while Aldh2 inhibition would protect the zebrafish melanocytes and yeast cells from 5-nitrofuran activity, ALDH2 inhibitors might not protect trypanosomes from 5-nitrofuran sensitivity (Figure 6A). We grew the bloodstream-form *T. brucei* (strain 427) in HMI9 media and determined the trypanocidal activity of nifurtimox in the absence and presence of daidzin. Trypanosomes were stained with an Alamar Blue vital dye as an indicator of *Trypanosoma* survival. We found that nifurtimox was equally effective in the absence (ED_{50} = 2.12 ± 0.17 μM; slope 1.00) and presence (ED_{50} = 2.18 ± 0.10 μM; slope 0.98) of daidzin (Figure 6B). The trypanocidal effect of nifurtimox against bloodstream *T. brucei* obtained in these assays was comparable to previously observed effects (Priotto et al., 2009; Sokolova et al., 2010). Daidzin treatment alone showed no trypanocidal effect up to 100 μM (data not shown). We conclude that daidzin does not interfere with 5-nitrofuran trypanocidal activity, consistent with a lack of an *ALDH2* in trypanosomes.

DISCUSSION

We have used a multispecies, chemical-biology approach to identify 5-nitrofurans as substrates for ALDH2. We have identified a series of 5-nitrofuran compounds by phenotypic screening in zebrafish and have shown that 5-nitrofuran-specific melanocytotoxicity in vivo is mediated at least in part by Aldh2 (Figures 1 and 3). Zebrafish gene products are usually conserved in humans and are often sensitive to clinically active drugs at physiological concentrations (Zon and Peterson, 2005). As shown here, phenotypic chemical screens in zebrafish are effective because (1) the rapid and cell-type-specific toxicity of 5-nitrofurans can be visualized in real time (Movie S1), (2) the whole animal is amenable to pharmacological studies (Figures 1A and 1B), and (3) initial structure activity relationships can be determined to enable the design of biologically relevant probes for affinity purification (Figure 2; Table 1).

Despite the benefits of phenotypic screens in zebrafish, target identification remains a challenge in chemical biology (Laggner et al., 2012; Taylor et al., 2010; Zon and Peterson, 2005). Here, we use parallel approaches to enable identification of an important target of 5-nitrofurans. First, we used affinity chromatography to identify Aldh2 as a 5-nitrofuran binding partner and confirmed the dependence on the 5-NO_2 functional group using an inactive furan probe (Figure 2). Second, we used computational modeling to predict that the ALDH2 inhibitor daidzin would be active in zebrafish (Figure 3A), and used two chemically distinct ALDH2 inhibitors (daidzin and DSF) to confirm the biological relevance of the 5-nitrofuran-Aldh2 interaction in vivo (Figures 3B and 3C). Third, we showed cross-species conservation of the drug-drug interactions in the evolutionarily distant budding yeast system (Figures 4A and 4B). Fourth, we used genetic mutants in yeast and gene knockdowns in zebrafish to validate a genetic dependence on ALDH activity for 5-nitrofuran activity in vivo (Figures 4C–E). Fifth, we showed that the 5-nitrofuran-ALDH2 interaction is maintained with human ALDH2 (Figure 5A). Finally, using a literature-precedent method, we showed that 5-nitrofurans are direct substrates of human ALDH2 (Figures 5B–5D).

We find that zebrafish melanocytes are sensitive to the 5-nitrofurans because unlike human melanocytes, zebrafish melanocytes use ALDH2 to elicit a melanocyte background adaptation response (camouflage; Figure 3D). While additional host enzymes, possibly including other ALDHs, may bioactivate 5-nitrofurans in patients, we speculate that, in line with our studies in zebrafish and yeast, daidzin may protect cells that specifically express ALDH2, such as the liver and dopaminergic neuronal cells (Figure 6A). Although 500 million individuals worldwide have an ALDH2-inactive variant (Druesne-Pecollo et al., 2009), it is unknown whether these genetic variants contribute to the variability of 5-nitrofuran-associated side effects; our chemical-genetic data in yeast and zebrafish (Figure 4) suggest that this hypothesis could be examined in the clinic. 5-Nitrofurans have also recently become anticancer agents, and nifurtimox is currently in clinical trials for relapsed/refractory pediatric neuroblastoma and medulloblastoma (Saulnier Sholler et al., 2011). It is possible that 5-nitrofuran bioactivation by ALDH2 explains the sensitivity of these dopaminergic cancers to nifurtimox. We find that human melanoma cells are also sensitive to nitrofurans, that DNA damage occurs, and that this activity is dependent on the NO_2 functional group present in NFN1 (Figure S4). Taken together with the hypersensitivity of yeast DNA-damage mutants to NFN1, these results suggest that once activated, the cytotoxic effects of 5-nitrofurans arise through a similar DNA-damage-dependent mechanism across species, although it is unclear at this time whether NTR- and ALDH2-mediated activation of 5-nitrofurans leads to exactly the same toxic intermediates.

We argue that NFN1, but not the no-nitro NFN1.1, is a substrate for recombinant human ALDH2 in vitro (Figure 5).

Analogous observations have been made in ALDH2 bioactivation of nitroglycerin (Chen et al., 2010; Wenzel et al., 2007), thereby raising the interesting question of how 5-nitrofurans are bioactivated by ALDH2. ALDH2 enzymes have reducing potential as well as dehydrogenase activity (Chen et al., 2002; Marchitti et al., 2008), and we envision that ALDH2 may reduce the nitro group of 5-nitrofurans, potentially generating nitroso-, hydroxylamine, and/or amine intermediates with concomitant oxidation of the enzyme. Interestingly, dithiothreitol (DTT) can react with 5-nitrofurans, leading to oxidation of DTT to the corresponding disulfide (L.Z. and N.W., unpublished data). As DTT contains two thiols in close proximity, in an analogous manner to the active site of ALDH2, we suggest that the reactions of 5-nitrofurans with ALDH2 and DTT may be linked by a common mechanism.

5-Nitrofurans are important therapeutic agents, yet many patients suffer from unacceptable drug-induced toxic side effects. One approach to solving this problem is to identify new antitrypanosome drug targets, such as the recently identified *N*-myristoyltransferase inhibitors (Frearson et al., 2010) that have been validated in mouse trypanosomiasis models. Based on our studies in model systems and in vitro, we propose a complementary approach that involves targeting and minimizing the toxic side effects of current therapies, thereby allowing more patients to benefit from approved treatment regimes that are already available (Figure 6A). If the 5-nitrofuran-ALDH2 interaction is conserved in patients, then combination therapy to treat 5-nitrofuran toxic side effects may be testable, because (1) ALDH2 is a targetable enzyme; (2) the ALDH2 inhibitors daidzin and DSF are both currently available at low cost and show activity in humans with limited toxicity; and (3) our analysis indicates that *T. brucei* and *T. cruzi* do not have a close ALDH2 homolog (Figure S2), nor is *T. brucei* protected from nifurtimox by daidzin (Figure 6B). Our findings provide impetus for addressing the role of ALDH2 in 5-nitrofuran activation in the preclinical and clinical setting.

SIGNIFICANCE

Discovering how drugs work in vivo and identifying unintended drug targets is a fundamental challenge in chemical biology. Nifurtimox is one of only two drugs used to treat Chagas disease, caused by *Trypanosoma cruzi* infection, which is estimated to affect over 10 million people per year and kills between 15,000 and 50,000 annually. Like other 5-nitrofurans, nifurtimox is a prodrug that is activated by parasite-specific nitroreductases to a toxic form. Despite the absence of nitroreductases in humans, 5-nitrofurans cause significant clinical off-target toxic side effects that interfere with patients' ability to complete the treatment course. There has been no significant improvement in trypanosome disease treatment for 40 years, and there is currently no treatment strategy in patients to reduce the burden of these toxic side effects of existing drugs.

Here, we use model organism chemical genetics to explore the basis for this toxicity. We use the zebrafish model (1) to identify toxic effects of 5-nitrofuran compounds; (2) as a platform for structure-activity relationships and target identification; and (3) to show that the toxicity of 5-nitrofurans in zebrafish can be prevented by cotreatment with aldehyde dehydrogenase 2 (ALDH2) inhibitors. We then show that the ALDH2-5-nitrofuran interaction is conserved in yeast and with human ALDH2 and argue that 5-nitrofurans are a direct substrate of human ALDH2. We extend these findings to show that the 5-nitrofuran nifurtimox also has Aldh2-dependent activity in zebrafish, and that it is a direct substrate of human ALDH2. Thus, we show in model systems that drug treatments combining ALDH2 inhibitors with 5-nitrofurans block the 5-nitrofuran unintended biological activity, and we propose that similar treatments based on a readily available combination of inexpensive approved drugs may prevent some of the clinical side effects caused by 5-nitrofurans.

EXPERIMENTAL PROCEDURES

Zebrafish Small-Molecule Screens and Treatments

All zebrafish work was done in accordance with United Kingdom Home Office Animals (Scientific Procedures) Act (1986) and approved by the University of Edinburgh Ethical Review Committee. The chemical library was a collection of 1576 Maybridge compounds (Ishizaki et al., 2010). Two 4 hpf embryos were arrayed in 96 well plates containing 10 μM of compound in 1% DMSO in 300 μl of E3 embryo medium. Embryos were assessed and imaged for phenotypic changes at 28, 36, 48, and 56 hpf. For the screening of The Screen-Well Kinase Inhibitor Library (Enzo Life Sciences), five embryos (24 hpf) were placed into each well of a 24 well plate (Corning) containing 20 μM NFN1 (BTB05727, Maybridge Screening compounds) and 5, 10, or 20 μM of a corresponding compound (total volume 1 ml per well). For cotreatment experiments, five 36–48 hpf embryos were arrayed in 24 well plates in 600 μl to 1 ml of E3 embryo medium and pretreated with ALDH or PKC inhibitors (1–7 hr), and then treated with 0.5–5 μM NFN1 or 50 μM nifurtimox.

Affinity Purification and Coimmunoprecipitation with 5-Nitrofuran Beads

Lysate was generated from approximately 900 3 dpf zebrafish in 300 μl of RIPA buffer (2 M Tris pH 7.5, 5 M NaCl, 1% NP40, Na-deoxycholate, 10% SDS, 0.5 M NaF, 1 M β-glycosyl phosphate and protease-inhibitor cocktail tablet [Roche]), centrifuged at 4°C (25 min), transferred to a new tube, and kept on ice. Protein capture was performed using a pull-down biotinylated protein:protein interaction kit (Pierce) using the biotinylated chemical probe (5 μl 10 mg/ml DMSO solution), and bead complexes were washed with 0.1 M NaCl TBS buffer four times to reduce nonspecific binding. Beads were boiled in 3× Laemmli buffer with DTT for 5 min and run on 10% SDS-PAGE gel for electrophoresis. Captured proteins were visualized with a Silverquest silver-staining kit and/or Colloidal blue-staining kit (Invitrogen). The mass spectroscopy was analyzed in the University of Dundee FingerPrints Proteomics Facility. For western blotting, protein was detected using rabbit anti-zebrafish Aldh2 (1:1000) and goat anti-rabbit antibody (1.5:5000; Calbiochem).

In Vitro Binding Assay

ALDH2 human recombinant protein (ProSpec) was added to 4 μl 10 mg/ml of chemical probe with 100 μl TBS buffer and incubated at room temperature for 1 hr. Streptavidin bead suspension (50 μl) was added to the mixture (room temperature; 1 hr), the supernatant was removed, and beads were washed with 4 × 0.1 M NaCl TBS buffer, boiled in 3× Laemmli buffer with DTT for 5 min, and run on 10% SDS-PAGE gel for electrophoresis. The bands were detected by silver staining (Invitrogen).

Molecular Modeling

Using methods analogous to those used previously (Medda et al., 2009), the zebrafish Aldh2b homology model was generated using the Swiss model server using bovine ALDH2 (PDB code 2AG8). The daidzin structure was generated using the PRODRG server. The docking studies were performed

using the program GOLD. All visualization and analysis was performed using Pymol.

Yeast Growth Assays

Overnight *S. cerevisiae* BY4741 cultures in SC media were diluted (OD_{600} 0.025) and dispensed into 96 well Corning Costar assay plates. Quantitative growth curves were generated in Tecan Sunrise plate readers at 30°C 564 rpm with automated absorbance reads every 15 min. Growth-curve data were used to determine when control cultures reached late log phase, and OD values of the entire plate at that time point were used to calculate normalized growth values. Data were analyzed with custom R scripts to generate plots. For the deletion-strain growth curves, normalization was performed against control wells for each strain.

Trypanocidal Studies

The trypanocidal activity of nifurtimox in the absence and presence of daidzin (100 μM) against *Trypanosoma brucei* bloodstream form (strain 427) were cultured at 37°C in HMI9 medium supplemented with 2.5 μg ml^{-1} G418, and viability was determined using the Alamar Blue test, as described previously (Mikus and Steverding, 2000). The data were fitted using GraFit software to obtain ED_{50} ± SD and slope factors.

Supplemental Experimental Procedures

The synthesis of all the NFNs and NFN-based affinity probes is described in the Supplemental Information.

SUPPLEMENTAL INFORMATION

Supplemental Information includes four figures, one table, Supplemental Experimental Procedures, and one movie and can be found with this article online at http://dx.doi.org/10.1016/j.chembiol.2012.05.017.

ACKNOWLEDGMENTS

We are grateful to I. Jackson, D. Harrison, K. Ball, M. Frame, and N. Hastie for discussions and reading of the manuscript, V. Vasiliou for the zebrafish Aldh2 antibody, and G. Sholler and S. Wilkinson for nifurtimox reagents. This work was funded by the NIH (S.L.J.), the Wellcome Trust (T.K.S.), a Royal Society University Research Fellowship (N.J.W.), a Royal Society Wolfson Research Merit Award (M.T.), a Scottish Universities Life Sciences Alliance Research Chair (M.T.), the European Research Council (233457-SCG to M.T.), Cancer Research UK (L.Z. and N.J.W.), the European Commision FP-7 ZF-CANCER project (E.E.P.), Medical Research Scotland (E.E.P. and H.I.), and the Medical Research Council (E.E.P., K.T., Z.Z., and P.G.).

Received: March 6, 2012
Revised: May 10, 2012
Accepted: May 14, 2012
Published: July 26, 2012

REFERENCES

Arolfo, M.P., Overstreet, D.H., Yao, L., Fan, P., Lawrence, A.J., Tao, G., Keung, W.M., Vallee, B.L., Olive, M.F., Gass, J.T., et al. (2009). Suppression of heavy drinking and alcohol seeking by a selective ALDH-2 inhibitor. Alcohol. Clin. Exp. Res. *33*, 1935–1944.

Aslett, M., Aurrecoechea, C., Berriman, M., Brestelli, J., Brunk, B.P., Carrington, M., Depledge, D.P., Fischer, S., Gajria, B., Gao, X., et al. (2010). TriTrypDB: a functional genomic resource for the Trypanosomatidae. Nucleic Acids Res. *38* (Database issue), D457–D462.

Castro, J.A., de Mecca, M.M., and Bartel, L.C. (2006). Toxic side effects of drugs used to treat Chagas' disease (American trypanosomiasis). Hum. Exp. Toxicol. *25*, 471–479.

Chen, C.H., Budas, G.R., Churchill, E.N., Disatnik, M.H., Hurley, T.D., and Mochly-Rosen, D. (2008). Activation of aldehyde dehydrogenase-2 reduces ischemic damage to the heart. Science *321*, 1493–1495.

Chen, C.H., Sun, L., and Mochly-Rosen, D. (2010). Mitochondrial aldehyde dehydrogenase and cardiac diseases. Cardiovasc. Res. *88*, 51–57.

Chen, Z., Zhang, J., and Stamler, J.S. (2002). Identification of the enzymatic mechanism of nitroglycerin bioactivation. Proc. Natl. Acad. Sci. USA *99*, 8306–8311.

Coura, J.R., and Viñas, P.A. (2010). Chagas disease: a new worldwide challenge. Nature *465*, S6–S7.

Cross, G.A. (2005). Trypanosomes at the gates. Science *309*, 355.

de Oliveira, I.M., Henriques, J.A., and Bonatto, D. (2007). In silico identification of a new group of specific bacterial and fungal nitroreductases-like proteins. Biochem. Biophys. Res. Commun. *355*, 919–925.

Druesne-Pecollo, N., Tehard, B., Mallet, Y., Gerber, M., Norat, T., Hercberg, S., and Latino-Martel, P. (2009). Alcohol and genetic polymorphisms: effect on risk of alcohol-related cancer. Lancet Oncol. *10*, 173–180.

Dubuisson, M.L., De Wergifosse, B., Kremers, P., Marchand-Brynaert, J., Trouet, A., and Rees, J.F. (2001). Protection against nitrofurantoin-induced oxidative stress by coelenterazine analogues and their oxidation products in rat hepatocytes. Free Radic. Res. *34*, 285–296.

Frearson, J.A., Brand, S., McElroy, S.P., Cleghorn, L.A., Smid, O., Stojanovski, L., Price, H.P., Guther, M.L., Torrie, L.S., Robinson, D.A., et al. (2010). N-myristoyltransferase inhibitors as new leads to treat sleeping sickness. Nature *464*, 728–732.

Ishizaki, H., Spitzer, M., Wildenhain, J., Anastasaki, C., Zeng, Z., Dolma, S., Shaw, M., Madsen, E., Gitlin, J., Marais, R., et al. (2010). Combined zebrafish-yeast chemical-genetic screens reveal gene-copper-nutrition interactions that modulate melanocyte pigmentation. Dis. Model Mech. *3*, 639–651.

Ito, T., Ando, H., Suzuki, T., Ogura, T., Hotta, K., Imamura, Y., Yamaguchi, Y., and Handa, H. (2010). Identification of a primary target of thalidomide teratogenicity. Science *327*, 1345–1350.

Jawaid, S., Khan, T.H., Osborn, H.M., and Williams, N.A. (2009). Tyrosinase activated melanoma prodrugs. Anticancer. Agents Med. Chem. *9*, 717–727.

Keung, W.M., and Vallee, B.L. (1993a). Daidzin and daidzein suppress free-choice ethanol intake by Syrian golden hamsters. Proc. Natl. Acad. Sci. USA *90*, 10008–10012.

Keung, W.M., and Vallee, B.L. (1993b). Daidzin: a potent, selective inhibitor of human mitochondrial aldehyde dehydrogenase. Proc. Natl. Acad. Sci. USA *90*, 1247–1251.

Laggner, C., Kokel, D., Setola, V., Tolia, A., Lin, H., Irwin, J.J., Keiser, M.J., Cheung, C.Y., Minor, D.L., Jr., Roth, B.L., et al. (2012). Chemical informatics and target identification in a zebrafish phenotypic screen. Nat. Chem. Biol. *8*, 144–146.

Lassen, N., Estey, T., Tanguay, R.L., Pappa, A., Reimers, M.J., and Vasiliou, V. (2005). Molecular cloning, baculovirus expression, and tissue distribution of the zebrafish aldehyde dehydrogenase 2. Drug Metab. Dispos. *33*, 649–656.

Logan, D.W., Burn, S.F., and Jackson, I.J. (2006). Regulation of pigmentation in zebrafish melanophores. Pigment Cell Res. *19*, 206–213.

Lowe, E.D., Gao, G.Y., Johnson, L.N., and Keung, W.M. (2008). Structure of daidzin, a naturally occurring anti-alcohol-addiction agent, in complex with human mitochondrial aldehyde dehydrogenase. J. Med. Chem. *51*, 4482–4487.

Marchitti, S.A., Brocker, C., Stagos, D., and Vasiliou, V. (2008). Non-P450 aldehyde oxidizing enzymes: the aldehyde dehydrogenase superfamily. Expert Opin. Drug Metab. Toxicol. *4*, 697–720.

Maya, J.D., Cassels, B.K., Iturriaga-Vásquez, P., Ferreira, J., Faúndez, M., Galanti, N., Ferreira, A., and Morello, A. (2007). Mode of action of natural and synthetic drugs against *Trypanosoma cruzi* and their interaction with the mammalian host. Comp. Biochem. Physiol. A Mol. Integr. Physiol. *146*, 601–620.

Medda, F., Russell, R.J., Higgins, M., McCarthy, A.R., Campbell, J., Slawin, A.M., Lane, D.P., Lain, S., and Westwood, N.J. (2009). Novel cambinol analogs as sirtuin inhibitors: synthesis, biological evaluation, and rationalization of activity. J. Med. Chem. *52*, 2673–2682.

Mikus, J., and Steverding, D. (2000). A simple colorimetric method to screen drug cytotoxicity against *Leishmania* using the dye Alamar Blue. Parasitol. Int. *48*, 265–269.

Nussbaum, K., Honek, J., Cadmus, C.M., and Efferth, T. (2010). Trypanosomatid parasites causing neglected diseases. Curr. Med. Chem. *17*, 1594–1617.

O'Reilly-Pol, T., and Johnson, S.L. (2008). Neocuproine ablates melanocytes in adult zebrafish. Zebrafish *5*, 257–264.

Paulos, C., Paredes, J., Vasquez, I., Thambo, S., Arancibia, A., and Gonzalez-Martin, G. (1989). Pharmacokinetics of a nitrofuran compound, nifurtimox, in healthy volunteers. Int. J. Clin. Pharmacol. Ther. Toxicol. *27*, 454–457.

Priotto, G., Kasparian, S., Mutombo, W., Ngouama, D., Ghorashian, S., Arnold, U., Ghabri, S., Baudin, E., Buard, V., Kazadi-Kyanza, S., et al. (2009). Nifurtimox-eflornithine combination therapy for second-stage African *Trypanosoma brucei* gambiense trypanosomiasis: a multicentre, randomised, phase III, non-inferiority trial. Lancet *374*, 56–64.

Rao, D.N., and Mason, R.P. (1987). Generation of nitro radical anions of some 5-nitrofurans, 2- and 5-nitroimidazoles by norepinephrine, dopamine, and serotonin. A possible mechanism for neurotoxicity caused by nitroheterocyclic drugs. J. Biol. Chem. *262*, 11731–11736.

Rao, D.N., Harman, L., Motten, A., Schreiber, J., and Mason, R.P. (1987). Generation of radical anions of nitrofurantoin, misonidazole, and metronidazole by ascorbate. Arch. Biochem. Biophys. *255*, 419–427.

Rihel, J., Prober, D.A., Arvanites, A., Lam, K., Zimmerman, S., Jang, S., Haggarty, S.J., Kokel, D., Rubin, L.L., Peterson, R.T., and Schier, A.F. (2010). Zebrafish behavioral profiling links drugs to biological targets and rest/wake regulation. Science *327*, 348–351.

Saulnier Sholler, G.L., Bergendahl, G.M., Brard, L., Singh, A.P., Heath, B.W., Bingham, P.M., Ashikaga, T., Kamen, B.A., Homans, A.C., Slavik, M.A., et al. (2011). A phase 1 study of nifurtimox in patients with relapsed/refractory neuroblastoma. J. Pediatr. Hematol. Oncol. *33*, 25–30.

Sobreira, T.J., Marlétaz, F., Simões-Costa, M., Schechtman, D., Pereira, A.C., Brunet, F., Sweeney, S., Pani, A., Aronowicz, J., Lowe, C.J., et al. (2011). Structural shifts of aldehyde dehydrogenase enzymes were instrumental for the early evolution of retinoid-dependent axial patterning in metazoans. Proc. Natl. Acad. Sci. USA *108*, 226–231.

Sokolova, A.Y., Wyllie, S., Patterson, S., Oza, S.L., Read, K.D., and Fairlamb, A.H. (2010). Cross-resistance to nitro drugs and implications for treatment of human African trypanosomiasis. Antimicrob. Agents Chemother. *54*, 2893–2900.

Song, W., Zou, Z., Xu, F., Gu, X., Xu, X., and Zhao, Q. (2006). Molecular cloning and expression of a second zebrafish aldehyde dehydrogenase 2 gene (aldh2b). DNA Seq. *17*, 262–269.

Taylor, K.L., Grant, N.J., Temperley, N.D., and Patton, E.E. (2010). Small molecule screening in zebrafish: an in vivo approach to identifying new chemical tools and drug leads. Cell Commun. Signal. *8*, 11.

Thisse, B., Pflumio, S., Fürthauer, M., Loppin, B., Heyer, V., Degrave, A., Woehl, R., Lux, A., Steffan, T., Charbonnier, X.Q., and Thisse, C. (2001). Expression of the Zebrafish Genome during Embryogenesis (Eugene, OR: ZFIN, University of Oregon).

Wenzel, P., Hink, U., Oelze, M., Schuppan, S., Schaeuble, K., Schildknecht, S., Ho, K.K., Weiner, H., Bachschmid, M., Münzel, T., and Daiber, A. (2007). Role of reduced lipoic acid in the redox regulation of mitochondrial aldehyde dehydrogenase (ALDH-2) activity. Implications for mitochondrial oxidative stress and nitrate tolerance. J. Biol. Chem. *282*, 792–799.

Yang, C.T., and Johnson, S.L. (2006). Small molecule-induced ablation and subsequent regeneration of larval zebrafish melanocytes. Development *133*, 3563–3573.

Yao, L., Fan, P., Jiang, Z., Gordon, A., Mochly-Rosen, D., and Diamond, I. (2008). Dopamine and ethanol cause translocation of epsilonPKC associated with εRACK: cross-talk between cAMP-dependent protein kinase A and protein kinase C signaling pathways. Mol. Pharmacol. *73*, 1105–1112.

Yao, L., Fan, P., Arolfo, M., Jiang, Z., Olive, M.F., Zablocki, J., Sun, H.L., Chu, N., Lee, J., Kim, H.Y., et al. (2010). Inhibition of aldehyde dehydrogenase-2 suppresses cocaine seeking by generating THP, a cocaine use-dependent inhibitor of dopamine synthesis. Nat. Med. *16*, 1024–1028.

Zon, L.I., and Peterson, R.T. (2005). In vivo drug discovery in the zebrafish. Nat. Rev. Drug Discov. *4*, 35–44.

9990–10004 *Nucleic Acids Research, 2012, Vol. 40, No. 20* *Published online 31 August 2012*
doi:10.1093/nar/gks818

SURVEY AND SUMMARY

DNA repair endonuclease ERCC1–XPF as a novel therapeutic target to overcome chemoresistance in cancer therapy

Ewan M. McNeil and David W. Melton*

MRC Institute of Genetics and Molecular Medicine, University of Edinburgh, MRC Human Genetics Unit, Western General Hospital, Crewe Road, Edinburgh EH4 2XU, UK

Received May 9, 2012; Revised July 31, 2012; Accepted August 5, 2012

ABSTRACT

The ERCC1–XPF complex is a structure-specific endonuclease essential for the repair of DNA damage by the nucleotide excision repair pathway. It is also involved in other key cellular processes, including DNA interstrand crosslink (ICL) repair and DNA double-strand break (DSB) repair. New evidence has recently emerged, increasing our understanding of its requirement in these additional roles. In this review, we focus on the protein–protein and protein–DNA interactions made by the ERCC1 and XPF proteins and discuss how these coordinate ERCC1–XPF in its various roles. In a number of different cancers, high expression of ERCC1 has been linked to a poor response to platinum-based chemotherapy. We discuss prospects for the development of DNA repair inhibitors that target the activity, stability or protein interactions of the ERCC1–XPF complex as a novel therapeutic strategy to overcome chemoresistance.

INTRODUCTION

The ERCC1–XPF heterodimer is a 5′-3′ structure-specific endonuclease that is involved in a number of DNA repair pathways in mammalian cells. It is essential for nucleotide excision repair (NER) and has important roles in interstrand crosslink (ICL) repair and double-strand break (DSB) repair. As such it has a key role in the response of cancers to a range of DNA-damaging chemotherapeutics. In the ERCC1–XPF heterodimer, ERCC1 is catalytically inactive and instead regulates DNA– and protein–protein interactions, whereas XPF provides the endonuclease activity and also contains an inactive helicase-like motif and is involved in DNA binding and additional protein–protein interactions.

ERCC1–XPF is essential for NER

UV irradiation-induced cyclobutane pyrimidine dimers (CPDs) and pyrimidine-(6,4)-pyrimidone photoproducts (6-4PPs), chemically-induced helix-distorting and bulky DNA lesions are all repaired by NER [reviewed earlier (1)]. *In vivo* NER requires around 30 proteins, but the incision step can be reconstructed *in vitro* with just six core factors, XPC/RAD23B, XPA, RPA, TFIIH, XPG and ERCC1–XPF (2). To complete NER *in vitro*, PCNA, DNA polymerases δ, ε and κ, DNA ligases I and III, RFC, RPA and XRCC1 are also involved. In global genomic NER [GG-NER, reviewed in ref. (3)], DNA damage is recognized by the XPC/RAD23B complex that detects helical distortions rather than the lesion itself. It is thought that XPC/RAD23B binding induces further bending of the DNA, which may act as the trigger for recruiting additional factors to the lesion. For recognition of DNA damage such as CPDs, which only mildly distort DNA, the XPE/UV-DDB complex is also required. In transcription-coupled NER [TC-NER, reviewed in ref. (4)], repair is triggered when RNA polymerase II stalls at a lesion, resulting in recruitment of several proteins including CSA and CSB. Following either of these damage recognition steps, a common repair mechanism proceeds with recruitment of the TFIIH complex, containing XPB and XPD, which possess ATP-dependent helicase activities to unwind DNA around the damage site to form an open complex. XPA and RPA proteins are then recruited to stabilize the NER intermediate. XPA recognizes a helical kink at the damage site (5) and acts as a scaffold for binding to TFIIH, RPA and ERCC1–XPF, whereas RPA binds to ss-DNA. ERCC1–XPF and XPG endonucleases are then recruited to incise the damaged DNA strand 5′ and 3′, respectively, to the lesion. Recruitment of ERCC1–XPF is thought to be mediated by both ERCC1/XPA and XPF/RPA interactions (6,7).

*To whom correspondence should be addressed. Tel: +44 1314 678449; Fax: +44 1314 678450; Email: David.Melton@ed.ac.uk

ERCC1–XPF is involved in DSB repair

Double-strand DNA breaks, induced by ionizing radiation, free radicals and chemotherapeutics, such as cisplatin, mitomycin-C and the topoisomerase inhibitor, etoposide, can be repaired by homologous recombination (HR), or non-homologous end-joining (NHEJ). Although the main HR pathway is error-free, NHEJ involves the ligation of free DNA ends in a Ku70/Ku86-dependent process resulting in error-prone repair, due to addition or loss of bases, or to ligation of the wrong ends. The importance of ERCC1–XPF in DSB repair (DSBR) was initially shown in budding yeast where mutations in RAD10, or RAD1, the yeast orthologues of ERCC1 and XPF, suppressed HR (8). Mammalian cells with mutant ERCC1–XPF are sensitive to DSBs (9) and both the HR and NHEJ pathways for DSBR are attenuated (10–12). The key activity of ERCC1–XPF in both types of DSBR is its ability to remove non-homologous 3′ single-stranded flaps at broken ends before they are rejoined (9). This is achieved in the error-prone RAD52-dependent single-strand annealing (SSA) subpathway of HR (13,14) and in the mechanistically distinct RAD52- and Ku70/Ku86-independent microhomology-mediated end-joining (MMEJ) subpathway of NHEJ [see reference (15) for a review of MMEJ and references (9,16) for the role of ERCC1–XPF].

ERCC1–XPF is involved in ICL repair

ICL repair operates to remove crosslinks induced by chemotherapeutics such as cisplatin, psoralens and mitomycin-C (17). Such lesions are particularly toxic because they prevent helix unwinding and so act as a potent block to transcription and replication. A review of the sensitivity of mammalian NER mutants to ICL agents found that, whereas all NER mutants were more sensitive than the wild-type cells, mutants in ERCC1 or XPF were in general, hypersensitive (17). In eukaryotes, the mechanism of ICL removal depends on the phase of the cell cycle during which the lesion is encountered (18). If incision adjacent to an ICL occurs in G0 or G1 then repair may be completed during this stage. Alternatively, if the ICL persists into S phase, it will be converted into a DSB when it causes replication to stall. Incisions are thought to be made to either side of the crosslink on one DNA strand to unhook the lesion and allow stalled replication complexes to proceed. The DNA is repaired by HR using the newly synthesized strand as template and may use a NER-dependent mechanism to remove the remaining lesion (19). Although the precise mechanism is not known, most models for ICL repair employ an ERCC1–XPF-dependent step (17,18). Importantly, ERCC1–XPF is able to incise to either side of an ICL (20) and, although not the only nuclease involved, ERCC1–XPF has been shown to be required for both S-phase-dependent and -independent ICL repair (21,22).

Non-repair related roles for ERCC1 and XPF

ERCC1–XPF is involved in telomere maintenance and the interactions made with the telomere protein, TRF2, are described in a later section. A role for ERCC1, but not XPF, in mitotic progression has been suggested by the observation that knock-down of ERCC1, but not XPF, in human hepatocellular carcinoma cells caused cell cycle delay and multinucleation (23). This result is not readily reconcilable with the premature polypoidy observed in the livers of both ERCC1 knockout (24) and XPF knockout mice (25) and could result from unrepaired endogenously generated interstrand crosslinks uncoupling the normal relationship between replication and cell division, rather than a non-repair-related role for ERCC1. A similar role in mitosis, but this time for XPF, has been proposed from studies where knocking down XPF in cultured cells led to abnormal nuclear morphology and mitosis (26). XPF was found to interact and co-localize with the kinesin protein, Eg5 (26). Again the effect of XPF knock-down on mitosis could be indirect, resulting from unrepaired endogenous DNA damage rather than a direct role in mitosis. An alternative explanation perhaps made more likely by the observation that Eg5 boosted ERCC1–XPF activity in the standard *in vitro* assay.

NER deficiency disorders

Inherited defects in human NER genes result in the rare syndromes xeroderma pigmentosum (XP), Cockayne syndrome (CS) and trichothiodystrophy. Whereas XP is considered a repair syndrome, CS and trichothiodystrophy are regarded as transcription syndromes (1). Diagnostic features of XP are dry scaly skin, abnormal pigmentation patterning in sun-exposed areas and severe photosensitivity, resulting in >1000-fold increased risk of developing UV-induced skin cancers (27). In 20–30% of XP patients, there is also progressive neurological degeneration, emphasizing the importance of NER in repair of endogenous DNA damage (1). CS patients are also photosensitive, but do not exhibit pigmentation abnormalities, or an increased cancer risk (1,27). CS patients also show developmental defects and neurological symptoms (1). In XP, GG-NER is always defective and TC-NER may also be affected, whereas in CS, TC-NER is lost, but GG-NER is retained (1,27).

Characterization of the *ERCC1* (28) and *XPF* genes (29,30) made possible the identification of mutations in XP patients. Mutations in the *ERCC1* or *XPF* genes can result in the even rarer XF-E syndrome (31). Patients show characteristics of XP and CS, but also exhibit additional neurologic, hepatobiliary, musculoskeletal and haematopoietic symptoms (31). In addition to a complete loss of TC- and GG-NER, cells derived from XF-E patients also show hypersensitivity to ICL agents due to the additional role of ERCC1–XPF in ICL repair (31). This distinguishes the XF-E syndrome from either XP, CS or combined XP/CS (31).

Patients with ERCC1–XPF mutations

Only two patients with *ERCC1* mutations have been observed: one (XP202DC) harbouring a Lys226X nonsense mutation with a IVS6-26G-A splice mutation, a second (165TOR) with a Gln158Stop mutation inherited from the mother and a Phe231Leu mutation from the

father (32,33). *XPF* mutations have been characterized in 14 patients, 9 harbour an Arg799Trp mutation (32). This is proposed to be situated in an interaction domain between the XPF nuclease and ERCC1 central domains (34). An Arg153Pro mutation in the helicase-like domain may disrupt protein–protein interactions resulting in XF-E syndrome (31). Other mutations observed are Pro379Ser and Arg589Trp, both in the helicase-like domain (32). Although it is yet to be shown for any of the XPF mutations that they actually disrupt specific protein–protein interactions, there is evidence that the Arg153Pro XF-E mutation results in the protein failing to reach the nucleus, probably due to misfolding (35). The locations of *ERCC1* and *XPF* mutations resulting in amino acid substitutions are shown in Figure 1.

ERCC1 is a target to overcome chemoresistance

ERCC1–XPF is required for the repair of DNA damage caused by many chemotherapeutics, including the commonly used platinum compounds, such as cisplatin (36). Testicular cancers have very low levels of ERCC1 and are effectively treated by cisplatin (37). High expression of ERCC1 has been linked with poor responses to chemotherapy in numerous cancer types, including non-small cell lung cancer, squamous cell carcinoma and ovarian cancer (38–45). Although it has not been linked to altered ERCC1 expression, the T variant of a silent *ERCC1* polymorphism at codon 118 was predictive of poor survival for cisplatin-treated non-small cell lung cancer patients (46). The same association has not been seen consistently in other studies and the role of particular *ERCC1* alleles needs further clarification [for review, see ref. (36)].

Increased levels of ERCC1 mRNA have been reported in melanoma and ovarian cancer cell lines in response to cisplatin-induced DNA damage (47,48). In ovarian cancer cells, increased levels of the transcriptional activators, c-fos and c-jun, were involved in the cisplatin response (48). Treatment of melanoma cell lines with cisplatin resulted in increased phosphorylation of the extracellular signal-regulated kinase (ERK) (49). The MAPK pathway also has an important role in the regulation of ERCC1 expression by epidermal growth factor in human hepatoma cells (50). Importantly, MAPK pathway-dependent increased levels of both ERCC1 and XPF proteins have been demonstrated after cisplatin treatment of melanoma cells (47). This led us to propose that inhibition of ERCC1–XPF could be used to overcome chemoresistance in many cancers. To demonstrate this, we used a mouse xenograft model of melanoma to show that, whereas ERCC1-proficient xenografts were resistant to cisplatin treatment, isogenic ERCC1-deficient melanoma xenografts could be cured by just two cisplatin treatments (51).

We now review the known protein–protein and protein–DNA interactions made by the ERCC1–XPF complex to better understand its mechanistic role in DNA repair and consider which of these interactions might be targeted in order to overcome chemoresistance.

THE ERCC1–XPF STRUCTURE-SPECIFIC ENDONUCLEASE

The ERCC1–XPF complex is a structure-specific endonuclease which cleaves DNA at ds- to ss-junctions, nicking the ds-DNA on the 5′ strand, two nucleotides from the junction (52). This structure-specificity was first demonstrated for RAD10-RAD1, the yeast orthologues of ERCC1 and XPF (53). ERCC1–XPF is active in *in vitro* endonuclease assays utilizing a variety of substrates, including stem–loops and structures with 3′ overhangs (52). The minimum loop size required for cleavage is 6 nt, but the preference is for larger, 22–40 nt loops (52,54).

Domain architecture of the ERCC1–XPF complex

The ERCC1 protein is thought to have arisen from a gene duplication of XPF in the eukaryotic lineage (55). In Archaebacteria only XPF is present, forming homodimers with each protein containing nuclease and HhH_2 domains. Archaeal XPF monomers interact primarily through HhH_2 domains, with an additional interaction through the β5 strand of the nuclease domains (34). In addition to

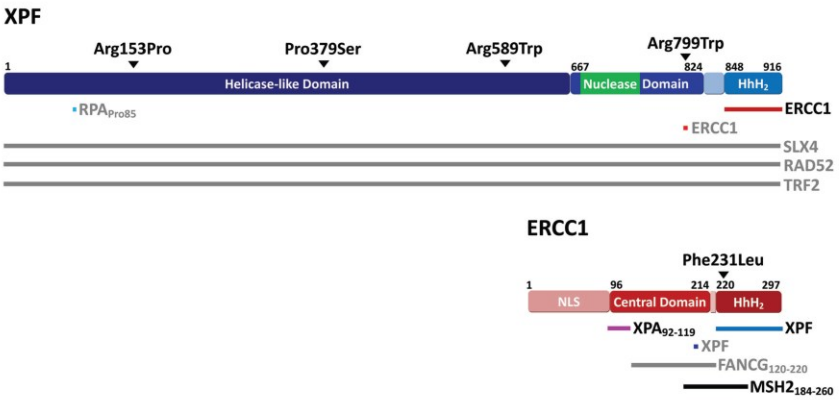

Figure 1. Domain architecture of ERCC1 and XPF proteins. The active site within the XPF nuclease domain is shown as a green box. Confirmed protein–protein interacting regions are mapped and identified with black text; undefined or unconfirmed protein–protein interactions are identified by grey text. Amino acid substitution mutations identified in XP or XF-E patients are also indicated. The same colour scheme shown here to identify the protein domains is used in all the figures. NLS, putative nuclear localization signal.

nuclease and C-terminal HhH_2 domains, mammalian XPF also contains an N-terminal helicase-like domain, but lacks residues essential for helicase activity (56). An overview of the ERCC1 and XPF domains is shown in Figure 1. The ERCC1 protein differs from XPF in that it contains a catalytically inactive central domain and lacks the helicase-like domain. ERCC1 mediates DNA binding and many of the protein–protein interactions of the ERCC1–XPF complex. The HhH_2 domains of ERCC1 and XPF show a high degree of conservation (55,57). In human XPF, the second HhH motif lacks the characteristic GhG hairpin, instead being replaced by a short three residue β-turn, nevertheless XPF still adopts a canonical HhH_2 folded structure (57).

Dimerization of ERCC1 and XPF occurs through their HhH_2 domains

The key protein–protein interaction of ERCC1 and XPF is the dimerization of their hydrophobic C-terminal regions to form a stable heterodimer through the double helix–hairpin–helix motifs in their HhH_2 domains (57,58). It is thought that during protein folding XPF acts as a scaffold for ERCC1 and that ERCC1 may be unable to fold correctly *in vitro* in the absence of XPF (57). Without dimerization it was conventionally thought that neither protein was stable and each was rapidly degraded due to aggregation following exposure of their hydrophobic interaction regions (57,59). However, recent siRNA experiments have indicated that, although XPF protein levels were decreased when ERCC1 was knocked down, the converse was not true (60). There is no catalytic activity in the absence of dimerization. Indeed, although the catalytic domain is within XPF and ERCC1 is catalytically inactive, ERCC1 remains indispensable for activity of the complex (57).

What residues are essential for dimerization?

The ERCC1 and XPF HhH_2 domains have a 1534Å^2, predominantly hydrophobic, interacting surface (57). Each domain forms five core α-helical structures (XPF: H1, 849–853; H2, 860–868; H3, 873–877; H4, 881–887; H5, 891–903. ERCC1: H1, 233–240; H2, 247–257; H3, 260–265; H4, 268–272; H5, 280–288), with ERCC1 forming an additional α-helical structure in its N-terminus (ERCC1, 226–229) (59). In both ERCC1 and XPF the H1 and H2 helices constitute the first HhH motif, with H4 and H5 constituting the second motif (57). From cross-saturation techniques, XPF residues from Gln849 to Ala906 appear to interact with ERCC1 residues Arg234 to Leu294 (59).

Two residues essential for interaction are XPF Phe905 and ERCC1 Phe293, which anchor the two proteins together (Figure 2). ERCC1 Phe293 positions into a 280Å^2 hydrophobic pocket on XPF (57). This interaction is protected by ERCC1 Leu294 which locks Phe293 in position (57). In mutational studies, deletion of ERCC1 Phe293 resulted in abolition of dimerization and enzyme activity (29,61). A reciprocal arrangement exists for the XPF Phe905 residue, which positions into a 220Å^2 hydrophobic pocket on ERCC1, although no mutational studies have been performed on this XPF residue (57). In the human patient 165TOR, ERCC1 encoded by the allele with the Gln158Stop mutation cannot form active protein due to its inability to heterodimerize. The second allele from this patient, with the Phe231Leu mutation, does produce functional protein. Reduced binding affinity for XPF Phe905, due to the Phe231Leu mutation in the ERCC1 interaction pocket, could explain the reduced levels of ERCC1–XPF complex and moderate sensitivity to UV and crosslinking agents observed in cells from this patient (33).

How does DNA binding by the HhH_2 domains influence endonuclease activity?

It has been proposed that the ERCC1–XPF HhH_2 domains form two independent binding sites to complex with ss-DNA (57,58). This interaction is thought to be necessary for the proper orientation of ERCC1–XPF at the ds- to ss-DNA junction (52). Tripsianes *et al.* (57) monitored chemical shift perturbations upon DNA binding and found that both hairpin regions of ERCC1 contacted DNA, proposing that residues Val245 and Asn246 of the first HhH motif and Gly276, Leu277, Gly278 and Lys281 of the second hairpin interact with DNA. Under their experimental conditions, Tripsianes *et al.* (57) could not detect DNA interaction by XPF. Similarly, Tsodikov *et al.* (58) proposed DNA contacts to be made by ERCC1 residues Lys243 and Lys247 of the first and Gly276 and Gly278 of the second HhH domains. In contrast, however, they proposed XPF makes DNA interactions via Gly857, Lys861 and Gly889. They showed that the recombinant ERCC1–XPF HhH_2 domain complex binds with 6-fold preference to two ss-DNA strands over ds-DNA and measured the binding affinity (Kd) to be 0.2 μM (58). Interestingly, Su *et al.* showed that recombinant ERCC1–XPF protein harbouring ERCC1 Lys247Ala and Lys281Ala mutations had a 2-fold reduced DNA-binding affinity and was inactive *in vitro*, whereas XPF harbouring Lys861Ala and Arg864Ala mutations had a 1.6-fold reduction in DNA-binding affinity and retained *in vitro* activity (62). Furthermore, *in vivo* only the ERCC1 double mutant resulted in a mild NER defect, suggesting that defects in DNA binding of the ERCC1–XPF complex can be partly overcome by other NER proteins (62). Das *et al.* utilized an XPF HhH_2 homodimer and demonstrated that this can bind ds-DNA and form a stable complex with ss-DNA (63). They showed that upon binding of two 10-nt ss-DNA fragments to the homodimer, chemical shift perturbations were observed for XPF residues between Lys861 and Val870 and proposed that Lys861, Arg864, Ser865, His868, His869 and Asn890 were directly involved in making DNA contacts (63). In addition, they showed that the bases are orientated away from the HhH_2 domain with the exception of one base that orientates into a 140Å^2 pocket in the XPF HhH_2 domain (63). This pocket is formed due to an altered conformation for Lys861 and Asn890 upon DNA binding and proposed hydrogen bond formation with the side chain of Asn890 (63).

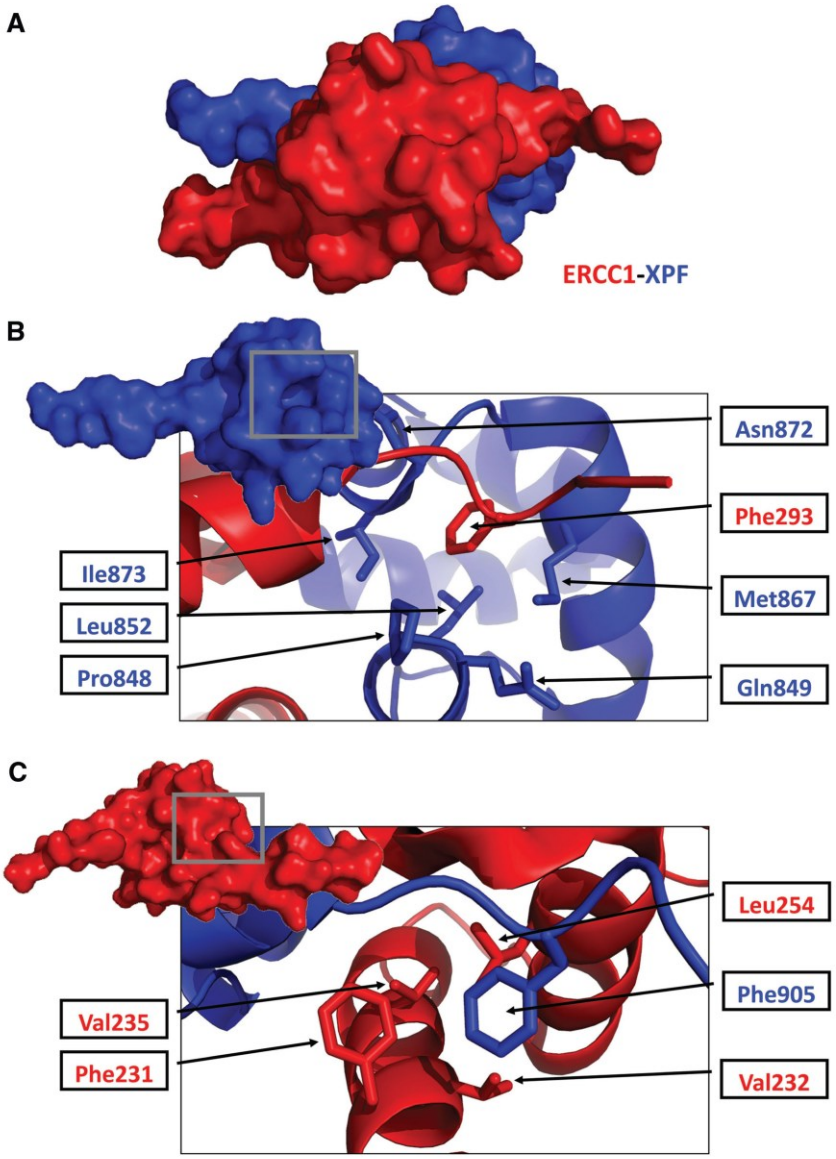

Figure 2. Interaction of ERCC1 and XPF through their HhH_2 domains. (**A**) Heterodimer of the HhH_2 domains of ERCC1 (red) and XPF (blue). (**B**) Expanded cartoon representation of the region boxed on XPF, identifying key interacting residues in the XPF pocket for ERCC1 Phe293. (**C**) Expanded cartoon representation of the region boxed on ERCC1, identifying key interacting residues in the ERCC1 pocket for XPF Phe905. Figure created using PyMOL v0.99 with the ERCC1–XPF HhH_2 domain crystal structure (PDB code 2A1J) (58).

A model for the structure of ERCC1–XPF bound to DNA

Das *et al.* proposed a model for ERCC1–XPF whereby the ds- and ss-DNA binding of the ERCC1–XPF HhH_2 domains position the complex at the ds- to ss-DNA junction, incorporating the nucleotide-binding pocket that they mapped onto the XPF HhH_2 domain in the XPF HhH_2 homodimer crystal structure (63). In their model, the ERCC1 central domain does not make contact with DNA as shown by Tsodikov *et al.* (58,64). In addition, the non-cleaved DNA strand winds around the back of the ERCC1–XPF HhH2 domain before contacting the nucleotide-binding domain and the model does not show how the central and HhH_2 domains of ERCC1 are connected.

Bowles *et al.* (54) showed in an *in vitro* endonuclease assay that ERCC1–XPF may have a sequence-specific preference for nucleotides immediately surrounding the cleavage site. As a result, they have also proposed a model, whereby XPF contains a nucleotide-binding pocket, but instead, although there is no evidence in support, they suggest that this may reside in the nuclease domain, rather than in the XPF HhH_2 domain as shown above by Das *et al.* (63). Their very schematic model shows the helicase domain inside the loop of the stem–loop substrate DNA. The minimum loop size for ERCC1–XPF enzymatic activity is six nucleotides (52,54). Based upon our homology model, the narrowest part of the XPF helicase-like domain would require a minimum loop size of ~12 nt to be accommodated, so this model seems unlikely. In addition, in their model the ERCC1 central and XPF HhH_2 domains do not make the DNA contacts shown by Tsodikov *et al.* (58,64).

The alternative model that we propose takes into account all the known protein–protein and protein–DNA interactions by ERCC1 and XPF (Figure 3). Unlike the other models, our model also has the C-terminal end of each ERCC1 and XPF domain in close proximity to the N-terminal end of the next domain in the sequence. Similar to the other models, we show the ERCC1 HhH_2 domain making contact with ds-DNA, however after the DNA strands have separated, we additionally show the ERCC1 central domain also making contact with ss-DNA. With regards to XPF, instead of a nucleotide-binding domain on the XPF central domain as suggested by Bowles *et al.* (54), we show the nucleotide-binding domain to be present in the HhH_2 region of XPF as demonstrated by Das *et al.* (63). We further propose that this is localized adjacent to the XPF nuclease domain and so may act to present the DNA backbone towards the XPF nuclease domain for catalysis. Our predicted structure of the XPF helicase domain has a clamp-like structure and, although there is no evidence to indicate how it is positioned with respect to the rest of the protein, we have shown it clamped around the nuclease domain with its RPA-binding site in a suitable position to contact RPA bound to the non-damaged DNA strand.

Do ERCC1 and XPF interact through regions other than their HhH_2 domains?

It is unclear whether the XPF nuclease domain interacts with the central domain of ERCC1, similar to the nuclease domain interactions observed with Archaebacterial XPF (58). In several studies stable interactions between these domains did not form, although transient interactions cannot be excluded (58,61). In support of this notion, the XPF patient carrying the Arg799Trp mutation exhibited 5-fold decreased NER activity due to ERCC1–XPF instability. Based on sequence alignments to Archaeal Hef (similar to human XPF), Nishino *et al.* (34) mapped the Arg799Trp mutation to the middle of the β5 strand of the XPF nuclease domain, proposing an interaction with the ERCC1 central domain (34). Further evidence is required to prove the existence of this interaction in human ERCC1–XPF.

Inhibition of ERCC1–XPF dimerization as a target for drug discovery

ERCC1–XPF interaction through their HhH_2 domains is an obligate requirement for a stable ERCC1–XPF complex and so is essential for catalytic activity. Development of small molecule inhibitors of the HhH_2 domain interaction would be expected to sensitize cells to chemotherapeutics whose DNA-damaging effects are repaired by ERCC1–XPF-dependent pathways. Given the high affinity [we have estimated the Kd to be 5 nM by surface plasmon resonance assay (E. M. McNeil, M. Wear, M. Walkinshaw and D. W. Melton, unpublished observations)] and the hydrophobic nature of this interaction, it will be considerably more difficult to block than an enzyme active site. However, the successful development of the p53/MDM2 interaction inhibitor, nutlin, demonstrates what can be achieved (65). Mutagenesis studies indicate that disruption of the ERCC1 Phe293 interaction with XPF is sufficient to prevent complex formation (29,61). Furthermore, availability of an ERCC1–XPF HhH_2 domain crystal structure (PDB code 2A1J) (58) provides an attractive first step for rational drug design programmes.

Are human XPF homodimers of functional significance?

XPF HhH_2 interaction domains form homodimers *in vitro* mimicking the homodimerization of Archaeal XPF (66). In mixtures of ERCC1 and XPF HhH_2 domains at ambient temperatures, the heterodimer is the predominant form, but at temperatures >50°C ERCC1 HhH_2 domains aggregate leaving XPF HhH_2 domains to homodimerize. It has been proposed that XPF homodimers may act as an inactive storage complex in cells to protect against the risks of non-specific DNA cleavage (59). However, if human XPF does form homodimers *in vivo* it must be at very low levels because, in ERCC1-deficient cells, or after ERCC1 siRNA knock-down, only low levels of XPF are found (55,60).

The XPF nuclease domain

The nuclease site of the ERCC1–XPF complex has been mapped to XPF residues 681–751, it contains a $V/IERKX_3D$ motif conserved between XPF protein family members and binds Mg^{2+} or Mn^{2+} as a metal co-factor (67). The presence of the metal is not necessary for DNA binding and does not alter to the DNA-binding affinity.

Key residues for catalytic activity

Active site mutations identified Asp687, Asp715, Lys727 and Asp731 as essential for catalytic activity, whereas mutation of residues Arg689 and Arg726 resulted in residual activity (67). Asp687, Glu690, Asp715 and Glu725 have all been directly implicated in metal binding (67). Enzlin and Schärer proposed that residues Asp687 and Asp715 coordinate metal ion binding and residue Asp731 may function to activate a water molecule to act as a nucleophile for phosphodiester bond hydrolysis (67). Mutation of residues Glu690 and Glu725 led to reduced nuclease activity in the presence of Mg^{2+} but not Mn^{2+}, suggesting an altered active site incompatible with the greater stringency requirements for Mg^{2+} compared with Mn^{2+} binding (67). This suggests that the biologically relevant metal co-factor is Mg^{2+}, but in *in vitro* ERCC1–XPF endonuclease assays, Mn^{2+} is the preferred metal (54,58). Although an Arg689Ala mutation resulted in residual nuclease activity *in vitro,* activity was retained *in vivo* but with a shifted incision pattern, suggesting that this residue may be involved in correct positioning of the substrate in the active site for incision (62). Positioning of key amino acids in the nuclease site of XPF is shown in Figure 4.

Inhibition of the XPF nuclease domain as a target for drug discovery

Inhibition of the XPF catalytic domain would inhibit all known functions of ERCC1–XPF in DNA repair. The presence of Mg^{2+} coordinated in the active site provides

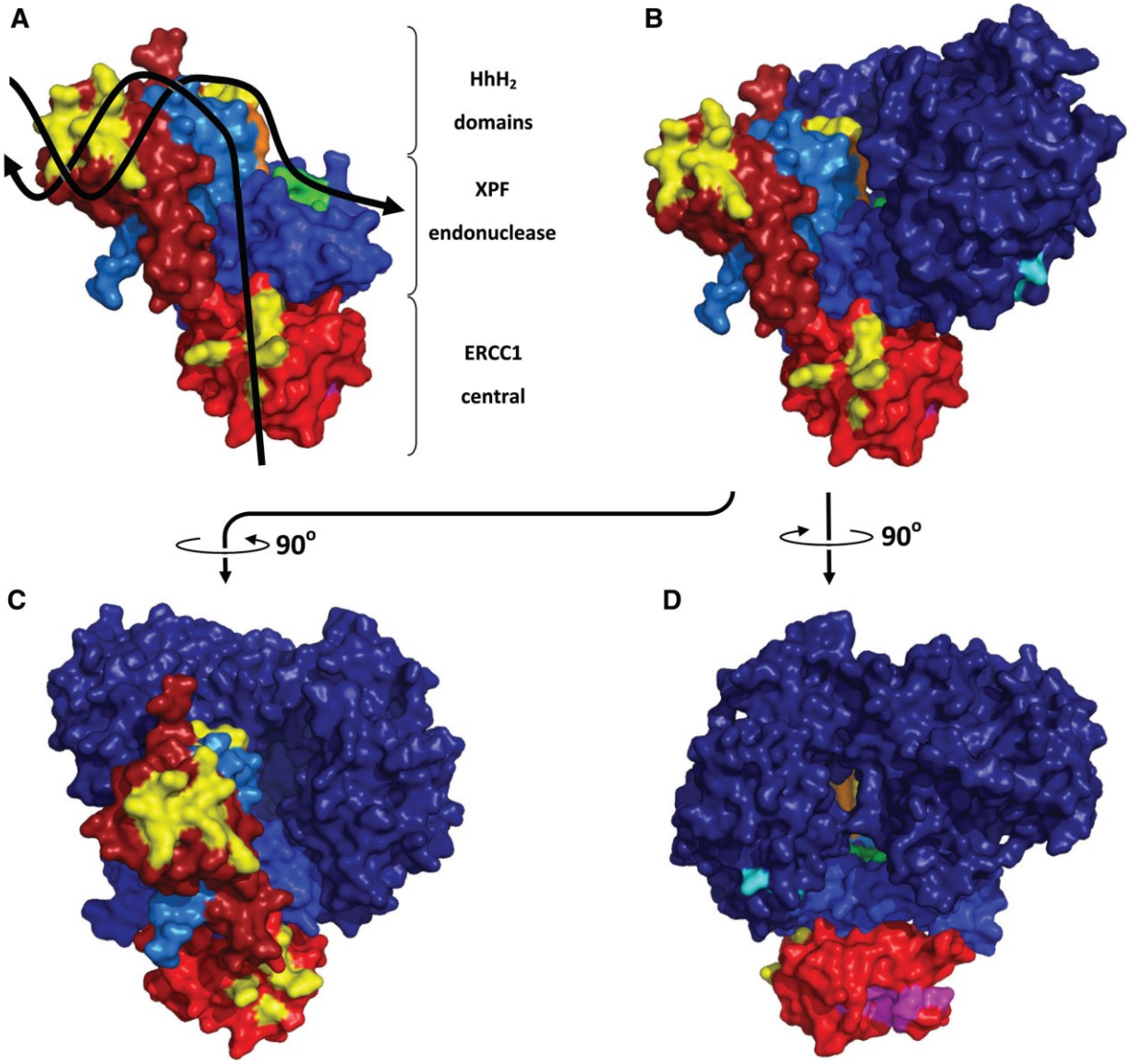

Figure 3. Proposed model for ERCC1–XPF interaction with the DNA substrate. (**A**) Showing the ERCC1 HhH_2 and central domains (red) and XPF HhH_2 and nuclease domains (blue). DNA-binding regions are shown in yellow; the XPF nuclease active site is shown in green; the nucleotide-binding pocket on the XPF HhH_2 domain is shown in orange; the XPA-binding site on the ERCC1 central domain is coloured magenta. The ERCC1 N-terminal region ($ERCC1_{1–98}$) and the XPF domain linking regions (XPF_{666} and $XPF_{825–847}$) are not shown as crystal structures are not available and there is insufficient sequence conservation for homology modelling. (**B**) Same view as in (A), but with the addition of the proposed position of the XPF helicase-like domain and omitting the DNA substrate. The RPA-binding site on the XPF helicase-like domain is shown in cyan. (**C**) As in (B), but with a 90° anti-clockwise rotation of the ERCC1–XPF complex. (**D**) As in (B), but with a 90° clockwise rotation of the ERCC1–XPF complex. Figure created in PyMOL v0.99 using the ERCC1–XPF HhH_2 domain crystal structure (PDB code 2A1J) (58), the ERCC1 central domain crystal structure (PDB code 2A1I) (58) and PHYRE-generated homology models of the XPF endonuclease and helicase-like domains.

an ideal target for metal ion chelation with only weak DNA contacts being made by this domain. There is currently no crystal structure for the human XPF endonuclease domain, although the Archaebacterial XPF crystal structure (PDB code 2BGW) (69) has been used to generate a human homology model that could aid the search for active site inhibitors (Figure 4). Inhibition of the nuclease domain of XPF is, however, problematic due to shared mechanistic activity with closely related nucleases, thus designing the necessary specificity into inhibitors will be challenging. It is of note that drug discovery programmes have been, or are currently being pursued for another structure-specific endonuclease, Flap Endonuclease 1 (FEN1), involved in the final ligation step of NER and base excision repair (BER) (70–72), for Apurinic/apyrimidinic Endonuclease (APE1) required for BER (73,74) and the RAD51 recombinase, involved in HR (75).

The XPF helicase-like domain

The XPF helicase-like domain is related to superfamily-2 helicases, it comprises five subdomains, but lacks critical

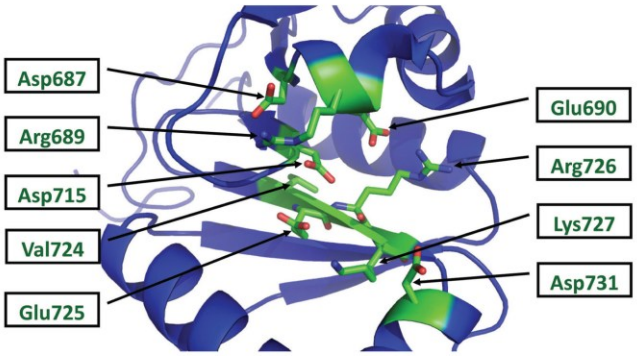

Figure 4. The nuclease domain of XPF. Cartoon representation of XPF identifying amino acids and their side chains. Residues Asp687, Glu690, Asp715 and Glu725 are implicated in metal binding (67). No metal ion has been shown. Figure created using PyMOL v0.99 with a homology model of XPF generated using the Protein Homology/analogY Recognition Engine v2.0 (PHYRE) (68).

residues essential for helicase activity (55,56,76). In the first of the Walker A motifs, usually required for ATP and DNA binding, the GKT consensus is not present (56,77). The second Walker B motif lacks acidic residues present in the DEAD/DExH box motif, meaning that Mg^{2+} is unable to bind and catalytic activity is lost (56,77). Instead, it is thought that the helicase-like domain binds at the junction between ds- and ss-DNA and contributes to substrate specificity (55,76). The presence of leucine-rich motifs indicates a potential role for protein–protein interactions (78,79). An Arg153Pro substitution within this domain resulted in XF-E syndrome, with hypersensitivity to UV-irradiation and ICL agents (31). Although hypersensitivity may have resulted from disruption of protein–protein interactions required for both NER and ICL repair, it is most likely this was due to XPF misfolding resulting from substitution of the basic Arginine residue for the hydrophobic Proline. This is in agreement with the reduction in nuclear ERCC1–XPF levels observed (31).

Inhibition of the XPF helicase-like domain as a target for drug discovery

The helicase-like domain could be an attractive target for drug discovery, particularly when considering the single Arg153Pro substitution resulted in hypersensitivity to UV and ICL agents (31). It would also be anticipated that inhibition of this domain would result in decreased nuclease activity, because truncated $_{\Delta 95}$ERCC1–$_{\Delta 666}$XPF shows 60-fold reduced activity *in vitro* compared with the full-length complex (58). However, our current understanding of the DNA– and protein–protein interactions is insufficient for a drug screening programme to target this region. In addition, no crystal structures exist for this domain and a homology model would likely be of only limited value due to insufficient sequence homology to other helicases with known crystal structures.

The ERCC1 central domain

The ERCC1 central domain is weakly homologous to the XPF nuclease domain, but has lost the active site residues required for metal binding and catalytic activity (58). Instead, the ERCC1 central domain has acquired the ability to bind DNA and form additional protein–protein interactions, particularly with XPA to recruit the ERCC1–XPF complex for NER. Deletion of the first 91 amino acids of ERCC1 does not affect endonuclease activity, whereas deletion of an additional 11 residues into the central domain results in a loss of activity (29).

Central domain binding to DNA

The ERCC1 central domain surface has a V-shaped groove lined by basic (Arg106, Arg108, Arg144, Arg156) and aromatic (Phe140, Tyr145 and Tyr152) residues, thought to constitute both the DNA binding and XPA interaction domains (58,64). Through chemical shift perturbations the DNA interacting region has been identified as residues Asn99, Ile102, Leu132, Lys213, Ala214 and Gln134 (80). This region binds preferentially to ss-DNA in an orientation-dependent manner, with an 8-fold greater preference for 5′ than 3′ overhangs (58). In low salt conditions, the ERCC1 central domain binds ds-DNA with comparable affinity to ss-DNA (58). However, at physiologically relevant salt concentrations, it has a binding affinity (Kd) of 2.5–10 μM for ss-DNA, whereas binding of ds-DNA is almost undetectable (58,80).

Central domain interaction with XPA

The interaction between ERCC1 and XPA maps to ERCC1 residues 92–119 and XPA residues 59–114 (6,81). In the XPA-binding domain on ERCC1, two motifs are present; a TGGGFI motif essential for binding, and an EEEEEEE motif shown to be contributory, but not essential for interaction (81). Interestingly, the TGGGFI motif was not identified in any other mammalian proteins (64). Binding studies, with a truncated $XPA_{59–93}$ peptide, confirmed the involvement of Gly72, Gly73 and Gly74 in the binding to ERCC1 (64). A second truncated XPA_{67-80} peptide bound stably to $ERCC1_{96-214}$ in a stoichiometric 1:1 ratio, with a binding affinity (Kd) of 0.78 μM (64).

An XPA peptide bound to the hydrophobic V-shaped groove on ERCC1 with the Gly72, Gly73 and Gly74 residues of XPA forming a U-turn in the 1039Å^2 ERCC1 binding site (64). A number of interactions between individual XPA and ERCC1 residues have been described at this binding site, although there are some differences in interpretation of the same crystal structure (64,82,83). There is main chain hydrogen bonding between XPA Gly72, Gly73 and Gly74 and adjacent ERCC1 residues and stacking of aromatic side chains, making the binding site an attractive candidate for small molecule ligands (see below). Furthermore, an XPA Phe75Ala mutation abrogates binding to ERCC1 (64). Tsodikov *et al.* (64) and Tripsianes *et al.* (80) have measured the binding affinity (Kd) of XPA to ERCC1 to be 540 nM and 1 μM, respectively.

Is simultaneous binding of ERCC1 to DNA and XPA possible?

Interaction of XPA and ERCC1 is required for NER activity *in vivo*, confirming its role in recruiting

ERCC1–XPF to DNA damage, but *in vitro* nuclease activity of ERCC1–XPF does not require XPA (64). It is controversial whether ERCC1 is able to bind DNA and XPA simultaneously. Tsodikov *et al.* (64) used fluorescence anisotropy and measured competitive binding of XPA and DNA to the ERCC1 central domain. In contrast, Tripsianes *et al.* (80) monitored chemical shift perturbations upon XPA binding, showing that the strongest response from ERCC1 was in residues Leu139, Phe140 and Phe141 in the deep hydrophobic groove. Other residues important for ERCC1/XPA interaction were Gln107, Asn110, Ser142, Arg144, Asn147 and Arg156 (80). Tripsianes *et al.* (80) concluded that XPA and DNA have distinct binding sites on ERCC1 and suggested that simultaneous binding is possible.

How does the ERCC1–XPF complex associate with XPA?

XPA binds at ds- to ss-DNA junctions and localizes at the junction 5′ to the lesion to recruit ERCC1–XPF (84). However, in light of a model proposed by Das *et al.*, positioning ERCC1–XPF at the DNA junction 5′ to the damage lesion (63), Shell and Chazin argued that, for steric reasons, XPA must instead localize to the 3′ DNA junction (85). For this latter model to be correct and for the ERCC1/XPA interaction to occur, both DNA junctions would need to be in close proximity. Instead, we propose that XPA binds at the 5′ DNA junction and recruits the ERCC1–XPF complex, forcing the DNA junction to advance and so make space for ERCC1–XPF to bind DNA. In support of this, partial unwinding of the DNA junction occurs *in vitro* facilitating XPF cleavage 2 nt upstream of the junction. This process could be driven by a domain rearrangement within ERCC1–XPF upon DNA binding, similar to that known to occur in Archaeal XPF (69).

Mutation of the XPA-binding site of ERCC1 affects NER but does not affect repair of interstrand crosslinks

Endonuclease activity and DNA binding of the ERCC1–XPF heterodimer were not affected by ERCC1 mutations lacking the Asn110, Tyr145 and Tyr152 residues required for interaction with XPA (82). Proteins containing the XPA-binding site mutations expressed in ERCC1-deficient cells failed to associate with XPA and were only able to partially restore UV resistance (82). However, expression of these mutant proteins in ERCC1-deficient cells fully restored resistance to mitomycin-C, cisplatin and ionizing radiation (82), suggesting that the ERCC1/XPA interaction is required for NER, but not for ICL or DSB repair. Given that cisplatin causes mainly monoadducts and intrastrand crosslinks, which are both repaired by NER, in addition to the much less frequent, but more genotoxic, interstrand crosslinks that are repaired by a combination of endonucleolytic cleavage and HR, partial, rather than complete restoration of cisplatin resistance by an ERCC1 protein that cannot interact with XPA would have been anticipated.

Identification of ERCC1/XPA interaction inhibitors

The non-specific PK-C and CHK1 inhibitor, UCN-01, inhibited NER by causing a reduction in ERCC1 binding to XPA (86). Upon DNA damage and UCN-01 treatment, an accumulation of DNA-bound XPA was observed, but there was a decrease in DNA-bound ERCC1. *In silico* modelling of UCN-01 binding to ERCC1 calculated a binding energy of −4.81 kcal/mol (83). UCN-01 was proposed to bind into the XPA interaction site on ERCC1, disrupting the interaction of Tyr145 and Tyr152 in ERCC1, with several hydrogen bonds stabilizing the UCN-01/ERCC1 interaction (83). An *in silico* screen for potential inhibitors of the XPA interaction site on ERCC1 was performed, but no compounds were investigated for *in vitro* or *in vivo* activity (83).

Inhibition of the ERCC1/XPA interaction is an attractive drug target due to the existence of crystal structures and known inhibitors. Inhibition of this site *in vitro* and *in vivo* has been shown with a synthetic XPA peptide and is also proposed for UCN-01 (64,83). However, an inhibitor of this interaction would only disrupt NER and would not affect the role of ERCC1–XPF in ICL or DSB repair. Thus, synergistic use of an ERCC1/XPA inhibitor with a DNA crosslinking agent, such as cisplatin, would likely only be of limited benefit, although the result for ERCC1 protein that cannot interact with XPA, discussed in the previous section, that fully restores cisplatin resistance to ERCC1-deficient cells may indicate otherwise (82).

Interaction of XPF with RPA

During NER the ERCC1–XPF complex binds to the ss-DNA-binding protein RPA, which protects the undamaged strand, in addition to XPA, but the RPA interaction is less well understood (7,87–89). Using affinity columns, Bessho *et al.* (7) demonstrated that XPA binds ERCC1, whereas interaction with RPA was mediated by XPF. Furthermore, in a pull-down assay ERCC1–XPF bound weakly to DNA and binding was unaffected by XPA addition (87). However, upon adding RPA, the ERCC1–XPF complex was recruited to DNA more efficiently (87). Mutant XPF constructs and a yeast two-hybrid approach showed that XPF binds to the p70 subunit of RPA via its N-terminus (88). In addition, XPF containing a Pro85Ser substitution was unable to interact with RPA, but still interacted with ERCC1 and retained nuclease activity *in vitro*, although the interpretation was complicated by the additional observation that the mutant XPF was mislocalized to the cytoplasm (88). XPF Arg86Ala and Thr89Ala substitutions may also inhibit interaction with RPA (88). Furthermore, addition of RPA increased specificity and activity of ERCC1–XPF cleavage of DNA in *in vitro* endonuclease assays, whereas addition of XPA had no effect (87). When wild-type and Pro85Ser mutant XPF were expressed in XPF-defective CHO UV41 cells, only the control protein fully restored NER ability and UV resistance, suggesting that the XPF/RPA interaction is required for NER (87).

Inhibition of the XPF/RPA interaction as a target for drug discovery

Inhibition of the XPF/RPA interaction may prove to be an effective drug target as RPA has a role in both NER and ICL repair, thus inhibition could potentiate toxicity of

a range of chemotherapeutic agents. However, not enough is known about the interaction site and no crystal structures of interaction exist, so a drug discovery programme based on this target would be premature.

IMPORTANT NON-NER-RELATED INTERACTIONS OF ERCC1–XPF

XPF/SLX4 interaction in ICL repair

Recent research has identified SLX4 (also known as FANCP) as a molecular scaffold for endonucleases SLX1, ERCC1–XPF and MUS81/EME1 to facilitate the processing of branched DNA substrates (90–95). The SLX4 scaffold may also bind additional factors, such as mismatch repair proteins MSH2/MSH3, telomere-binding proteins TRF2/RAP1 and polo-like kinase 1 (91). Depletion of SLX4 induced hypersensitivity to DNA crosslinking agents, but not to UV-induced DNA damage (90,96). In a comparison of SLX4- and ERCC1-deficient mouse embryonic fibroblast (MEF) cell lines with two Fanconi anaemia cell lines (FANCA, FANCC), where there is hypersensitivity to ICLs, the SLX4 and ERCC1 mutants showed the greatest sensitivity and only the ERCC1-deficient cell line also showed hypersensitivity to UV (96).

Size exclusion chromatography indicated two cellular pools of ERCC1–XPF, one associated with the SLX4 complex and presumed responsible for the HR/ICL repair activities of ERCC1–XPF, and the other interacting with XPA and RPA and presumed responsible for NER (90). Direct interaction of the ERCC1–XPF complex with SLX4 has been demonstrated by yeast two-hybrid assays. The interaction is mediated within the N-terminal 669 residues of SLX4, probably through a conserved MLR domain, but the interaction domain on XPF is unmapped (90,91). Expression of SLX4 lacking the SLX1 interacting motif (a C-terminal deletion mutant) in SLX4-deficient MEF cells was sufficient to complement hypersensitivity to mitomycin-C, while expression of SLX4 deficient in the interaction with XPF (N-terminal deletion) was unable to complement mitomycin-C hypersensitivity, indicating the importance of the SLX4/XPF interaction in ICL repair (96). Interestingly, an endonuclease assay, utilizing a DNA stem–loop to determine cleavage specificity of ERCC1–XPF and SLX4/SLX1, showed that SLX1 nicked ds-DNA on the opposite strand to ERCC1–XPF (92).

Inhibition of the XPF/SLX4 interaction as a target for drug discovery

The XPF/SLX4 interaction is an emerging drug target. Disruption would sensitize cells to interstrand crosslinking agents without disrupting the role of ERCC1–XPF in NER. Currently, a drug discovery programme targeting this interaction would be challenging as the XPF/SLX4 interaction site awaits detailed mapping. Furthermore, the relevant crystal structures are unavailable and low SLX4 sequence conservation between species would hamper confidence in homology modelling.

FANCG and the ERCC1 central domain

FANCG-deficient cells are sensitive to ICL agents due to an inability to make a dual incision at the site of a crosslink [for review, see (18)]. In a yeast two-hybrid assay the ERCC1 central domain was reported to interact with FANCG, which forms part of the Fanconi anaemia core complex (97). The ERCC1/FANCG interaction is believed necessary to recruit ERCC1–XPF to the crosslink. Direct interaction of ERCC1 with FANCG could explain how XPF has previously been shown to co-localize with FANCA in cells, presumably through a ternary complex with FANCG (98). Site-directed mutagenesis indicated that the FANCG/ERCC1 interaction occurred through tetratricopeptide repeats (TPR) in FANCG (97). Complementation of FANCG-deficient cells with mutant FANCG proteins indicated that TPR 1, 2, 5 and 6 were all important in correcting sensitivity to the crosslinking agent mitomycin-C (99).

Inhibition of the ERCC1/FANCG interaction site as a target for drug discovery

If the interaction between ERCC1 and FANCG is confirmed, it could represent an attractive and novel drug target that would specifically block the role of ERCC1–XPF in ICL repair. Deletion of ERCC1 or FANCG interacting regions results in sensitivity to crosslinking agents, but it is unknown whether mutation of specific interaction sites on either protein is sufficient to sensitize cells. Further mapping of the interaction site would be necessary before attempting to identify inhibitors of this interaction.

MSH2 interaction with ERCC1

Using a yeast two-hybrid approach, it has been proposed that the mismatch repair protein MSH2 interacts with RAD10, the yeast homologue of human ERCC1, along with several other NER proteins (100). In humans, MSH2 forms a heterodimer with MSH6 (heterodimer known as MutSα), or MSH3 (known as MutSβ) (101). To facilitate repair, MutSβ recognizes an ICL, then in association with ERCC1–XPF, is required for the initial processing and unhooking of the lesion (101). It is thought that the ERCC1/MSH2 interaction, involving ERCC1 residues 184–260, is required for ICL repair and cisplatin resistance in an XPA-independent mechanism (102).

RAD52 interaction with XPF

ERCC1–XPF and RAD52 are important for single-strand annealing (SSA), a DNA DSBR mechanism that involves annealing homologous single-stranded ends to bridge DSBs (103). Direct physical interaction has been demonstrated between ERCC1–XPF and RAD52 *in vitro* (104). It is thought that the interaction promotes cleavage of 3′ overhangs allowing processing of non-homologous ends for repair (103). XPF interacts with the N-terminal DNA-binding region of RAD52 in a DNA-independent manner (104). RAD52 forms a heptamer around DNA and when a 6:1 ratio of RAD52:XPF is reached, the endonuclease activity of ERCC1–XPF increases 3-fold.

Super-stoichiometric amounts of RAD52 inhibit XPF activity, presumably by binding to DNA and inhibiting ERCC1–XPF recruitment (104).

TRF2 interaction with ERCC1–XPF in telomere maintenance

ERCC1–XPF is involved in telomere maintenance and it is thought that this occurs by its interaction with the TRF2 complex independent of DNA binding (105). To protect telomeres from being recognized as DSBs, 3′ overhangs at the ends of chromosomes, known as G-strands, loop back and insert into duplex DNA to form t-loops (105). TRF2 promotes t-loops and associates with ERCC1–XPF at telomeres (105). In TRF2-deficient cells, a partial loss of telomeres and associated 3′ overhangs was observed that was dependent on ERCC1–XPF expression (105,106). Overhangs are retained in ERCC1-deficient cells following inhibition of TRF2, suggesting that ERCC1–XPF is the main nuclease responsible for 3′ overhang cleavage and is inhibited by TRF2 (105).

Only a minor fraction (~1%) of ERCC1–XPF complexes with TRF2, whereas other proteins essential for NER did not associate, suggesting an NER-independent mechanism for ERCC1–XPF in telomere maintenance (105). As no direct interaction of ERCC1–XPF to TRF2 has been demonstrated, the interaction may occur through a tertiary complex. TRF2 can interact with SLX4 independently of XPF and it is therefore possible that interaction with XPF is through the SLX4 scaffold (91,92).

It has also been proposed that XPF may have a nuclease-independent role in negatively regulating TRF2-mediated control of telomeres (107). Mutant XPF proteins with nuclease site mutations deficient in endonuclease activity still localized with TRF2 and were able to complement TRF2-mediated telomere shortening in XPF-deficient cells, with activity similar to that of wild-type XPF (106,107). However, nuclease activity of XPF is required for TRF2 binding to telomeric DNA, suggesting the mechanism of negative regulation of TRF2 by nuclease inactive XPF is due to ternary complex formation with TRF2, likely via SLX4 and inhibiting DNA binding (108).

REQUIREMENTS FOR AN ERCC1–XPF DRUG DISCOVERY PROGRAMME

Production of recombinant ERCC1–XPF protein

For a drug discovery programme, significant quantities of recombinant ERCC1–XPF would be required. Expression of full-length ERCC1–XPF in *Escherichia coli* leads to predominantly aggregated protein, whereas only small quantities of soluble protein can be purified from expression in Hela cells or baculovirus-infected Sf9 insect cells (58,67). Expression of a truncated ERCC1–XPF complex in *E.coli* is possible in greater yields using $_{\Delta 95}$ERCC1–$_{\Delta 666}$XPF, lacking the ERCC1 N-terminus and the XPF helicase-like domain (58). Tsodikov *et al.* (58) showed that this truncation is active in an endonuclease assay, having the same structure-specificity as the full-length protein, but with a 60-fold slower reaction rate. In contrast, Bowles *et al.* (54) reported that recombinant ERCC1–XPF lacking the helicase-like domain is inactive *in vitro*, although this may be due to expression of ERCC1–$_{\Delta 640}$XPF containing an additional acidic linker on XPF that may inhibit the active site or bind DNA. Consequently, Bowles *et al.* (54) proposed that the endonuclease activity of truncated ERCC1–XPF observed by Tsodikov *et al.* may be non-specific nuclease activity. However, in agreement with Tsodikov *et al.*, our results show that $_{\Delta 95}$ERCC1–$_{\Delta 666}$XPF has the characteristic structure-specific nuclease activity (E. M. McNeil, and D. W. Melton, unpublished observations). We believe that expression of truncated ERCC1–XPF could be sufficient for a drug discovery programme, unless specific protein–protein interactions of the XPF helicase-like domain are being targeted.

An *in vitro* endonuclease assay for ERCC1–XPF

For a drug discovery programme, a convenient *in vitro* ERCC1–XPF endonuclease assay suitable for high-throughput screening of compounds is required. Previously, an assay based upon specific cleavage of a radioactively labelled stem12–loop22 oligonucleotide has been used routinely (58). Recently, this assay has been modified to incorporate a fluorescein label at the 5′-end and a quencher at the 3′-end of the stem [ref. (54) and E. M. McNeil, and D. W. Melton, unpublished observations]. In the presence of recombinant ERCC1–XPF, the stem–loop is cleaved 2 bp 5′ of the ss- to ds-DNA junction. ERCC1–XPF has a preference for the DNA sequence situated around the cleavage site, suggesting the presence of a T-/U-binding pocket on XPF (54). However, because ERCC1–XPF does not have a damage recognition role and is recruited to the site of DNA damage by other proteins, the biological significance of this preference is unknown.

Favoured ERCC1–XPF targets for a drug discovery programme

Developing inhibitors against the ERCC1–XPF complex will be challenging. The most tractable target is the XPF endonuclease site itself, due to lower affinity for the DNA substrate than the affinity of the various protein–protein interactions involved in the different repair roles of ERCC1–XPF. Inhibition of this site would block all the known functions of ERCC1–XPF needed for the repair of chemotherapy-induced DNA damage. However, the lack of a crystal structure for this domain of human XPF and the existence of a number of endonucleases with similar divalent cation-based cleavage mechanisms will complicate the search for compounds of the desired specificity. The only other target whose inhibition would prevent all repair roles of ERCC1–XPF is the interaction domain needed for heterodimer formation. The large hydrophobic surface area of the interaction domain makes this a formidable target, but a single amino acid deletion in this region does completely block the activity (29,61).

Inhibition of other protein–protein interactions made by the complex could also be tractable to a drug discovery

programme. For instance, if there is a requirement to enhance sensitivity to a chemotherapeutic that causes lesions repaired exclusively by NER, then targeting the ERCC1/XPA interaction site should be considered and has the advantage of existing crystal structures and drug and peptide inhibitors. If instead the requirement is to block repair of just ICLs, then inhibitors of ERCC1/XPF interactions with SLX4 or RAD52 may also be effective therapies, but these interactions are not yet sufficiently well understood to be the direct focus of drug discovery programmes.

CONCLUSION

The ERCC1–XPF complex is essential for nucleotide excision repair and its important role in a variety of other key repair pathways, such as ICL repair and DSBR, is increasingly being understood. This makes this protein a particularly attractive target to overcome the resistance of cancer cells to a range of important chemotherapeutic agents. To facilitate the development of ERCC1–XPF inhibitors we have described the mechanism of heterodimerization and the DNA binding and nuclease activity of the ERCC1–XPF complex. We have also reviewed the known protein–protein interactions made by ERCC1–XPF that are essential for nucleotide excision repair, or for its role in other repair pathways and we have proposed novel approaches for drug design to overcome chemoresistance.

FUNDING

PhD Scholarship from Cancer Research UK (to E.M.M.); Medical Research Council Technology, Scottish Chief Scientist Office (to D.W.M.); Charon Fund (to D.W.M.). Funding for open access charge: Medical Research Council Technology Development Gap Fund [Award A853-0118].

Conflict of interest statement. None declared.

REFERENCES

1. Friedberg,E.C., Walker,G.C., Siede,W., Wood,R.D., Schultz,R.A. and Ellenberger,T. (2006) *DNA Repair and Mutagenesis*, 2nd edn. ASM Press, Washington, D.C., U.S.A.
2. Aboussekhra,A., Biggerstaff,M., Shivji,M.K., Vilpo,J.A., Moncollin,V., Podust,V.N., Protić,M., Hübscher,U., Egly,J.M. and Wood,R.D. (1995) Mammalian DNA nucleotide excision repair reconstituted with purified protein components. *Cell*, **80**, 859–868.
3. Naegeli,H. and Sugasawa,K. (2011) The xeroderma pigmentosum pathway: decision tree analysis of DNA quality. *DNA Repair*, **10**, 673–683.
4. Hanawalt,P.C. and Spivak,G. (2008) Transcription-coupled DNA repair: two decades of progress and surprises. *Nat. Rev. Mol. Cell Biol.*, **9**, 958–970.
5. Camenisch,U., Dip,R., Schumacher,S.B., Schuler,B. and Naegeli,H. (2006) Recognition of helical kinks by xeroderma pigmentosum group A protein triggers DNA excision repair. *Nat. Struct. Mol. Biol.*, **13**, 278–284.
6. Li,L., Elledge,S.J., Peterson,C.A., Bales,E.S. and Legerski,R.J. (1994) Specific association between the human DNA repair proteins XPA and ERCC1. *Proc. Natl Acad. Sci. USA*, **91**, 5012–5016.
7. Bessho,T., Sancar,A., Thompson,L.H. and Thelen,M.P. (1997) Reconstitution of human excision nuclease with recombinant XPF-ERCC1 complex. *J. Biol. Chem.*, **272**, 3833–3837.
8. Schiestl,R.H. and Prakash,S. (1990) RAD10, an excision repair gene of Saccharomyces cerevisiae, is involved in the RAD1 pathway of mitotic recombination. *Mol. Cell. Biol.*, **10**, 2485–2491.
9. Ahmad,A., Robinson,A.R., Duensing,A., van Drunen,E., Beverloo,H.B., Weisberg,D.B., Hasty,P., Hoeijmakers,J.H.J. and Niedernhofer,L.J. (2008) ERCC1-XPF endonuclease facilitates DNA double-strand break repair. *Mol. Cell. Biol.*, **28**, 5082–5092.
10. Sargent,R.G., Rolig,R.L., Kilburn,A.E., Adair,G.M., Wilson,J.H. and Nairn,R.S. (1997) Recombination-dependent deletion formation in mammalian cells deficient in the nucleotide excision repair gene ERCC1. *Proc. Natl Acad. Sci. USA*, **94**, 13122–13127.
11. Niedernhofer,L.J., Essers,J., Weeda,G., Beverloo,B., de Wit,J., Muijtjens,M., Odijk,H., Hoeijmakers,J.H. and Kanaar,R. (2001) The structure-specific endonuclease Ercc1-Xpf is required for targeted gene replacement in embryonic stem cells. *EMBO J.*, **20**, 6540–6549.
12. Al-Minawi,A.Z., Saleh-Gohari,N. and Helleday,T. (2008) The ERCC1/XPF endonuclease is required for efficient single-strand annealing and gene conversion in mammalian cells. *Nucleic Acids Res.*, **36**, 1–9.
13. Fishman-Lobell,J. and Haber,J.E. (1992) Removal of nonhomologous DNA ends in double-strand break recombination: the role of the yeast ultraviolet repair gene RAD1. *Science*, **258**, 480–484.
14. Prado,F. and Aguilera,A. (1995) Role of reciprocal exchange, one-ended invasion crossover and single-strand annealing on inverted and direct repeat recombination in yeast: different requirements for the RAD1, RAD10, and RAD52 genes. *Genetics*, **139**, 109–123.
15. McVey,M. and Lee,S.E. (2008) MMEJ repair of double-strand breaks (director's cut): deleted sequences and alternative endings. *Trends Genet.*, **24**, 529–538.
16. Ma,J.-L., Kim,E.M., Haber,J.E. and Lee,S.E. (2003) Yeast Mre11 and Rad1 proteins define a Ku-independent mechanism to repair double-strand breaks lacking overlapping end sequences. *Mol. Cell. Biol.*, **23**, 8820–8828.
17. Wood,R.D. (2010) Mammalian nucleotide excision repair proteins and interstrand crosslink repair. *Environ. Mol. Mutagen*, **51**, 520–526.
18. Deans,A.J. and West,S.C. (2011) DNA interstrand crosslink repair and cancer. *Nat. Rev. Cancer*, **11**, 467–480.
19. Niedernhofer,L.J., Lalai,A.S. and Hoeijmakers,J.H.J. (2005) Fanconi anemia (cross)linked to DNA repair. *Cell*, **123**, 1191–1198.
20. Kuraoka,I., Kobertz,W.R., Ariza,R.R., Biggerstaff,M., Essigmann,J.M. and Wood,R.D. (2000) Repair of an interstrand DNA cross-link initiated by ERCC1-XPF repair/recombination nuclease. *J. Biol. Chem*, **275**, 26632–26636.
21. Niedernhofer,L.J., Odijk,H., Budzowska,M., van Drunen,E., Maas,A., Theil,A.F., de Wit,J., Jaspers,N.G.J., Beverloo,H.B., Hoeijmakers,J.H.J. *et al.* (2004) The structure-specific endonuclease Ercc1-Xpf is required to resolve DNA interstrand cross-link-induced double-strand breaks. *Mol. Cell. Biol.*, **24**, 5776–5787.
22. Bhagwat,N., Olsen,A.L., Wang,A.T., Hanada,K., Stuckert,P., Kanaar,R., D'Andrea,A., Niedernhofer,L.J. and McHugh,P.J. (2009) XPF-ERCC1 participates in the Fanconi anemia pathway of cross-link repair. *Mol. Cell. Biol.*, **29**, 6427–6437.
23. Rageul,J., Frëmin,C., Ezan,F., Baffet,G. and Langouët,S. (2011) The knock-down of ERCC1 but not of XPF causes multinucleation. *DNA Repair*, **10**, 978–990.
24. McWhir,J., Selfridge,J., Harrison,D.J., Squires,S. and Melton,D.W. (1993) Mice with DNA repair gene (ERCC-1) deficiency have elevated levels of p53, liver nuclear abnormalities and die before weaning. *Nat. Genet.*, **5**, 217–224.
25. Tian,M., Shinkura,R., Shinkura,N. and Alt,F.W. (2004) Growth retardation, early death, and DNA repair defects in mice deficient for the nucleotide excision repair enzyme XPF. *Mol. Cell. Biol.*, **24**, 1200–1205.

26. Tan,L.J., Saijo,M., Kuraoka,I., Narita,T., Takahata,C., Iwai,S. and Tanaka,K. (2012) Xeroderma pigmentosum group F protein binds to Eg5 and is required for proper mitosis: implications for XP-F and XFE. *Genes Cells*, **17**, 173–185.
27. Hoeijmakers,J.H.J. (2009) DNA damage, aging, and cancer. *N. Engl. J. Med.*, **361**, 1475–1485.
28. van Duin,M., de Wit,J., Odijk,H., Westerveld,A., Yasui,A., Koken,M.H., Hoeijmakers,J.H. and Bootsma,D. (1986) Molecular characterization of the human excision repair gene ERCC-1: cDNA cloning and amino acid homology with the yeast DNA repair gene RAD10. *Cell*, **44**, 913–923.
29. Sijbers,A.M., van der Spek,P.J., Odijk,H., van den Berg,J., van Duin,M., Westerveld,A., Jaspers,N.G., Bootsma,D. and Hoeijmakers,J.H. (1996) Mutational analysis of the human nucleotide excision repair gene ERCC1. *Nucleic Acids Res.*, **24**, 3370–3380.
30. Brookman,K.W., Lamerdin,J.E., Thelen,M.P., Hwang,M., Reardon,J.T., Sancar,A., Zhou,Z.Q., Walter,C.A., Parris,C.N. and Thompson,L.H. (1996) ERCC4 (XPF) encodes a human nucleotide excision repair protein with eukaryotic recombination homologs. *Mol. Cell. Biol.*, **16**, 6553–6562.
31. Niedernhofer,L.J., Garinis,G.A., Raams,A., Lalai,A.S., Robinson,A.R., Appeldoorn,E., Odijk,H., Oostendorp,R., Ahmad,A., van Leeuwen,W. *et al.* (2006) A new progeroid syndrome reveals that genotoxic stress suppresses the somatotroph axis. *Nature*, **444**, 1038–1043.
32. Gregg,S.Q., Robinson,A.R. and Niedernhofer,L.J. (2011) Physiological consequences of defects in ERCC1–XPF DNA repair endonuclease. *DNA Repair*, **10**, 781–791.
33. Jaspers,N.G.J., Raams,A., Silengo,M.C., Wijgers,N., Niedernhofer,L.J., Robinson,A.R., Giglia-Mari,G., Hoogstraten,D., Kleijer,W.J., Hoeijmakers,J.H.J. *et al.* (2007) First reported patient with human ERCC1 deficiency has cerebro-oculo-facio-skeletal syndrome with a mild defect in nucleotide excision repair and severe developmental failure. *Am. J. Hum. Genet.*, **80**, 457–466.
34. Nishino,T., Komori,K., Ishino,Y. and Morikawa,K. (2003) X-ray and biochemical anatomy of an archaeal XPF/Rad1/Mus81 family nuclease: similarity between its endonuclease domain and restriction enzymes. *Structure*, **11**, 445–457.
35. Ahmad,A., Enzlin,J.H., Bhagwat,N.R., Wijgers,N., Raams,A., Appledoorn,E., Theil,A.F.J., Hoeijmakers,J.H., Vermeulen,W.J., Jaspers,N.G. *et al.* (2010) Mislocalization of XPF-ERCC1 nuclease contributes to reduced DNA repair in XP-F patients. *PLoS Genet.*, **6**, e1000871.
36. Kirschner,K. and Melton,D.W. (2010) Multiple roles of the ERCC1-XPF endonuclease in DNA repair and resistance to anticancer drugs. *Anticancer Res.*, **30**, 3223–3232.
37. Usanova,S., Piée-Staffa,A., Sied,U., Thomale,J., Schneider,A., Kaina,B. and Köberle,B. (2010) Cisplatin sensitivity of testis tumour cells is due to deficiency in interstrand-crosslink repair and low ERCC1-XPF expression. *Mol. Cancer*, **9**, 248.
38. Simon,G.R., Sharma,S., Cantor,A., Smith,P. and Bepler,G. (2005) ERCC1 expression is a predictor of survival in resected patients with non-small cell lung cancer. *Chest*, **127**, 978–983.
39. Olaussen,K.A., Dunant,A., Fouret,P., Brambilla,E., André,F., Haddad,V., Taranchon,E., Filipits,M., Pirker,R., Popper,H.H. *et al.* (2006) DNA repair by ERCC1 in non-small-cell lung cancer and cisplatin-based adjuvant chemotherapy. *N. Engl. J. Med.*, **355**, 983–991.
40. Wang,L., Wei,J., Qian,X., Yin,H., Zhao,Y., Yu,L., Wang,T. and Liu,B. (2008) ERCC1 and BRCA1 mRNA expression levels in metastatic malignant effusions is associated with chemosensitivity to cisplatin and/or docetaxel. *BMC Cancer*, **8**, 97.
41. Jun,H.J., Ahn,M.J., Kim,H.S., Yi,S.Y., Han,J., Lee,S.K., Ahn,Y.C., Jeong,H.-S., Son,Y.-I., Baek,J.-H. *et al.* (2008) ERCC1 expression as a predictive marker of squamous cell carcinoma of the head and neck treated with cisplatin-based concurrent chemoradiation. *Br. J. Cancer*, **99**, 167–172.
42. Kwon,H.-C., Roh,M.S., Oh,S.Y., Kim,S.-H., Kim,M.C., Kim,J.-S. and Kim,H.-J. (2007) Prognostic value of expression of ERCC1, thymidylate synthase, and glutathione S-transferase P1 for 5-fluorouracil/oxaliplatin chemotherapy in advanced gastric cancer. *Ann. Oncol.*, **18**, 504–509.
43. Matsubara,J., Nishina,T., Yamada,Y., Moriwaki,T., Shimoda,T., Kajiwara,T., Nakajima,T.E., Kato,K., Hamaguchi,T., Shimada,Y. *et al.* (2008) Impacts of excision repair cross-complementing gene 1 (ERCC1), dihydropyrimidine dehydrogenase, and epidermal growth factor receptor on the outcomes of patients with advanced gastric cancer. *Br. J. Cancer*, **98**, 832–839.
44. Bellmunt,J., Paz-Ares,L., Cuello,M., Cecere,F.L., Albiol,S., Guillem,V., Gallardo,E., Carles,J., Mendez,P., de la Cruz,J.J. *et al.* (2007) Gene expression of ERCC1 as a novel prognostic marker in advanced bladder cancer patients receiving cisplatin-based chemotherapy. *Ann. Oncol.*, **18**, 522–528.
45. Kim,M.K., Cho,K.-J., Kwon,G.Y., Park,S.-I., Kim,Y.H., Kim,J.H., Song,H.-Y., Shin,J.H., Jung,H.Y., Lee,G.H. *et al.* (2008) ERCC1 predicting chemoradiation resistance and poor outcome in oesophageal cancer. *Eur. J. Cancer*, **44**, 54–60.
46. Zienolddiny,S., Campa,D., Lind,H., Ryberg,D., Skaug,V., Stangeland,L., Phillips,D.H., Canzian,F. and Haugen,A. (2006) Polymorphisms of DNA repair genes and risk of non-small cell lung cancer. *Carcinogenesis*, **27**, 560–567.
47. Li,W. and Melton,D.W. (2012) Cisplatin regulates the MAPK kinase pathway to induce increased expression of DNA repair gene ERCC1 and increase melanoma chemoresistance. *Oncogene*, **31**, 2412–2422.
48. Li,Q., Gardner,K., Zhang,L., Tsang,B., Bostick-Bruton,F. and Reed,E. (1998) Cisplatin induction of ERCC-1 mRNA expression in A2780/CP70 human ovarian cancer cells. *J. Biol. Chem.*, **273**, 23419–23425.
49. Mirmohammadsadegh,A., Mota,R., Gustrau,A., Hassan,M., Nambiar,S., Marini,A., Bojar,H., Tannapfel,A. and Hengge,U.R. (2007) ERK1/2 is highly phosphorylated in melanoma metastases and protects melanoma cells from cisplatin-mediated apoptosis. *J. Invest. Dermatol.*, **127**, 2207–2215.
50. Andrieux,L.O., Fautrel,A., Bessard,A., Guillouzo,A., Baffet,G. and Langouët,S. (2007) GATA-1 is essential in EGF-mediated induction of nucleotide excision repair activity and ERCC1 expression through ERK2 in human hepatoma cells. *Cancer Res.*, **67**, 2114–2123.
51. Song,L., Ritchie,A.-M., McNeil,E.M., Li,W. and Melton,D.W. (2011) Identification of DNA repair gene Ercc1 as a novel target in melanoma. *Pigment Cell Melanoma Res.*, **24**, 966–971.
52. de Laat,W.L., Appeldoorn,E., Jaspers,N.G. and Hoeijmakers,J.H. (1998) DNA structural elements required for ERCC1-XPF endonuclease activity. *J. Biol. Chem.*, **273**, 7835–7842.
53. Bardwell,A.J., Bardwell,L., Tomkinson,A.E. and Friedberg,E.C. (1994) Specific cleavage of model recombination and repair intermediates by the yeast Rad1-Rad10 DNA endonuclease. *Science*, **265**, 2082–2085.
54. Bowles,M., Lally,J., Fadden,A.J., Mouilleron,S., Hammonds,T. and McDonald,N.Q. (2012) Fluorescence-based incision assay for human XPF-ERCC1 activity identifies important elements of DNA junction recognition. *Nucleic Acids Res.*, **40**, e101.
55. Gaillard,P.H. and Wood,R.D. (2001) Activity of individual ERCC1 and XPF subunits in DNA nucleotide excision repair. *Nucleic Acids Res.*, **29**, 872–879.
56. Sgouros,J., Gaillard,P.H. and Wood,R.D. (1999) A relationship betweena DNA-repair/recombination nuclease family and archaeal helicases. *Trends Biochem. Sci.*, **24**, 95–97.
57. Tripsianes,K., Folkers,G., Ab,E., Das,D., Odijk,H., Jaspers,N.G.J., Hoeijmakers,J.H.J., Kaptein,R. and Boelens,R. (2005) The structure of the human ERCC1/XPF interaction domains reveals a complementary role for the two proteins in nucleotide excision repair. *Structure*, **13**, 1849–1858.
58. Tsodikov,O.V., Enzlin,J.H., Schärer,O.D. and Ellenberger,T. (2005) Crystal structure and DNA binding functions of ERCC1, a subunit of the DNA structure-specific endonuclease XPF-ERCC1. *Proc. Natl Acad. Sci. USA*, **102**, 11236–11241.
59. Choi,Y.-J., Ryu,K.-S., Ko,Y.-M., Chae,Y.-K., Pelton,J.G., Wemmer,D.E. and Choi,B.-S. (2005) Biophysical characterization of the interaction domains and mapping of the contact residues in the XPF-ERCC1 complex. *J. Biol. Chem.*, **280**, 28644–28652.
60. Arora,S., Kothandapani,A., Tillison,K., Kalman-Maltese,V. and Patrick,S.M. (2010) Downregulation of XPF-ERCC1 enhances cisplatin efficacy in cancer cells. *DNA Repair*, **9**, 745–753.

61. de Laat,W.L., Sijbers,A.M., Odijk,H., Jaspers,N.G. and Hoeijmakers,J.H. (1998) Mapping of interaction domains between human repair proteins ERCC1 and XPF. *Nucleic Acids Res.*, **26**, 4146–4152.
62. Su,Y., Orelli,B., Madireddy,A., Niedernhofer,L.J. and Schärer,O.D. (2012) Multiple DNA binding domains mediate the function of the ERCC1-XPF protein in nucleotide excision repair. *J. Biol. Chem.*, **287**, 21846–21855.
63. Das,D., Folkers,G.E., van Dijk,M., Jaspers,N.G.J., Hoeijmakers,J.H.J., Kaptein,R. and Boelens,R. (2012) The structure of the XPF-ssDNA complex underscores the distinct roles of the XPF and ERCC1 helix- hairpin-helix domains in ss/ds DNA recognition. *Structure*, **20**, 667–675.
64. Tsodikov,O.V., Ivanov,D., Orelli,B., Staresincic,L., Shoshani,I., Oberman,R., Schärer,O.D., Wagner,G. and Ellenberger,T. (2007) Structural basis for the recruitment of ERCC1-XPF to nucleotide excision repair complexes by XPA. *EMBO J.*, **26**, 4768–4776.
65. Vassilev,L.T., Vu,B.T., Graves,B., Carvajal,D., Podlaski,F., Filipovic,Z., Kong,N., Kammlott,U., Lukacs,C., Klein,C. *et al.* (2004) In vivo activation of the p53 pathway by small-molecule antagonists of MDM2. *Science*, **303**, 844–848.
66. Das,D., Tripsianes,K., Jaspers,N.G.J., Hoeijmakers,J.H.J., Kaptein,R., Boelens,R. and Folkers,G.E. (2008) The HhH domain of the human DNA repair protein XPF forms stable homodimers. *Proteins*, **70**, 1551–1563.
67. Enzlin,J.H. and Schärer,O.D. (2002) The active site of the DNA repair endonuclease XPF-ERCC1 forms a highly conserved nuclease motif. *EMBO J.*, **21**, 2045–2053.
68. Kelley,L.A. and Sternberg,M.J.E. (2009) Protein structure prediction on the Web: a case study using the Phyre server. *Nat. Protoc.*, **4**, 363–371.
69. Newman,M., Murray-Rust,J., Lally,J., Rudolf,J., Fadden,A., Knowles,P.P., White,M.F. and McDonald,N.Q. (2005) Structure of an XPF endonuclease with and without DNA suggests a model for substrate recognition. *EMBO J.*, **24**, 895–905.
70. Dorjsuren,D., Kim,D., Maloney,D.J., Wilson,D.M. and Simeonov,A. (2011) Complementary non-radioactive assays for investigation of human flap endonuclease 1 activity. *Nucleic Acids Res.*, **39**, e11.
71. Tumey,L.N., Bom,D., Huck,B., Gleason,E., Wang,J., Silver,D., Brunden,K., Boozer,S., Rundlett,S., Sherf,B. *et al.* (2005) The identification and optimization of a N-hydroxy urea series of flap endonuclease 1 inhibitors. *Bioorg. Med. Chem. Lett.*, **15**, 277–281.
72. Tumey,L.N., Huck,B., Gleason,E., Wang,J., Silver,D., Brunden,K., Boozer,S., Rundlett,S., Sherf,B., Murphy,S. *et al.* (2004) The identification and optimization of 2,4-diketobutyric acids as flap endonuclease 1 inhibitors. *Bioorg. Med. Chem. Lett.*, **14**, 4915–4918.
73. Rai,G., Vyjayanti,V.N., Dorjsuren,D., Simeonov,A., Jadhav,A., Wilson,D.M. 3rd and Maloney,D.J. (2012) Synthesis, biological evaluation, and structure-activity relationships of a novel class of apurinic/apyrimidinic Endonuclease 1 inhibitors. *J. Med. Chem.*, **55**, 3101–3112.
74. Manvilla,B.A., Wauchope,O., Seley-Radtke,K.L. and Drohat,A.C. (2011) NMR studies reveal an unexpected binding site for a redox inhibitor of AP endonuclease 1. *Biochemistry*, **50**, 10540–10549.
75. Huang,F., Motlekar,N.A., Burgwin,C.M., Napper,A.D., Diamond,S.L. and Mazin,A.V. (2011) Identification of specific inhibitors of human RAD51 recombinase using high-throughput screening. *ACS Chem. Biol.*, **6**, 628–635.
76. Nishino,T., Komori,K., Tsuchiya,D., Ishino,Y. and Morikawa,K. (2005) Crystal structure and functional implications of Pyrococcus furiosus hef helicase domain involved in branched DNA processing. *Structure*, **13**, 143–153.
77. Caruthers,J.M. and McKay,D.B. (2002) Helicase structure and mechanism. *Curr. Opin. Struct. Biol.*, **12**, 123–133.
78. Schneider,R. and Schweiger,M. (1991) The yeast DNA repair proteins RAD1 and RAD7 share similar putative functional domains. *FEBS Lett.*, **283**, 203–206.
79. Sijbers,A.M., de Laat,W.L., Ariza,R.R., Biggerstaff,M., Wei,Y.F., Moggs,J.G., Carter,K.C., Shell,B.K., Evans,E., de Jong,M.C. *et al.* (1996) Xeroderma pigmentosum group F caused by a defect in a structure-specific DNA repair endonuclease. *Cell*, **86**, 811–822.
80. Tripsianes,K., Folkers,G.E., Zheng,C., Das,D., Grinstead,J.S., Kaptein,R. and Boelens,R. (2007) Analysis of the XPA and ssDNA-binding surfaces on the central domain of human ERCC1 reveals evidence for subfunctionalization. *Nucleic Acids Res.*, **35**, 5789–5798.
81. Li,L., Peterson,C.A., Lu,X. and Legerski,R.J. (1995) Mutations in XPA that prevent association with ERCC1 are defective in nucleotide excision repair. *Mol. Cell. Biol.*, **15**, 1993–1998.
82. Orelli,B., McClendon,T.B., Tsodikov,O.V., Ellenberger,T., Niedernhofer,L.J. and Schärer,O.D. (2010) The XPA-binding domain of ERCC1 is required for nucleotide excision repair but not other DNA repair pathways. *J. Biol. Chem.*, **285**, 3705–3712.
83. Barakat,K.H., Torin Huzil,J., Luchko,T., Jordheim,L., Dumontet,C. and Tuszynski,J. (2009) Characterization of an inhibitory dynamic pharmacophore for the ERCC1-XPA interaction using a combined molecular dynamics and virtual screening approach. *J. Mol. Graph. Model*, **28**, 113–130.
84. Krasikova,Y.S., Rechkunova,N.I., Maltseva,E.A., Petruseva,I.O. and Lavrik,O.I. (2010) Localization of xeroderma pigmentosum group A protein and replication protein A on damaged DNA in nucleotide excision repair. *Nucleic Acids Res.*, **38**, 8083–8094.
85. Shell,S.M. and Chazin,W.J. (2012) XPF-ERCC1: On the Bubble. *Structure*, **20**, 566–568.
86. Jiang,H. and Yang,L.Y. (1999) Cell cycle checkpoint abrogator UCN-01 inhibits DNA repair: association with attenuation of the interaction of XPA and ERCC1 nucleotide excision repair proteins. *Cancer Res.*, **59**, 4529–4534.
87. Matsunaga,T., Park,C.H., Bessho,T., Mu,D. and Sancar,A. (1996) Replication protein A confers structure-specific endonuclease activities to the XPF-ERCC1 and XPG subunits of human DNA repair excision nuclease. *J. Biol. Chem.*, **271**, 11047–11050.
88. Fisher,L.A., Bessho,M., Wakasugi,M., Matsunaga,T. and Bessho,T. (2011) Role of interaction of XPF with RPA in nucleotide excision repair. *J. Mol. Biol.*, **413**, 337–346.
89. de Laat,W.L., Appeldoorn,E., Sugasawa,K., Weterings,E., Jaspers,N.G. and Hoeijmakers,J.H. (1998) DNA-binding polarity of human replication protein A positions nucleases in nucleotide excision repair. *Genes Dev.*, **12**, 2598–2609.
90. Muñoz,I.M., Hain,K., Déclais,A.-C., Gardiner,M., Toh,G.W., Sanchez-Pulido,L., Heuckmann,J.M., Toth,R., Macartney,T., Eppink,B. *et al.* (2009) Coordination of structure-specific nucleases by human SLX4/BTBD12 is required for DNA repair. *Mol. Cell*, **35**, 116–127.
91. Svendsen,J.M., Smogorzewska,A., Sowa,M.E., O'Connell,B.C., Gygi,S.P., Elledge,S.J. and Harper,J.W. (2009) Mammalian BTBD12/SLX4 assembles a Holliday junction resolvase and is required for DNA repair. *Cell*, **138**, 63–77.
92. Fekairi,S., Scaglione,S., Chahwan,C., Taylor,E.R., Tissier,A., Coulon,S., Dong,M.-Q., Ruse,C., Yates,J.R. 3rd, Russell,P. *et al.* (2009) Human SLX4 is a Holliday junction resolvase subunit that binds multiple DNA repair/recombination endonucleases. *Cell*, **138**, 78–89.
93. Andersen,S.L., Bergstralh,D.T., Kohl,K.P., LaRocque,J.R., Moore,C.B. and Sekelsky,J. (2009) Drosophila MUS312 and the vertebrate ortholog BTBD12 interact with DNA structure-specific endonucleases in DNA repair and recombination. *Mol. Cell*, **35**, 128–135.
94. Kim,Y., Lach,F.P., Desetty,R., Hanenberg,H., Auerbach,A.D. and Smogorzewska,A. (2011) Mutations of the SLX4 gene in Fanconi anemia. *Nat. Genet.*, **43**, 142–146.
95. Stoepker,C., Hain,K., Schuster,B., Hilhorst-Hofstee,Y., Rooimans,M.A., Steltenpool,J., Oostra,A.B., Eirich,K., Korthof,E.T., Nieuwint,A.W.M. *et al.* (2011) SLX4, a coordinator of structure-specific endonucleases, is mutated in a new Fanconi anemia subtype. *Nat. Genet.*, **43**, 138–141.
96. Crossan,G.P., van der Weyden,L., Rosado,I.V., Langevin,F., Gaillard,P.-H.L., McIntyre,R.E., Gallagher,F., Kettunen,M.I., Lewis,D.Y., Brindle,K. *et al.* (2011) Disruption of mouse Slx4, a regulator of structure-specific nucleases, phenocopies Fanconi anemia. *Nat. Genet.*, **43**, 147–152.

97. Wang,C. and Lambert,M.W. (2010) The Fanconi anemia protein, FANCG, binds to the ERCC1-XPF endonuclease via its tetratricopeptide repeats and the central domain of ERCC1. *Biochemistry*, **49**, 5560–5569.
98. Sridharan,D., Brown,M., Lambert,W.C., McMahon,L.W. and Lambert,M.W. (2003) Nonerythroid alphaII spectrin is required for recruitment of FANCA and XPF to nuclear foci induced by DNA interstrand cross-links. *J. Cell. Sci.*, **116**, 823–835.
99. Blom,E., van de Vrugt,H.J., de Vries,Y., de Winter,J.P., Arwert,F. and Joenje,H. (2004) Multiple TPR motifs characterize the Fanconi anemia FANCG protein. *DNA Repair*, **3**, 77–84.
100. Bertrand,P., Tishkoff,D.X., Filosi,N., Dasgupta,R. and Kolodner,R.D. (1998) Physical interaction between components of DNA mismatch repair and nucleotide excision repair. *Proc. Natl Acad. Sci. USA*, **95**, 14278–14283.
101. Zhang,N., Lu,X., Zhang,X., Peterson,C.A. and Legerski,R.J. (2002) hMutSbeta is required for the recognition and uncoupling of psoralen interstrand cross-links in vitro. *Mol. Cell. Biol.*, **22**, 2388–2397.
102. Lan,L., Hayashi,T., Rabeya,R.M., Nakajima,S., Kanno,S.I., Takao,M., Matsunaga,T., Yoshino,M., Ichikawa,M., Riele,H. *et al.* (2004) Functional and physical interactions between ERCC1 and MSH2 complexes for resistance to cis-diamminedichloroplatinum(II) in mammalian cells. *DNA Repair*, **3**, 135–143.
103. Bennardo,N., Cheng,A., Huang,N. and Stark,J.M. (2008) Alternative-NHEJ is a mechanistically distinct pathway of mammalian chromosome break repair. *PLoS Genet.*, **4**, e1000110.
104. Motycka,T.A., Bessho,T., Post,S.M., Sung,P. and Tomkinson,A.E. (2004) Physical and functional interaction between the XPF/ERCC1 endonuclease and hRad52. *J. Biol. Chem.*, **279**, 13634–13639.
105. Zhu,X.-D., Niedernhofer,L., Kuster,B., Mann,M., Hoeijmakers,J.H.J. and de Lange,T. (2003) ERCC1/XPF removes the 3' overhang from uncapped telomeres and represses formation of telomeric DNA-containing double minute chromosomes. *Mol. Cell*, **12**, 1489–1498.
106. Muñoz,P., Blanco,R., Flores,J.M. and Blasco,M.A. (2005) XPF nuclease-dependent telomere loss and increased DNA damage in mice overexpressing TRF2 result in premature aging and cancer. *Nat. Genet.*, **37**, 1063–1071.
107. Wu,Y., Zacal,N.J., Rainbow,A.J. and Zhu,X.-D. (2007) XPF with mutations in its conserved nuclease domain is defective in DNA repair but functions in TRF2-mediated telomere shortening. *DNA Repair*, **6**, 157–166.
108. Wu,Y., Mitchell,T.R.H. and Zhu,X.-D. (2008) Human XPF controls TRF2 and telomere length maintenance through distinctive mechanisms. *Mech. Ageing Dev.*, **129**, 602–610.

10 Chapter 10: Appendix

10.1 Cell culture dose-response curves on A375 human melanoma cells

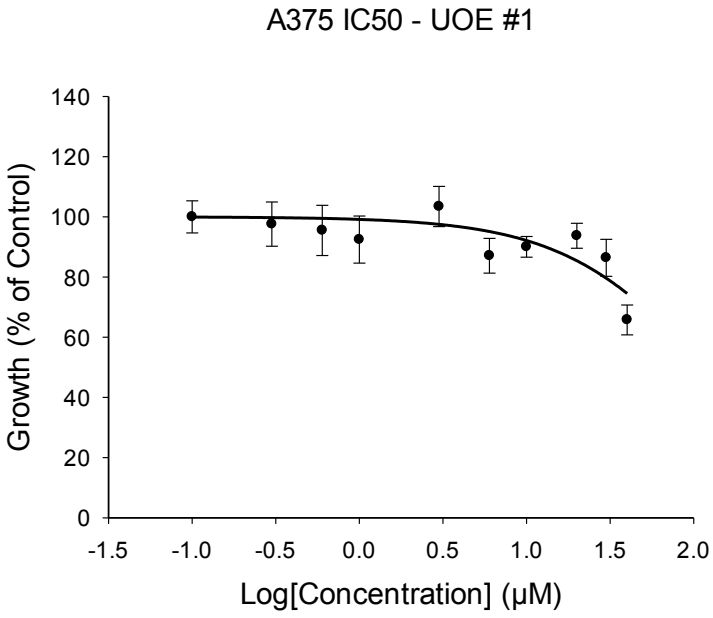

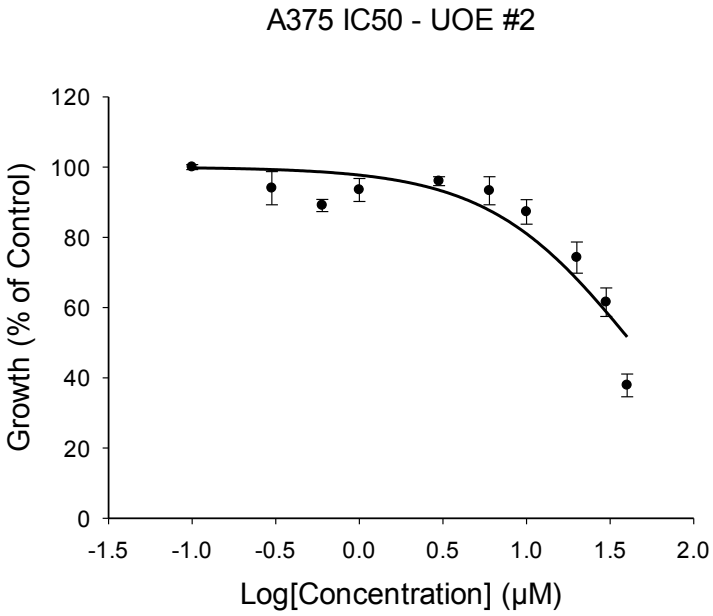

A375 IC50 - UOE #18

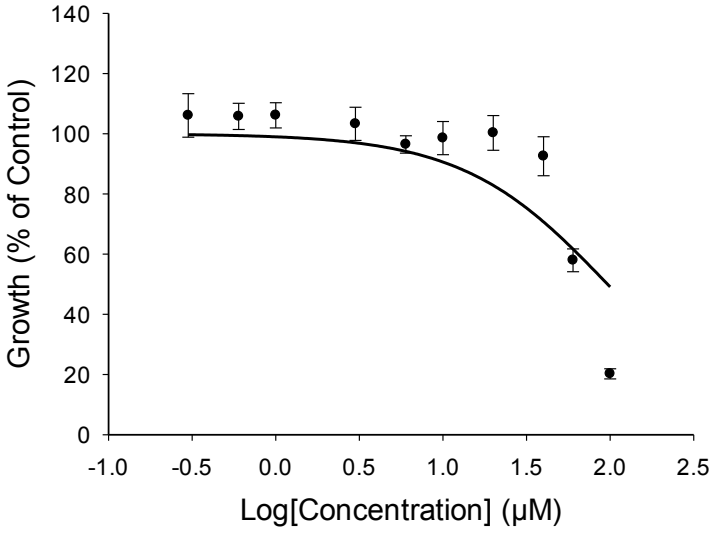

A375 IC50 - UOE #26

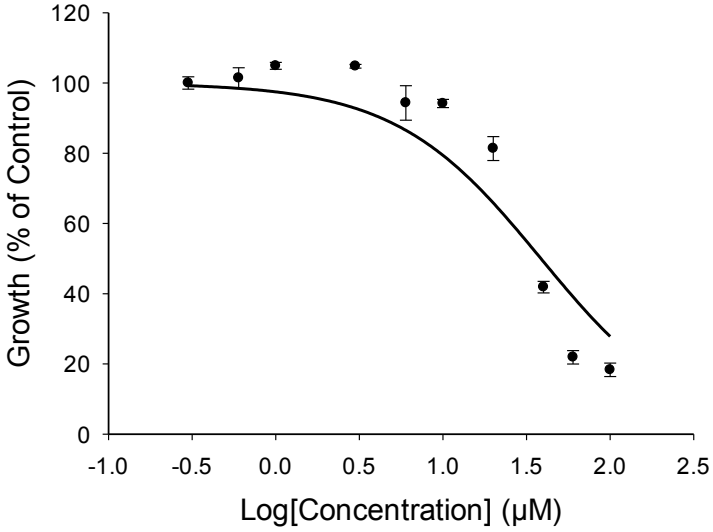

A375 IC50 - UOE #38

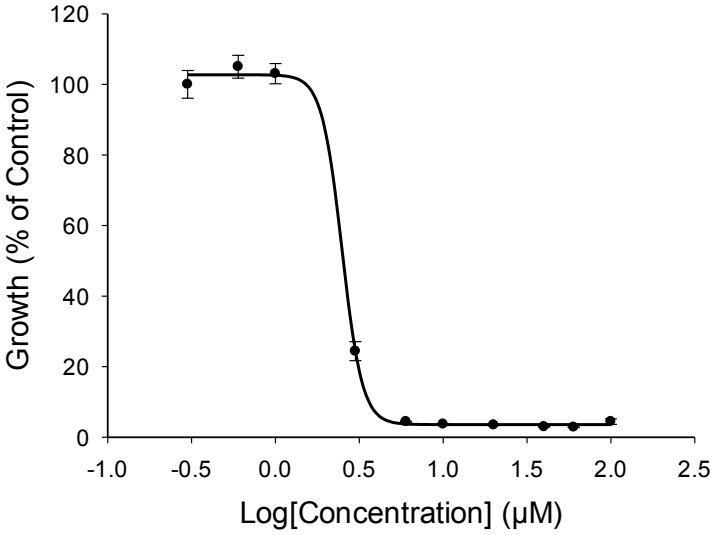

A375 IC50 - UOE #44

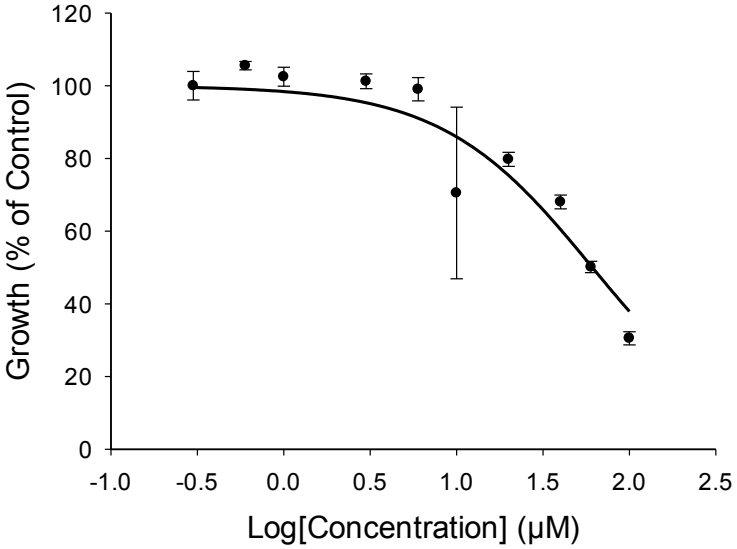

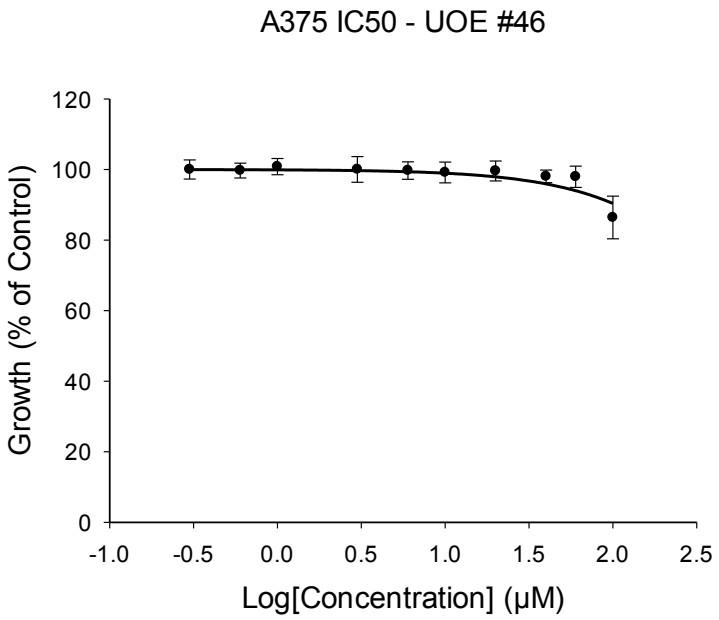

10.2 Standard ERCC1-XPF assay dose-response curves

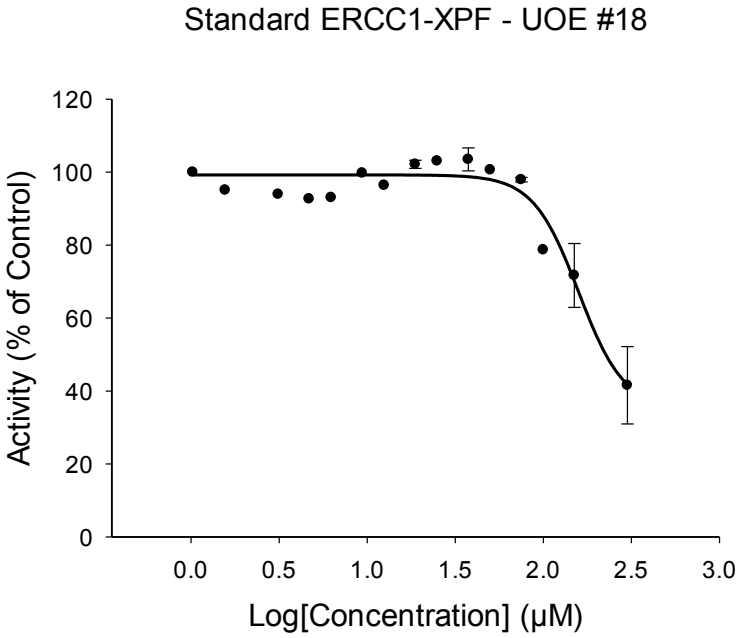

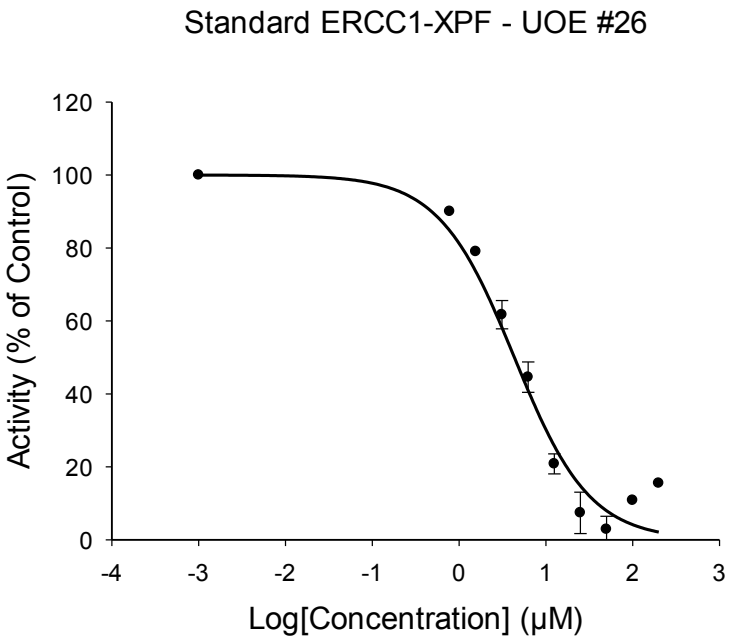
Standard ERCC1-XPF - UOE #26
Activity (% of Control)
120
100
80
60
40
20
0
-4
-3
-2
-1
0
1
2
3
Log[Concentration] (µM)

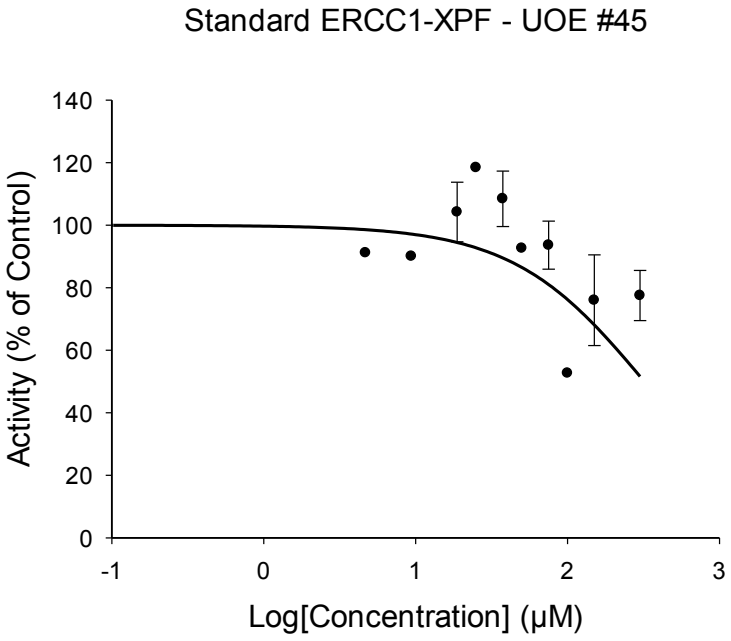
Standard ERCC1-XPF - UOE #45
Activity (% of Control)
140
120
100
80
60
40
20
0
-1
0
1
2
3
Log[Concentration] (µM)

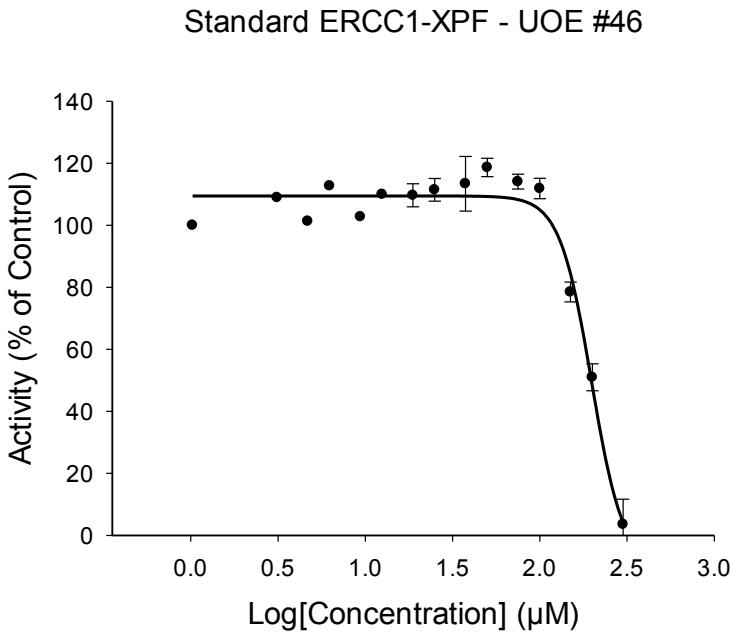
Standard ERCC1-XPF - UOE #46
Activity (% of Control)
140
120
100
80
60
40
20
0
0.0
0.5
1.0
1.5
2.0
2.5
3.0
Log[Concentration] (µM)

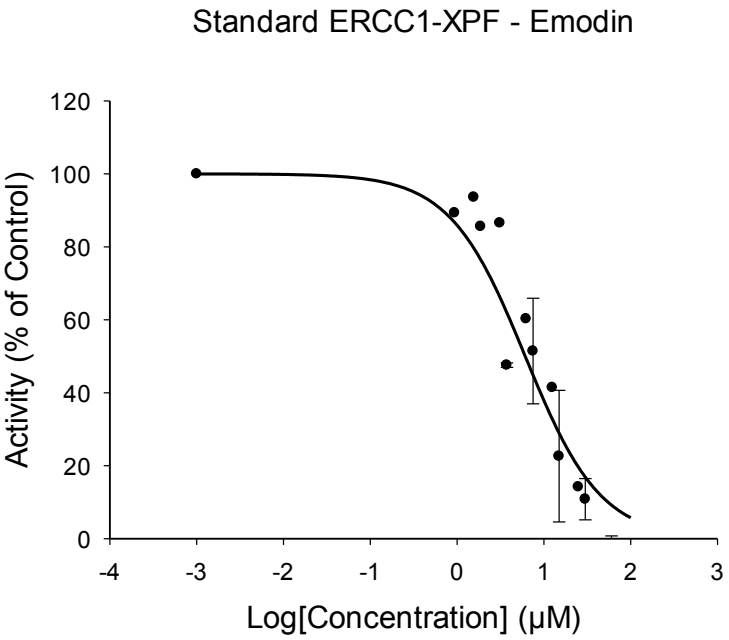
Standard ERCC1-XPF - Emodin
Activity (% of Control)
120
100
80
60
40
20
0
-4
-3
-2
-1
0
1
2
3
Log[Concentration] (µM)

10.3 Pre-incubated ERCC1-XPF assay dose-response curves

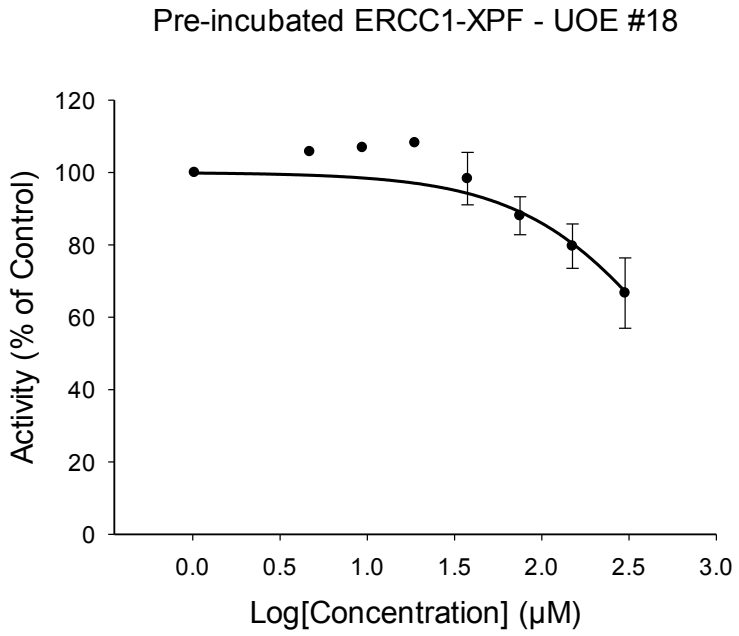

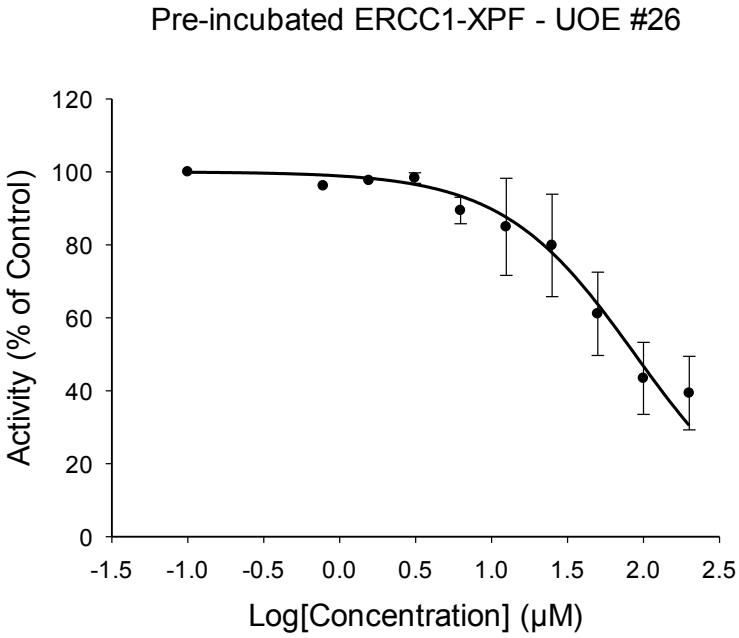

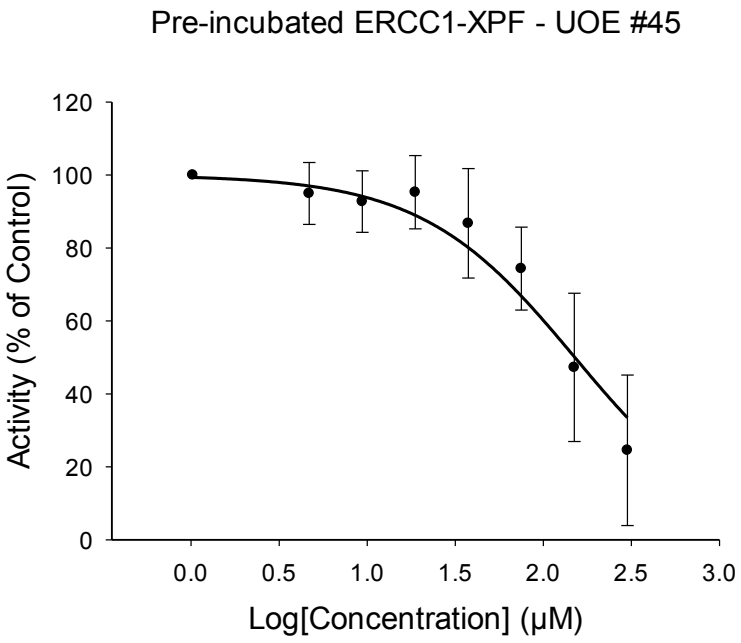
Pre-incubated ERCC1-XPF - UOE #45
Activity (% of Control)
120
100
80
60
40
20
0
0.0
0.5
1.0
1.5
2.0
2.5
3.0
Log[Concentration] (µM)

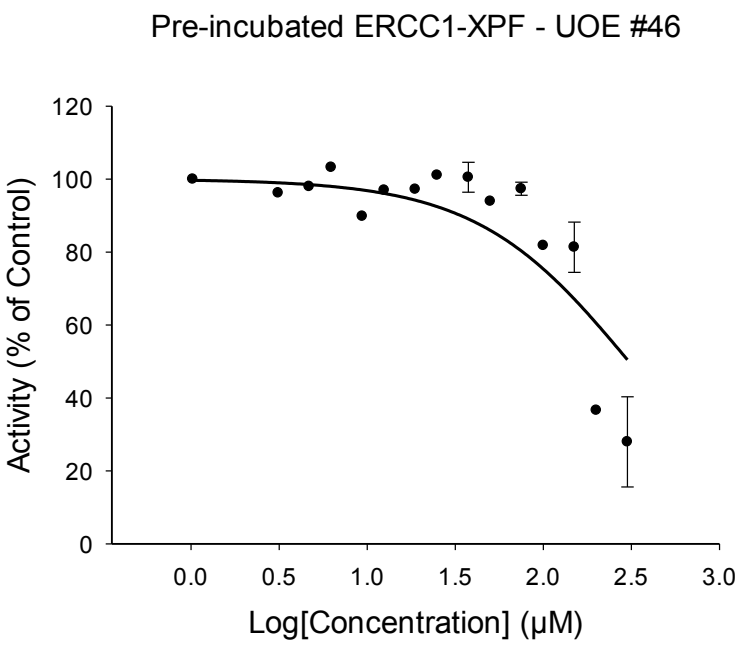
Pre-incubated ERCC1-XPF - UOE #46
Activity (% of Control)
120
100
80
60
40
20
0
0.0
0.5
1.0
1.5
2.0
2.5
3.0
Log[Concentration] (µM)

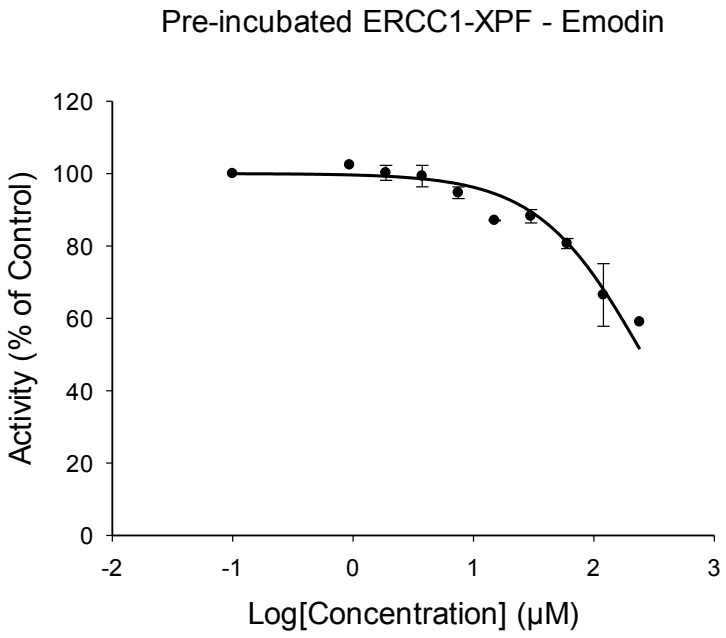

10.4 FEN1 assay dose-response curves

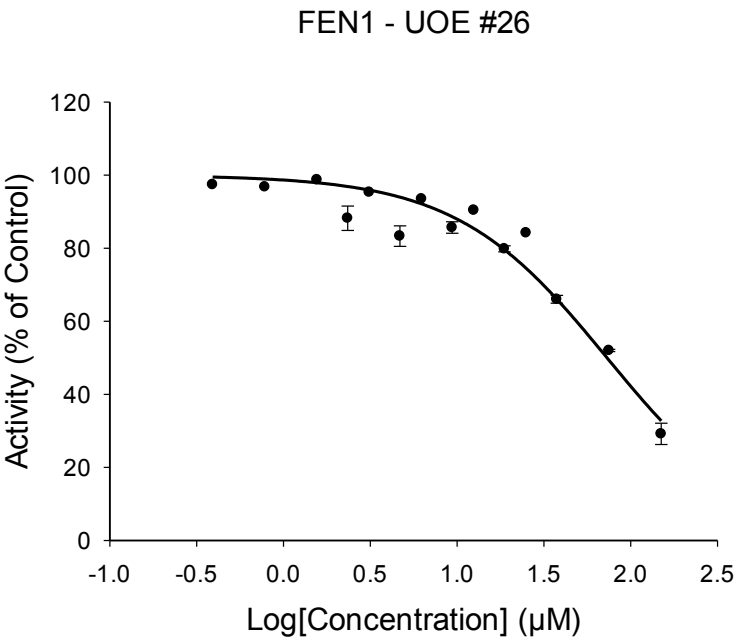

10.5 DNase1 assay dose-response curves